

---

Award Number: DAMD17-00-1-0316

TITLE: Dual-Energy Digital Mammography with a Full-Field aSi/CsI  
Flat-Panel Imager

PRINCIPAL INVESTIGATOR: Chris C. Shaw, Ph.D.

CONTRACTING ORGANIZATION: The University of Texas M.D. Anderson  
Cancer Center  
Houston, Texas 77030

REPORT DATE: September 2001

TYPE OF REPORT: Annual

PREPARED FOR: U.S. Army Medical Research and Materiel Command  
Fort Detrick, Maryland 21702-5012

DISTRIBUTION STATEMENT: Approved for Public Release;  
Distribution Unlimited

The views, opinions and/or findings contained in this report are those of the author(s) and should not be construed as an official Department of the Army position, policy or decision unless so designated by other documentation.

20020124 266

# REPORT DOCUMENTATION PAGE

*Form Approved*  
**OMB No. 074-0188**

Public reporting burden for this collection of information is estimated to average 1 hour per response, including the time for reviewing instructions, searching existing data sources, gathering and maintaining the data needed, and completing and reviewing this collection of information. Send comments regarding this burden estimate or any other aspect of this collection of information, including suggestions for reducing this burden to Washington Headquarters Services, Directorate for Information Operations and Reports, 1215 Jefferson Davis Highway, Suite 1204, Arlington, VA 22202-4302, and to the Office of Management and Budget, Paperwork Reduction Project (0704-0188), Washington, DC 20503

<b>1. AGENCY USE ONLY (Leave blank)</b>	<b>2. REPORT DATE</b> September 2001	<b>3. REPORT TYPE AND DATES COVERED</b> Annual (1 Sep 00 - 31 Aug 01)
---	---	--

<b>4. TITLE AND SUBTITLE</b> Dual-Energy Digital Mammography with a Full-Field aSi/CsI Flat-Panel Imager	<b>5. FUNDING NUMBERS</b> DAMD17-00-1-0316
---	---

<b>6. AUTHOR(S)</b> Chris C. Shaw, Ph.D.	
---	--

<b>7. PERFORMING ORGANIZATION NAME(S) AND ADDRESS(ES)</b>  The University of Texas M.D. Anderson Cancer Center Houston, Texas 77030  E-Mail: cshaw@di.mdacc.tmc.edu	<b>8. PERFORMING ORGANIZATION REPORT NUMBER</b>
--	---

<b>9. SPONSORING / MONITORING AGENCY NAME(S) AND ADDRESS(ES)</b>  U.S. Army Medical Research and Materiel Command Fort Detrick, Maryland 21702-5012	<b>10. SPONSORING / MONITORING AGENCY REPORT NUMBER</b>
--	---

**11. SUPPLEMENTARY NOTES**

<b>12a. DISTRIBUTION / AVAILABILITY STATEMENT</b> Approved for Public Release; Distribution Unlimited	<b>12b. DISTRIBUTION CODE</b>
--	-------------------------------

**13. Abstract (Maximum 200 Words) (abstract should contain no proprietary or confidential information)**  
The large goals of this project are to develop and investigate dual-energy subtraction imaging technique for use with an amorphous silicon/cesium iodide based flat panel digital mammography system. With this technique, cluttered tissue structures can be cancelled out to enhance the detection and visualization of microcalcifications. In the first year, we have performed necessary theoretical and numerical studies to investigate the calcification signal-to-noise ratio in the subtraction image as a function of x-ray spectrum combination, exposure distribution, scintillator material, calcification thickness, breast thickness and tissue composition. We have demonstrated with numerical computations that with 1000 mR un-attenuated total exposure at detector, the proposed dual-energy technique can be used to image and detect calcifications as small as 250 microns. We have also shown that 25 kVp Mo/Mo and 50 kVp W/La x-rays would provide optimal spectrum combination for best calcification SNR in the subtraction image. To prepare for actual implementation and further investigation, we have also measured, modeled and validated image signal as a function of x-ray technique, breast thickness and breast composition. Current mean glandular dose calculation has been extended to high kVp applications.

<b>14. Subject Terms (keywords previously assigned to proposal/abstract or terms which apply to this award)</b> Digital mammography, amorphous silicon/cesium iodide flat panel Dual-energy subtraction imaging, detection of microcalcifications,	<b>15. NUMBER OF PAGES</b> 320
	<b>16. PRICE CODE</b>

<b>17. SECURITY CLASSIFICATION OF REPORT</b> Unclassified	<b>18. SECURITY CLASSIFICATION OF THIS PAGE</b> Unclassified	<b>19. SECURITY CLASSIFICATION OF ABSTRACT</b> Unclassified	<b>20. LIMITATION OF ABSTRACT</b> Unlimited
--	---	--	--

## Table of Contents

Cover.....	1
SF 298.....	2
Table of Contents.....	3
Introduction.....	4
Body.....	5
Key Research Accomplishments.....	10
Reportable Outcomes.....	11
Conclusions.....	13
References.....	15
Appendices.....	16

## Introduction

The large goals of this research is to investigate the feasibility of implementing and using dual-energy subtraction imaging technique with an aSi:H/CsI:Tl flat-panel digital mammography unit for improved calcification imaging in background limited situations. To achieve these goals, we plan to proceed with the following tasks:

1. Model the detector system as well as the dual-energy subtraction imaging technique. Develop the framework for numerical studies.
2. Estimate and optimize calcification SNR as function of various imaging parameters.
3. Devise and implement the dual-energy subtraction technique.
4. Perform phantom studies to validate the modeling and numerical studies.
5. Perform a limited patient study to demonstrate the feasibility of the proposed technique.

## Body

In this part of report, we summarize the research progress according to the original Statement of Work.

### MDACC:

#### *Task 1: Modeling of imaging chain (months 1-15)*

The modeling and numerical studies at MDACC began even before we were awarded this grant and before we received the aSi:H/CsI:Tl flat-panel based Full Field Digital Mammography (FFDM) unit (GE Medical Systems, Milwaukee, WI). We have emphasized on issues independent of the detector systems and focused more on the dual-energy subtraction imaging technique itself. The efforts can be summarized as follows:

#### 1. Modeling

We have developed a theoretical framework to allow the calcification SNR to be estimated as a function of the spectrum combination, exposures, breast thickness and breast composition. The model has been described in M. Lemacks' thesis (Chapter 4) and in Ref. 5. With the modeling we have accomplished two objectives:

- A) Formulation of the dual-energy calcification imaging problem (ML Thesis, Section 4.2 and Reference 5)

We have converted the calcification imaging problem into a dual-material (glandular tissue and calcification) and dual-energy problem assuming that the breast thickness can be measured externally for the compressed part of the breast. Alternatively, the thickness of the uncompressed part of the breast can be measured through dual-energy subtraction imaging while ignoring the sparsely present calcifications. We have demonstrated the

analytical solution of the dual-energy problem by assuming that the x-rays used are mono-energetic. We have also formulated the problem for the poly-energetic case. However, the problem cannot be solved analytically but through calibration and interpolation.

#### B) Derivation of the calcification SNR (ML Thesis, Section 4.2 and Reference 5)

We have derived and expressed the calcification SNR in the subtraction images as a function of unattenuated low and high energy input spectra, attenuation coefficients for breast tissues, calcification and detector materials, calcification size, exposures, breast thickness and tissue composition. This constitutes the basic framework for our SNR study.

### 2. SNR study

We have used the model in conjunction with published spectral data, attenuation coefficients to estimate the calcification SNR and optimize the selection of some imaging parameters, notably the weighting ratios for exposure distribution and selection of kVp, target and filter for low and high energy x-rays. The results were described and discussed in details in both M. Lemacks' thesis (Chapter 4) and Ref. 5. The results are summarized as follows: (Figure numbers refer to those in Reference 5)

A) The CsI:Tl scintillator has a higher absorption ratio than Gd<sub>2</sub>O<sub>2</sub>S:Tb at energies greater than ~33 keV (Figure 2) due to its K-edges at 33.2 keV and 36 keV. Since more photons are detected for a given exposure by CsI, the calcification images with CsI scintillator have lower noise (higher SNR) compared with GdOS. A  $\mu$ C size of 250  $\mu$ m yielded an object CNR of approximately 3:1 with the CsI scintillator and approximately 2:1 with the GdOS scintillator (Figures 7 and 8). Hence, CsI is better suited for dual-energy subtraction mammography than the GdOS scintillator.

B) The *CCNR* and *CCBR* were calculated for energies ranging from 25–140 keV (Figure 6) which showed that there is not an advantage in using higher energies (>50 keV) for dual-energy subtraction mammography because as the energy increases, both the *CCNR* and the *CCBR* decrease. The limitation of the  $\mu$ C visibility due to the *CCBR* can be eliminated by performing dual-energy subtraction.

C) It was also shown that as the calcification image noise,  $\sigma_c$  decreased as the spectral energy separation increased (Figure 9). Using 25 kVp Mo/Mo as the low-energy and 50 kVp W/La as the high-energy spectra resulted in the lowest noise. This results in a calcification SNR of about 3 for a calcification size of 250 microns. Thus, we can conclude that with this spectrum combination, we can detect calcifications as small as 250 microns. However, the presence of scatter and other image artifacts may further degrade the SNR and make the minimum detectable calcification size larger. Furthermore, although Mo/Rh (rhodium) dual-target tubes are available, a Mo/W dual-target tube is not currently available; such a tube could provide an advantage for implementation of dual-energy digital mammography.

D) Simulations were also done with varying tissue compositions (Figure 10) and total breast thickness (Figure 11). As expected, the noise,  $\sigma_t$ , increased as the attenuation in the breast increased as a result of a higher glandular tissue content or thicker breast. It was also determined that evenly splitting the exposure between the low- and high-energy images would be sufficient to keep the noise,  $\sigma_t$ , within 10% of the minimum. The low/high kVp exposure can be varied from 30%/70% to 40%/60% without significantly effecting the image quality. The greatly simplifies the practical implementation of dual-energy calcification imaging technique.

### ***Task 3: Phantom studies (months 7-18)***

We have conducted a few phantom studies to attempt dual-energy calcification imaging with our FFDM unit. These studies are reported in the Michael Lemacks' thesis attached with this report. They are summarized as follows:

#### **1. Dual-energy subtraction imaging with a meat phantom:**

Animal tissue structures (meat phantom) were placed and compressed in a Lucite water container to simulate a compressed breast. Chalk powders were placed over the phantom to simulate calcifications. The phantom was imaged with low (25 kVp Mo/Mo) and high (49 kVp Ro/Ro) energy x-rays. The resulting images were subtracted in a weighted fashion in an attempt to cancel out tissue structures and enhance calcifications. The low energy and subtraction (calcification) images are shown in Figures 1 and 2, respectively. The signal profiles of the low energy and subtraction image are shown in Figure 3. The tissue structures are largely flattened out in the subtraction image. The calcification contrast in the low energy and subtraction images is shown in Figure 4. In the low energy image (left), the calcification contrast-to-noise ratio is higher but the calcification contrast overlaps with spatially varying tissue structure signal. In the subtraction image (right), the calcification contrast-to-noise ratio is lower but the background structure is flatter due to energy subtraction processing.

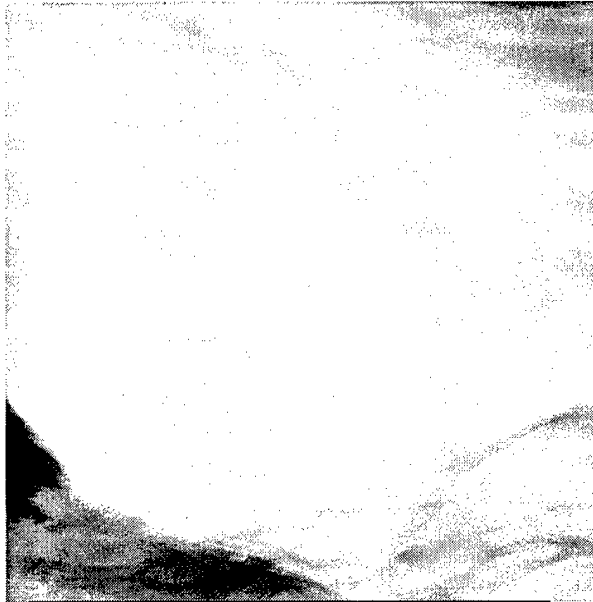


Figure 1 Low energy image.

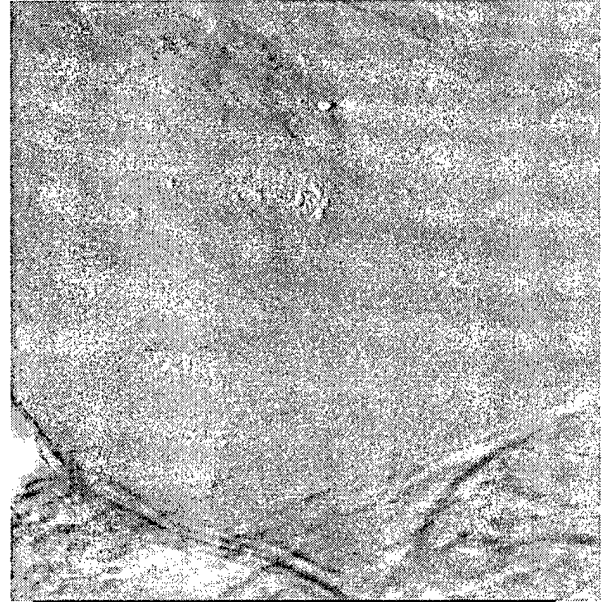


Figure 2 Calcification subtraction image.

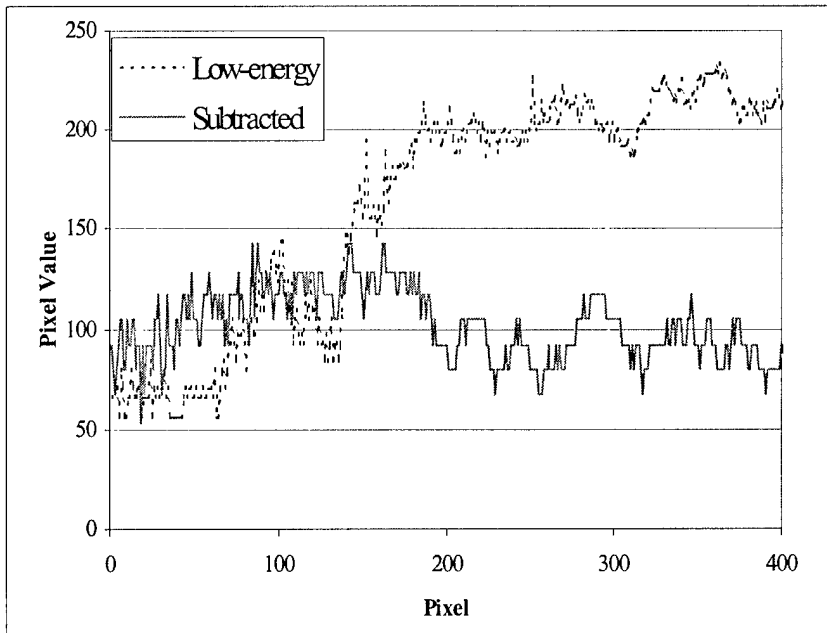


Figure 3 Signal profiles in low energy and subtraction (calcification) images.

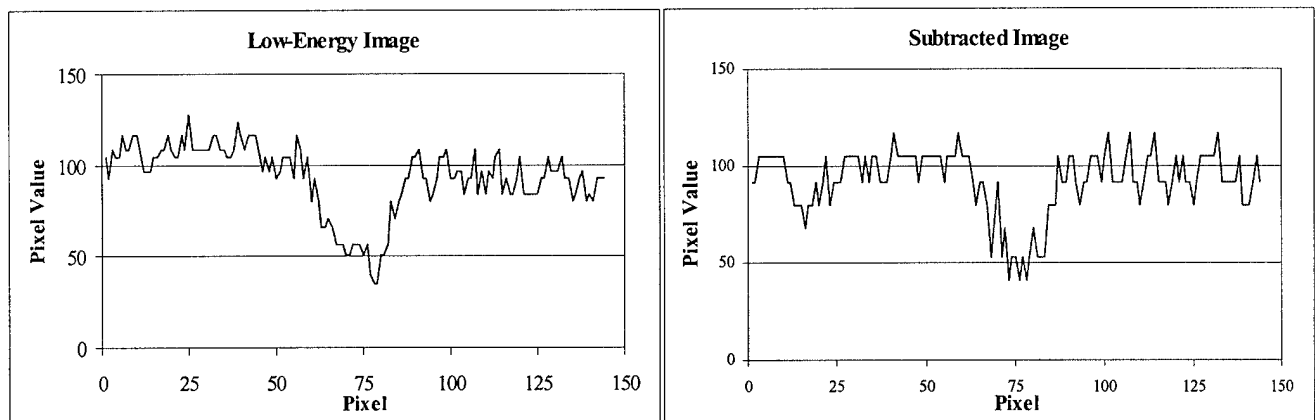


Figure 4 Calcification contrast difference between low-energy (left) and subtraction (right) images. CNR in low-energy image is 3.7 and the CNR in the subtraction image is 2.1.

## 2. Evaluation of FFDM unit

To prepare our FFDM unit for dual-energy subtraction imaging, we have measured the physical image quality of our unit and compare it with those of CCD and CR based systems. We have also conducted various perception studies to compare FFDM with three different mammography systems: CCD, CR and screen/film. The results are summarized as follows:

### A) Physical image quality measurement

We have developed the methodology to measure the Modulation Transfer Function (MTF), Noise Power Spectrum (NPS), Noise Equivalent Quanta (NEQ) and Detective Quantum Efficiency (DQE). We have used the methodology to measure the physical image quality for the FFDM and CR and CCD based systems for mammographic imaging. The results were reported in References 1 and 7. We have found that although the MTF of the FFDM was lower than that of the CCD based system, its DQEs are better than those of the CCD and CR based systems. Similar methodology was also used to measure the physical image quality for a aSi/CsI flat panel digital chest unit and a CR based system for chest imaging. The results were reported in References 1 and 6.

### B) Evaluation with perception studies

We have used simulated calcification phantom to conduct a perception study to compare the low contrast performance for the FFDM, CR and CCD systems. The results of the perception studies were reported in References 2 and 4. We have found that the microcalcification detectability of the FFDM was consistently and significantly better than those of the CR, CCD and SF based systems. This was demonstrated by both the average confidence level scores and the areas under the ROC curves. An earlier

perception study based on contrast detail curves was also performed to compare the low contrast performance of a aSi/CsI flat panel digital chest unit and a CR based system for chest imaging. The results are reported on in References 2 and 4.

### **GE-CRD:**

Due to negotiation of the research agreement between MDACC, GE Medical Systems and GE-CRD, the starting date of the GE-CRD efforts have been delayed to April of 2001. Therefore, the GE-CRD efforts have been limited to that appropriate of about 6 months.

The effort at GE-CRD has so far emphasized on developing a technique to measure the glandular tissue density of the breast. Signal and noise values were measured as a function of the x-ray technique, compressed breast thickness, and breast composition. The measurements were fitted to a model. Predications based on this model were then compared to the measurements acquired using another detector for validation. Dose as a function of x-ray technique was calculated to determine the optimal exposure distribution for various compressed breast thicknesses and glandular compositions.

The formalism is as follows: assume (1) a 2-tissue (fat and glandular) model of the breast and (2) the total height or compressed breast thickness ( $H$ ) is known. Then the image signal in log-count domain using a single exposure can be modeled as the observation of a breast composed of fat only plus the adjustment due to the additional density contributed from the glandular tissue.

$$y = -\log(\text{counts}) = \mu^f h^f + \mu^g h^g = \mu^f H + (\mu^g - \mu^f)h^g ; \text{ since } H = h^f + h^g$$

#### ***Task 1: Modeling of imaging chain (months 1-24)***

The first task was to measure the image signal and noise as a function of the x-ray technique, compressed breast thickness, and breast composition (in terms of the percent glandular tissue). Measurements were made (with GE Tomosynthesis prototype) for each of Mo/Mo, Mo/Rh, and Rh/Rh filter/anode combinations for the lowest, middle and highest allowable kVp for that filter/anode combination. For each filter/anode combination a 2-cm, 5-cm, and 8-cm set of breast phantoms were imaged through a 2-mm pinhole camera. For each breast thickness three compositions (0 % glandular (100% fat), 50 % glandular and 100% glandular) of CIRS phantoms were imaged. The measurements of the detector signal [counts/mAs] were fit for each filter/anode combinations as a function of the kVp, composition and thickness. The noise was also measured and modeled as a function of the detector counts.

The above model was validated by comparing its predication to the measured calibration curves for counts and noise taken on another scanner (Seno 2000D). Both the calibration curves for the signal level and noise level captures the salient features of the signal level

and noise curves measured on another system for x-ray techniques interpolated from the measurements.

In order, to use the model for signal level and noise as a function of the x-ray technique, it is also necessary to understand dose as a function of the technique. The patient dose in mammography is evaluated by the mean glandular dose. An extension of published data has been performed to calculate the mean glandular dose for any x-ray spectra, breast thickness and glandular percentage. Assuming a fixed mean glandular dose as a function of breast thickness, the x-ray technique that minimizes the mean glandular dose was chosen as the optimal technique.

### **Key Research Accomplishments**

#### **MDACC:**

1. Developed and applied methodology for measuring and comparing the imaging properties of the aSi:H/CsI:Tl flat-panel detector systems with CR and CCD based detector systems.
2. Developed theoretical framework for numerical studies of the SNR properties in dual-energy calcification imaging.
3. Estimated calcification SNR as a function of the input x-ray spectra (kVp, target/filter material), exposures, scintillator (material/thickness), breast thickness, tissue composition. Determined the optimal selection of the imaging parameters.
4. Evaluated and compared the imaging properties of our aSi/CsI flat-panel digital mammography system with CR, CCD, and SF based systems. Both physical image quality measurement and perception studies were used for the evaluation and comparison.

#### **GE-CRD:**

1. Developed the formalism to measure breast density (glandular tissue ratio).
2. Modeled signal and noise level as a function of x-ray techniques, breast thickness and breast compositions for single energy imaging. The results can be extended for use in dual-energy subtraction imaging.
3. Extended mean glandular dose calculation to higher kVp values. This will allow the mean glandular dose to be used as the parameter for normalization in image quality optimization or comparison.

## Reportable Outcomes

### *Manuscripts:*

1. Liu, X., Shaw, C., Rong, X., Lemacks, M. "Comparison of a-Si:H/CsI Flat-Panel Digital Imaging Systems with CR and CCD Based Systems □ Image Quality Measurements." In Proceedings of the SPIE 2001 Physics of Medical Imaging Conference, 4320(89): 389-398. San Diego, CA, 2001. (attached)
2. Rong, J., Shaw, C., Johnston, D., Lemacks, M., Liu, X., Whitman, G., Thompson, S., Krugh, K. "Comparison of a-Si:H CsI Flat-Panel Digital Imaging Systems with a CCD Based System, CR Systems, and Conventional Screen-Film Systems – A Contrast-Detail Phantom Study." In Proceedings of the SPIE 2001 Physics of Medical Imaging Conference, 4320(88): 381-388. San Diego, CA, 2001. (attached)
3. Rong, J., Shaw, C., Liu, X., Lemacks, M., Thompson, S.K., "Comparison of an amorphous silicon/cesium iodide flat-panel digital chest radiography system with screen/film and computed radiography systems- a contrast-detail phantom study. To be published in the November 2001 issue of Medical Physics. (attached)
4. Rong, J., Shaw, C., Johnston, D., Lemacks, M., Liu, X., Whitman, G., Dryden, M., Stephens, T., Thompson, S., Krugh, K., "Microcalcification Detectability for Four Mammographic Detectors: Flat-Panel, CCD, CR and Screen/Film." Manuscript submitted to *Medical Physics* for publishing. (attached)
5. Lemacks, M., Kappadath, S.C., Shaw, C.C., Liu, X.L., "Dual-Energy Subtraction Imaging for Enhanced Detection and Visualization of microcalcifications." Manuscript submitted to *Medical Physics* for publishing. (attached)
6. Liu, X., Shaw, C.C., "aSi:H/CsI:Tl flat-panel imaging versus CR for chest imaging: image quality measurement, in preparation for submission to *Medical Physics*. (attached)
7. Liu, X., Shaw, C.C., "aSi:H/CsI:Tl flat-panel imager versus CCD and CR based imaging systems for mammographic imaging- image quality measurement, in preparation for submission to *Medical Physics*.

### *Thesis:*

Michael Lemacks, "Two methods for improving the detectability of microcalcifications in digital mammography", submitted to the Graduate School of Biomedical Sciences, The University of Texas Health Science Center at Houston, as partial requirement for Mater of Science degree, December 2000. (attached)

### *Abstracts:*

1. Shaw C, Liu X, and Whitman, G. A Dual-Energy Subtraction Imaging Technique for Enhanced Microcalcification Imaging and Tissue Composition Measurement in Digital Mammography. *Radiology* 213(p) 1999; p.368.
2. Lemacks, M., Liu, X. Shaw, C., Whitman, G.J., Rong, X., Dual-energy digital mammography with a full field amorphous silicon/cesium iodide flat-panel detector,

- World Congress on Medical Physics and Biomedical Engineering, Chicago, IL, July 23-28, 2000, CD-ROM Program Book, Paper TU-E307-06.
3. Liu, X., Shaw, C., Rong, J., Lemacks, M. "Comparison of a-Si:H/CsI Flat-Panel Digital Imaging Systems with CR and CCD Based Systems- Image Quality Measurements." SPIE International Symposium on Medical Imaging 2001 program book, p.40.
  4. Rong, J., Shaw, C., Johnston, D., Lemacks, M., Liu, X., Whitman, G., Thompson, S., Krugh, K. "Comparison of a-Si:H CsI Flat-Panel Digital Imaging Systems with a CCD Based System, CR Systems, and Conventional Screen-Film Systems – A Contrast-Detail Phantom Study." SPIE International Symposium on Medical Imaging 2001 program book, p.39.
  5. Liu, X., Shaw, C., Rong, X. "Comparison of flat-panel, CR and CCD based detectors for digital mammography: MTF and DQE measurements." *Medical Physics*, Vol. 28, No.8, 2001, p.1821.
  6. Rong, J., Shaw, C., Johnston, D., Lemacks, M., Liu, X., Whitman, G., Thompson, S., Dryden, M., Krugh, K. "Micro-calcification Detectability for Four Mammographic Detectors: Flat-Panel, CCD, CR and Screen/Film." *Medical Physics*, Vol. 28, No.8, 2001, p.1821.
  7. Liu, X., Shaw, C., Rong, X. "Comparison of an a-Si:H/CsI:Tl Flat-Panel Based Digital Mammography System with CR and CCD Based Systems." To be published in *Radiology*.

***Presentations:***

1. Shaw C, Liu X, and Whitman, G. A Dual-Energy Subtraction Imaging Technique for Enhanced Microcalcification Imaging and Tissue Composition Measurement in Digital Mammography. Presented at the 85<sup>th</sup> Scientific Assembly and Annual Meeting of the Radiological Society of North America, Chicago, IL, November 28-December 3, 1999.
2. Lemacks, M., Liu, X., Shaw, C., Whitman, G.J., Rong, X., Dual-energy digital mammography with a full field amorphous silicon/cesium iodide flat-panel detector, Poster presented at the World Congress on Medical Physics and Biomedical Engineering, Chicago, IL, July 23-28, 2000.
3. Liu, X., Shaw, C., Rong, X., Lemacks, M. "Comparison of a-Si:H/CsI Flat-Panel Digital Imaging Systems with CR and CCD Based Systems □ Image Quality Measurements." Poster presentation at SPIE International Symposium on Medical Imaging 2001, Feb. 17-22, 2001, San Diego, CA.
4. Rong, J., Shaw, C., Johnston, D., Lemacks, M., Liu, X., Whitman, G., Thompson, S., Krugh, K. "Comparison of a-Si:H CsI Flat-Panel Digital Imaging Systems with a CCD Based System, CR Systems, and Conventional Screen-Film Systems – A Contrast-Detail Phantom Study." Received ***Honorable Mention Poster Award***, Poster presentation at SPIE International Symposium on Medical Imaging 2001, Feb. 17-22, 2001, San Diego, CA.
5. Liu, X., Shaw, C., Rong, X. "Comparison of flat-panel, CR and CCD based detectors for digital mammography: MTF and DQE measurements." Poster presentation at the

- 43<sup>rd</sup> Annual Meeting of the American Association of Physicists in Medicine Meeting, July 22-26, 2001, Salt Lake City, Utah.
6. Rong, J., Shaw, C., Johnston, D., Lemacks, M., Liu, X., Whitman, G., Thompson, S., Dryden, M., Krugh, K. "Microcalcification Detectability for Four Mammographic Detectors: Flat-Panel, CCD, CR and Screen/Film." Poster presentation at the 43<sup>rd</sup> Annual Meeting of the American Association of Physicists in Medicine Meeting, July 22-26, 2001, Salt Lake City, Utah.
  7. Liu, X., Shaw, C., Rong, X. "Comparison of an a-Si:H/CsI:Tl Flat-Panel Based Digital Mammography System with CR and CCD Based Systems." Accepted for oral presentation at the 87<sup>th</sup> Scientific Assembly and Annual Meeting of the Radiological Society of North America, November 25 – 30, 2001, Chicago, IL.

### ***Degrees:***

1. Michael R. Lemacks, Master of Science degree received from the Graduate School of Biomedical Sciences, The University of Texas Health Science Center at Houston, December, 2000.

### **Conclusions**

#### **MDACC**

1. Calcification imaging in mammography can be reduced from three material/energy problem to a dual material/energy problem if the breast thickness is known independently.
2. Calcification SNR in the subtraction image is rather insensitive to exposure distribution between low and high energy images. A 50%/50% distribution should be adequate for most cases without compromising the image quality.
3. 25 kVp Mo/Mo and 50 kVp W/La would result in an optimum calcification SNR in dual-energy subtraction image.
4. CsI:Tl is a better scintillator than Gd<sub>2</sub>O<sub>2</sub>S:Tb in dual-energy subtraction imaging due to its K-edge absorption at 33.2 and 36 keV.
5. With 1000 mR unattenuated total detector exposure, microcalcifications as small as 250 microns can be detected (SNR ~ 3) in a breast with 2.5 cm adipose and 2.5 cm glandular tissue with 25 kVp Mo/Mo and 50 kVp W/La spectrum combination.
6. FFDM has been found to have better DQEs and better microcalcification detectability than CR or CCD based systems.

#### **GE-CRD**

1. Image signal and noise were measured, modeled and validated as a function of x-ray technique, breast thickness and breast composition.
2. Mean glandular dose was extended to higher kVp values.

**Plan for the coming year:**

**MDACC**

1. Wrap up the modeling and numerical study
2. Perform calibration measurements to obtain x-ray transmission measurement as a function of the breast thickness, glandular tissue thickness and calcification thickness for various x-ray spectra.
3. Develop a functional and robust energy subtraction algorithm to convert x-ray transmission measurements into glandular tissue and calcification thickness signals.
4. Demonstrate the dual-energy calcification imaging technique with phantoms.

**GE-CRD**

1. Improve the accuracy of the model
2. Optimize the spacing of technique combinations for tissue composition alone using dual-energy approaches
3. Optimize the spacing of technique combinations for theoretical microcalcification detection using dual energy approaches
4. Extend the available technique range in filter/anode combination choice

## References

1. Liu, X., Shaw, C., Rong, X., Lemacks, M. "Comparison of a-Si:H/CsI Flat-Panel Digital Imaging Systems with CR and CCD Based Systems □ Image Quality Measurements." In Proceedings of the SPIE 2001 Physics of Medical Imaging Conference, 4320(89): 389-398. San Diego, CA, 2001
2. Rong, J., Shaw, C., Johnston, D., Lemacks, M., Liu, X., Whitman, G., Thompson, S., Krugh, K. "Comparison of a-Si:H CsI Flat-Panel Digital Imaging Systems with a CCD Based System, CR Systems, and Conventional Screen-Film Systems – A Contrast-Detail Phantom Study." In Proceedings of the SPIE 2001 Physics of Medical Imaging Conference, 4320(88): 381-388. San Diego, CA, 2001
3. Rong, J., Shaw, C., Liu, X., Lemacks, M., Thompson, S.K., "Comparison of an amorphous silicon/cesium iodide flat-panel digital chest radiography system with screen/film and computed radiography systems- a contrast-detail phantom study. To be published in the November 2001 issue of Medical Physics.
4. Rong, J., Shaw, C., Johnston, D., Lemacks, M., Liu, X., Whitman, G., Dryden, M., Stephens, T., Thompson, S., Krugh, K., "Microcalcification Detectability for Four Mammographic Detectors: Flat-Panel, CCD, CR and Screen/Film." Manuscript submitted to *Medical Physics* for publishing.
5. Lemacks, M., Kappadath, S.C., Shaw, C.C., Liu, X.L., "Dual-Energy Subtraction Imaging for Enhanced Detection and Visualization of microcalcifications." Manuscript submitted to *Medical Physics* for publishing. (attached)
6. Liu, X., Shaw, C.C., "aSi:H/CsI:Tl flat-panel imaging versus CR for chest imaging: image quality measurement, in preparation for submission to *Medical Physics*.
7. Liu, X., Shaw, C.C., "aSi:H/CsI:Tl flat-panel imager versus CCD and CR based imaging systems for mammographic imaging- image quality measurement, in preparation for submission to *Medical Physics*.
8. Lemacks, M., "Two methods for improving the detectability of microcalcifications in digital mammography", submitted to the Graduate School of Biomedical Sciences, The University of Texas Health Science Center at Houston, as partial requirement for Mater of Science degree, December 2000.
9. Kaufhold, J., Annual report from GE-CRD.

## Appendices

1. Kaufhold, J., Annual Report for April 1 to August 31 2001 from GE-CRD.
2. Liu, X., Shaw, C., Rong, X., Lemacks, M. "Comparison of a-Si:H/CsI Flat-Panel Digital Imaging Systems with CR and CCD Based Systems □ Image Quality Measurements." In Proceedings of the SPIE 2001 Physics of Medical Imaging Conference, 4320(89): 389-398. San Diego, CA, 2001.
3. Rong, J., Shaw, C., Johnston, D., Lemacks, M., Liu, X., Whitman, G., Thompson, S., Krugh, K. "Comparison of a-Si:H CsI Flat-Panel Digital Imaging Systems with a CCD Based System, CR Systems, and Conventional Screen-Film Systems – A Contrast-Detail Phantom Study." In Proceedings of the SPIE 2001 Physics of Medical Imaging Conference, 4320(88): 381-388. San Diego, CA, 2001.
4. Rong, J., Shaw, C., Liu, X., Lemacks, M., Thompson, S.K., "Comparison of an amorphous silicon/cesium iodide flat-panel digital chest radiography system with screen/film and computed radiography systems- a contrast-detail phantom study. To be published in the November 2001 issue of Medical Physics.
5. Rong, J., Shaw, C., Johnston, D., Lemacks, M., Liu, X., Whitman, G., Dryden, M., Stephens, T., Thompson, S., Krugh, K., "Microcalcification Detectability for Four Mammographic Detectors: Flat-Panel, CCD, CR and Screen/Film." Manuscript submitted to *Medical Physics* for publishing.
6. Lemacks, M., Kappadath, S.C., Shaw, C.C., Liu, X.L., "Dual-Energy Subtraction Imaging for Enhanced Detection and Visualization of microcalcifications." Manuscript submitted to *Medical Physics* for publishing.
7. Liu, X., Shaw, C.C., "aSi:H/CsI:Tl flat-panel imaging versus CR for chest imaging: image quality measurement, in preparation for submission to *Medical Physics*.
8. Lemacks, M., "Two methods for improving the detectability of microcalcifications in digital mammography", submitted to the Graduate School of Biomedical Sciences, The University of Texas Health Science Center at Houston, as partial requirement for Mater of Science degree, December 2000.

REPORT for DAMD17-00-1-0316

“Dual-Energy Digital Mammography with a  
Full-Field aSi/CsI “Flat-Panel Imager”

September 28, 2001

By John Kaufhold, Ph.D.

General Electric Corporate Research and Development

The General Electric Corporate Research and Development Center (CRD) efforts on dual energy mammography started from March 27 when the subcontract was signed by both institutions (MD Anderson and GE CRD). Given this late start date, the CRD contributions to the collaborative effort are approximately on target for the grant schedule. That is, in the first two quarters, the first task in the statement of work for GE CRD is to come to a “basic” physics understanding of the dual energy methodology and its application to mammography; this modeling is well underway. We describe our progress on this task in this document.

## **TASK 1: Modeling of imaging chain**

This first task in the grant has specifically four foci. These are: 1) to model the image noise as a function of x-ray technique, compressed breast thickness, and breast composition (in terms of percent glandular tissue) 2) validate that the system model agrees with measurements of signal level and noise level 3) to measure the half-value layers of the system as a function of x-ray technique to understand the dose as a function of x-ray technique and 4) to prescribe an optimal exposure or exposure distribution for various compressed breast thicknesses and glandular compositions.

To describe our progress to date on Task 1, in each of the 4 subtasks, we will use a model of the x-ray imaging system. Assume each image pixel value on the detector,  $C(i, j)$ , can be expressed as

$$C(i, j) = \int_{\text{Energy}} P_0(E) \exp \left[ \int_{\text{pathlength}} -\mu(x, y, z, E) dp \right] dE \quad \text{Equation (1)}$$

where  $C$  is proportional to the amount of charge (counts) at an individual pixel,  $\mu(x, y, z, E)$  is the x-ray energy-dependent attenuation coefficient of the sample at each point in space between the detector and x-ray source, the integral over energy indicates that the pixel intensity is due to a polyenergetic spectrum of x-rays, and the integral over pathlength is the description of the trajectory of the individual rays of the x-ray beam to the pixel location.  $P_0(E)$  is the energy spectrum incident on the sample, whose shape is a strong function of kVp, filter, and anode, and whose amplitude is proportional to the mAs. Nominally, the attenuation coefficients in equation (1) span a wide range, which include attenuation due to parenchymal tissue, glandular (fibrous) tissue, fatty tissue, and calcium salts. In the dual energy x-ray approach, we assume two x-ray exposures are acquired at different energies (different  $P_0(E)$  's). In practice, the polyenergetic x-ray spectrum can be replaced by a monoenergetic model. If we approximate the polychromatic beam in equation (1) as a monoenergetic beam for each energy in the dual energy x-ray approach, the counts for each x-ray image are:

$$C_1(i, j) = \int_{\text{pathlength}} P_1 \exp[-\mu_1(x, y, z)] dp \quad \text{Equation (2)}$$

$$C_2(i, j) = \int_{\text{pathlength}} P_2 \exp[-\mu_2(x, y, z)] dp \quad \text{Equation (3)}$$

We assume the compressed breast thickness can be accurately measured for our analysis. Thus, if we restrict our investigation to estimation in the compressed breast region, the net attenuation along any ray from source to detector can be described for each image as a net attenuation coefficient over the thickness of the object. Defining a transformation of a pixel in the count domain  $y_i$ , such that

$$y_i = -\log(C_i) \quad \text{Equation (4)}$$

If we assume a 2-tissue model of the breast (as in [3]), where the two tissues are fat and glandular, we have the following model for the noise-free log-count domain data:

$$y_i = \mu_i^F h_F + \mu_i^G h_G$$

where  $h_F$  is the height of fatty tissue,  $h_G$  is the height of glandular tissue the x-ray beam passes through before scintillating at the detector, and the subscript,  $i$ , denotes the energy of the beam, either high or low. Because the fat and glandular components partition the 1-dimensional ray passing through the  $H_{cm}$  of compressed breast tissue, the total height,  $H$ , *which we assume is known*<sup>1</sup>, is the sum of  $h_F$  and  $h_G$ :

$$H = h_F + h_G \rightarrow h_F = H - h_G$$

Therefore, the noise-free log-count domain data is

$$y_i = \mu_i^F (H - h_G) + \mu_i^G h_G$$

or

$$y_i = \underbrace{\mu_i^F H}_{y_i^F} + (\mu_i^G - \mu_i^F) h_G$$

Given this noise-free model, based on our previous work in the U.S. Navy Grant, 3D Full-field Digital Mammography (ONR Contract # MDA 905-00-1-0041), we can write the observation equation relating a pixel's counts and its percent glandular composition in the following way:

$$y_i = a_i g + r_i \quad r_i \sim N(y_i^F, R_i(g)) \quad \text{Equation (5)}$$

where the notation,  $x \sim N(\mu, \Sigma)$  means  $x$  is a Gaussian random variable distributed with mean,  $\mu$ , and covariance,  $\Sigma$ . The scalar variables for each pixel in each exposure,  $y_i$ , are as follows:  $y_i^F$  is the log-count intensity corresponding to fat,  $g$  is the percent glandular metric, and  $a_i$  is a scalar precomputed from the calibration curve (or published data) for the  $i^{\text{th}}$  technique describing the sensitivity of  $y_i$  to  $g$ . The noise variance in the log count domain,  $R_i(g)$ , is due primarily to the counting statistics of the scintillated photons. This noise is obviously a function of the breast thickness and composition (small for thinner more fatty breasts and higher for thicker more glandular breasts). However, for mammo energy ranges, if the glandular composition noise in the log count domain is computed as a percent of the total thickness, the representative value of  $R_i(50\%)$  is a reasonable approximation for any given thickness. Thus, the model above is that the observation in the log-count domain is simply  $\cdot H_{cm}$  of fat plus the adjustment due to additional density contributed from glandular tissue scaled by  $a_i$ . The quantity,  $g$ , the percentage of

<sup>1</sup> Although current sensors for compressed breast height are lacking in resolution, and in practice, only an approximation of the compressed height is available from the compression paddle assembly readout, software methods to estimate the compressed breast height are available to both dual energy and single exposure approaches. Further, the hardware compressed breast height estimator may be improved to any desired accuracy, given enough sensors.

glandular tissue composing a given x-ray, is the value we seek to estimate. From the development above, percent glandular tissue can be expressed as

$$g = \frac{100h_g}{H}$$

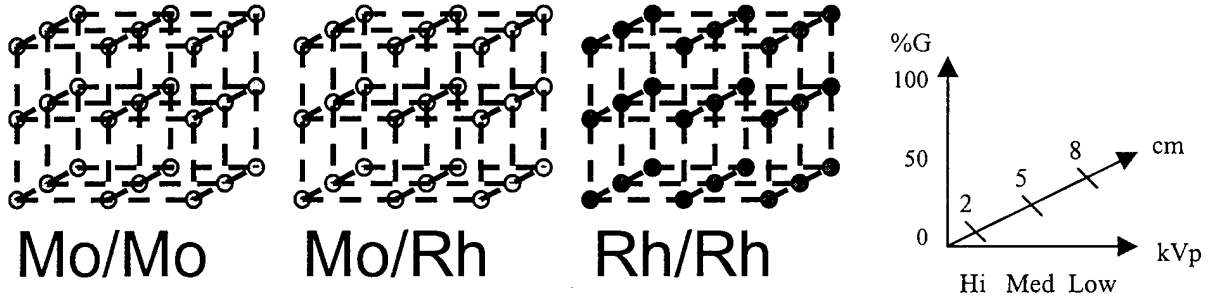


Figure 1: Describing the sampling approach for CRD system characterization.

Note that the percent glandular metric is used here but is linearly related to the thickness of glandular tissue,  $h_g$ , and the two are interchangeable. For instance, a ray which passes through a 4cm compressed breast which has a composition of 50% glandular tissue is the same as saying that that ray passed through 2cm of glandular tissue. The overall model in Equation 5 (measurement of  $a_i$ ,  $y_i^F$ , and  $R_i$ ) can be calculated without calibration curves from published attenuation coefficients according to the following equation:

$$a_i = \frac{H(\mu_i^G - \mu_i^F)}{100} \%$$

### **TASK 1 SUBTASK 1: Signal and Noise Level Models**

The first subtask of Task 1 is to model the system image noise and signal level as a function of the x-ray technique, breast thickness, and breast composition. To accomplish this system modeling for the available techniques on our tomosynthesis prototype at CRD, we measured the system signal level and noise for a set of techniques and compositions which span the full available range on the scanner. Measurements were made for each of three filter/anode combinations (Mo/Mo, Mo/Rh, and Rh/Rh) for the lowest, middle and highest allowable kVp for that filter track anode combination. For each filter/anode combination a 2cm, 5cm, and 8cm set of breast phantoms were imaged through a 2mm pinhole (to reject scatter). For each height, a 100% fat (0% glandular) composition CIRS phantom, a 50% glandular composition CIRS phantom, and a 100% glandular composition CIRS phantom were imaged. A pictorial diagram of the 81 sampled filter/anode combinations, kVps, thicknesses, and compositions is shown in Figure 1. From these measurements, we fit the hypersurface for each filter-anode combination with a quadratic polynomial in kVp, thickness, and composition. From this hypersurface we have a model of the x-ray system detector counts/mAs for a given technique when imaging a breast of a given height and composition. The detector counts per mAs completely characterize the mean signal level because the mean detector counts

dependence on mAs has been shown to be linear with an exceptionally low error in the linear fit. An example of the detector counts versus mAs is shown in Figure 2.

The noise was also measured and modeled as a function of the detector counts. In the pinhole imaging paradigm, the expectation is that the noise is predominantly due to quantum noise. In other work (ONR Contract # MDA 905-00-1-0041), we have shown that the effects of noise due to system electronics is negligible until the mAs is decreased to approximately  $1/40^{\text{th}}$  of the mAs for a standard dose image. Thus, we expect the noise to be mostly quantum—which is typically modeled as Poisson. The interesting result for this noise measurement/model was that the noise, itself, did not appear to be Poisson. For Poisson noise, it is expected that the variance increases linearly with the counts. The data seem to suggest that a Poisson noise fit is reasonable, but that the noise increases as the square of the counts. This is true whether the noise is measured against filter/anode, kVp, thickness, or breast composition. The measured noise standard deviation in the count domain as a function of counts is plotted in Figure 3. Each subplot is labeled according to its value in the sample space described above and diagrammed in Figure 1.

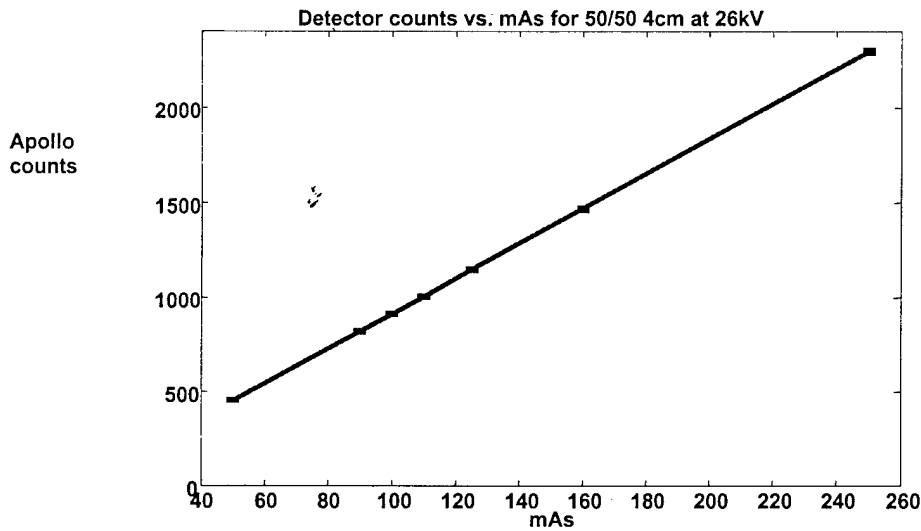
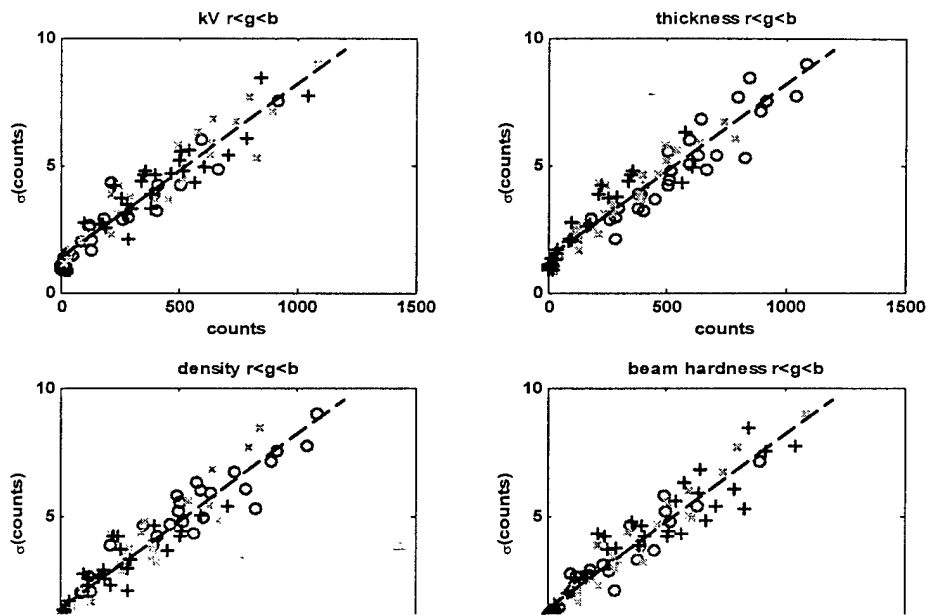


Figure 2: Linearity of counts vs. mAs



## TASK 1 SUBTASK 2: System Model Validation

We validated the model counts and noise in the count domain as a function of thickness, composition, kVp, and filter/anode by comparing measured calibration curves for counts and noise taken on another scanner in another program (ONR Contract # MDA 905-00-1-0041) to the values predicted by the polynomial hypersurface model calculated in subtask 1. It is important to note that the calibration data was simply available to CRD from another program, and was not acquired using resources from this grant, but rather on ONR Contract # MDA 905-00-1-0041. The x-ray techniques used to generate the emulated calibration curves for the other scanner did not include the techniques used to fit the model. These two calibration curves are shown in Figures 4 and 5.

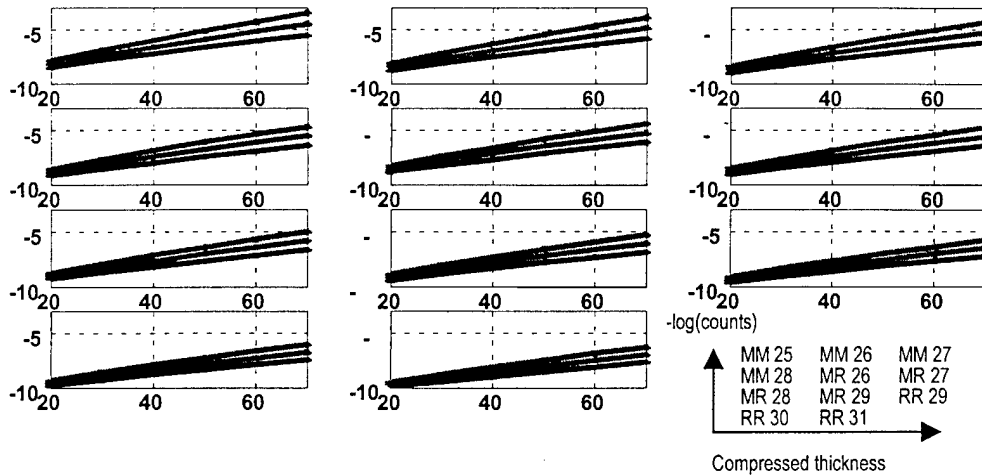


Figure 4: Calibration Curves Measured on Seno 2000D

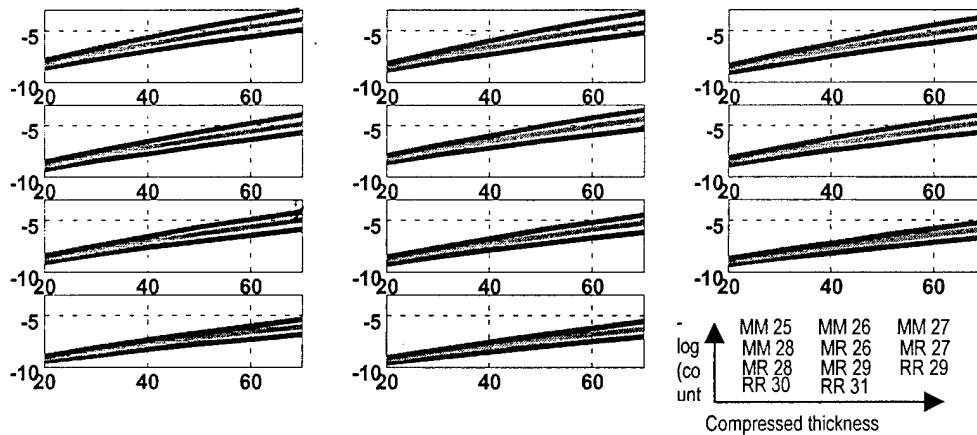


Figure 5: Emulated Calibration Curves from System Model calculated in Subtask 1

The calibration curves in Figures 4 and 5 are log count domain representations of the attenuation curves for 100% fat, a 50% glandular tissue, and 100% glandular tissue in blue, green, and red, respectively. On the x-axis of each plot is the compressed breast thickness in mm and on the y-axis is the  $-\log$  of the counts for the technique indicated in the lower left of each figure. The fidelity of the measured data on a different machine to the model predictions indicates that the polynomial hypersurface fit to the measurements on the CRD x-ray tomo prototype system is a reasonable model which captures the salient properties of the technique, breast thickness, and composition dependence. Note that these techniques are almost all interpolated techniques, which also indicates that the model fit from 81 data points was not “overfit” to the specific measurements.

Similarly, to validate the noise model, we compared available calibration curve measurements of noise at a number of different mAs for the same scanner as was used to validate the nominal count behavior of the model. Because the measured data acquired on the Seno 2000D were not all acquired with the same mAs, a point-to-point comparison is not possible, but the general shape of the noise as a function of composition and thickness

should be similar. Thus, what is important is to fit the general shape of the noise as a function of imaging parameters, not the absolute noise sigma values—although the agreement should be to within an order of magnitude because the mAs range of the measured data was between 50 and 250 (the same mAs for a given filter/anode combination), whereas all measured data was for an mAs of 110. These comparison plots are shown in Figures 6 and 7.

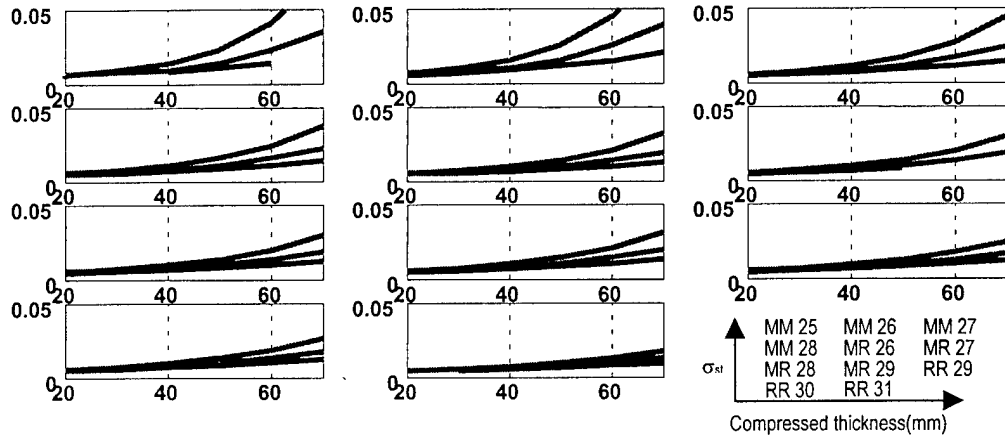


Figure 6: Log count domain noise calibration curves measured on Seno 2000D

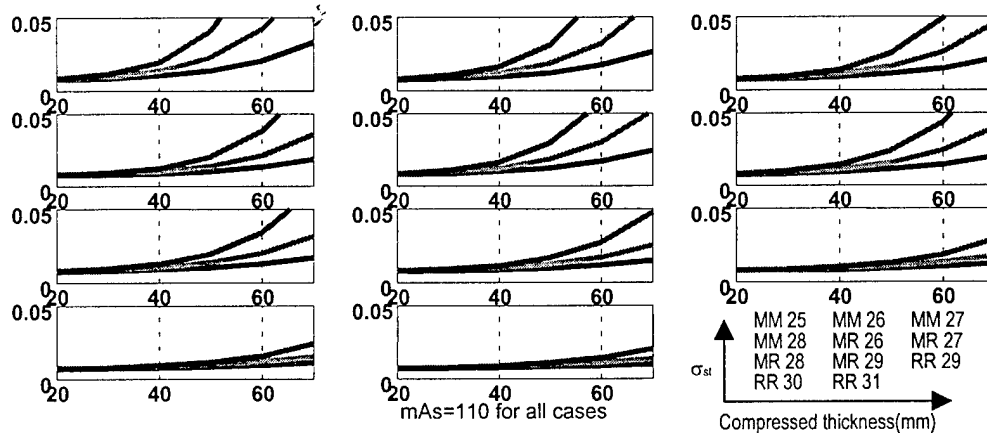


Figure 7: Model emulated log count domain noise calibration curves for mAs=110

Both the calibration curves for the signal level and noise level capture the salient features of the signal level and noise curves measured on another system for x-ray techniques interpolated from the measurements at CRD which indicates the model fidelity is satisfactory to answer the dual energy optimization questions raised by the rest of the grant.

Because we have used data from ONR Contract # MDA 905-00-1-0041 for validation, it is important to describe exactly what work was done on this program and what on the Navy contract. Specifically, all the measurement to characterize the system were done on this program, the model fit was done on this program, the emulation of the

Seno2000D calibration data was done on this program, and the corresponding measured curves to compare against were simply taken from the results on the 3D FFD program. Thus, the message is that we leveraged the information gleaned from the ONR contract in a way that is useful to this program, not that we did the Seno 2000D measurements on this program.

### **TASK 1 SUBTASK 3: HVL Measurements and Dose versus Technique**

In order to use the model for signal level and noise as a function of x-ray technique in any practical sense, it is also necessary to understand dose as a function of technique. Much of the dose as a function of technique measurements can be culled from the literature. In fact, measurements of entrance skin exposure or air kerma as a function of technique are readily available in the literature for the standard range of techniques. In addition, DgN conversion factor tools from either entrance skin exposure or air kerma are also available (given HVL measurements for the particular system). Taken together, dose can be calculated straightforwardly using available tools. However, in the dual energy task, we may be interested in using nonconventional filtration (such as Cu, Al, or W). Thus, to understand dose for these x-ray techniques, we require HVL measurements and some understanding of the absorption in the breast. In the system model described above, and in the use of the system model and dose estimates given x-ray techniques and compositions, we will use published dose calculation tables. However, the development in this section describes approaches for estimating dose for higher energy x-ray spectra which may be of interest in this program. That is, this section can be thought of as independent of the system modeling, but that it can also be used together with the system modeling in the event that understanding the effects of using very high energy beams becomes important in this program.

At CRD, in other programs, a tool was developed to model a number of system characteristics including MTF, DQE, noise etc., as a function of x-ray technique. In this modeling tool, the published SRS tables were used for generating x-ray spectra for each technique. For mammography, however, the published x-ray spectra are only available up to 32 kVp. Dose calculations without significant extrapolation are also only available for this x-ray energy range. Further, the x-ray spectra and dose calculations are considered to be critical to simulate dual energy mammography. Thus, one important part of this program is to extend the available dose tables as a function of technique. Specifically, from a literature search, we found no published dose data for x-ray spectra for x-ray above 40 kVp for either Molybdenum or Rhodium anodes. These are commonly used for standard mammography. The closest match we found was John Boone's published work [7]. In that paper, a third order polynomial fit is used to model x-ray spectra for techniques up to 40 kVp. Data cover up to 42 kVp, raw data were not shown). The x-ray spectra are fitted into polynomial formalism for each energy bin of produced x-ray spectra. It is stated that fitted results generally within a few percent of measured data for all energy bins and kVp settings where data were measured. The polynomial fits to the x-ray spectra are defined functionally as follows:

$$\Phi(keV) = a_0 + a_1kVp + a_2kVp^2 + a_3kVp^3$$

where  $a_3 = 0$  when kVp  $\geq 26$  keV,  $a_2 = 0$  when kVp  $\geq 36$  keV.

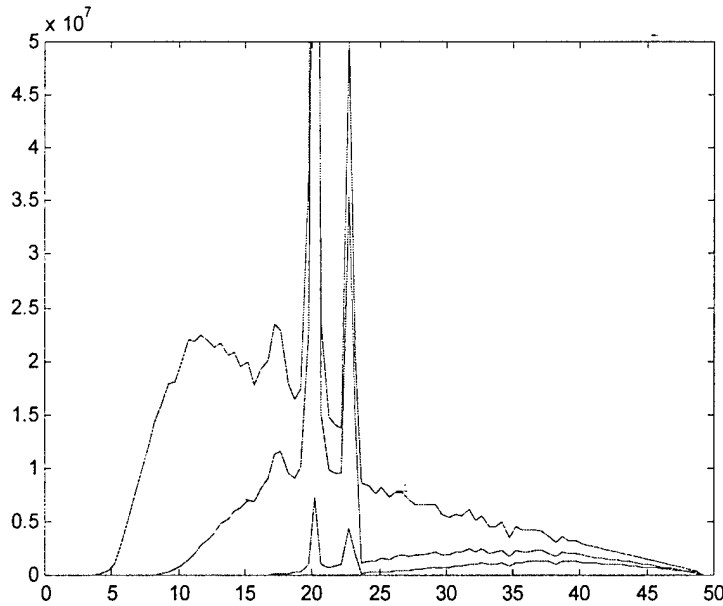


Figure 8: Extended Boone model for x-ray spectra for  $kVp > 36$  keV.

For x-ray energy above 36 kVp, linear fits were used for all  $a_i$  coefficients in the energy bins in Boone's model. Such an approach assumes that such formalism can be extended to the neighborhood of 41 to 50 kVp. Following this assumption and applying the constraint that the x-ray energy cannot exceed the kVp setting, the x-ray spectra can be obtained for kVps between 40 and 50 keV. Figure 8 shows the x-ray spectra with a Rh/Rh anode/filter combination at 49 kVp. It is planned that exposure and HVL will be measured and compared to the results as obtained by this extended model. It is also important to note that the system modeling in other sections of this report is independent of this extended model. This work is ongoing for verification of the extension, which may enable us to extend by association the system model described in the preceding sections of this report.

Keeping in mind our overall program objective, which is to enhance the visibility of calcifications through dual energy imaging techniques, we still require a model of dose for these high kVp x-ray techniques. Specifically, the total dose of the two shots combined must be less than the ACR limit for a single shot ( $< 300$  mrad) for comparison. Patient dose is estimated by mean glandular dose and entrance skin exposure as indicated in the literature. To calculate the glandular dose, an extension has been performed so that for any given x-ray spectra, breast thickness and glandular percentage, the mean glandular dose can be calculated. This is done by passing the x-ray spectra through a model of a breast which accounts for both breast thickness and composition. The model assumes a uniform distribution of adipose and glandular tissue.

Specifically,

$$\text{Mean glandular dose} = (\text{total glandular energy absorption})/(\text{glandular mass}).$$

The skin contribution to dose is ignored in this simulation, but can be included straightforwardly if necessary. Mass-energy-absorption coefficients obtained by using the NIST web tool were used for this calculation. For standard x-ray mammography energies, the results from this calculation were compared to results in literature, e.g. by Barns et. al. [5] and found to be within 10%. No results were found in the literature for energies of 40 kVp and above for mammography. Table 1 shows sample results of glandular dose as calculated using the approach described. Note that this work is also independent of the modeling effort described in the preceding sections. However, if early experiments in microcalcification visibility indicate that high energy mammography spectra are required for improved microcalcification visibility, these results can be incorporated into the model described above and can also be used to verify some parts of the model described above.

**5.0 cm breast thickness, 50/50 adipose/glandular, skin ignored SID**

	HVL (mmAl)	Avg E(keV)	mRad/ mR	Entrance expo(mR)	Glandular dose (mGy)
Mo26Mo	0.268	16.2	0.122	30.3	0.03683
Mo30Mo	0.322	16.9	0.134	45.9	0.06146
Rh26Rh	0.308	17.3	0.137	18.2	0.02502
Rh30Rh	0.375	18.4	0.153	28.1	0.04305
Rh49Rh	0.558	22.2	0.192	90.0	0.01725
W30Al0.5mm	0.335	19.3	0.147	45.0	0.06623
W49Al2mm	1.307	31.5	0.302	29.5	0.08891
W70Al2mm	1.736	38.7	0.358	6.96	0.02488
W70Al2mmCu0.1	2.058	43.3	0.415	2.94	0.01222

Table 1 (Xspect was used to generate x-ray spectra at 1m/cm<sup>2</sup> mAs)

**TASK 1 SUBTASK 4: Optimal spectra for various tissue compositions and sizes**

Given the model of the system signal level and noise level as a function of technique and breast composition, coupled with the model of dose as a function of technique (using published results, not the extended model described in the previous section), a straightforward approach to optimizing the percent glandular sigma as a function of technique was developed. In this approach, the maximum dose for a given breast thickness is set and a list of all the x-ray techniques which yield a dose less than that maximum dose are computed. Each of these x-ray techniques is then used to compute a percent glandular sigma. The dose which minimizes the percent glandular sigma is chosen as the optimal technique. An example optimization surface for a 7cm 50% glandular breast is shown in Figure 10. Note that in this case, a 37kVp Rh/Rh technique was optimal. A chart of optimal techniques given compressed breast thicknesses and compositions is shown in Table 3. In the table, the technique is given as a kVp, mAs pair

in each breast height and composition cell. The filter/anode combination is labeled via the color. Blue indicates a Mo/Mo technique, green indicates Mo/Rh, and red indicates Rh/Rh. The corresponding z values are shown in the lower half of the table. The z metric is the tolerance (5% in percent glandular composition) divided by the percent glandular estimation error standard deviation for that optimal technique. Note that dose was increased linearly from 50mrads for a 2cm breast to 300mrads for an 8cm breast in the technique chart, which is why the thicker breasts have a counterintuitively higher z value.

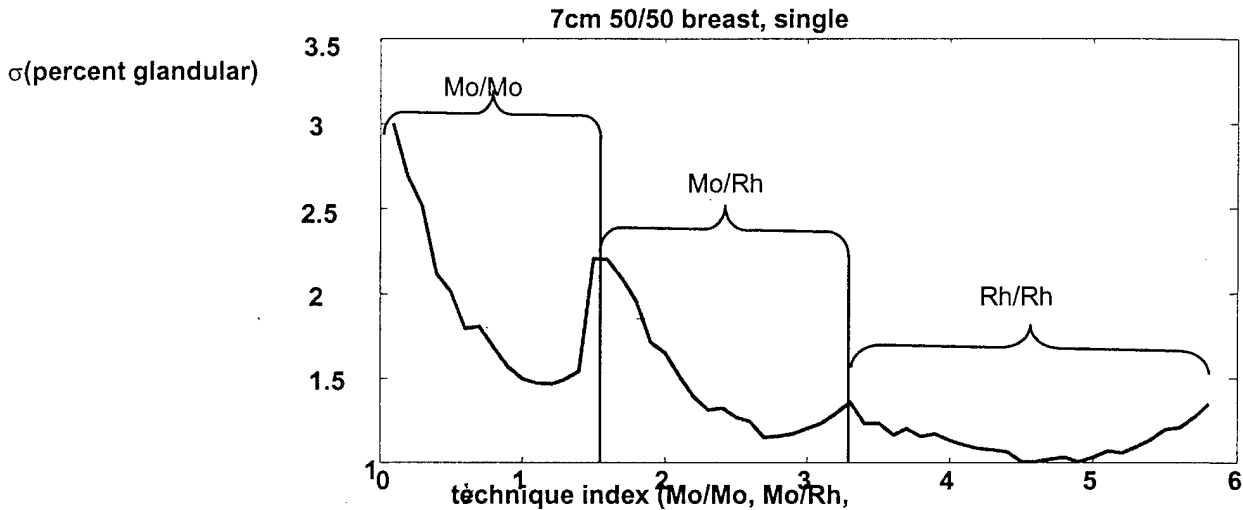


Figure 10: Percent Glandular Estimation Error Standard Deviation Versus X-Ray Technique (minimum is optimal technique)

	2cm	4cm	6cm	8cm
0%	28,12.5	27,56	25,180	33,90
25%	26,18	27,63	31,80	37,71
50%	29,12	25,110	33,71	36,90
75%	27,18	26,100	38,50	40,71
100%	29,14	33,45	40,45	42,63
0%	1.75	2.94	3.37	3.32
25%	1.65	2.70	3.01	3.05
50%	1.61	2.50	2.80	2.82
75%	1.55	2.32	2.64	2.63
100%	1.49	2.21	2.46	2.39

Table 3: Prescribed Technique Chart for Optimal Glandular/Fatty Tissue Discrimination

Because there is general agreement between the trends in the prescribed technique chart in Table 3 and available technique charts (harder beam for thicker breasts, e.g.), the dose, signal level, and noise as a function of x-ray technique appear self-consistent and applicable to the dual energy tasks outlined in the proposal.

### **Summary and Timeline**

Described above are the four subtasks listed under **Task 1** in the **Statement of Work** of the grant proposal. In the coming months, we intend to 1) increase the fidelity of the model in subtask 1 and measure its accuracy against new data points, 2) optimize the space of technique combinations for tissue composition alone using dual energy approaches 3) optimize the space of technique combinations for theoretical microcalcification detection using dual energy approaches, and 4) extend the available technique range in filter/anode combination choice. The projected timeline for these subtasks of task 1 are nominally on target for the grant schedule considering that the effective CRD "on time" has been since late March. CRD was originally projected to spend \$125k of the \$289k in the first fiscal year; to date, due to the delay in contract agreement, we have only spent \$61k and intend to carry over the residual for accelerated redistribution among the subsequent two years of the grant.

### References for Dose vs. Technique, Breast Composition:

Numerous people have done both theoretical and experimental investigation on dual energy mammography Most recent or direct on mammography are

1. John M. Boone and Gary S. Shaber and Melvin Tecotzky, "Dual energy mammography: A detector analysis" *Med. Phys.* 17(4), 665(1990). (different phosphor combinations)
2. Paul C. Johns and Martin J. Yaffe, "Theoretical optimization of dual energy x-ray imaging with application to mammography", *Med. Phys.* 12(3) 289(1985)
3. Ralph Highnam and Michael Brady, "Mammographic Image Analysis" Computational Imaging and Vision Series, Kluwer Academic Publishers, 1999.
4. Paul C. Johns, Dick J. Drost, Martin J. Yaffe and Aaron Fenster, "Dual Energy mammography: Initial experimental results", *Med. Phys.* 12 (3) 297(1985).
5. Xizeng, Gary Barnes, Douglas M. Tucker, "Spectral Dependence of Glandular Tissue Dose in Screen-Film Mammography", *Radiology* Vol 179, No 1, 143(1991)
6. G. Richard Hammerstein et al, "Absorbed Radiation Dose in Mammography", *Radiology*, 1979 130:485-491
7. John M. Boone, Thomas R. Fewell and Robert J. Jennings, "Molybdenum, Rhodium, and Tungsten anode spectral models using interpolating polynomials with application to mammography", *Med. Phys.* 24 (12) 1863(1997)
8. Douglas N. Tucker, Gary T. Barnes and Dev P. Chakraborty, "Semiempirical model for generating tungsten target x-ray spectra", *Med. Phys.* 18(2) 211(1991)
9. Douglas M. Tucker, Gary T. Barnes and Xizeng Wu, "Molybdenum target x-ray spectra: A semiempirical model", *Med. Phys.* 18(3) 402(1991)

PROGRESS IN BIOMEDICAL OPTICS AND IMAGING

Vol. 2, No. 25  
ISSN 1605-7422

*Medical Imaging 2001*

---

**Physics of Medical Imaging**

**Larry E. Antonuk**

**Martin J. Yaffe**

*Chairs/Editors*

**18-20 February 2001**  
**San Diego, USA**

**Proceedings of SPIE**  
**Volume 4320**

# Comparison of a-Si:H/CsI Flat-Panel Digital Imaging Systems with CR and CCD Based Systems — Image Quality Measurements

Xinming Liu, Chris C. Shaw, Xiujiang J. Rong, Michael Lemacks  
Department of Diagnostic Radiology  
Univ. of Texas M.D. Anderson Cancer Center, Houston, TX 77030

## ABSTRACT

The amorphous silicon/cesium iodide (a-Si:H/CsI:TI) flat-panel imaging systems have recently become commercially available for both chest and mammographic imaging applications. This new detector technology is considered to be a significant improvement over CR techniques. In this work, we measured the image properties for two commercial flat-panel systems and compared them with those measured for CR and CCD based imaging systems. Image quality measurements related to detector properties such as linearity, MTF, NPS and DQE are presented and compared at selected chest and mammographic imaging techniques. Factors and issues related to these measurements are discussed. For chest imaging, the flat-panel system was found to have slightly lower MTFs but significantly higher DQEs than the CR system. For mammographic imaging, the CCD-based system was found to have the highest MTF, followed in order by the flat-panel and CR systems. The flat-panel system was found to have the highest DQEs, followed in the order by the CCD-based and CR systems. The DQEs of the flat-panel systems were found to increase with exposure while those of the CR systems decrease slightly with the exposure in both chest and mammographic imaging. The DQEs of the CCD-based system were found to vary little for exposures ranging from 1 to 30 mR.

**Keywords:** Flat panel, computed radiography, CCD, modulation transfer function, noise power spectra, detective quantum efficiency, digital radiography, digital mammography

## 1. INTRODUCTION

Despite advances in new modalities, projection x-ray imaging remains as the primary tool for initial diagnosis of chest and breast diseases. Conventional projection x-ray imaging has relied on the use of screen/film combinations as the x-ray detector. Although they have been improved and optimized in quality over many decades, there are several drawbacks. Digital radiography techniques have been developed and investigated over the last two decades in the hope of improving the image quality and utilization of x-ray image data.<sup>1-17</sup> However, only in recent years, due to advances of digital and computer technology, has the concept of totally digital and filmless radiography operation become feasible. Thus, the incentives of finding a high quality yet economic digital image acquisition system for large scale implementation of digital radiography have grown high.

There have been several technologies which have become viable candidates for implementing digital radiography in different applications. More specifically, computer radiography (CR) and flat-panel (FP) systems have been developed for chest imaging while CR, FP and CCD based systems have been developed for mammographic imaging applications. The imaging properties of these systems have been extensively measured and reported on by various groups. However, most of these reports have focused on measurements for a specific imaging system or one type of technologies. Since the measurements were often conducted under different conditions or using different methodologies, it is difficult to perform a fair comparison of different technologies or systems from separate reports.

In this work, we attempted to measure the image properties of two different digital radiography techniques for chest imaging and three different techniques for mammographic imaging using identical methodology and under nearly identical conditions. These measurements were performed on clinical systems instead of prototype systems to provide a more realistic study of the image quality for clinical applications. In this paper, the methodologies for the measurements are described. The results of the image quality measurements are presented and compared.

## 2. METHODS AND MATERIALS

### 2.1 Image Acquisition

#### 2.1.1 Chest Imaging

For chest imaging, an a-Si:H/CsI:Tl flat-panel (FP) digital chest radiographic unit (Revolution XQ/i, General Electric Medical Systems, Milwaukee, WI) and a CR system (FCR-AC3 with ST-V<sub>N</sub> plate, Fuji Medical Systems, Stamford, CT) were measured and compared with each other at selected chest imaging techniques. The flat-panel detector uses a thallium-doped cesium iodide (CsI:Tl) scintillator as the x-ray detection material. The CsI:Tl is directly deposited onto a two-dimensional array of the amorphous silicon (a-Si:H) photodiodes and thin-film-transistor (TFT) switches (usually formed on a single glass substrate). The unique combination of x-ray scintillation properties and needle-like structure make CsI an attractive candidate as the x-ray absorbing layer for flat-panel detectors. The XQ/i provides both raw and processed image data. In this study, the raw image data were archived on to a CD-R disc and then transferred to a Sun workstation for further processing. For CR chest imaging, a ST-V<sub>N</sub> imaging plate (35×43 cm<sup>2</sup>) was exposed and scanned at sample rate of 5 pixels/mm. The CR scanner was operated in a fixed mode (Test/Linearity) with a sensitivity and latitude of 200, 3.0, respectively. The CR images were originally read at 12 bits and then log mapped into 10 bits digital values for data transfer and display. Log mapped CR images were transferred to a Sun workstation and then re-converted into 12 bits linear data prior to image quality measurement. Specifications of the FP and CR systems for chest imaging are listed and compared in Table 1.

Table 1. Specifications of FP and CR systems for chest imaging

Detector Type	FP	CR
Active Area	41×41 cm <sup>2</sup>	35×43 cm <sup>2</sup>
Matrix Size	2022×2022	1760×2140
Pixel Size	200μm	200μm
Image Depth	14 bits (linear)	10 bits (log)

All images were acquired at 70 kV<sub>p</sub> with a 0.5-mm thick copper filter added at the tube output. This technique was used by several other researchers to measure image properties of CR or flat-panel imaging systems.<sup>17-21</sup> The source-to-image distance was kept at 183 cm (72") for both FP and CR chest imaging. The x-ray tubes and generators used for FP and CR imaging were identical in make and model, allowing the measurement results to be compared under nearly identical conditions. The beam qualities for both FP and CR chest imaging were measured and listed in table 2. Measurements for the flat-panel chest unit were performed with the anti-scatter grid removed. For CR measurements, the imaging plates were exposed outside the Bucky.

Table 2. Beam qualities for FP and CR chest imaging at 70 kV<sub>p</sub>

Imaging Type	FP	CR
HVL (Al)	7.1 mm	6.9 mm
Fluence (photons/mm <sup>2</sup> /mR)	2.87×10 <sup>5</sup>	2.84×10 <sup>5</sup>

#### 2.1.2 Mammographic Imaging

For mammographic imaging, an a-Si:H/CsI:Tl flat-panel full-field digital mammography (FFDM) unit (SenoGraphe 2000, General Electric Medical Systems, Milwaukee, WI), a CCD based small-field digital mammography (SFDM) unit (SenoVision, GE Medical Systems, Milwaukee, WI) and a high resolution CR system (FCR-AC3 with HR-V plate) were measured and compared for their imaging properties. The FFDM unit consists of a solid-state detector similar to the one used in the flat-panel chest unit but differs in physical dimensions and imaging properties. The SFDM unit consists of a 6×6 cm<sup>2</sup> cooled CCD-based detector enclosed in an 18×24 cm<sup>2</sup> cassette with a pixel size of 30 μm. For CR imaging, an HR-V imaging plate (20.1×25.2 cm<sup>2</sup>) was exposed and scanned with a pixel size of 100 μm. The imaging plate was placed in a 24×30 cm<sup>2</sup>

cassette (at center against the chest side) and was exposed in the same x-ray unit used for the CCD detector. As in chest imaging, the CR scanner was operated with fixed sensitivity and latitude of 200 and 3.0. Specifications of the FP, CR and CCD systems for mammographic imaging are listed and compared in Table 3.

Table 3. Specifications of FP, CR and CCD systems for mammographic imaging

Detector Type	FP	CR	CCD
Active Area	19.2×23 cm <sup>2</sup>	20.1×25.2 cm <sup>2</sup>	6×6 cm <sup>2</sup>
Matrix Size	1914×2294	2000×2510	2048×2048
Pixel Size	100μm	100μm	30μm
Image Depth	14 bits (linear)	10 bits (log)	12 bits (linear)

All images were acquired at 28 kVp with a Mo-Mo target/filter combination. A 4.5-cm thick Lucite block was placed at the tube output to simulate x-ray attenuation by a typical compressed breast.<sup>6, 16</sup> The Lucite block was mounted on the tube side in order to minimize the scatter radiation. The source-to-image distance was maintained at 66 cm for all measurements. All images from the FFDM and SFDM units were transferred to a Sun workstation for further processing. The raw image data were linear in exposures and directly used for the quality measurements. The available CR image data were log mapped and needed to be re-converted to 12 bits linear data prior to image quality measurement. Measurements were performed with anti-scatter grids removed for all three different detectors.

## 2.2 Signal Linearity

Signal linearity is a basic requirement for measuring MTF, NPS and DQE. The signal transfer function is a plot of the detector signal versus entrance exposure. Mean signals were measured over a series of flat field images acquired at different exposure levels. A 100×100 pixels region-of-interest (ROI) was selected at the central area of the flat-field images for measuring the mean signals. For FP and CCD images, the raw image data were directly used to calculate and plot the mean signal as a function of exposures. With commercial CR systems, the digital data available were already logarithmically mapped and therefore needed to be re-converted to linear exposure scale for measurements. For such conversion, the mean pixel (logarithmic) values were calculated over the ROI and plotted as a function of the log<sub>10</sub> of exposures for calibration. The plots were then fitted to the following equation:

$$Q = a \cdot \log E + b \quad (1)$$

where  $Q$  is the digital value of unprocessed CR images;  $E$  is the exposure in mR at which the CR image was acquired;  $a$  and  $b$  are the gradient and intercept of the plot. The plot is often referred to as "characteristic response curve" of the CR system. The image signal was then linearized by using an inverse relationship derived from Eq. (1) to convert  $Q$  into  $E$ . This step is essential before the image data transferred from CR scanner can be used to measure the MTF, NPS and DQE.

## 2.3 Pre-sampling MTF Measurement

The pre-sampling MTFs were determined using a tilted-slit method. A slightly tilted x-ray slit camera (Nuclear Associates, Model 07-624) was imaged to measure the line spread functions (LSF). LSFs from subsequent lines were then combined into an effectively over-sampled LSF, which was then used to compute the pre-sampling MTF. This technique and experimental procedure has been described in detail by Fujita *et al.*<sup>22</sup> The slit used was 10 μm wide (with 4° relief angles on each jaw), 8 mm long, and made of 1.5-mm thick tantalum. For each measurement, the slit camera was placed right in front of the detectors to minimize image parallax and focal spot blurring. The slit was positioned at a slight angle (2~3°) to the anode-cathode axis at the center of the detector for chest imaging or at the center against chest side for mammographic imaging. The experimental setup for MTF measurement is illustrated in figure 1. This arrangement was used to generate a series of LSFs with the slit center positioned at various locations between two sampling points. These LSFs were then combined into a single LSF with effectively many more sampling points or a much shorter sampling distance.

The slit images were acquired at 70 kV<sub>p</sub> and 200 mAs with an additional 0.5-mm thick copper filter added for chest imaging. For mammographic imaging, they were acquired at 28 kVp and 80-200 mAs with a Mo-Mo target/filter combination. The small focal spot (0.6-mm for chest imaging and 0.1-mm for mammographic imaging) was used to reduce focal spot blurring

in MTF measurement. Special effort was made to minimize the scatter and glare component which generates a DC bias in the LSF data. The x-ray field was collimated outside the slit camera to minimize scatter and glare component. This procedure also helped prevent the flat-panel imager from being over-exposed and resulting in ghost image signals.

Correction was made on the slit images acquired to compensate for signal variation along the slit and biases outside the slit. About 25 successive image lines were synthesized to form a finely sampled composite LSF and normalized to its peak value. The Fourier transform (FT) was then applied to the finely sampled LSF. Finally, the modulus of the resultant FT was divided by a *sinc* function in the frequency domain to form a pre-sampling MTF. The *sinc* function was computed assuming the finite width (10  $\mu\text{m}$ ) of the slit resulted in a stop function shaped LSF:

$$MTF(f) = \frac{|FT(LSF(x))|}{\text{sinc}(af)} \quad (2)$$

where  $a$  is the slit width.

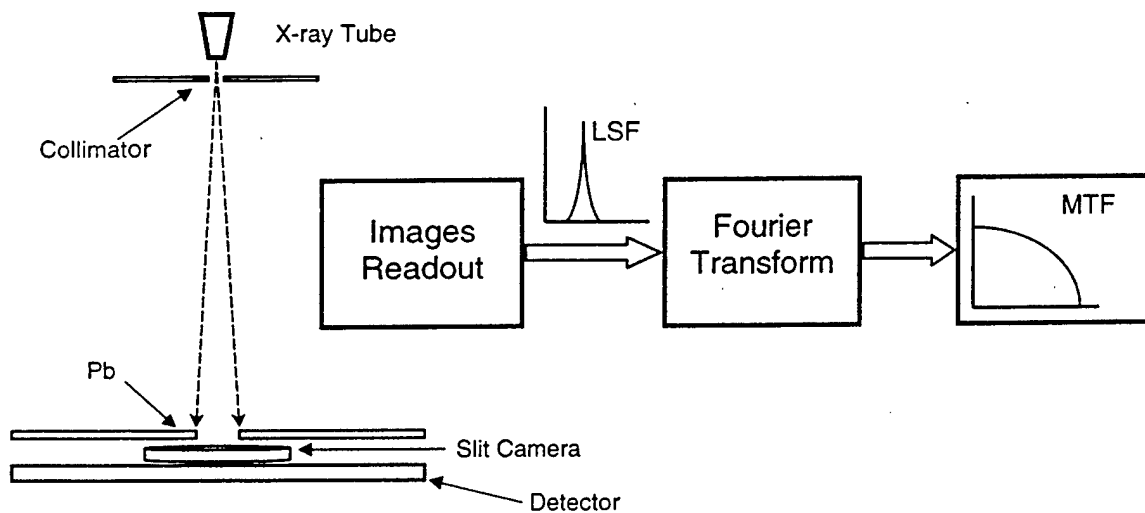


Figure 1. Experimental setup for MTF measurement using a 10- $\mu\text{m}$  slit camera.

## 2.4 NPS, NEQ and DQE Measurements

Uniform exposure images were acquired to compute NPS, NEQ and DQE. Four identically exposed images were acquired and the central 1280 $\times$ 1280 section was used for NPS measurement. These images were then normalized and subtracted from each other to form six noise only images. The low-frequency non-uniformity associated with the heel effect and gain variation can be readily removed with this process. Each image was multiplied with  $1/\sqrt{2}$  to compensate for noise increase due to subtraction. The resulting noise image was then equally divided into a 10 $\times$ 10 array of ROIs (128 $\times$ 128 pixels in each) for computing two-dimensional NPS. This resulted in 600 NPSs which were then averaged to yield a much smoother NPS at each exposure level. The NPS for each ROI was computed and normalized to mean signal by dividing the noise data by the mean signal value in each ROI prior to applying Fourier transform so that the NPS was no longer dependent on the digital value:

$$NPS_{normalized}(f_x, f_y) = \frac{\langle |FT(I(x, y))|^2 \rangle}{N_x \cdot N_y} \cdot p_x \cdot p_y \quad (3)$$

where The  $NPS_{normalized}$  is the normalized NPS;  $I(x, y)$  is the noise image as computed from the subtraction images;  $\langle \rangle$  represents the ensemble average over results from all 600 ROIs;  $N_x$  and  $N_y$  are the numbers of element in  $x$  and  $y$  directions (both of which are equal to 128 in our measurements);  $p_x$  and  $p_y$  are the pixel sizes in  $x$  and  $y$  axes (which are equal in our

measurements); and  $S$  is the mean signal for each ROI. The two-dimensional NPS better describes the noise properties of a detector and can also be used to identify any artifacts in images. However, the one-dimensional NPSs are often plotted and used to compute NEQs and DQEs along either horizontal or vertical direction for presentation. In our measurement, the 2-D NPS data along four lines on each side of the central horizontal axis were averaged to compute the one-dimensional NPSs.

Noise equivalent quanta (NEQs) were derived from the expectation MTF (EMTF) and the normalized NPS data as follows:

$$NEQ(f) = \frac{EMTF^2(f)}{NPS(f)_{normalized}} \quad (4)$$

where the  $EMTF$  is the average of digital MTFs over all relative positions of the slit center between two sampling points. NEQ expresses the apparent number of quanta per unit area contributing to an image if all noise sources in the system are quanta limited. This measure yields the output image signal-to-noise ratio squared as a function of spatial frequency.

The DQE provides a measure of the dose efficiency of an imaging system as a function of spatial frequency. The DQE is defined and computed as follows:

$$DQE(f) = \frac{NEQ(f)}{SNR_{in}^2} = \frac{EMTF^2(f)}{NPS(f)_{normalized} \cdot X \cdot C} \quad (5)$$

where  $X$  is the x-ray exposure (mR) on to the detector; and  $C$  is the x-ray fluence per exposure (photons/mm<sup>2</sup>/mR). Therefore the product of  $X$  and  $C$  is the numbers of x-ray photons incident on to the detector per unit area.

## 2.5 X-ray Exposure and Photon Fluence

X-ray exposures were measured for the linearity check and computing DQEs. All exposures were measured using a Keithley model 35050A dosimeter and a calibrated ionization chamber (Model: 96035B). The chamber has two different detection sides: Diagnostic Focus for chest imaging and Mammography Focus for mammographic imaging. Measurement was performed using separate exposures to prevent the ion chamber shadows from appearing in the images. The ionization chamber was placed between the detector and the x-ray tube and centered in the field of view. Three successive exposure readings were taken and averaged. The averaged readings were then used to estimate the exposure at the detector using the inverse square law. This helped eliminate the influence of scattered radiation either from x-ray tube side (caused by copper filter or Lucite block) or the detector.

The photon fluence was estimated using computer simulation based on published method and tables.<sup>23, 24</sup> The x-ray fluence per exposure,  $C$ , is expressed by following equation:

$$C = \frac{\int c(E)q(E)dE}{\int q(E)dE} \quad (6)$$

where  $c(E)$  is the photon fluence per exposure as a function of energy,  $E$ , and  $q(E)$  is the x-ray fluence per unit energy as a function of photon energy. The photon fluence for chest imaging were calculated and listed in table 2. The photon fluence for mammographic imaging is adopted from published data to be  $5.33 \times 10^4$  photons/mm<sup>2</sup>/mR.<sup>6, 16</sup>

## 3. RESULTS

### 3.1 Linearity

The signals versus exposure curves of the flat-panel digital chest unit and ST-CR system are plotted for comparison in figure 2(a). The linearity curve of the flat-panel mammographic unit (FFDM), CR and CCD-based digital mammographic unit (SFDM) were plotted in figure 2(b) for comparison. The data points represent the mean signal intensities of each flat field

image at various exposure levels and the solid lines represent the linear fit to the data. The sensitivity of the imaging systems and the error of the linearity curves can be determined from the plots as well.

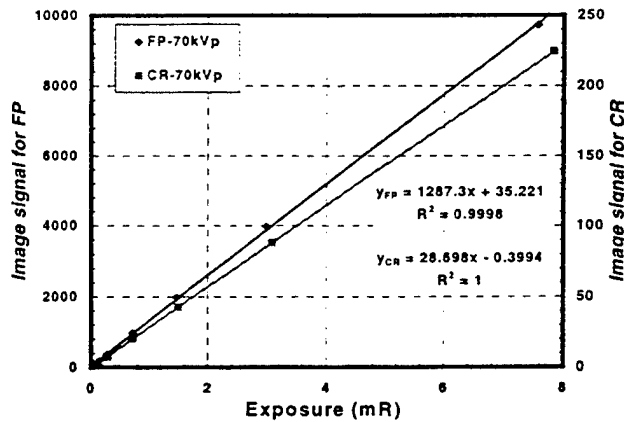


Figure 2(a). Signal versus exposure for FP and CR chest imaging at 70kV<sub>p</sub>. A 0.5-mm copper plate was added to simulate the patient attenuation.

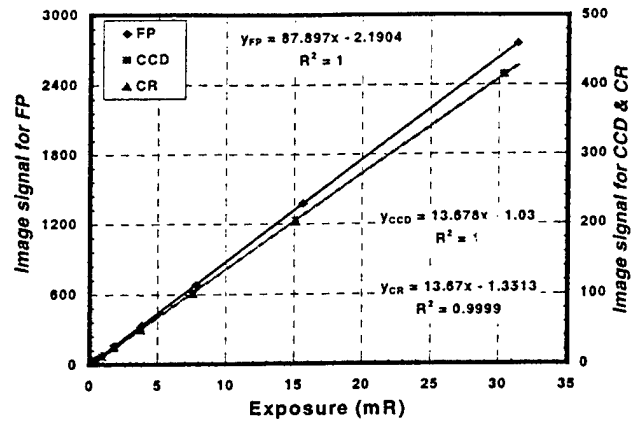


Figure 2(b). Signal versus exposure for FP, CCD and CR mammographic imaging at 28 kV<sub>p</sub>. A 4.5-cm Lucite block was added to simulate the tissue attenuation.

### 3.2 Pre-sampling MTF

The pre-sampling MTFs of the flat-panel digital chest unit and ST-CR system are plotted as a function of the spatial frequency for comparison in figure 3(a). Both systems have a pixel size of 0.2 mm corresponding to a Nyquist frequency of 2.5 lp/mm. The plots show that the MTF of the flat-panel unit is slightly lower but comparable to that of CR system.

The pre-sampling MTFs of the flat panel FFDM unit, HR-CR system, and the CCD-based SFDM unit are plotted as a function of the spatial frequency for comparison in figure 3(b). Both FFDM unit and HR CR system have a pixel size of 0.1 mm while the SFDM unit has a pixel size of 0.03 mm, corresponding to a Nyquist frequency of 5 lp/mm and 16.7 lp/mm, respectively. The SFDM unit was found to have the highest MTF, followed in order by the FFDM and HR-CR systems. Notice that the EMTFs, rather than pre-sampling MTFs, were used for computing the DQEs. These pre-sampling MTFs are presented here to illustrate and compare the spatial resolution properties of the different detector systems studied here.

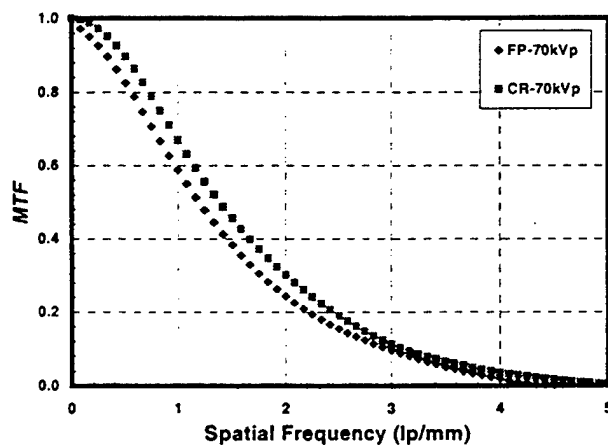


Figure 3(a). Pre-sampling MTF versus spatial frequency for FP and CR chest imaging at 70kV<sub>p</sub>. A 0.5-mm copper filter was added to simulate the patient attenuation.

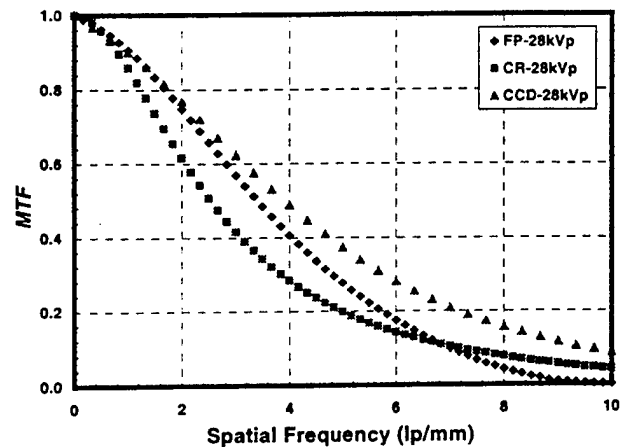


Figure 3(b). Pre-sampling MTF versus spatial frequency for FP, CR and CCD mammographic imaging at 28kV<sub>p</sub>. A 4.5-cm Lucite block was added to simulate tissue attenuation.

### 3.3 NPS results

The measured NPS values for the flat-panel digital chest unit and ST-CR system are plotted as a function of the spatial frequency for comparison in figures 4(a). The NPSs of the flat-panel unit were substantially lower than those of ST-CR system and decreased with spatial frequency at a faster rate.

The NPSs of the flat-panel FFDM unit, HR-CR system, and the CCD-based SFDM unit are plotted as a function of the spatial frequency for comparison in figure 4(b). Unlike NPSs for the digital chest units, the NPSs for the three digital mammographic systems weren't significantly different from each other. However the plots show that the flat-panel system has the lowest NPS, followed closely in order by CCD-based unit and CR system. The NPSs for the three detector systems were also measured and compared at various exposure levels either for chest or mammographic imaging.<sup>25, 26</sup>

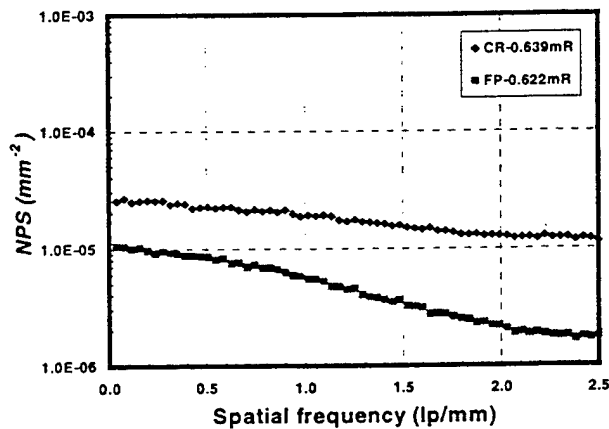


Figure 4(a). NPS versus spatial frequency for FP and CR chest imaging at 70kV<sub>p</sub>. A 0.5-mm copper plate was added to simulate the patient attenuation.

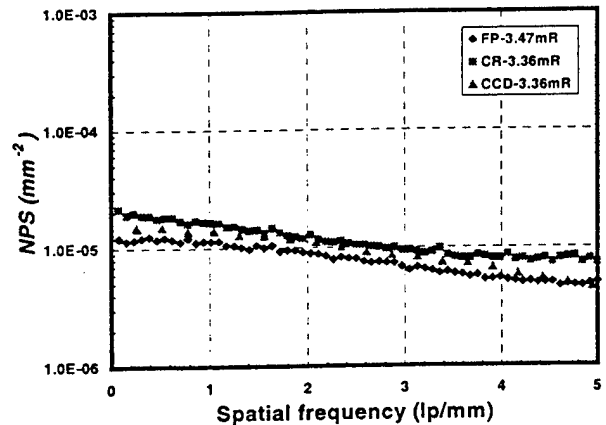


Figure 4(b). NPS versus spatial frequency for FP, CCD and CR mammographic imaging at 28 kV<sub>p</sub>. A 4.5-cm Lucite block was added to simulate the tissue attenuation.

### 3.4 NEQ and DQE results

The NEQs for the flat-panel digital chest unit and ST-CR system are plotted as a function of the spatial frequency in figures 5(a) for chest imaging. Those for the flat-panel FFDM unit, HR-CR system, and the CCD-based SFDM unit are plotted as a function of the spatial frequency for comparison in figure 5(b).

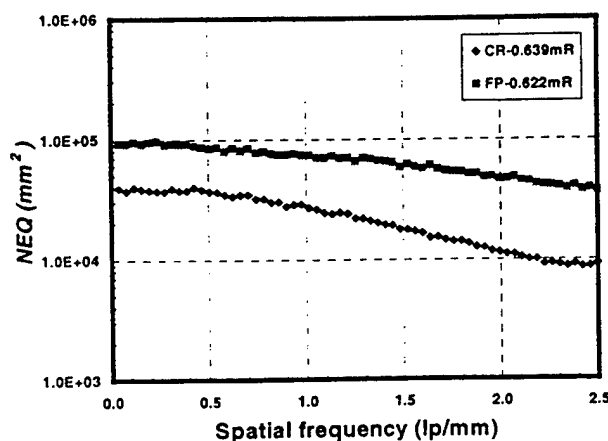


Figure 5(a). NEQ versus spatial frequency for FP and CR chest imaging at 70kV<sub>p</sub>. A 0.5-mm copper plate was added to simulate the patient attenuation.

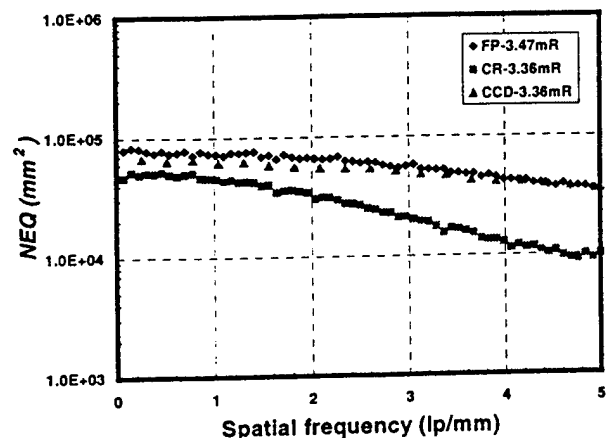


Figure 5(b). NEQ versus spatial frequency for FP, CCD and CR mammographic imaging at 28 kV<sub>p</sub>. A 4.5-cm Lucite block was added to simulate the tissue attenuation.

The DQEs for the flat-panel digital chest unit and ST-CR system were plotted as a function of the spatial frequency in figures 6(a). The DQEs of the flat-panel unit were substantially higher than those of CR system. This may be explained as a result of the much improved x-ray absorption efficiency while maintaining similar spatial through use of CsI:TI as the scintillator. The DQEs of the flat-panel FFDM unit, HR-CR system, and the CCD-based SFDM unit are plotted as a function of the spatial frequency in figure 6(b). The DQEs for the flat-panel unit was found to be slightly higher than those for CCD-based unit at 0-3 lp/mm. At higher frequencies, there was little difference observed. However, the DQEs for the HR-CR system were found to be considerably lower throughout the entire frequency range. As indicated by the MTF and NPS plots in figures 3(b) and 4(b) this may be explained as largely the result of the differences in their MTFs rather than in x-ray absorption efficiencies. The DQEs were also measured and compared at various exposure levels.<sup>25, 26</sup>

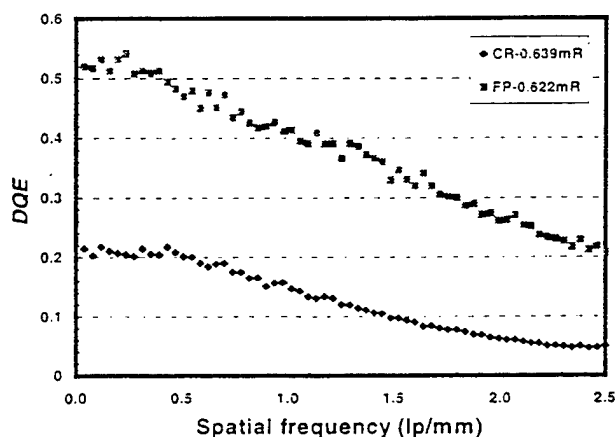


Figure 6(a). DQE versus spatial frequency for FP and CR chest imaging at 70kV<sub>p</sub>. A 0.5-mm copper plate was added to simulate the patient attenuation.

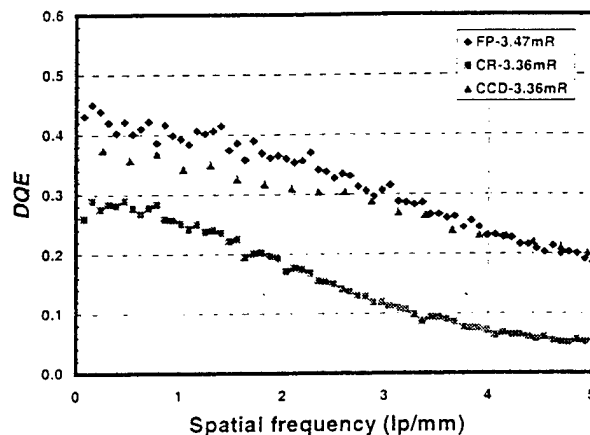


Figure 6(b). DQE versus spatial frequency for FP, CCD and CR mammographic imaging at 28 kV<sub>p</sub>. A 4.5-cm Lucite block was added to simulate the tissue attenuation.

### 3.5 Effects of Detector Packaging:

It should be noted that this study although we have avoided using the anti-scatter grid or Bucky, all images were acquired in their commercial packaging and were subject to x-ray attenuation by additional objects in the x-ray path. For the FP system, this would include the ion chamber and a front cover (for chest unit) or table top (part of detector/cassette holder). For CCD based SFDM unit, the images were acquired with a table top (part of detector/cassette holder) in the x-ray path. For CR imaging systems, no additional covers or table top were in the x-ray path. However, the x-rays were attenuated by the front cover of the CR cassettes before reaching the imaging plates. Thus, measurements for different detectors may be subject to different degrees of additional x-ray attenuation. Although this additional attenuation is relative small, it would affect NPS and NEQ measurements. Since the input exposures were measured without these additional objects in the x-ray path, they would also reduce the DQE values. Thus, our measurements should not be directly compared with those performed on prototype units for which these additional objects were generally removed for measurements. Our DQE values should be generally lower than those measured for prototypes. However, our values should better reflect the imaging conditions in actual clinical applications as these additional objects, including various covers, table tops and ion chambers are all present and result in additional x-ray attenuation which would degrade the DQE values.

## 4 CONCLUSIONS

We have measured the image properties for two commercial flat-panel systems and compared them with those measured for CR and CCD based imaging systems. For chest imaging, the flat-panel system was shown to have slightly lower MTF but significantly higher DQEs than the CR system. For mammographic imaging, the CCD-based system was found to have the highest MTF, followed in order by the flat-panel and CR systems. The flat-panel system was found to have the highest DQEs, followed in order by the CCD-based and CR systems. The DQEs of the flat-panel systems were found to increase with

exposure while those of the CR systems decrease slightly with the exposure in both chest and mammographic imaging. The DQEs of the CCD-based system were found to vary little for exposures ranging from 1 to 30 mR.

## ACKNOWLEDGMENTS

This work was supported in part by a research grant CA51248 from the National Cancer Institute and a research grant DAMD17-00-1-0316 from the US Army Breast Cancer Research Program.

## REFERENCES

1. R. Schaetzing, B. R. Whiting, A. R. Lubinsky, and J. F. Owen. "Digital radiography using storage phosphors." in *Digital Imaging in Diagnostic Radiology*, edited by J. D. Newell, Jr. and C. A. Kelsey (Churchill Livingstone, New York, 1990), pp. 107-138.
2. S. Arakawa, H. Yasuda, K. Kohda, and T. Suzuki. "Improvement of image quality in CR mammography by detection of emissions from dual sides of an imaging plate." *Proc. SPIE* **3977**, pp. 590-600, 2000.
3. F. L. Thaete, C. R. Fuhrman, J. H. Oliver, C. A. Britton, W. L. Campbell, J. H. Feist, W. H. Straub, P. L. Davis, and M. B. Plunkett. "Digital radiography and conventional imaging of the chest: A comparison of observer performance." *Am. J. Radiol.* **162**, pp. 575-581, 1994.
4. D. S. Brettle, S. C. Ward, G. J. S. Parkin, A. R. Cowen, and H. J. Sumison. "A clinical comparison between conventional and digital mammography utilizing computed radiography." *Br. J. Radiol.* **67**, pp. 464-468, 1994.
5. J. Wilson, F. A. Mann, W. A. Murphy, Jr., B. S. Monsees, and M. R. Linn. "Photostimulable phosphor digital radiography of the extremities: Diagnostic accuracy compared with conventional radiography." *Am. J. Radiol.* **157**, pp. 533-538, 1989.
6. S. Vedantham, A. Karellas, S. Suryanarayanan, I. Levis, M. Sayag, R. Kleehammer, R. Heidsieck, and C. J. D'Orsi. "Mammographic imaging with a small format CCD-based digital cassette: Physical characteristics of a clinical system." *Med. Phys.* **27**, pp. 1832-1840, 2000.
7. W. D. Jardin, C. Parks, H. Doan, N. Kurfiss, and K. Wetzel. "A large format, high-performance CCD sensor for medical x-ray applications." *Proc. SPIE* **3977**, pp. 167-175, 2000.
8. H. Liu, J. Xu, G. Halama, and J. McAdoo. "Digital fluoroscopy using an optically coupled CCD: Preliminary investigation." *Proc. SPIE* **2976**, pp. 256-261, 1997.
9. A. Jalink, J. McAdoo, G. Halama, and H. Liu. "CCD-mosaic technique for large field digital mammography." *IEEE Trans. Med. Imag.* **15**, pp. 260-267, 1996.
10. M. Choquette, H. Rougeot, J. P. Martin, L. Laperriere, Z. Shukri, and B. Polischuk. "Direct selenium x-ray detector for fluoroscopy, R&F, and radiography." *Proc. SPIE* **3977**, pp. 128-136, 2000.
11. E. L. Gingold, D. L. Y. Lee, L. S. Jeromin, B. Rodricks, M. G. Hoffberg, C. L. Williams. "Development of a novel high-resolution direct conversion x-ray detector." *Proc. SPIE* **3977**, pp. 185-193, 2000.
12. R. L. Weisfield, M. Hartney, R. Schneider, K. Aflatooni, and R. Lujan. "High performance amorphous silicon image sensor for x-ray diagnostic medical imaging applications." *Proc. SPIE* **3659**, pp. 307-317, 1999.
13. C. Chaussat, J. Chabbal, T. Ducourant, V. Spinnler, G. Vieux, and R. Neyret. "New CsI/a-Si 17 x 17-in. x-ray flat-panel detector provides superior detectivity and immediate digital output for general radiography systems." *Proc. SPIE* **3336**, pp. 45-57, 1998.
14. R. E. Colbeth, V. N. Cooper III, D. L. Gilblom, R. Harris, I. D. Job, M. E. Klausmeier-Brown, M. Marc, J. Pavkovich, E. J. Seppi, E. G. Shapiro, M. D. Wright, and J. M. Yu. "Characterization of a third generation, multi-mode sensor panel." *Proc. SPIE* **3659**, pp. 491-500, 1999.
15. L. E. Antonuk, Y. El-Mohri, J. H. Siewerdsen, J. Yorkston, W. Huang, V. E. Scarpine, and R. A. Street. "Empirical investigation of the signal performance of a high-resolution, indirect detection, active matrix flat-panel imager (AMFPI) for fluoroscopic and radiographic operation." *Med. Phys.* **24**, pp. 51-70, 1997.
16. S. Vedantham, A. Karellas, S. Suryanarayanan, D. Albagli, S. Han, E. J. Tkaczyk, C. E. Landberg, B. Opsahl-Ong, P. R. Granfors, I. Levis, C. J. D'Orsi, and R. E. Hendrick. "Full breast digital mammography with an amorphous silicon-based flat panel detector: Physical characteristics of a clinical prototype." *Med. Phys.* **27**, pp. 558-567, 2000.
17. P. R. Granfors and R. Aufrichtig. "Performance of a 41x41-cm<sup>2</sup> amorphous silicon flat panel x-ray detector for radiographic imaging applications." *Med. Phys.* **27**, pp. 1324-1331, 2000.
18. J. T. Dobbins III, D. L. Ergun, L. Rutz, D. A. Hinshaw, H. Blume, and D. C. Clark. "DQE(f) of four generations of computed radiography acquisition devices." *Med. Phys.* **22**, pp. 1581-1593, 1995.

19. C. D. Bradford, W. W. Pepler, and J. T. Dobbins III, "Performance characteristics of a Kodak computed radiography system." *Med. Phys.* **26**, pp. 27-37, 1999.
20. S. M. Kengyelics, A. G. Davies, and A. R. Cowen, "A comparison of the physical imaging properties of Fuji ST-V, ST-V.A. and ST-VN computed radiography image plates." *Med. Phys.* **25**, pp. 2163-2169, 1998.
21. M. J. Flynn and E. Samei, "Experimental comparison of noise and resolution for 2k and 4k storage phosphor radiography systems." *Med. Phys.* **26**, pp. 1612-1623, 1999.
22. H. Fujita, D.-Y. Tsai, T. Itoh, K. Doi, J. Morishita, K. Ueda, and A. Ohtsuka, "A simple method for determining the modulation transfer function in digital radiography." *IEEE Trans. Med. Imaging* **11**, 34-39, 1992.
23. H. E. Johns and J. R. Cunningham, *The Physics of Radiology*, Charles C. Thomas, Springfield, IL, 1983.
24. R. Birch, M. Marshall, and G. M. Ardran, "Catalogue of Spectral Data for Diagnostic X-rays." Hospital Physicists' Association, UK, 1979.
25. X. Liu, C. C. Shaw, X. Rong, and M. Lemacks, "Comparison of an amorphous silicon flat-panel imager with a CR system for chest imaging applications: Image Quality Measurement." (submitted to Medical Physics)
26. X. Liu, C. C. Shaw, X. Rong, M. Lemacks, and G. Whiteman, "Comparison of Three Detector Systems for Digital Mammographic Imaging: an a-Si/CsI Flat Panel Imager, a CCD Based Imager and a High Resolution CR System- Image Quality Measurements." (submitted to Medical Physics)

PROGRESS IN BIOMEDICAL OPTICS AND IMAGING

Vol. 2, No. 25  
ISSN 1605-7422

*Medical Imaging 2001*

---

***Physics of Medical Imaging***

**Larry E. Antonuk**  
**Martin J. Yaffe**  
*Chairs/Editors*

**18–20 February 2001**  
**San Diego, USA**

**Proceedings of SPIE**  
**Volume 4320**

# Comparison of a-Si:H CsI Flat-Panel Digital Imaging Systems with a CCD based System, CR Systems, and Conventional Screen-Film systems – A Contrast-Detail Phantom Study

John X. Rong, Chris C. Shaw, Dennis A. Johnston, Michael R. Lemacks,  
Xinming Liu, Gary J. Whitman, Stephen K. Thompson, and Kerry Krugh  
Department of Diagnostic Radiology  
Univ. of Texas M.D. Anderson Cancer Center, Houston, TX 77030

## ABSTRACT

Low-contrast detail detectability was evaluated and compared for a flat-panel digital chest system, a computed radiography (CR) system and a conventional screen/film (SF) system. Images of a contrast-detail phantom were acquired using these three systems under identical conditions. Additional images were acquired at varied exposures to study the potential for reduction of patient exposure using the flat-panel system. The results demonstrated that in chest imaging, the flat-panel system performed significantly better than the CR and the SF systems while the latter two performed about the same. Alternatively, an exposure reduction of at least 50% is possible if the same performance is maintained. For mammographic imaging, detectability for microcalcifications ( $\mu$ Cs) was evaluated and compared for a flat-panel based full-field digital mammography (FFDM) system, a charge-coupled device (CCD) -based small-field system, a high resolution CR system and a conventional SF system. Images of simulated calcifications of three size ranges were acquired and evaluated by readers for detectability of the  $\mu$ Cs. A Receiver Operating Characteristics (ROC) analysis was also performed to compare the overall detection accuracy for these four mammographic imaging systems. Our results show that in both the detectability analysis and the ROC analysis, the flat-panel systems performed the best followed by the screen/film system. The CCD based system showed better detection accuracy compared to the CR system in the ROC analysis. However, there was no significant difference between the CCD and the CR systems in the detectability analysis.

**Keywords:** Flat-panel, charge-coupled-device, computed radiography, film/screen, chest radiography, mammography

## 1. INTRODUCTION

Amorphous silicon/cesium iodide (a-Si:H/CsI) flat-panel digital imaging systems have recently become commercially available for both chest and mammographic x-ray imaging applications. Detailed descriptions of these systems are available elsewhere<sup>1,2</sup> and many investigations on imaging characteristics of these types of detectors have been conducted and reported.<sup>3,4,5</sup> Perception studies based on simulated  $\mu$ Cs or low contrast objects have also been used to directly compare the low contrast detectability of different imaging systems.<sup>6,7,8,9,10</sup> In this study, phantom images of a flat-panel digital chest system and a flat-panel digital mammography system were evaluated and compared with those acquired for CCD based, CR and conventional screen/film systems.

For chest imaging, a commercially available contrast detail phantom was used to compare a flat-panel digital chest system, a CR system and a conventional screen/film system. The results of the contrast-detail measurements are presented and compared. Factors and issues related to the contrast detail study are discussed.

For mammographic imaging, we designed a phantom of simulated calcifications to compare a flat-panel system, a CCD-based system, a high resolution CR system and a conventional screen/film combination. Images of simulated calcifications of three different size ranges were acquired and evaluated to determine the minimum detectability for various imaging modalities. A ROC analysis<sup>11</sup> was also performed to compare the detection accuracy for these systems.

## 2. METHODS AND MATERIALS

### 2.1 Chest Radiography

#### 2.1.1 Imaging Systems

Three chest x-ray imaging systems were compared in this study: a flat-panel system, a CR system and a conventional screen/film system. The flat-panel system, GE Revolution XQ/i chest radiography system (GE Medical Systems, Milwaukee, WI), was an amorphous silicon/cesium iodide flat-panel (FP) based digital chest radiography system. Active area of the detector is  $41 \times 41 \text{ cm}^2$ , corresponding to a  $2048 \times 2048$  matrix with a pixel size of  $200 \mu\text{m}$ . The use of needle structure CsI scintillator balances the x-ray absorption and spatial resolution. It is a detector/tube integrated, dedicated digital chest system with anti-scatter grid. The CR system studied was Fuji AC-3 reader (Fuji Medical Systems USA, Inc, Stamford, CT) used with ST-VN imaging plates of  $35.5 \times 43 \text{ cm}^2$ . Readout pixel size is also  $200 \mu\text{m}$ . For screen/film imaging, Agfa Ultra Rapid (Agfa Medical, Ridgefield Park, NJ) screen/film combination for SF chest x-ray was used. This is the standard screen/film combination used for chest examinations at our institution. CR and SF imaging were performed using a wall Bucky and tube of the same make and model as used for the flat-panel system.

#### 2.1.2 Contrast Detail Phantom

The contrast detail phantom used in this study was a CDRAD type 2.0 digital/conventional radiography phantom (Nuclear Associates, Carle Place, NY). A photographic picture of this phantom is shown in Figure 1. The CDRAD phantom is specially designed for quality control of radiography systems and observer performance study. It consists of a  $26.5 \times 26.5 \times 1 \text{ cm}^3$  Plexiglas plate divided into a  $15 \times 15$  array of  $1.5 \text{ cm}$  wide squares, in which circular recesses of various depths and diameters were milled to create objects of various contrast levels and sizes. These depths and diameters range between  $0.3$  to  $8.0 \text{ mm}$  with 15 steps increasing logarithmically. For objects of  $4 \text{ mm}$  and smaller, an additional object was created and placed randomly at one of the four corners. Accurate localization of these objects was used as the criteria in correcting the reading results.

#### 2.1.3 Image Acquisition

With manually selected mAs, tube outputs of the two x-ray systems were measured at  $125 \text{ kVp}$  using a  $150 \text{ CC}$  ion chamber and dosimeter (Inovision Radiation Measurements, Cleveland, OH) and compared to ensure that their difference is negligible. Table 1 lists exposures measured at the detector entrance surface ( $183 \text{ cm}$ ) with the use of a  $0.5 \text{ mm}$  Cu filter at the tube output. The output differences were found to be less than 12% for the two identical tubes. During image acquisition, the CDRAD phantom was positioned at the center of the x-ray field against the detector-Bucky assembly. A  $0.5\text{-mm}$  thick copper plate was placed at the tube output to simulate the attenuation of the patient.

Table 1. Exposures measured for the outputs of the identical tube used for the FP system and the CR/SF systems

Output selection mAs	Measured exposures		Ratio (%)
	(1) CR and SF	(2) FP	(1)/(2)
0.25	0.223	0.23	-3.0
0.5	0.503	0.496	1.4
1	1.063	1.011	5.1
1.6	1.74	1.636	6.4
2.5	2.79	2.61	6.9
3.2	3.59	3.3	8.8
4	4.74	4.32	9.7
5	6.17	5.52	11.8

Automatic exposure control (AEC) was used to determine the x-ray techniques required for achieving optical density of 1.5 in SF images:  $2 \text{ mAs}$ ,  $125 \text{ kVp}$ ,  $1.25 \text{ mm}$  focal spot and a source-to-image receptor distance (SID) of  $183 \text{ cm}$  ( $72''$ ). The corresponding exposure was measured to be  $2.09 \text{ mR}$  at this setting. Use this setting, images of contrast-detail phantom were acquired with each of the three chest imaging systems. To study the effects of exposure on low contrast detectability, additional flat-panel images were acquired at exposures of  $0.25$ ,  $0.5$  and  $1 \text{ mAs}$ , corresponding to an exposure of  $0.23$ ,  $0.50$

and 1.01 mR, respectively, at the entrance of the phantom.

The exposed film was processed using an automated film processor (CDS 300, Sterling Diagnostic Imaging, Newark, DE). The flat-panel and CR images were printed on films using a laser film printer (Drystar 3000, Agfa Medical, Ridgefield Park, NJ). Digital images were processed and printed with protocols designed for clinical chest examinations. Figure 2 shows a sample CDRAD phantom image acquired using the flat-panel system at the standard exposure setting of 125 kVp and 2 mAs.

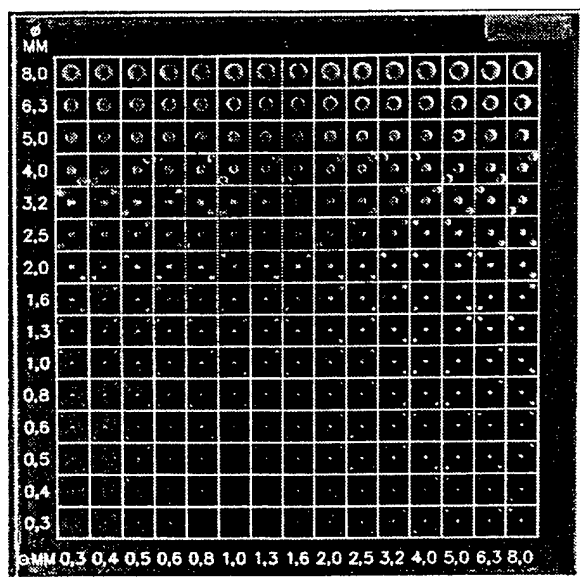


Figure 1. Photograph of the CDRAD phantom

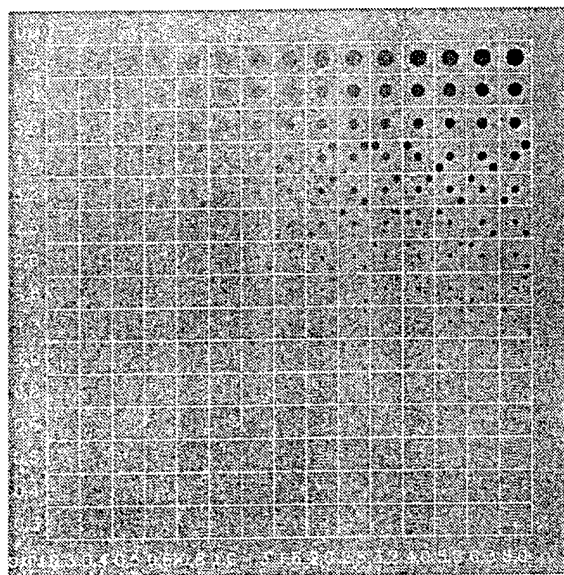


Figure 2. A CDRAD phantom image acquired using the flat-panel chest imaging system

### 2.1.4 Reading and Analysis

The CDRAD images acquired (SF) or printed (FP and CR) were masked with black tape and randomly ordered for reading. Although the conventional film was different from the printed films for digital images, the readers could not distinguish the FP images from the CR images. To optimize the viewing conditions, stray light from light box was blocked and ambient room light was kept low. Films were displayed in random order and reviewed by five readers with normal or corrected vision. There were no restrictions on viewing distance and use of a magnifying glass. The smallest depth, which represents the lowest contrast level required for detecting and correctly identifying both center and corner objects, was identified for objects of 4 mm and smaller. The additional objects randomly placed at the corners were used to verify and correct the results of reading. The images were evaluated in transition region where visibility of the objects changes from non-existent to marginal and then to very good. The region generally covered three or four different depths for each object size. Objects in the transition region were reviewed by readers and the locations of the objects were entered on the score form. One score form was filled by each reader and for each image. The score forms were compared to the truth table which contains information on the correct locations of all corner objects to determine if the location of an object is correct. Both true and false readings were evaluated and corrected following the instructions provided in the manufacturer's manual.<sup>12</sup> Following correction, a minimum detectable depth (contrast) was determined for each object size. The results were averaged over the five readers and plotted as a function of the object diameter to form contrast-detail curves.

## 2.2 Mammography

### 2.2.1 Imaging Systems

Four mammographic imaging systems were compared in this study: a flat-panel system, a CCD-based system, a high resolution CR (HRCR) system and a screen/film system. GE SenoGrappe 2000 full-field mammography system (GE Medical

Systems, Milwaukee, WI) was an aSi/CsI flat-panel digital system (FFMD). The image matrix size is  $191 \times 2254$  corresponding to a field size of  $19 \times 23 \text{ cm}^2$ . The pixel size is  $100 \mu\text{m}$ . A Bucky grid is integrated with the flat-panel detector. The small-field CCD based system was GE SenoVision (GE Medical Systems, Milwaukee, WI). The x-ray converter on the top of the CCD detector is a Kodak MinR 2000 mammographic screen (Eastman Kodak, Rochester, NY). The detector is  $6 \times 6 \text{ cm}^2$  in size and enclosed in a  $18 \times 24 \text{ cm}^2$  cassette, which is designed to fit into the cassette tray of a mammographic machine. The image matrix size is  $2048 \times 2048$  and the pixel size is  $30 \mu\text{m}$ . The HRCR system studied was Fuji AC-3 reader used with HR-V imaging plates of  $20 \times 25 \text{ cm}^2$ . Readout pixel size is  $100 \mu\text{m}$ . Kodak MinR 2000 screen/film combination ( $18 \times 24 \text{ cm}^2$ ) was used to acquire the SF images. The CCD, HRCR and SF images were acquired using the same GE SenoGraphe DMR+ (GE Medical Systems, Milwaukee, WI) mammography unit. The FP system is an integrated system with identical x-ray tube and generator.

### 2.2.2 Phantom Design

Three size groups of pre-sifted microcalcifications ( $\mu\text{Cs}$ ) (Computerized Imaging Reference Systems, Norfolk, VA) were used to construct the mammography phantom. Table 2 lists the size ranges of the  $\mu\text{Cs}$ . A cluster of four  $\mu\text{Cs}$  was attached to a  $2 \times 2 \text{ cm}^2$ , 3-mm thick Lucite square. One  $\mu\text{C}$  was missing from the five possible positions: four corners plus the center. Figure 3 shows a simulated  $\mu\text{C}$  cluster in which the upper right  $\mu\text{C}$  is missing. Three phantom pieces were assembled for each size group and a total of nine pieces were tiled into a  $6 \times 6 \text{ cm}^2$  phantom. During image acquisition, placement and orientation of the nine  $2 \times 2 \text{ cm}^2$  Lucite squares (therefore the simulated  $\mu\text{C}$  clusters) were varied to produce various patterns. To simulate breast attenuation, the tiled  $3 \times 3$  Lucite squares were sandwiched between two 1-cm thick 50% adipose/50% glandular (50/50) simulated tissue slabs (Computerized Imaging Reference Systems, Norfolk, VA) for a total Lucite thickness of 2.3 cm (Figure 4).

Table 2. Sizes of the simulated  $\mu\text{Cs}$  were used for constructing the mammographic phantom

Size range ( $\mu\text{m}$ )	Typical size ( $\mu\text{m}$ )
150-160	155
125-140	133
112-125	119

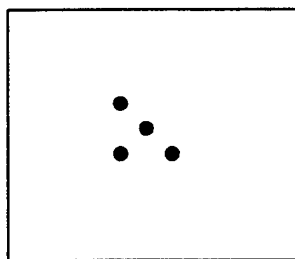


Figure 3. A sample pattern of a simulated  $\mu\text{C}$  cluster in which the upper right  $\mu\text{C}$  is missing.

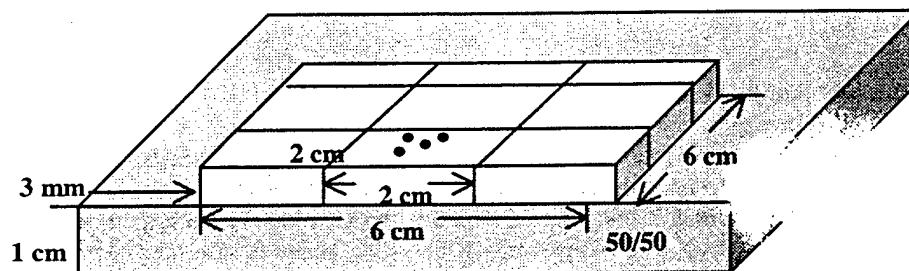


Figure 4. Phantom of  $3 \times 3$  tiled Lucite squares on a 1-cm thick 50% adipose/50% glandular simulated tissue slab. An additional slab was placed on the top for imaging. Placement and orientation of simulated  $\mu\text{C}$  clusters were randomized for each image acquisition.

### 2.2.3 Image Acquisition

Phantom images were acquired at 160 mAs, 25 kVp, 660 mm SID, with 0.3 mm focal spot size, a Mo/Mo target/filter combination. The use of the 160 mAs setting was determined by using the AEC to expose the SF cassette for pre-set film density and contrast. Five images were acquired for each modality. Patterns and sizes of the  $\mu\text{C}$  cluster were varied for each image. The phantom was positioned at the center of the table side of the cassette.

The flat-panel and CCD image data were linear and needed to be converted into log data for printing. The CR image data were in log. The FP and CR images were cut into  $875 \times 840$  sub-images to eliminate the areas outside of the phantom. A FFPM image of  $3 \times 3$  simulated  $\mu\text{C}$  clusters is shown in Figure 5.

### 2.2.4 Reading and Analysis

All images were serialized for identifying the detector types,  $\mu\text{C}$  sizes, and cluster patterns. Screen/film images were reviewed using a standard mammographic light box with all of the ambient light blocked and the room lights turned off. The readers were allowed to use a magnifying glass. Digital images were displayed one at a time on a CRT with window/level adjustment and zooming allowed. Ambient room lights were turned off. Phantom images were reviewed by five readers including four physicists and a radiologist (specialized in mammography) with normal or corrected vision. The readers were asked to assign a confidence level of 1-5 for detectability of  $\mu\text{C}$  at each of the five prospective locations of a  $\mu\text{C}$  cluster: 1- clearly absent, 2- probably absent, 3- absence/presence uncertain, 4- probably present, 5- clearly present. Average score was calculated and sorted for each  $\mu\text{C}$  size group, modality, and reader (one physicist and one radiologist). Scores of different modalities were averaged and compared for three different  $\mu\text{C}$  size ranges and two readers. In addition, a ROC analysis was performed for each modality using the combined scores for all three  $\mu\text{C}$  size ranges and from all five readers.

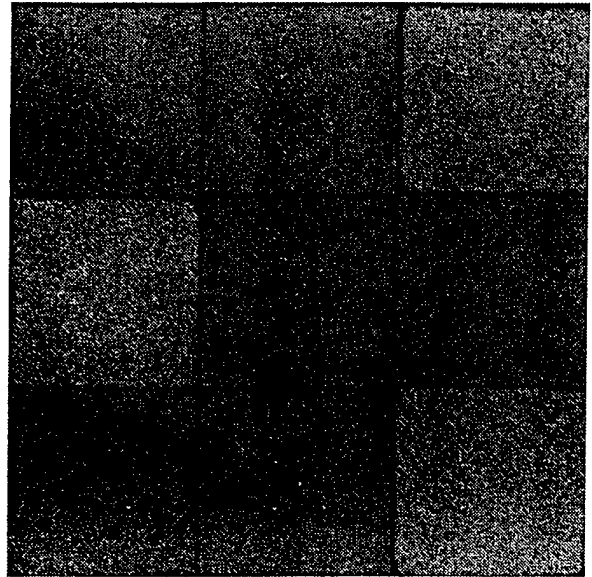


Figure 5. A sample image of mammographic phantom acquired using the FFDM system

## 3. RESULTS

### 3.1 Chest Radiography

In Figure 6, the minimum detectable contrasts (depths) are plotted as a function of the object diameter to form contrast-detail curves for the three chest imaging systems. To show the differences of the threshold contrasts at each diameter between the flat-panel and the screen/film and the differences between the CR and the screen/film, the flat-panel and the CR threshold contrasts were normalized to those of the screen/film for each diameter size. The normalized flat-panel and CR values were then plotted in Figure 7. From Figures 6 and 7, it can be clearly seen that the flat-panel chest imaging system showed the best low contrast performance over all sizes of objects studied. In Figure 7, the CR system is slightly better than the screen/film combination for the object sizes between 0.5 to 2 mm. However, no significant difference between the CR and SF systems in low contrast performance was observed.

Contrast-detail curves obtained at reduced exposure levels for the flat-panel system were compared with that (at 2 mAs) for the screen/film system in Figure 8. Figure 9 shows the corresponding normalized threshold depths for better comparison with the screen/film combination. In Figure 9, the flat-panel image acquired at 1 mAs performed clearly better than screen/film image acquired at 2 mAs over all objects sizes, indicating that a dose reduction by at least 50% is possible to maintain the same level of performance as the screen/film combination. With the exposure reduced to 0.5 mAs (25% of the exposure used for the screen/film imaging), the flat-panel system still demonstrated better low contrast performance than the screen/film combination for an object size of 0.6 mm or larger. Therefore, a dose reduction by ~75% is possible for objects 0.6 mm or larger by using the flat-panel imaging system.

To compare the overall low contrast detectability of different imaging systems and the techniques used, the volume of all minimum detectable objects were computed and summed together for each different modality/technique combination. The resultant total volumes were then normalized to that of the SF system and listed in Table 3 for comparison. A smaller minimum detectable volume shows a better overall system detectability. It can be seen from Table 3 that even at an exposure reduced by 75%, the flat-panel system still performed equally or better than the other two systems over all sizes of objects studied. In agreement with Figures 6 and 7, the CR system performed slightly better than the screen/film system at the same exposure level.

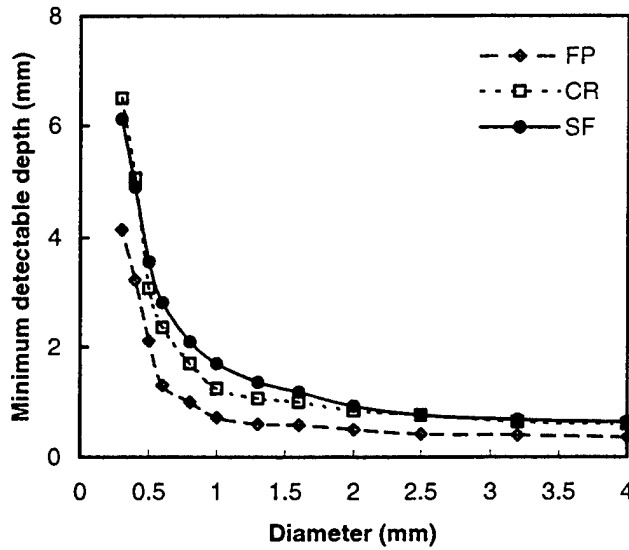


Figure 6. Contrast-detail curves of the screen/film, flat-panel, and CR imaging systems evaluated

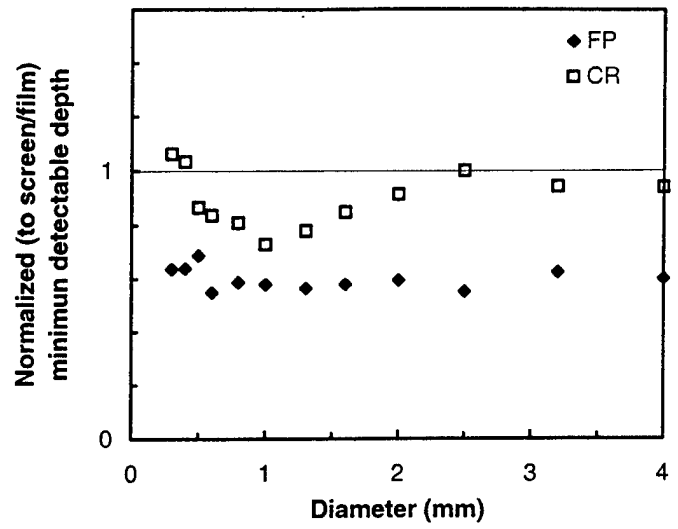


Figure 7. Minimum detectable depths of the flat-panel and CR systems were normalized to that of the screen/film system for each size of objects.

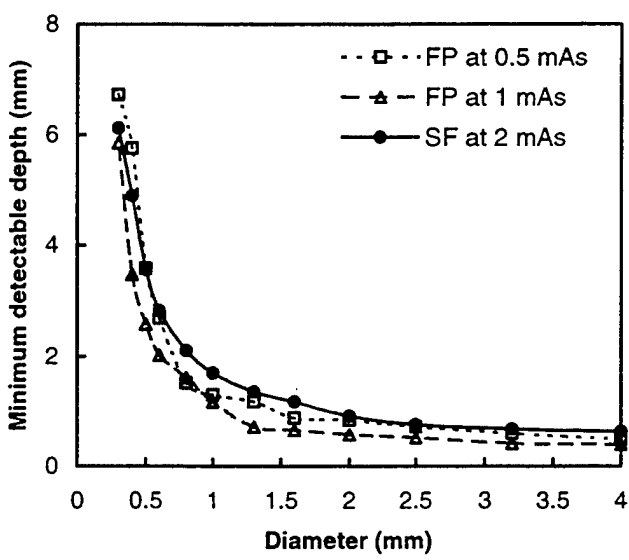


Figure 8. Contrast-detail curves of the flat-panel obtained at reduced exposure levels and the contrast-detail curve of the screen/film combination obtained at the standard exposure (2 mAs)

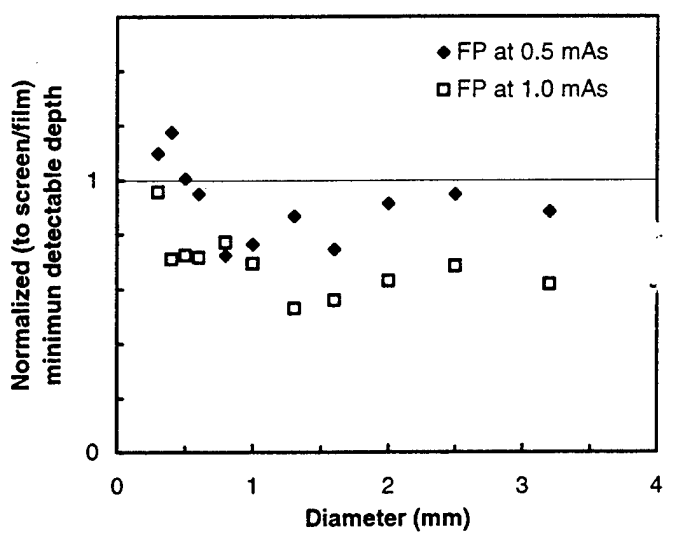


Figure 9. Minimum detectable depths of the flat-panel acquired at two reduced exposure levels were normalized to that of the screen/film system (2 mAs) for each size of objects.

Table 3. Use of minimum detectable volume as an index to compare the overall low contrast detectability of the imaging systems

Modality	FP			SF	CR
mAs	0.5	1	2	2	2
Volume (mm <sup>3</sup> )	25.1	18.7	15.9	29.2	26.7
Normalized to SF (%)	86	64	54	100	91

### 3.2 Mammography

The radiologist's scores for three  $\mu\text{C}$  size groups are plotted in Figure 10 to compare the minimum detectability of four detection modalities studied. As expected, the larger the  $\mu\text{C}$ s, the higher the scores. This was observed for all four detector systems. From Figure 10, it appears that the large (150 – 160  $\mu\text{m}$ )  $\mu\text{C}$ s can be easily detected and the small (112 – 125  $\mu\text{m}$ )  $\mu\text{C}$ s was a little too small to be seen. Therefore, the radiologist's scores for the medium size (125 – 140  $\mu\text{m}$ ) of the  $\mu\text{C}$ s are plotted in Figure 11. To study the variations between readers, the physicist's scores are plotted side-by-side to the radiologist's scores. For both readers, the flat-panel system received the highest scores among the four systems studied. The screen/film system ranked the second and received scores significantly higher than both the CR and CCD systems. The CR system scored a little higher compared to the CCD system, however, the difference was not significant for either reader.

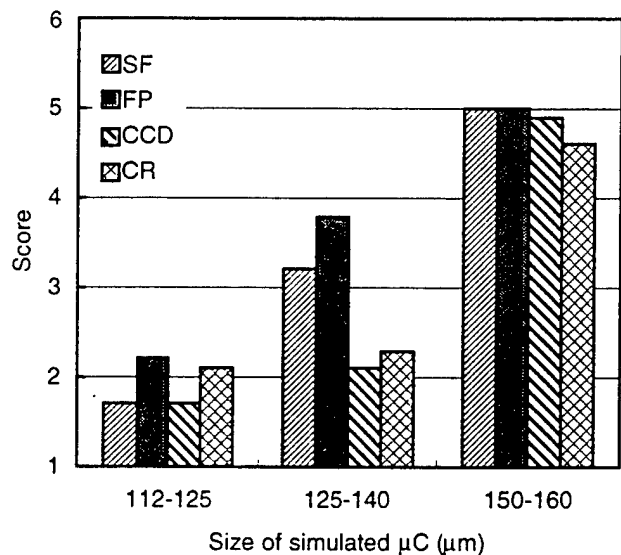


Figure 10. A radiologist's score for three simulated  $\mu\text{C}$  size ranges

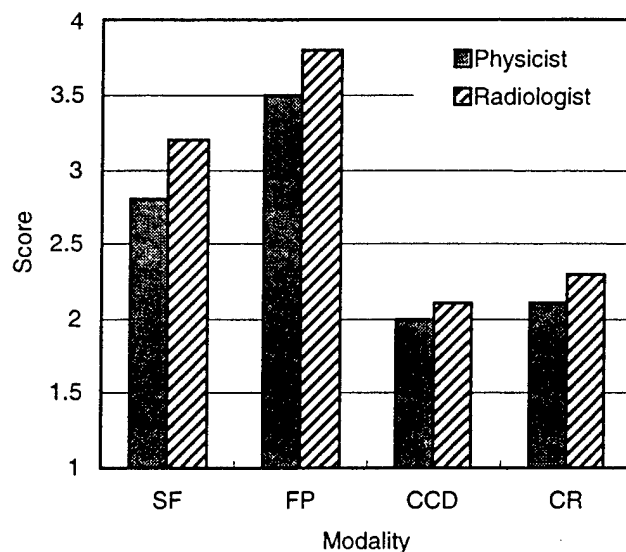
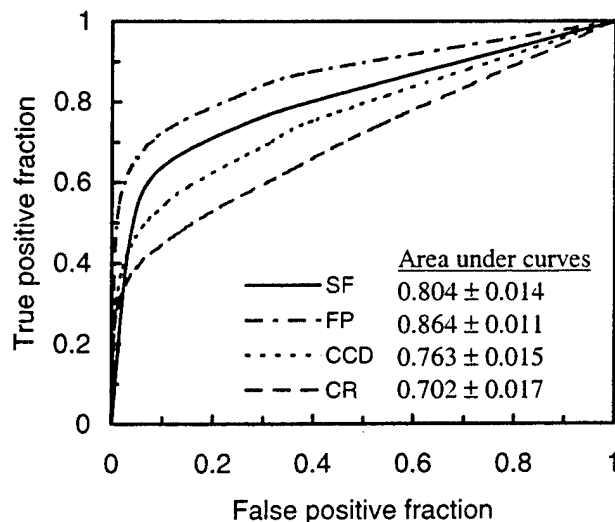


Figure 11. Scores of two readers for the 125 – 140  $\mu\text{m}$  simulated  $\mu\text{C}$  size range

The scores from five readers and all  $\mu\text{C}$  size groups were combined and analyzed together to form ROC curves shown in Figure 12. The area under each ROC curve was listed to show the differences in their detection accuracy. Both ROC curve and the area under the curve show that the FP ranked the best, the SF the second, the CCD the third, and the CR the last in their detection accuracy.

Figure 12. ROC analysis of five readers' score for three simulated  $\mu\text{C}$  size ranges



#### 4. SUMMARY

The flat-panel chest radiography system demonstrated significantly better contrast-detail performance than the screen/film CR systems for chest radiography. No significant difference was observed in low-contrast performances between the screen/film chest combination and the CR system. With the flat-panel technique for chest x-ray imaging, it is possible to reduce the exposure by at least 50% while maintaining the same level of performance as the conventional screen/film technique.

The flat-panel mammography system demonstrated the best performance in the minimum detectability analysis and the ROC analysis. Second to the flat-panel system, the screen/film combination performed significantly better than the CCD based system and the CR system in both the minimum detectability analysis and the ROC analysis. In the ROC study, the CCD based system showed better detection accuracy with respect to the CR system. However, no significant difference was observed in the minimum detectability analysis between the CCD and the CR systems.

#### ACKNOWLEDGMENTS

This work is supported in part by a research grant CA51248 from the National Cancer Institute and a research grant DAMD17-00-1-0316 from the Department of Army Breast Cancer Research Program.

#### REFERENCES

- <sup>1</sup> P. R. Granfors and R. Aufrichtig, "Performance of a 41 x 41-cm<sup>2</sup> amorphous silicon flat panel x-ray detector for radiographic imaging applications," *Med. Phys.* **27**, 1324 – 1331 (2000).
- <sup>2</sup> S. Vedantham, A. Karellas, S. Suryanarayanan, D. Albagli, S. Han, E. J. Tkaczyk, C. E. Landberg, B. Opsahl-Ong, P. R. Granfors, I. Levis, C. J. D'Orsi, and R. E. Hendrick, "Full breast digital mammography with an amorphous silicon-based flat panel detector: Physical characteristics of a clinical prototype," *Med. Phys.* **27** (3) 558 - 567 (2000).
- <sup>3</sup> L.E. Antonuk, J.M. Boudry, Y. El-Mohri, W. Huang, J.H. Siewerdsen, J. Yorkston, and R.A. Street, "Large-area, flat-panel amorphous silicon imagers," *Proc. SPIE* **2432**, 216 – 227 (1995).
- <sup>4</sup> J. Chabbal, C. Chaussat, T. Ducourant, L. Fritsch, J. Michailos, V. Spinnler, G. Viex, M. Arques, G. Hahm, M. Hoheisel, H. Horbaschek, R. Schulz, and M. Spahn, "Amorphous silicon x-ray image sensor," *Proc. SPIE* **2708**, 499 – 510 (1995).
- <sup>5</sup> X. Liu, C.C. Shaw, X.J. Rong, M. Lemacks, "Comparison of a-Si:H/CsI Flat-Panel Digital Imaging Systems with CR and CCD Based Systems — Image Quality Measurements," submitted to SPIE 2001.
- <sup>6</sup> J.T. Dobbins III, J.J. Rice, and C.A. Beam, "Threshold perception performance with computed and screen-film implications for chest radiography," *Radiology* **183**, 179-187 (1992).
- <sup>7</sup> L.T. Cook, M.F. Insana, M.A. McFadden, T.J. Hall, and G.G. Cox, "Comparison of the low-contrast detectability of a screen-film system and third generation computed radiography," *Med. Phys.* **21**(5), 691-695 (1994).
- <sup>8</sup> J.H. Launders and A.R. Cowen, "A comparison of the threshold detail detectability of a screen-film combination and computed radiology under conditions relevant to high-kVp chest radiography," *Phys. Med. Biol.* **40**, 1393 – 1398 (1995).
- <sup>9</sup> U. Neitzel, A. Bohm, and I. Maack, "Comparison of low-contrast detail detectability with five different conventional and digital radiographic imaging systems," *Proc SPIE* **3981**, 216 – 223 (2000).
- <sup>10</sup> R. Aufrichtig, "Comparison of low contrast detectability between a digital amorphous silicon and a screen-film based imaging system for thoracic radiography," *Med. Phys.* **26**, 1349-1358 (1999).
- <sup>11</sup> C. E. Metz, "ROC methodology in radiologic imaging," *Investigative Radiology* **21**(9), 720 – 733 (1986).
- <sup>12</sup> M.A.O.Thijssen, K.R. Bijkerk, and R.J.M. van der Burght, Manual contrast-detail phantom CDRAD type 2.0, Project quality assurance in radiology. Department of Radiology, University Hospital Nijmegen, St. Radboud, The Netherlands (1998).

# Comparison of an amorphous silicon/cesium iodide flat-panel digital chest radiography system with screen/film and computed radiography systems — A contrast-detail phantom study<sup>a)</sup>

Xiujiang J. Rong,<sup>b)</sup> Chris C. Shaw, Xinming Liu, Michael R. Lemacks,  
and Stephen K. Thompson

Department of Diagnostic Radiology, University of Texas M. D. Anderson Cancer Center, Houston,  
Texas 77030-4009

(Received 5 February 2001; accepted for publication 9 August 2001)

Flat-panel (FP) based digital radiography systems have recently been introduced as a new and improved digital radiography technology; it is important to evaluate and compare this new technology with currently widely used conventional screen/film (SF) and computed radiography (CR) techniques. In this study, the low contrast performance of an amorphous silicon/cesium iodide-based flat-panel digital chest radiography system is compared to those of a screen/film and a computed radiography system by measuring their contrast-detail curves. Also studied were the effects of image enhancement in printing the digital images and dependence on kVp and incident exposure. It was found that the FP system demonstrated significantly better low contrast performance than the SF or CR systems. It was estimated that a dose savings of 70%–90% could be achieved to match the low contrast performance of the FP images to that of the SF images. This dose saving was also found to increase with the object size. No significant difference was observed in low-contrast performances between the SF and CR systems. The use of clinical enhancement protocols for printing digital images was found to be essential and result in better low-contrast performance. No significant effects were observed for different kVps. From the results of this contrast-detail phantom study, the aSi/CsI-based flat-panel digital chest system should perform better under clinical situations for detection of low-contrast objects such as lung nodules. However, proper processing prior to printing would be essential to realizing this better performance. © 2001 American Association of Physicists in Medicine. [DOI: 10.1118/1.1408620]

Key words: chest radiography, computed radiography, contrast-detail phantom, film/screen, flat-panel

## INTRODUCTION

Despite development and advances in new imaging modalities, chest radiography remains to be the primary tool for the initial detection and diagnosis of pulmonary diseases. Approximately half of all radiographs obtained in medical institutions are images of the chest. Currently the majority of chest radiographs are acquired with conventional screen/film (SF) x-ray techniques. The advantages of SF techniques include low costs, reasonably good image quality with proper exposure, and ease of viewing. However, even though SF combinations have been improved and optimized over the years for chest radiography, there are some critical disadvantages. Intrinsic to the use of film as the image recording medium are the limited exposure range, washed out contrast in both heavily and lightly attenuated regions, high retake rate, inflexible image display, expenses, and inflexibility in film managements. Thus, there is a need for alternative im-

age acquisition and processing techniques to improve the diagnostic use and management of chest images.

As digital and computer technology advances, there have been various digital radiographic techniques developed for the replacement of the conventional SF technique. These techniques generally offer a linear signal response, wide dynamic range, flexibility in image display, processing and printing, and interface to a Picture Archival and Communication System (PACS) for digital image management. Due to the compatibility with existing radiographic equipment, the storage phosphor-based computed radiography (CR) has been commercialized and widely used in general radiographic applications. Conflicting opinions have been reported on the image quality of CR images as compared to the SF images. Dobbins *et al.*<sup>1</sup> showed that CR requires more exposure than the SF technique to achieve comparable low-contrast performance for general chest radiography. Other studies<sup>2–5</sup> showed that there were no significant differences between CR and SF techniques in low-contrast performance. However, there has been a general concern on the adequacy of image quality. As a result, there has been only limited success in using CR to replace the SF combinations for a primary diagnosis in chest imaging. Thus, efforts to develop

<sup>a)</sup>The scientific content of this paper was first presented at the Chicago 2000 World Congress on Medical Physics and Biomedical Engineering held in July 2000.

<sup>b)</sup>Corresponding author. Department of Diagnostic Radiology, University of Texas M. D. Anderson Cancer Center, 1515 Holcombe Boulevard, Box 57, Houston, Texas 77030-4009. Telephone: 713-745-2835; fax: 713-745-0581; electronic mail: jrongo@di.mdacc.tmc.edu

high quality digital radiography systems for chest imaging have continued.

In recent years, a number of flat-panel (FP) based digital radiography systems<sup>6,7</sup> have been introduced for clinical use in chest imaging. Some of these systems employ a direct coating of thallium doped cesium iodide (CsI:Tl) or a separate scintillator plate (CsI:Tl or x-ray phosphor) to convert x rays into light, which are then detected and read out by an amorphous silicon (*a*Si:H) FP detector containing a two-dimensional photodiode array and thin film transistor (TFT) switches.<sup>8-10</sup> Others employ a layer of amorphous selenium (*a*Se) to directly convert x rays into charges that are then collected and read out by an *a*Si:H array of capacitors and TFTs.<sup>11-14</sup> Comparing to CR, the FP-based system provides fast image acquisition and display, thus greatly improving patient throughput. Studies<sup>15-24</sup> have shown that FP detectors developed for use in general radiography have a significantly higher detective quantum efficiency (DQE) than both SF and CR systems. This higher DQE may lead to a better low contrast performance that should be evaluated and investigated with reception studies. One such study relies on the measurement and comparison of contrast-detail curves for a comparison of various imaging systems and techniques.

To obtain the contrast-detail curves, images of objects of various sizes and contrast are acquired with the imaging systems or techniques being studied and compared. The images are then visually examined to determine and plot the minimum detectable contrast level as a function of the object size. The resulting graphs are generally referred to as the contrast-detail curves. Curves closer to the origin (zero object contrast and size) indicate a better low-contrast performance, which may translate into the better detection and visualization of low-contrast object such as lung nodules and pneumothoraces in chest images.

Contrast detail curves have been widely used to evaluate and compare the low-contrast performance of different imaging systems or techniques in both tomographic and projection radiography.<sup>25-35</sup> Contrast-detail curves of different digital chest systems have been independently studied without being compared to each other. Due to inter-reader variations are differences in study conditions (x-ray techniques, reading and scoring, etc.), it is difficult to obtain a meaningful comparison of different imaging systems. In this study, the contrast-detail curves of an amorphous silicon (*a*Si:H)/cesium iodide (CsI:Tl) based FP digital chest unit were measured and studied. Effects of image of processing, exposure level, and kVp on the contrast-detail curves were also investigated. Curves of a CR system and a SF system were also measured under identical imaging conditions and compared to those of the FP system for their relative low-contrast performance.

## MATERIALS AND METHODS

### Imaging systems

The FP system investigated in this study was a CsI:Tl/*a*Si:H-based FP system (Revolution XQ/i, GE Medical Systems, Milwaukee, WI). The system employs a directly depos-

ited layer of CsI:Tl over an *a*Si:H plate containing an array of photodiodes and TFT switches for light detection and signal readout, respectively. The active area of the detector is 41×41 cm<sup>2</sup>, corresponding to a 2048×2048 matrix with a pixel size of 200 μm.<sup>23</sup> The needle structure of the CsI:Tl scintillator allows for more x-ray absorption without sacrificing the spatial resolution. The detector is integrated with a stationary antiscatter grid (78 lines/cm, 13:1 grid ratio) and x-ray generator/tube/control as a stand-alone chest radiography system.

The CR system studied was an FCR AC-3 image reader (Fuji Medical Systems USA, Inc., Stamford, CT) used in conjunction with 35.5×43 cm<sup>2</sup> ST-VN imaging plates. With this reader/plate combination, the plates were scanned and read out with a pixel size of 200 μm. The SF combination used was the Agfa Ultra Rapid (Agfa Medical, Ridgefield Park, NJ). SF and CR imaging were performed using a wall Bucky (44 lines/cm, 10:1 grid) radiographic system.

The noise Power Spectrum (NPS) and Detective Quantum Efficiency (DQE) of the FP and CR systems have been measured and reported in a separate manuscript.<sup>24</sup> The MTFs of the FP system were slightly lower than those of the CR system. However, the DQEs of the FP system were significantly higher (by 100% or higher) than those of the CR system. The MTF of the SF system, as measured by the manufacturer, is much better than those of the CR and FP systems. The DQEs of the SF system, on the other hand, are better than that of the CR but significantly lower than those of the FP system.<sup>36</sup>

### Contrast-detail phantom

The contrast-detail phantom used in this study was a CDRAD-type 2.0 digital/conventional radiography phantom (Nuclear Associates, Carle Place, NY).<sup>37</sup> Photographic pictures of this phantom are shown in Fig. 1. The CDRAD phantom is specially designed for evaluating the low-contrast performance of radiography systems. It consists of a 26.5×26.5×1 cm<sup>3</sup> Plexiglas plate containing a 15×15 array of 1.5×1.5 cm<sup>2</sup> regions, in which circular recesses of various depths and diameters were milled to create objects of various contrast levels and sizes. These depths and diameters range between 0.3–8.0 mm with 15 steps increasing logarithmically. For 4 mm and smaller objects, an additional object was created and placed randomly at one of the four corners. These additional objects are used to help minimize potential biases due to *a priori* knowledge on the presence of objects in every square region. This is achieved by requiring the readers to identify the locations of the corner objects if considered visible. True or false identifications are then used to correct the reading results for better accuracy and less fluctuations in determining the contrast-detail curves.

### Image acquisition

A schematic layout of the experimental setup for image acquisition is shown in Fig. 2. The x-ray tube and generator used for CR and SF imaging was identical in make and model to the one used for the FP system. With manually selected mAs, the tube outputs of the two x-ray systems were

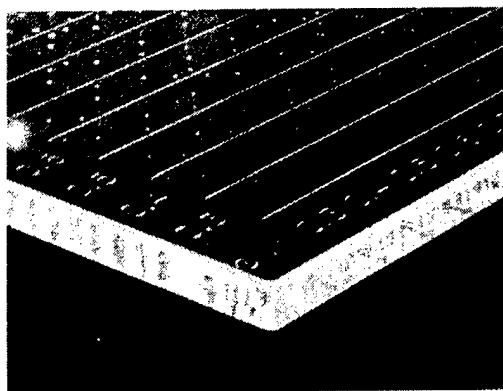
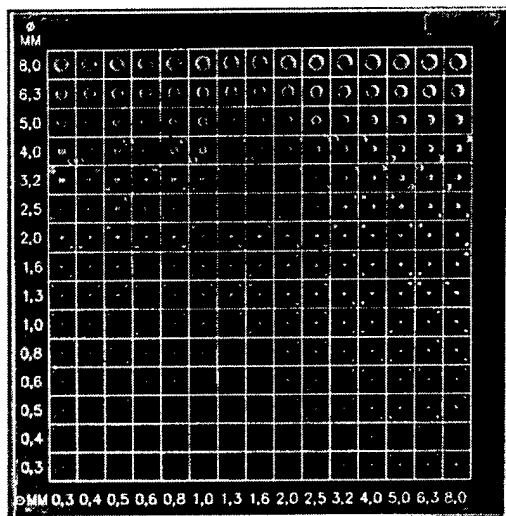


FIG. 1. Photograph of the CDRAD phantom.

measured and compared with each other using a 150 cm<sup>3</sup> ion chamber and dosimeter (Inovision Radiation Measurements, Cleveland, OH). The outputs of the FP system were found to be generally lower than those of the CR/SF system. However, the differences were found to be 12% or smaller for the techniques used in this study. During image acquisition, the CDRAD phantom was positioned at the center of the x-ray field against the detector-grid assembly. A 0.5-mm thick copper plate was placed at the tube output to simulate attenuation by the patient.

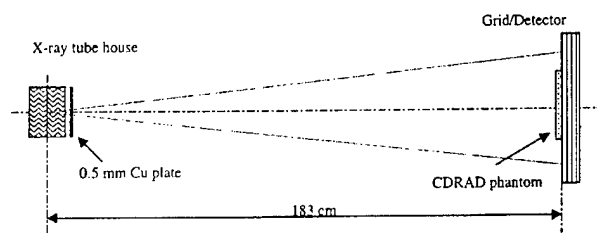


FIG. 2. Schematic layout of the experimental setup for a contrast-detail measurement.

Using the automatic exposure control (AEC) with the SF combination, a standard exposure setting was determined to be 2 mAs at 125 kVp with a 1.250-mm focal spot and a source-to-image receptor distance (SID) of 183 cm (72 in.). This setting was used to acquire images of the contrast-detail phantom with the SF, CR, and FP systems. At this setting, the exposure at the entrance of the phantom was measured to be 0.54 C/kg (or 2.09 mR). To study the effects of exposure on low-contrast performance, four additional FP images were acquired at 0.25, 0.5, 1, and 5 mAs, respectively, corresponding to an exposure of 0.06, 0.13, 0.26, and 1.42 C/kg (0.23, 0.50, 1.01, and 5.52 mR) at the entrance of the phantom. To study the effects of kVp on contrast-detail curves, two additional FP images were acquired at 80 and 100 kVp, respectively. The images were acquired in the AEC mode to keep the detector entrance exposure at the same level ( $\sim 0.54$  C/kg).

### Image processing and printing

All digital images were first processed and printed on films using their respective clinical enhancement protocols. These protocols were designed to optimally enhance the contrast of chest anatomy. Although the pattern of a contrast-detail phantom image is much different from those of chest images, these protocols still generated images of improved contrast when compared to those of the SF images. In Fig. 3, the FP, CR, and SF images of the CDRAD phantom acquired with the standard exposure setting (125 kVp and 2 mAs) are shown. Among them, the FP and CR images were processed and printed using their respective clinical enhancement protocols. The SF image was obtained by processing the exposed film using an automated film processor and loader CDS 300, Sterling Diagnostic Imaging, Newark, DE). The original SF images, as recorded on film, are much less contrasty when compared to the printed digital images. However, the contrast of the reproduced SF image was somewhat enhanced during the printing process.

To study the effects of image enhancement on low-contrast performance, a "film look" lookup table (LUT) was also created and used to process and print the digital images. Optical densities in the SF image of a step wedge were measured at various locations and used to calibrate the compute the "film look" LUTs for CR and FP images, respectively. These LUTs were developed to allow the FP and CR images to be printed with density and contrast that are similar to the SF image. Digital FP and CR images processed and printed with "film look" were also used to obtain additional-contrast detail curves in the observer study. These curves were compared to those obtained from images processes and printed using clinical enhancement protocols.

### Image reading

CDRAD images on film were masked using black tape and randomly ordered for reading. Although the conventional film could be easily distinguished from films for digital images, the films for the FP and CR images could not be distinguished from each other. To optimize the viewing con-

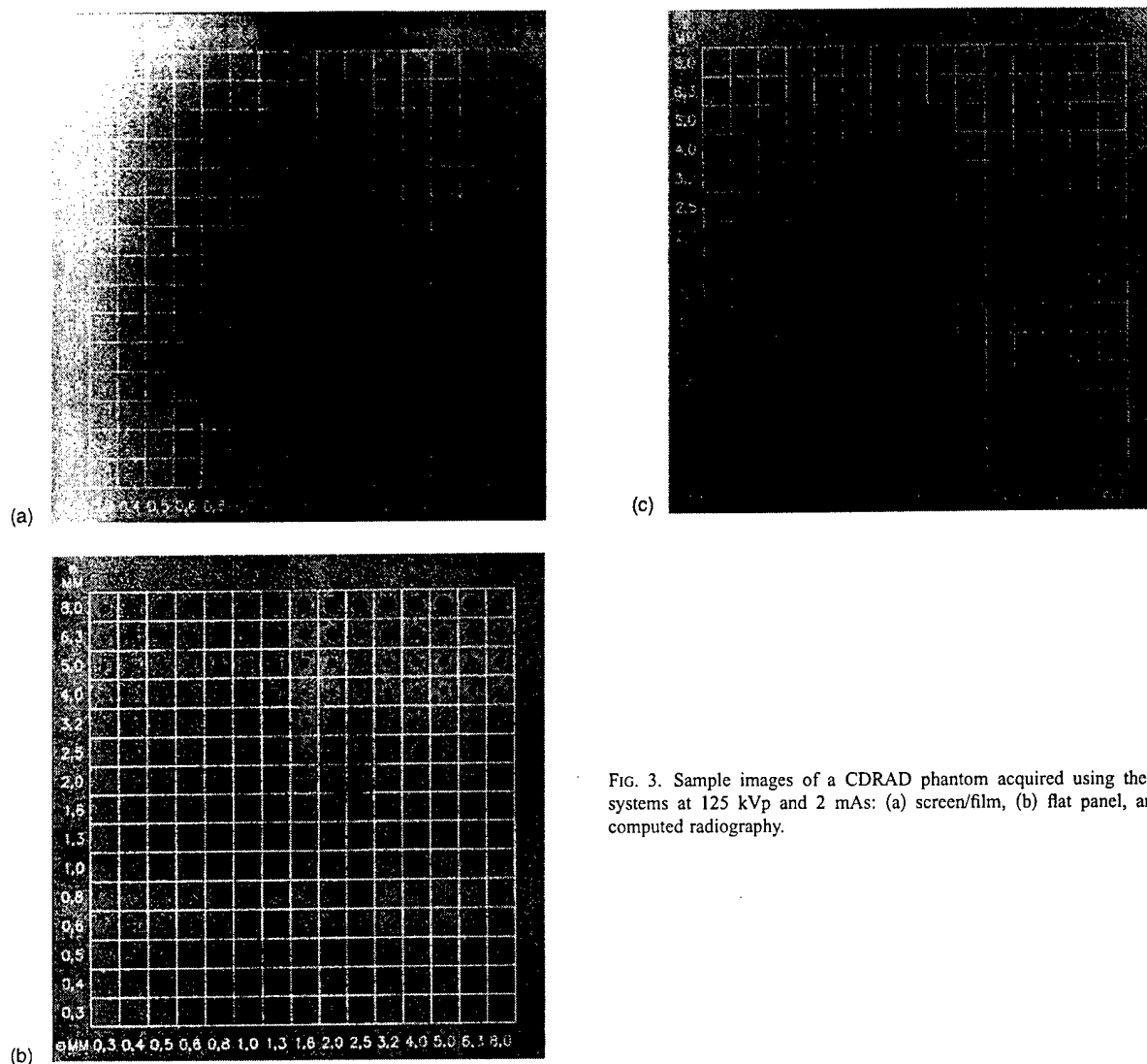


FIG. 3. Sample images of a CDRAD phantom acquired using the three systems at 125 kVp and 2 mAs: (a) screen/film, (b) flat panel, and (c) computed radiography.

ditions, stray light on the light box was blocked and ambient room light was kept low. Films were displayed in random order and reviewed by five readers with normal or corrected vision. The readers read films one at a time. The readers in this study consisted of three physicists: a graduate student and an undergraduate student. Previous studies<sup>2,38</sup> have shown that for images of a contrast-detail phantom there were no significant differences in observer responses between radiologists and nonradiologists and that there was no noticeable improvement in the readers' performance with increasing experience.<sup>38</sup> Therefore, the use of a nonradiologist and inexperienced readers in this study should be acceptable.

There were no restrictions on viewing distance or the use of a magnifying glass while reading the images. The minimum detectable object contrast, as represented by the corresponding depth, was determined as a function of the object diameter. A transition region where the visibility of the objects changes from nonexistent to marginal and then to very good was identified by the readers for scoring. This region

generally covered three to four different contrast levels (depths) for each different object diameter. Objects in the transition region were closely examined for the detection of both center and corner objects. In addition, the readers had to identify the locations of the corner objects if both center and corner objects were considered to be detected. The results were then entered on a score form for each image reviewed.

#### Data analysis

Prior to forming the contrast-detail curves, the contrast-detail data were corrected by comparing the score forms with a reference form containing the correct locations of all corner objects. The results were then corrected by following the criteria recommended by the manufacturer.<sup>37</sup> With these criteria, the detection of objects (at both the center and corner) is considered "true" if the corner object is correctly located and "false" if incorrectly located or undetected (hence not located). A true detection in a certain region is valid only if

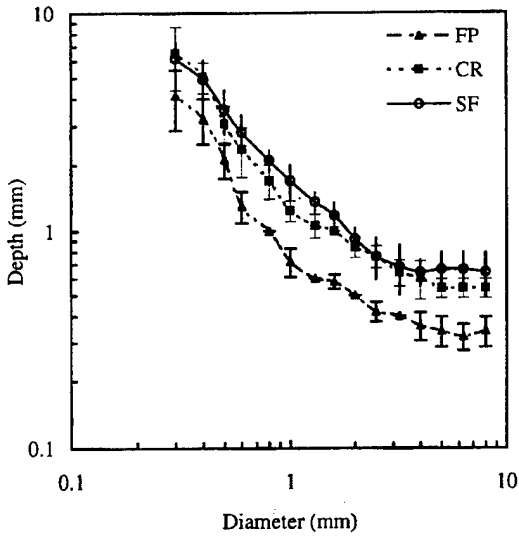


FIG. 4. Contrast-detail curves of the screen/film, flat-panel, and computed radiography systems evaluated. Images acquired using the flat-panel and computed radiography systems were printed with clinical default protocols.

true detection exists in two or more neighboring regions (to the right, left, up, or down). In other words, the true detection does not count if true detection exists in one neighboring region or none. A false detection or no detection is converted to a valid detection if true detection exists in three or four neighboring regions. These rules apply to all regions except those at the four corners of the phantom images.

For the corner regions, where there are only two neighboring regions, the true detection is considered valid if true detection exists in at least one neighboring region. A false or no detection is converted into a valid detection if true detection exists in both neighboring regions. Following the correction, the threshold contrast value was determined as the minimum depth in regions of valid detection for each different diameter. The results were averaged over the five readers and then plotted as the function of the object diameter to form the contrast-detail curves.

## RESULTS AND DISCUSSIONS

In Figs. 4–8, the minimum detectable object contrast levels (depths) are plotted as a function of the object diameter for various imaging systems, printing protocols, or exposures. These plots are often referred to as the contrast-detail curves. With these curves, a better low-contrast performance is indicated by curves closer to the origin (zero object contrast and diameter) or lower contrast threshold for each different object diameter.

In Figs. 4 and 5, the contrast-detail curves from the FP, CR, and SF images were compared. The FP and CR images used to obtain the contrast-detail curves in Fig. 4 were printed using the clinical enhancement protocols. The FP and CR contrast-detail curves in Fig. 5 were obtained from images processed and printed with a specially designed “film look” protocol. Both figures show that the FP images have the best low-contrast performance, even for images pro-

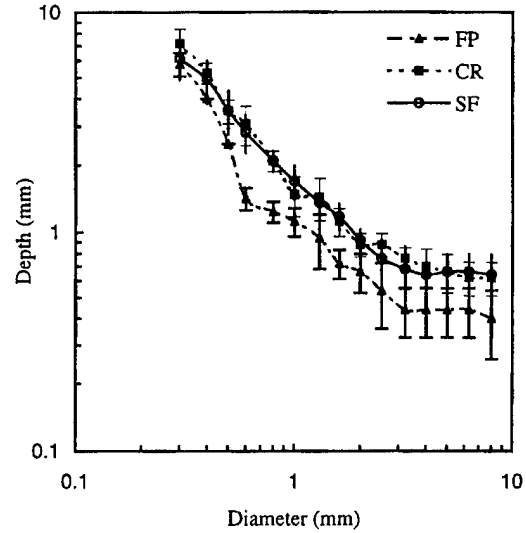


FIG. 5. Contrast-detail curves of the screen/film, flat-panel, and computed radiography systems evaluated. Images acquired using the flat-panel and computed radiography systems were printed with “film look” processing.

cessed and printed with the “film look” (Fig. 5). In Fig. 4, CR performs slightly better than SF for object diameters between 0.5–2 mm. However, over the entire range of object diameters, no significant difference between the contrast-detail curves for CR and SF was seen in Figs. 4 and 5.

In Figs. 6 and 7, the effects of the two different printing protocols were compared for FP and CR images, respectively. For both FP and CR images, the clinical enhancement protocols resulted in a better low-contrast performance than the “film-look” protocol. Even though the differences were only slight, they were consistent over all object diameters.

The effects of exposure on the low-contrast performance were demonstrated using the FP images as an example in

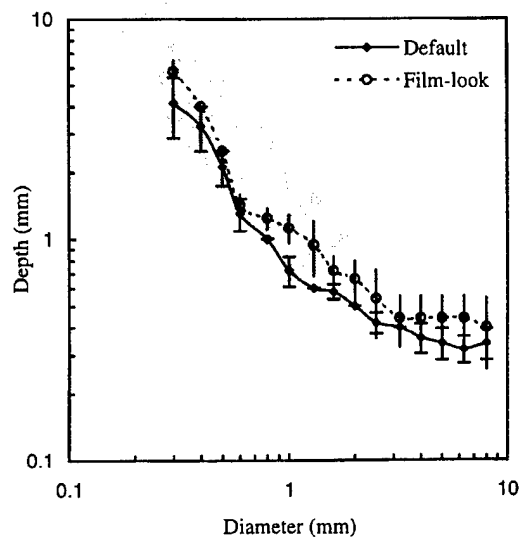


FIG. 6. Contrast-detail curves of an image acquired using the flat-panel system. The image was printed using two different protocols: clinical default protocol and “film look” protocol.

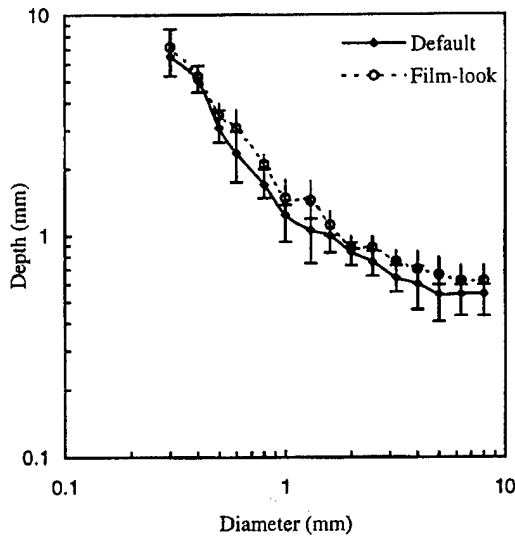


FIG. 7. Contrast-detail curves of an image acquired using the computed radiography system. The image was printed using two different protocols: clinical default protocol and "film look" protocol.

Fig. 8. the contrast-detail curve for the SF image acquired with the standard x-ray technique was also plotted as a reference. The plots show that the SF curve lies between FP curves for 0.23 and 0.5 mR. This indicates that with a 0.5 mR exposure, the FP images have equal or better low-contrast performance when compared to the SF image acquired with 2.09 mR exposure. Thus, the FP technique could result in a dose saving (reduction) of at least 75% if the low-contrast performance needs only to be kept at the same level as the SF technique. This dose saving can be shown to vary with the object diameter.

The percentages of exposures required for the FP technique to achieve the same performance as the SF image ac-

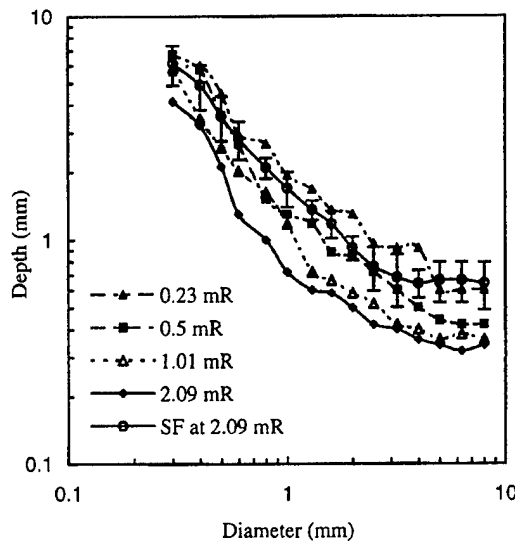


FIG. 8. Contrast-detail curves of images acquired using the flat-panel system at various exposures. The image was printed using clinical default protocol.

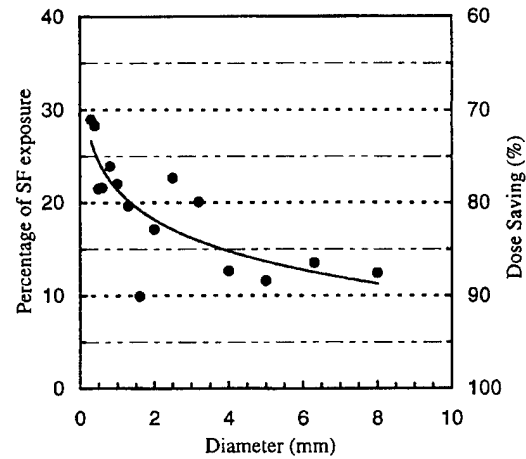


FIG. 9. Dose savings by using the flat-panel system to achieve the same performance as the screen/film system.

quired at 2.09 mR were calculated as a function of the object diameter. The results are plotted in Fig. 9. A separate scale is provided on the right side to show the percentage of dose saving as a function of the object diameter. The plot was obtained by analyzing the contrast-detail data from the five FP images taken as exposures of 0.06, 0.13, 0.26, 0.54, and 1.42 C/kg (0.23, 0.50, 1.01, 2.09, and 5.52 mR) at the entrance of the phantom. Using these data, the threshold contrast values were first plotted as a function of the exposure and then fitted to a curve for each different object diameter, as demonstrated in Fig. 10. Using the fitted curves, the exposure corresponding to the threshold contrast value for the SF image was determined for each object diameter. These

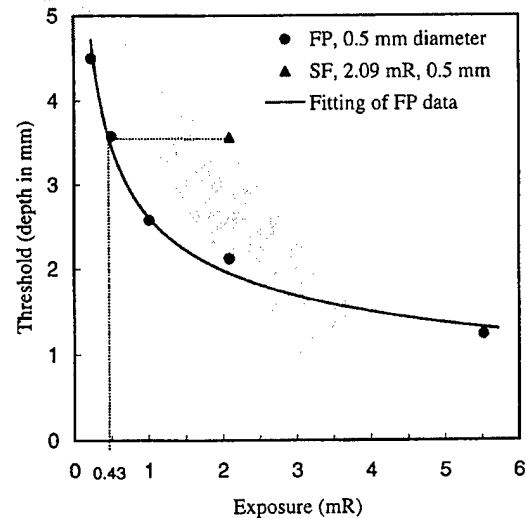


FIG. 10. The determination of exposure (0.43 mR) required for the flat-panel image so that it corresponds to the threshold contrast value of the screen/film image (2.09 mR) for 0.5 mm diam objects. Exposures required for objects of 0.3 mm–8.0 mm were also obtained and shown in Fig. 9. For 0.5 mm diam objects, the exposure for the FP image is about 21% of that used for the SF image corresponding to the same threshold value. Hence, the dose saving is about 79% for objects of 0.5 mm diam.

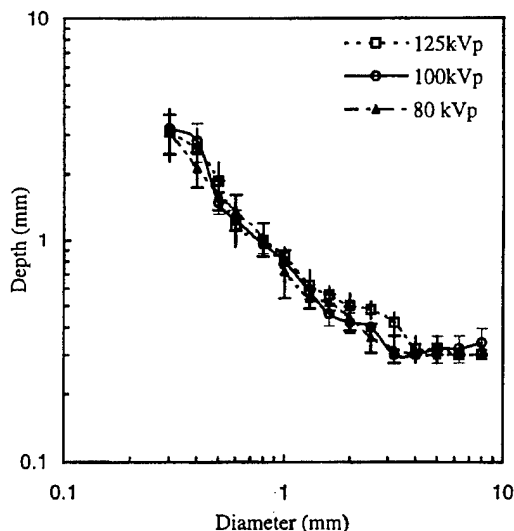


Fig. 11. Contrast-detail curves of images acquired using the flat-panel system at three kVps. AEC was used to assure the same exposure to the detector Bucky. The image was printed using clinical default protocol.

exposures were then normalized to that for the 2.09 mR exposure to obtain the percentage exposure that was plotted in Fig. 9. Figure 9 shows that the percentage exposure for the FP images to achieve a low-contrast performance comparable to that for the SF image decreases as the object diameter increases. In other words, the potential dose saving increases with the object diameter. This dose saving could range from 70% to 90% depending on the object diameter.

The effects of kVp on the contrast-detail curves of the FP system are demonstrated in Fig. 11. For the three different kVps studied, no significant differences were observed. The small differences may be due to the fact that DQEs for the FP system do not change appreciably when kV is raised from 80 to 125 kVp.<sup>24</sup>

## SUMMARY

In summary, the FP system has demonstrated significantly better low-contrast performance than the SF or CR systems as measured and compared by the contrast-detail curves. It allowed objects of lower contrast levels to be detected for the same diameter when compared to SF or CR systems. No significant difference was observed in the low-contrast performances between the SF and CR systems. The use of clinical default protocols for image processing and presentation was essential to the performance for both FP and CR. With the FP technique, exposure can be reduced approximately 70%–90% and maintain the same level of performance as the SF technique, depending on the object size. The percentage of dose saving was found to increase with object size and no significant effects were observed for the FP technique when using different kVps. From the results of this contrast-detail phantom study, the aSi/CsI-based flat-panel digital chess system should perform better under clinical situations

for the detection of low-contrast objects such as lung nodules. However, proper processing prior to printing would be essential to realizing this better performance.

## ACKNOWLEDGMENTS

This work is supported in part by research Grant No. CA51248 from the National Cancer Institute and Research Grant No. DAMD17-00-1-0316 from the Department of Army Breast Cancer Research Program.

- <sup>1</sup>J. T. Dobbins III, J. J. Rice, and C. A. Beam, "Threshold perception performance with computed and screen-film radiography: implications for chest radiography," *Radiology* **183**, 179–187 (1992).
- <sup>2</sup>L. T. Cook, M. F. Insana, M. A. McFadden, T. J. Hall, and G. G. Cox, "Comparison of the low-contrast detectability of a screen-film screen system and third generation computed radiography," *Med. Phys.* **21**, 691–695 (1994).
- <sup>3</sup>N. W. Marshall, K. Faulkner, H. P. Busch, and K. J. Lehmann, "The contrast-detail behavior of a photostimulable phosphor based computed radiography system," *Phys. Med. Biol.* **39**, 2289–2303 (1994).
- <sup>4</sup>J. H. Launders and A. R. Cowen, "A comparison of the threshold detail detectability of a screen-film combination and computed radiology under conditions relevant to high-kVp chest radiography," *Phys. Med. Biol.* **40**, 1393–1398 (1995).
- <sup>5</sup>U. Neitzel, A. Bohm, and I. Maack, "Comparison of low-contrast detail detectability with five different conventional and digital radiographic imaging systems," *Proc. SPIE* **3981**, 216–223 (2000).
- <sup>6</sup>M. J. Yaffe and J. A. Rowlands, "X-ray detectors for digital radiography," *Phys. Med. Biol.* **42**, 1–39 (1997).
- <sup>7</sup>L. E. Antonuk, K.-W. Jee, Y. El-Mohri, M. Maolinbay, S. Nassif, X. Rong, Q. Zhao, J. H. Siewerdsen, R. A. Street, and K. S. Shah, "Strategies to improve the signal and noise performance of active matrix, flat-panel imagers for diagnostic x-ray applications," *Med. Phys.* **27**, 289–306 (2000).
- <sup>8</sup>L. E. Antonuk, J. M. Boudry, Y. El-Mohri, W. Huang, J. H. Siewerdsen, J. Yorkston, and R. A. Street, "Large-area, flat-panel amorphous silicon imagers," *Proc. SPIE* **2432**, 216–227 (1995).
- <sup>9</sup>J. Chhabal, C. Chaussat, T. Ducourant, L. Fritsch, J. Michailos, V. Spinner, G. Viex, M. Arques, G. Hahm, M. Hoheisel, H. Horbaschek, R. Schulz, and M. Spahn, "Amorphous silicon x-ray imaging sensor," *Proc. SPIE* **2708**, 499–510 (1995).
- <sup>10</sup>T. Graeve, Y. Li, A. Fabians, and W. Huang, "High-resolution amorphous silicon image sensor," *Proc. SPIE* **2708**, 494–498 (1996).
- <sup>11</sup>D. L. Lee, L. K. Cheung, and L. S. Jeromin, "A new digital detector for projection radiography," *Proc. SPIE* **2432**, 237–249 (1995).
- <sup>12</sup>W. Zhao and J. A. Rowlands, "X-ray imaging using amorphous selenium: feasibility of a flat-panel self-scanned detector for digital radiology," *Med. Phys.* **22**, 1595–1604 (1995).
- <sup>13</sup>W. Zhao, I. Blevis, S. Germann, and J. A. Rowlands, "A flat panel detector for digital radiology using active matrix readout of amorphous selenium," *Proc. SPIE* **2708**, 523–531 (1996).
- <sup>14</sup>A. Tsukamoto, S. Yamada, T. Tomisaki, M. Tanaka, T. Sakaguichi, H. Asahina, and M. Nishiki, "Development of a selenium-based flat-panel detector for real-time radiography and fluoroscopy," *Proc. SPIE* **3336**, 388–395 (1996).
- <sup>15</sup>P. C. Bunch, K. E. Huff, and R. Van Metter, "Analysis of the detective quantum efficiency of a radiographic screen-film combination," *J. Opt. Soc. Am. A* **4**, 902–909 (1987).
- <sup>16</sup>R. V. Metter and R. Dickerson, "Objective performance characteristics of a new asymmetric screen-film system," *Med. Phys.* **21**, 1483–1490 (1994).
- <sup>17</sup>J. T. Dobbins III, D. L. Ergun, L. Rutz, D. A. Hinshaw, H. Blume, and D. C. Clark, "DQE(f) of four generations of computed radiography acquisition devices," *Med. Phys.* **22**, 1581–1593 (1995).
- <sup>18</sup>J. H. Siewerdsen, L. E. Antonuk, Y. El-Mohri, J. Yorkston, W. Huang, and I. A. Cunningham, "Signal, noise power spectrum, and detective quantum efficiency of indirect-detection flat-panel imagers for diagnostic radiology," *Med. Phys.* **25**, 614–628 (1998).

- <sup>19</sup>D. Lee, L. K. Cheung, B. G. Rodricks, and G. F. Powell, "Improved imaging performance of a 1417-in. Direct Radiography system using a-Se/TFT detector," *Proc. SPIE* **3336**, 14–23 (1998).
- <sup>20</sup>S. W. Kengyelics, A. G. Davies, and A. R. Cowen, "A comparison of the physical imaging properties of Fuji ST-V, ST-VA, and ST-VN computed radiography image plates," *Med. Phys.* **25**, 2163–2169 (1998).
- <sup>21</sup>C. D. Bradford, W. W. Pepler, and J. T. Dobbins III, "Performance characteristics of a Kodak computed radiography system," *Med. Phys.* **26**, 27–37 (1999).
- <sup>22</sup>M. J. Flynn and E. Samei, "Experimental comparison of noise and resolution for 2k and 4k storage phosphor radiography systems," *Med. Phys.* **26**, 1612–1623 (1999).
- <sup>23</sup>P. R. Granfors and R. Aufrichtig, "Performance of a 41×41-cm<sup>2</sup> amorphous silicon flat panel x-ray detector for radiographic imaging applications," *Med. Phys.* **27**, 1324–1331 (2000).
- <sup>24</sup>X. Liu, C. C. Shaw, X. J. Rong, and M. Lemacks, "Comparison of  $\alpha$ -Si:H/CsI flat-panel digital imaging systems with CR and CCD based systems — Image quality measurements," submitted to SPIE 2001.
- <sup>25</sup>G. Cohen and F. A. DiBianca, "The use of contrast-detail-dose evaluation of image quality in a computed tomographic scanner," *J. Comput. Assist. Tomogr.* **3**, 197–203 (1979).
- <sup>26</sup>G. Cohen, L. K. Wagner, S. R. Amtey, and F. A. DiBianca, "Contrast-detail-dose and dose efficiency analysis of a scanning digital and screen-film-grid radiographic system," *Med. Phys.* **8**, 358–567 (1981).
- <sup>27</sup>B. H. Hasegawa, R. K. Cacak, J. A. Mulvaney, and W. R. Hendee, "Problems with contrast-detail curves for CT performance evaluation," *Am. J. Roentgenol., Radium Ther. Nucl. Med.* **138**, 135–138 (1982).
- <sup>28</sup>L-D. N. Loo, K. Doi, M. Ishida, C. E. Metz, H-P. Chan, Y. Higashida, and Y. Kodera, "An empirical investigation of variability in contrast-detail diagram measurements," *Proc. SPIE* **419**, 68–76 (1983).
- <sup>29</sup>G. Cohen, D. L. McDaniel, and L. K. Wagner, "Analysis in contrast-detail experiments," *Med. Phys.* **11**, 469–473 (1984).
- <sup>30</sup>C. A. Kelsey, R. D. Moseley, Jr., J. F. Garcia, F. A. Mettler, Jr., T. W. Parker, and J. H. Juhl, "ROC and contrast detail image evaluation test compared," *Radiology* **154**, 629–631 (1985).
- <sup>31</sup>K. Faulkner and B. M. Moores, "Contast-detail assessment of computed tomography scanners," *Phys. Med. Biol.* **31**, 993–1003 (1986).
- <sup>32</sup>W. Hillen, U. Schiebel, and T. Zaengel, "Imaging performance of a digital storage phosphor system," *Med. Phys.* **14**, 744–751 (1987).
- <sup>33</sup>N. W. Marshall, K. Faulkner, C. J. Kotre, and K. Robson, "Analysis of variations in contrast-detail measurements performed on image intensifier-television systems," *Phys. Med. Biol.* **37**, 2297–2302 (1992).
- <sup>34</sup>R. Aufrichtig, "Comparison of low contrast detectability between a digital amorphous silicon and a screen-film based imaging system for thoracic radiography," *Med. Phys.* **26**, 1349–1358 (1999).
- <sup>35</sup>P. Xue, S. F. Schubert, and R. Aufrichtig, "Low contrast detectability and dose sayings with an amorphous silicon detector designed for x-ray radiography," *Proc. SPIE* **3981**, 194–200 (2000).
- <sup>36</sup>Du Pont Ultra-Vision film/screen system, "Du Pont Technical Publication, 1992, Du Pont, Wilmington, DE.
- <sup>37</sup>M. A. O. Thijssen, K. R. Bijkerk, and R. J. M. van der Burght, *Manual Contrast-Detail Phantom CDRAD type 2.0. Project Quality Assurance in Radiology, Department of Radiology, University Hospital Nijmegen, St. Radboud, The Netherlands, 1998.*
- <sup>38</sup>W. Huda, G. Qu, Z. Jing, B. G. Steinbach, and J. C. Honeyman, "How does observer training affect imaging performance in digital mammography?" *Proc. SPIE* **3981**, 259–266 (2000).

**Microcalcification Detectability for Four Mammographic Detectors:  
Flat-Panel, CCD, CR and Screen/Film \***

Xiujiang J. Rong, Chris C. Shaw, Dennis A. Johnston, Michael R. Lemacks,  
Xinming Liu, Gary J. Whitman, Mark Dryden, Tanya Stephens,  
Stephen K. Thompson, and Kerry T. Krugh

Department of Diagnostic Radiology, University of Texas M. D. Anderson Cancer Center  
Houston, Texas 77030-4009

Corresponding Author: Xiujiang J. Rong  
Department of Diagnostic Radiology  
University of Texas M. D. Anderson Cancer Center  
1515 Holcombe Boulevard, Box 57  
Houston, Texas 77030-4009  
Phone: 713-745-5345  
Fax: 713-745-0581  
Email: [jrong@di.mdacc.tmc.edu](mailto:jrong@di.mdacc.tmc.edu)

---

\* The scientific content of this paper was first presented at the 43<sup>rd</sup> AAPM annual Meeting held in July 2001 in Salt Lake City, Utah.

**ABSTRACT**

1  
2 Amorphous silicon/cesium iodide (a-Si:H/CsI:Tl) flat-panel based full-field digital  
3 mammography (FFDM) systems have recently become commercially available for  
4 clinical use. Some investigations on physical properties and imaging characteristics of  
5 these types of detectors have been conducted and reported on. In this perception study, a  
6 phantom containing simulated microcalcifications of various sizes was imaged with four  
7 detector systems: a flat-panel based, a charge coupled device (CCD) based, a high  
8 resolution computed radiography (CR) and a conventional screen/film system. The  
9 images were reviewed by mammographers as well as non-radiologist participants. Scores  
10 reflecting confidence levels were given and recorded for each detection task. The results  
11 were used to determine the minimum detectable calcification size. Receiver Operating  
12 Characteristics (ROC) analysis was also performed to evaluate and compare the overall  
13 detection accuracy for these four detector systems. Differences in microcalcification  
14 detectability were found to be insignificant for the larger group (150 - 160  $\mu\text{m}$  in size) or  
15 smaller group (112 - 125  $\mu\text{m}$  in size). For calcifications of 125 - 140  $\mu\text{m}$  in size, the flat-  
16 panel system was found to have the best performance: the smallest minimum detectable  
17 calcification size and the highest detection accuracy in the ROC analysis. The screen/film  
18 system was ranked the second with a performance significantly better than those of the  
19 CR or the CCD systems. In the ROC analysis, the CCD system showed significant better  
20 detection accuracy than the CR system. However, the CCD system performed only  
21 slightly better than the CR system in the minimum detectable calcification size analysis.  
22 Key words: charge coupled device, computed radiography, film/screen, flat-panel,  
23 mammography, microcalcification phantom

## 1 INTRODUCTION

2 Breast cancer is the most common cancer among woman and early detection is  
3 critical to diagnose and treat breast cancer.<sup>1,2</sup> To date, the best method for early detection  
4 of breast cancer has been mammography<sup>3,4</sup> and screen/film mammography has been the  
5 clinical standard for breast imaging. The advantages of screen/film mammography  
6 include low costs, reasonably good image quality with proper exposure, and ease of  
7 viewing. However, even though screen/film combinations have been improved and  
8 optimized over the years for breast imaging, there are some critical limitations including  
9 narrow exposure range, image artifacts and other film processing problems, and  
10 inflexibility in image processing and film management.

11 In recent years, there have been various digital mammographic techniques<sup>2,5,6</sup>  
12 developed to overcome some limitations of screen/film technique and to improve image  
13 quality. These digital techniques generally include wide dynamic range, flexibility in  
14 image display, post-image capture processing and printing capabilities, and interface to a  
15 Picture Archival and Communication System (PACS) for digital image management. In  
16 addition to image quality improvement, digital mammographic image acquisition opens  
17 the door for other advanced imaging applications such as dual-energy mammography,<sup>7,8</sup>  
18 tomosynthesis,<sup>9</sup> cone-beam volume breast imaging,<sup>10</sup> and computer-aided detection  
19 (CAD).<sup>11</sup>

20 Limited with a small field of view (typically  $6 \times 6 \text{ cm}^2$ ), clinical digital  
21 mammography systems using charge coupled device (CCD) has being used primarily for  
22 stereotactic imaging<sup>12,13</sup> and magnification mammography.<sup>14</sup> There have been efforts to  
23 develop a large-area detector by bonding an array of CCDs tightly together to cover the

1 full compressed breast.<sup>15,16</sup> The disadvantages of this approach include complexity such  
2 as gaps between the CCD modules and relatively high cost. The storage phosphor based  
3 computed radiography (CR) systems have been commercialized and widely used in  
4 general radiographic applications.<sup>17</sup> Even with its much higher dynamic range over  
5 screen/film, CR's poor spatial resolution capability limits its use in high resolution  
6 imaging applications such as mammographic imaging.<sup>18,19</sup> However, with continued  
7 efforts in improving CR imaging plates and scanning techniques, high resolution CR  
8 technique has a potential to be used for clinical mammographic imaging.<sup>20,21,22</sup>

9 In recent years, flat-panel based digital x-ray imaging systems have become  
10 commercially available for general radiography applications.<sup>23,24,25,26,27</sup> More recently, an  
11 amorphous silicon/cesium iodide (a-Si:H/CsI) flat-panel (FP) based full-field digital  
12 mammography system<sup>28</sup> has become commercially available. This system employs a  
13 direct coating of thallium doped cesium iodide (CsI:Tl) to convert x-rays into light which  
14 are then detected and read out by an amorphous silicon (aSi:H) FP detector containing a  
15 two-dimensional photodiode array and thin film transistor (TFT) switches.<sup>29,30</sup> There are  
16 other flat-panel based systems currently under development for clinical use of breast  
17 imaging. Along side with the amorphous silicon approach mentioned above, another  
18 general design of flat-panel based systems employ a layer of amorphous selenium (aSe)  
19 to directly convert x-rays into charges which are then collected and read out by an aSi:H  
20 array of capacitors and TFTs.<sup>31,32</sup> Detailed descriptions of these systems are available  
21 elsewhere<sup>33</sup> and many investigations on imaging characteristics of these two types of  
22 detectors have been conducted and reported.<sup>29-32</sup> Studies<sup>34,35,36,37,38</sup> have shown that FP  
23 based detectors generally have a significantly higher detective quantum efficiency (DQE)

1 than SF systems. This higher DQE may lead to a better low contrast performance which  
2 should be evaluated and investigated with perception studies. One such study based on  
3 the detection of simulated microcalcifications ( $\mu$ Cs) or low contrast objects to directly  
4 compare the low contrast detectability of various imaging systems.

5 In mammography, detection of breast cancer primarily relies on the detection of  
6  $\mu$ C clusters and/or soft tissue masses.<sup>39,40</sup> Breast cancers that are detected with  $\mu$ Cs as  
7 the only mammographic abnormality are more likely to be early stage cancers.<sup>41</sup>  
8 Therefore, improved detection of  $\mu$ Cs will likely lead to earlier detection of breast cancer.

9 To evaluate and compare the low contrast detectability of the FP system with  
10 those of CCD, CR and SF systems, we have designed and constructed a simulated  $\mu$ C  
11 phantom using calcium carbonate grains of various sizes. This phantom was imaged with  
12 three digital systems: a FP based, a CCD based, a high resolution CR, and a conventional  
13 screen/film system. A reading study was conducted for the acquired images. The  
14 reading results were analyzed for the overall score for all readers as well as for each  
15 individual reader to determine the minimum detectable calcification size. Receiver  
16 Operating Characteristics (ROC) analysis was also performed to evaluate and compare  
17 the overall detection accuracy for each detector system as well as other factors such as  
18 readers and  $\mu$ C sizes.

## 1 MATERIALS AND METHODS

### 2 A. Imaging systems

3 The FP system investigated in this study was a CsI:Tl/aSi:H based FP full-field  
4 digital mammography system (SenoGraphe 2000, GE Medical Systems, Milwaukee, WI).  
5 The system employs a directly deposited layer of CsI:Tl over an aSi:H circuitry plate  
6 containing two-dimensional array of photodiodes and TFT switches for light detection  
7 and signal readout, respectively. The needle structure of the CsI:Tl scintillator allows for  
8 more x-ray absorption without sacrificing the spatial resolution. The matrix size of the  
9 detector is 1914 x 2294, corresponding to a field size of 19 x 23 cm<sup>2</sup>. The pixel size is  
10 100 μm. A Bucky grid (31 lines/cm, 5:1 grid ratio) is integrated with the detector.

11 The CCD system studied was GE SenoVision (GE Medical Systems, Milwaukee,  
12 WI) small-field digital mammography system. The x-ray converter on top of the CCD  
13 detector is a mammographic screen similar to that that used in MinR 2000 (Eastman  
14 Kodak, Rochester, NY) screen/film combinations. The detector is 6 x 6 cm<sup>2</sup> in size and  
15 enclosed in an 18 x 24-cm<sup>2</sup> cassette, which is designed to fit into the cassette holder of a  
16 mammographic unit (SenoGraphe DMR+, GE Medical Systems, Milwaukee, WI). The  
17 image matrix size is 2048 x 2048 and the pixel size is 30 μm. The CR system studied  
18 consisted of a Fuji AC-3 image reader and 20 x 25 cm<sup>2</sup> HR-V high resolution imaging  
19 plates (Fuji Medical Systems USA, Inc, Stamford, CT). The plates were scanned and  
20 read out with a pixel size of 100 μm. For screen/film imaging, Kodak MinR 2000  
21 screen/film combination (18 x 24 cm<sup>2</sup> in size) was used. The CCD, CR and SF images  
22 were acquired using the same GE SenoGraphe DMR+ (GE Medical Systems, Milwaukee,  
23 WI) mammography unit with identical modules of x-ray tube, generator, filter

1 combinations, and grid. Table 1 summarizes the specifications of these four systems  
2 studied.

3 The Modulation Transfer Function (MTF), Noise Power Spectrum (NPS) and  
4 Detective Quantum Efficiency (DQE) of the FP, CCD and CR systems used have been  
5 measured and reported in a separate manuscript.<sup>37</sup> The study showed that the MTF of the  
6 FP system was slightly lower than that of the CCD system but higher than that of the CR  
7 system. The DQEs of the FP and CCD systems were significantly higher than those of the  
8 CR system. The DQEs of the FP system were generally higher than those of CCD  
9 system at higher (3.8 mR or above) exposure. The detailed physical characteristics of  
10 three detector systems have been reported by Vedantham et al. for the FP system<sup>28</sup> and  
11 the CCD system,<sup>13</sup> and Bunch for the SF screen/film combination.<sup>42</sup>

12

### 13 **B. Simulated microcalcification phantom**

14 Three size groups of pre-sifted calcium carbonate grains (Computerized Imaging  
15 Reference Systems, Norfolk, VA) were used to construct a simulated  $\mu\text{C}$  phantom  
16 (referred to as  $\mu\text{C}$  phantom in the rest of the paper). Table 2 lists the size ranges of the  
17  $\mu\text{C}$ s. A cluster of four  $\mu\text{C}$ s was attached to a  $2 \times 2 \text{ cm}^2$ , 3-mm thick Lucite square. One  
18  $\mu\text{C}$  was missing from the five possible positions: four corners plus the center. Figure 1  
19 shows an example of simulated  $\mu\text{C}$  clusters in which the upper right  $\mu\text{C}$  is missing. Three  
20 phantom pieces were constructed for each size group and a total of nine pieces were tiled  
21 into a  $6 \times 6 \text{ cm}^2$  phantom which just covered the detector. During image acquisition,  
22 placement and orientation of the nine  $2 \times 2 \text{ cm}^2$  Lucite squares (therefore the simulated  
23  $\mu\text{C}$  clusters) were varied to produce five patterns for five different phantom images. To

1 simulate breast attenuation, the tiled 3 x 3 Lucite squares were sandwiched between two  
2 1-cm thick 50% adipose/50% glandular simulated tissue slabs (Computerized Imaging  
3 Reference Systems, Norfolk, VA) for a total attenuating thickness of 2.3 cm (Figure 2).

#### 4 **C. Image acquisition and processing**

5 During image acquisition, the  $\mu\text{C}$  phantom was positioned on the breast support  
6 surface. One edge of the phantom was aligned to the chest wall edge of the breast  
7 support surface. With the selection of 9 x 9 cm<sup>2</sup> x-ray field size, the phantom was  
8 centered laterally in the field of view of the image receptor. Using the automatic  
9 exposure control (AEC) with the SF combination for pre-set film density and contrast, a  
10 standard exposure setting was determined to be 160 mAs at 25 kVp with a 0.3 mm focal  
11 spot, a source-to-image distance (SID) of 660 mm, and a Mo/Mo target/filter  
12 combination. This setting was used to acquire five images of the  $\mu\text{C}$  phantom with each  
13 of the four systems. For each image, patterns and sizes of the  $\mu\text{C}$  cluster were varied by  
14 randomizing the orientation and position of the nine 2 x 2 cm<sup>2</sup> Lucite squares.

15 The SF image was obtained by processing the exposed film using a automated  
16 film processor and loader (X-OMAT Multiloader 300, Eastman Kodak, Rochester, NY).  
17 Linear data of the FP and CCD images were logarithmically mapped for display. The CR  
18 image data were mapped and processed in the reader for display. For viewing  
19 convenience, The FP and CR images were then cut into 875 x 840 sub-images to  
20 eliminate the areas outside of the phantom. Figure 3 shows an image of 3 x 3 simulated  
21  $\mu\text{C}$  clusters, obtained using the FP system.

22

#### 1 **D. Image reading and data analysis**

2 All images were numbered for identifying the detector types,  $\mu\text{C}$  size groups, and  
3 cluster patterns. Screen/film images were reviewed using a standard mammographic  
4 light box with all of the ambient light blocked and the room lights turned off. The  
5 readers were allowed to use a magnifying glass. Digital images were displayed one at a  
6 time on a image workstation with a 1600 x 1200 image display with window/level  
7 adjustment and zooming allowed. Ambient room lights were turned off. Phantom  
8 images were reviewed by seven readers including four physicists and three  
9 mammographers with normal or corrected vision. The readers were asked to assign a  
10 confidence level of 1 - 5 for detection of  $\mu\text{C}$ s at each of the five prospective locations in  
11 the simulated cluster: 1 = clearly absent, 2 = probably absent, 3 = absence/presence  
12 uncertain, 4 = probably present, 5 = clearly present. A total of 225 scores (5  
13 positions/cluster x 9 clusters/image x 5 images) were collected and recorded from each  
14 reader.

15 Average scores were calculated and sorted for each  $\mu\text{C}$  size group, modality, and  
16 reader. Scores of different modalities were averaged over the seven readers to obtain the  
17 seven readers' "overall" scores for comparison of the three different  $\mu\text{C}$  size groups. Of  
18 the 225 scores from each reader, 45 scores of the missing locations (negatives) were  
19 excluded from the calculation. To include both false positive and false negative scores in  
20 the analysis, ROC analysis was performed for each modality using the combined scores  
21 ("overall" scores as it will be used in the rest of this paper) for all three  $\mu\text{C}$  size ranges  
22 and from all seven readers, as well as for each individual size group and each reader. The  
23 area under the ROC curve ( $A_z$ ) was used in the comparison of various situations.

## 1 RESULTS AND DISCUSSIONS

2 Seven readers' reading scores for three  $\mu\text{C}$  size groups were plotted in Figure 4 to  
3 compare the minimum  $\mu\text{C}$  detectability of four detection modalities studied. As  
4 expected, the larger the  $\mu\text{C}$ s, the higher the scores. This was observed for all four  
5 detector systems. From Figure 4, all three size groups demonstrated consistently that the  
6 FP received the highest scores among the four systems studied, the screen/film system  
7 ranked the second and received scores significantly higher than both the CCD and CR  
8 systems, and the CCD system received a higher score compared to the CR system. It also  
9 appears that the large (150 – 160  $\mu\text{m}$ )  $\mu\text{C}$ s can be easily detected (overall scores of all  
10 four systems are above 4.7) and the small (112 – 125  $\mu\text{m}$ )  $\mu\text{C}$ s were a little too small to  
11 be seen (all scores are below 2.7). The medium size group, scored from 2.6 (for CR) to  
12 4.1 (for FP), which are marginal to the assigned confidence level of 3 –  
13 “absence/presence uncertain”, exhibited the best comparison of the four detector systems  
14 studied. Therefore, only for the medium size (125 – 140  $\mu\text{m}$ ) group, the seven readers'  
15 individual and overall scores were plotted in Figure 5 to show inter-reader variations.

16 The scores from all seven readers and three size groups were combined and  
17 analyzed together to form ROC curves shown in Figure 6. The areas under each ROC  
18 curve ( $A_z$ s) are listed in Table 3 to show the differences in their detection accuracy. The  
19  $A_z$  has a theoretic minimum value of 0.5 (random guessing) and a maximum value of 1.0  
20 (100% of correct identification of positives and negatives). Both Figure 6 and Table 3  
21 show that the FP ranked the best, the SF the second, the CCD the third, and the CR the  
22 last in their overall detection accuracy. To show reading variations among readers,  
23 scores of each individual reader with all three size groups combined were analyzed and

1  $A_z$ s calculated. The results are listed in Table 3. In Figure 7a, the  $A_z$ s for the individual  
2 reader are plotted in groups for the four different systems to study inter-reader variations.  
3 In Figure 7b they are plotted in seven groups comparing  $A_z$ s of four detector system for  
4 each reader. Reader variations exist as expected. However, they are basically consistent  
5 as shown in Figures 7a and 7b. The overall trend shows again that the FP performed the  
6 best, the SF the second, the CCD the third, and the CR the last. Three readers had  
7 different rankings comparing to the overall trend. For reader 1, the  $A_z$ s for SF and CCD  
8 are about equal to each other. For readers 5 and 6, the  $A_z$ s for SF and CR are about equal  
9 to each other. For reader 6, the  $A_z$  for the SF is significantly lower than that for the CCD.  
10 However, the results show consistently that the FP system performed significantly better  
11 than all other three systems as scored by each of the readers. To demonstrate the system  
12 detection accuracy using different sizes of  $\mu$ Cs, the reading scores were grouped by size  
13 group then analyzed. The results are listed in Tables 4, 5 and 6 for the three different size  
14 groups. They are also plotted in Figures 8a, 8b, and 8c in eight groups for seven  
15 individual readers and all readers combined each showing differences of the four detector  
16 systems. For both the small size group (112 – 125  $\mu$ m) in Figure 8a and the medium size  
17 group (125 – 140  $\mu$ m) in Figure 8b, the FP system clearly has the highest detection  
18 accuracy for seven individual readers and all readers combined. For the medium size  
19 group, the standard deviations of the  $A_z$ s are relatively smaller for each modality  
20 comparing to those for the small size group. The overall  $A_z$ s in Figure 8b show more  
21 significant differences between the different modalities comparing to those in Figure 8a.  
22 These indicate that the medium size group of the  $\mu$ Cs is more suitable to be used in the  
23 comparisons. Obviously, the large size group (150 – 160  $\mu$ m) failed to distinguish the  $A_z$

1 differences between different modalities for majority of the readers, except for the reader  
2 6. In Figure 9,  $A_z$ s for all readers combined are plotted in order of  $\mu$ C size range (Table  
3 2: small = 119  $\mu$ m, medium = 133  $\mu$ m, large = 155  $\mu$ m) for the four detection systems. It  
4 clearly shows that the detection accuracy increases with the  $\mu$ C size. However,  $A_z$  for FP  
5 did not increase as much as those for other systems as the  $\mu$ C size increased from  
6 medium to large. This can be explained by that the  $A_z$  probably reaches 1.0 (the  
7 maximum value of  $A_z$ ) for size slightly above 140  $\mu$ m. Similarly, the  $A_z$  of CR probably  
8 reaches the minimum value of  $A_z$  (0.5) for  $\mu$ m size slightly smaller than 125  $\mu$ m. The  
9 presence of an upper threshold size and a lower threshold size for observer performance  
10 with both screen/film and CR was reported by Shaw et al<sup>43</sup>. The above observations  
11 indicate that the medium size group (125 – 140  $\mu$ m) is best suited for comparing the four  
12 imaging systems. Performance differences obviously become less significant or even  
13 indistinguishable as the sizes of the  $\mu$ Cs used for comparison are too large or too small,  
14 leading detection tasks either too easy or too difficult, respectively.

15

## 16 SUMMARY

17 Detection accuracy depends on the size of the  $\mu$ Cs for all four modalities studied.  
18 This perception study was conducted within the valid size range of simulated  $\mu$ Cs. The  
19 flat-panel mammography system demonstrated the best performance in both the  
20 minimum detectability analysis and the ROC analysis. Second to the flat-panel system,  
21 the screen/film combination performed significantly better than the CCD based system  
22 and the CR system in both the minimum detectability analysis and the ROC analysis. In  
23 the ROC study, the CCD based system showed significant better detection accuracy with

1 respect to the CR system. However, the CCD system performed only slightly better than  
2 the CR system in the minimum detectability analysis.

3

#### 4 **ACKNOWLEDGMENTS**

5 This work is supported in part by a research grant CA51248 from the National Cancer  
6 Institute and a research grant DAMD17-00-1-0316 from the Department of Army Breast  
7 Cancer Research Program.

1 **LIST OF TABLES**

2

3 Table 1 Specifications of the four x-ray imaging systems studied.

4

5 Table 2 Sizes of the simulated  $\mu$ Cs used for constructing the phantom.

6

7 Table 3 Area under the ROC curve ( $A_z$ ) and standard deviation ( $\sigma$ ) for all three  $\mu$ C  
8 sizes combined.

9

10 Table 4 Area under the ROC curve ( $A_z$ ) and standard deviation ( $\sigma$ ) for the small  
11  $\mu$ C size group (112 – 125  $\mu$ m).

12

13 Table 5 Area under the ROC curve ( $A_z$ ) and standard deviation ( $\sigma$ ) for the medium  
14  $\mu$ C size group (125 – 140  $\mu$ m).

15

16 Table 6 Area under the ROC curve ( $A_z$ ) and standard deviation ( $\sigma$ ) for the large  
17  $\mu$ C size group (150 – 160  $\mu$ m).

1 **LIST OF FIGURES**

2

3 Figure 1 Example of a simulated  $\mu\text{C}$  cluster. The upper right  $\mu\text{C}$  is missing.

4 Figure 2 Phantom of 3 x 3 tiled Lucite squares on a 1-cm thick 50% adipose/50%  
5 glandular simulated tissue slab. An additional slab was placed on the top  
6 for imaging. Placement and orientation of simulated  $\mu\text{C}$  clusters were  
7 randomized for each image acquired.

8 Figure 3 An example image of simulated  $\mu\text{C}$  phantom acquired with the FP system.

9 Figure 4 Seven readers' overall score for three simulated  $\mu\text{C}$  size ranges.

10

11 Figure 5 Seven readers' individual and overall scores for the 125 – 140  $\mu\text{m}$   
12 simulated  $\mu\text{C}$  size range.

13 Figure 6 ROC curves and  $A_2$ s obtained with seven readers' overall scores for three  
14 size groups.

15 Figure 7  $A_2$ s of the seven readers' individual and overall scores for three size  
16 groups.

17 Figure 8  $A_2$ s of the seven readers' individual and overall scores for a.) small size  
18 group, b.) medium size group, and c.) large size group.

19 Figure 9  $A_2$  as a function of  $\mu\text{C}$  size used.

## 1 Reference

- <sup>1</sup> L. Garfinkel, M.A. Catherind, C. Boring, and C.W. Heath, "Changing trends: an overview of breast cancer incidence and mortality," *Cancer* **74** (suppl 1), 222-227 (1994).
- <sup>2</sup> M.J. Yaffe, "Digital mammography," in J. Beutel, H. Kundel, and R.L. Van Metter (Eds.) *Physics and Psychophysics, Handbook of Medical Imaging Vol. 1*, Bellingham, Washington: SPIE press, 329-372 (2000).
- <sup>3</sup> J. Howard, "Using mammography for cancer control: an unrealized potential," *Cancer J. Clin.* **37**, 33-48 (1987).
- <sup>4</sup> A.L.M. Verbeek, J.H.C.L. Hendriks, R. Holland, M. Mravunac, F. Sturmans, and N.E. Day, "Reduction of breast cancer mortality through mass screening with modern mammography," *Lancet* **1**, 1222-1224 (1984).
- <sup>5</sup> E.D. Pisano, M.J. Yaffe, B.M. Hemminger et al., "Current status of full-field digital mammography," *Acad. Radiol.* **7**, 266-280 (2000).
- <sup>6</sup> M.B. Williams and L.L. Fajardo, "Digital mammography: Performance considerations and current detector designs," *Acad. Radiol.* **3**, 429-437 (1996).
- <sup>7</sup> P.C. Johns, D.J. Drost, J. M. Yaffe, and A. Fenster, "Dual energy mammography: initial experimental results," *Med. Phys.* **12**, 297-304 (1985).
- <sup>8</sup> H. Jafroudi, S. Lo, H. Li, D. Steller Artz, M.T. Freedman, S.K. Mun, "Dual-energy in mammography – feasibility study," *Proce. SPIE* **2708**, 278-293 (1996).
- <sup>9</sup> L.T. Niklason et al., "Digital tomosynthesis in breast imaging," *Radiology* **205**, 399-406 (1997).
- <sup>10</sup> B. Chen and R. Ning, "Cone-beam volume CT mammographic imaging: feasibility study," *Proc. SPIE* **4320**, 655-664 (2001).
- <sup>11</sup> Y. Jiang, R.M. Nishikawa, R.A. Schmidt, C.E. Metz, M.L. Giger, and K. Doi, "Improving breast cancer diagnosis with computer-aided diagnosis," *Acad. Radiol.* **6**, 22-33 (1999).
- <sup>12</sup> W. Des Jardin, C. Parks, H. Doan, N. Kurfiss, and K. Wetzel, "A large format, high-performance CCD sensor for medical x-ray applications," *Proc. SPIE* **3977**, 167-175 (2000).
- <sup>13</sup> S. Vedantham, A. Karellas, and S. Suryanarayanan, L. Levis, M. Sayag, R. Kleehammer, R. Heidsieck, and C.J. D'Orsi, "Mammographic imaging with a small format CCD-based digital cassette: physical characteristics of a clinical system," *Med. Phys.* **27** (8), 1832-1840 (2000).
- <sup>14</sup> E.P. Muntz, "On the comparison of actual and calculated improvements in the imaging of calcifications using magnification mammography," *Med. Phys.* **8** (4), 496-501 (1981).
- <sup>15</sup> D. Rosen, W. Phillips, M. Stanton, J. Xie, D. O'Mara, and A. Stewart, "A prototype CCD-based detector for whole breast digital mammography," *Proc. SPIE* **3032**, 52-58 (1997).
- <sup>16</sup> J.G. Mainprize, N.L. Ford, S. Yin, T. Tumer, and M.J. Yaffe, "Image quality of a prototype direct conversion detector for digital mammography," *Proc. SPIE* **3659**, 398-406 (1999).
- <sup>17</sup> E. Samei, J.A. Seibert, C.E. Willis, M.J. Flynn, E. Mah, and K.L. Junck, "Performance evaluation of computed radiography systems," *Med. Phys.* **28** (3), 361-371 (2001).

- <sup>18</sup> A. Workman, A. Cowen, and D. Brettle, "Physical evaluation of computed radiography as a mammographic x-ray imaging system," *Br. J. Radiol.* **67** (802), 988-995 (1994).
- <sup>19</sup> Y. Higashida, N. Moribe, K. Morita, et al., "Detection of subtle microcalcifications: comparison of computed radiography and screen-film mammography," *Radiology* **183**, 483-486 (1992).
- <sup>20</sup> R.J. Jennings, H. Jafroudi, R.M. Gagne, T.R. Fewell, P.W. Quinn, D.E. Steller Artz, J.J. Vucich, M.T. Freedman, and S.K. Mun, "Storage-phosphor-based digital mammography using a low-dose x-ray system optimized for screen-film mammography," *Proc. SPIE* **2708**, 202-232 (1996).
- <sup>21</sup> S. Arakawa, H. Yasuda, K. Kohda, and T. Suzuki, "Improvement of image quality in CR mammography by detection of emissions from dual sides of an imaging plate," *Proc. SPIE* **3977**, 590-600 (2000).
- <sup>22</sup> P.J.R. Leblans, L. Struye, P. Willems, "New needle-crystalline CR detector," *Proc. SPIE* **4320**, 59-67 (2001).
- <sup>23</sup> P. R. Granfors and R. Aufrecht, "Performance of a 41 x 41-cm<sup>2</sup> amorphous silicon flat panel x-ray detector for radiographic imaging applications," *Med. Phys.* **27**, 1324 – 1331 (2000).
- <sup>24</sup> G.S. Shaber, D.L. Lee, J. Bell, G. Powell, A.D.A. Maidment, "Clinical evaluation of a full field digital projection radiography detector," *Proc. SPIE* **3336**, 463-469 (1998).
- <sup>25</sup> A. Tsukamoto, S. Yamada, T. Tomisaki, M. Tanaka, T. Sakaguichi, H. Asahina, K. Suzuki, and M. Ikeda, "Development and evaluation of a large area selenium-based flat-panel detector for real-time radiography and fluoroscopy," *Proc. SPIE* **3659**, 14-23 (1999).
- <sup>26</sup> E.L. Gingold, D.L.Y. Lee, L.S. Jeromin, B. Rodricks, M.G. Hoffberg, and C.L. Williams, "Development of a novel high-resolution direct conversion x-ray detector," *Proc. SPIE* **3977**, 185-193 (2000).
- <sup>27</sup> C. Chaussat, J. Chabbal, T. Ducourant, V. Spinnler, G. Vieux, and R. Neyret, "New CsI/a-Si 17" x 17 x-ray flat-panel detector provides superior detectivity and immediate digital output for general radiography systems," *Proc. SPIE* **3336**, 45-55 (1998).
- <sup>28</sup> S. Vedantham, A. Karellas, and S. Suryanarayanan, "Full breast digital mammography with an amorphous silicon-based flat panel detector: physical characteristics of a clinical prototype," *Med. Phys.* **27** (3), 558-567 (2000).
- <sup>29</sup> L.E. Antonuk, J.M. Boudry, Y. El-Mohri, W. Huang, J.H. Siewerdsen, J. Yorkston, and R.A. Street, "Large-area, flat-panel amorphous silicon imagers," *Proc. SPIE* **2432**, 216 – 227 (1995).
- <sup>30</sup> T. Graeve, Y. Li, A. Fabans, and W. Huang, "High-resolution amorphous silicon image sensor," *Proc. SPIE* **2708**, 494 – 498 (1996).
- <sup>31</sup> D.L. Lee, L.K. Cheung, and L.S. Jeromin, "A new digital detector for projection radiography," *Proc. SPIE* **2432**, 237 – 249 (1995).
- <sup>32</sup> W. Zhao and J.A. Rowlands, "X-ray imaging using amorphous selenium: feasibility of a flat-panel self-scanned detector for digital radiology," *Med. Phys.* **22**(10), 1595 – 1604 (1995).
- <sup>33</sup> J.A. Rowlands, J. Yorkston, "Flat panel detectors for digital radiography," in J. Beutel, H. Kundel, and R.L. Van Metter (Eds.) *Physics and Psychophysics, Handbook of Medical Imaging Vol. 1*, Bellingham, Washington: SPIE press, 223-328 (2000).

- 
- <sup>34</sup> J.H. Siewerdsen, L.E. Antonuk, Y. El-Mohri, J. Yorkston, W. Huang, and I.A. Cunningham "Signal, noise power spectrum, and detective quantum efficiency of indirect-detection flat-panel imagers for diagnostic radiology," *Med. Phys.* **25**, 614 – 628 (1998).
- <sup>35</sup> W. Zhao and J.A. Rowlands, "Digital radiology using active matrix readout of amorphous selenium: Theoretical analysis of detective quantum efficiency," *Med. Phys.* **24**, 1819 – 1833 (1997).
- <sup>36</sup> D.L. Lee, K.C. Lawrence, L.S. Jeromin, E.F. Palecki, and B. Rodricks, "Radiographic imaging characteristics of a direct conversion detector using selenium and thin film," *Proc. SPIE* **3032**, 88–95 (1997).
- <sup>37</sup> X. Liu, C.C. Shaw, X.J. Rong, M. Lemacks, "Comparison of a-Si:H/CsI flat-panel digital imaging systems with CR and CCD based systems — image quality measurements," *Proc. SPIE* **4320**, 389–398 (2001).
- <sup>38</sup> E. Samei, M.J. Flynn, H.G. Chotas, and J.T. Dobbins III, "DQE of direct and indirect digital radiography systems," *Proc. SPIE* **4320**, 189–197 (2001).
- <sup>39</sup> R.R. Millis, R. Davis, and A.J. Stacey, "The detection and significance of calcifications in the breast: a radiological and pathological study," *Br. J. Radiol.* **49**, 12 (1976).
- <sup>40</sup> L. Tabar, S.W. Duffy, and U.B. Krusemo, "Detection method, tumor size and node metastases in breast cancers diagnosed during a trail of breast cancer screen," *Eur. J. Cancer Clin. Oncol.* **23**, 959-952 (1987).
- <sup>41</sup> G. Hermann, C. Janus, I. Schwartz, A. Papatostas, D.G. Hermann, and J.G. Rabinowitz, "Occult malignant breast lesions in 114 patients: relationship to age and the presence of microcalcifications," *Radiology*, **169**, 321 (1988).
- <sup>42</sup> P.C. Bunch, "The effects of reduced film granularity on mammographic image quality," *Proc. SPIE* **3032**, 302 – 317 (1997).
- <sup>43</sup> C.C. Shaw, T. Wang, J.L. King, D.S. Breitenstein, T.S. Chang, K.M. Harris, A.B. Baratz, M.A. Ganott, R. Reginella, J.H. Sumkin, D. Gur, "Computed radiography versus screen-film mammography in detection of simulated microcalcifications: a receiver operating characteristic study based on phantom images," *Acad. Radiol.* **5**, 173-180 (1998).

	Flat-panel	CCD	CR	Screen/film
Manufacture	GE Medical Systems	GE Medical Systems	Fuji Medical Systems	Kodak
Model	SenoGraph 2000	SenoVision	AC-3/HR V	MinR 2000
X-ray converter	CsI:Tl	Phosphor Gd <sub>2</sub> O <sub>2</sub> S:Tb	Storage Phosphor	Phosphor Gd <sub>2</sub> O <sub>2</sub> S:Tb
Image area (cm <sup>2</sup> )	19 x 23	6 x 6	20 x 25	18 x 24
Image matrix	1914 x 2294	2048 x 2048	2000 x 2510	NA
Pixel size (μm)	100	30	100	NA
Image depth (bits)	14 (linear)	12 (linear)	10 (log)	NA

Table 1. Specifications of the four x-ray imaging systems studied

Xiujiang Rong  
 Maedical Physics

Size range ( $\mu\text{m}$ )	Typical size ( $\mu\text{m}$ )
150 – 160	155
125 – 140	133
112 – 125	119

Table 2. Sizes of the simulated  $\mu\text{Cs}$  used for constructing the phantom

Xiujiang Rong  
Maedical Physics

Reader	SF		FP		CCD		CR	
	$A_z$	$\sigma$	$A_z$	$\sigma$	$A_z$	$\sigma$	$A_z$	$\sigma$
1	0.844	0.032	0.904	0.021	0.844	0.031	0.733	0.037
2	0.854	0.026	0.933	0.017	0.764	0.035	0.734	0.035
3	0.817	0.033	0.872	0.025	0.803	0.030	0.673	0.039
4	0.799	0.029	0.829	0.029	0.764	0.032	0.661	0.039
5	0.767	0.034	0.828	0.028	0.712	0.037	0.717	0.037
6	0.628	0.042	0.800	0.032	0.694	0.035	0.592	0.042
7	0.848	0.029	0.884	0.025	0.778	0.033	0.679	0.037
Overall	0.786	0.013	0.857	0.010	0.756	0.013	0.682	0.015

Table 3. Area under the ROC curve ( $A_z$ ) and standard deviation ( $\sigma$ ) for all three  $\mu$ C sizes combined

Xiujiang Rong  
Medical Physics

Reader	SF		FP		CCD		CR	
	$A_z$	$\sigma$	$A_z$	$\sigma$	$A_z$	$\sigma$	$A_z$	$\sigma$
1	0.563	0.088	0.646	0.073	0.547	0.080	0.473	0.085
2	0.701	0.071	0.797	0.059	0.463	0.084	0.494	0.083
3	0.665	0.082	0.762	0.060	0.626	0.076	0.579	0.092
4	0.588	0.077	0.648	0.069	0.537	0.081	0.499	0.085
5	0.531	0.082	0.669	0.066	0.506	0.084	0.592	0.076
6	0.519	0.090	0.633	0.068	0.575	0.075	0.508	0.086
7	0.644	0.082	0.730	0.061	0.576	0.081	0.453	0.083
Overall	0.585	0.031	0.684	0.025	0.540	0.030	0.523	0.032

Table 4. Area under the ROC curve ( $A_z$ ) and standard deviation ( $\sigma$ ) for the small  $\mu\text{C}$  size group (112 – 125  $\mu\text{m}$ )

Xiujiang Rong  
Medical Physics

Reader	SF		FP		CCD		CR	
	$A_z$	$\sigma$	$A_z$	$\sigma$	$A_z$	$\sigma$	$A_z$	$\sigma$
1	0.853	0.044	0.902	0.038	0.817	0.061	0.599	0.072
2	0.792	0.055	0.946	0.026	0.677	0.071	0.681	0.068
3	0.786	0.052	0.908	0.034	0.763	0.059	0.637	0.075
4	0.803	0.053	0.931	0.028	0.733	0.059	0.622	0.070
5	0.767	0.062	0.876	0.039	0.609	0.074	0.631	0.072
6	0.664	0.067	0.893	0.036	0.593	0.074	0.562	0.077
7	0.820	0.056	0.929	0.029	0.749	0.065	0.587	0.079
Overall	0.770	0.022	0.898	0.014	0.678	0.026	0.611	0.028

Table 5. Area under the ROC curve ( $A_z$ ) and standard deviation ( $\sigma$ ) for the medium  $\mu\text{C}$  size group (125 – 140  $\mu\text{m}$ )

Xiujiang Rong  
Medical Physics

Reader	SF		FP		CCD		CR	
	$A_z$	$\sigma$	$A_z$	$\sigma$	$A_z$	$\sigma$	$A_z$	$\sigma$
1	1	0	1	0	1	0	0.971	0.018
2	1	0	1	0	1	0	0.982	0.013
3	0.964	0.038	0.967	0.038	0.997	0.004	0.981	0.014
4	1	0	0.963	0.039	1	0	0.919	0.046
5	1	0	0.967	0.038	0.992	0.010	0.951	0.024
6	0.808	0.061	0.932	0.053	0.991	0.009	0.849	0.071
7	1	0	0.966	0.038	0.979	0.015	0.984	0.011
Overall	0.974	0.010	0.970	0.013	0.993	0.003	0.939	0.015

Table 6. Area under the ROC curve ( $A_z$ ) and standard deviation ( $\sigma$ ) for the large  $\mu$ C size group (150 – 160  $\mu$ m)

Xiujiang Rong  
Medical Physics

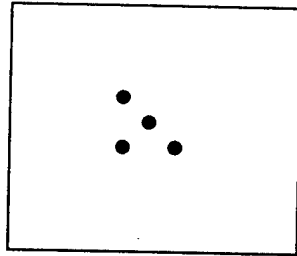


Figure 1. Example of a simulated  $\mu$ C cluster. The upper right  $\mu$ C is missing.

Xiujiang Rong  
Medical Physics

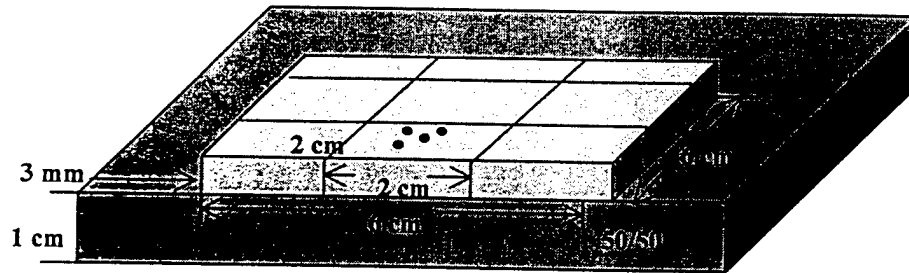


Figure 2. Phantom of 3 x 3 tiled Lucite squares on a 1-cm thick 50% adipose/50% glandular simulated tissue slab. An additional slab was placed on the top for imaging. Placement and orientation of simulated  $\mu\text{C}$  clusters were randomized for each image acquired.

Xiujiang Rong  
Medical Physics

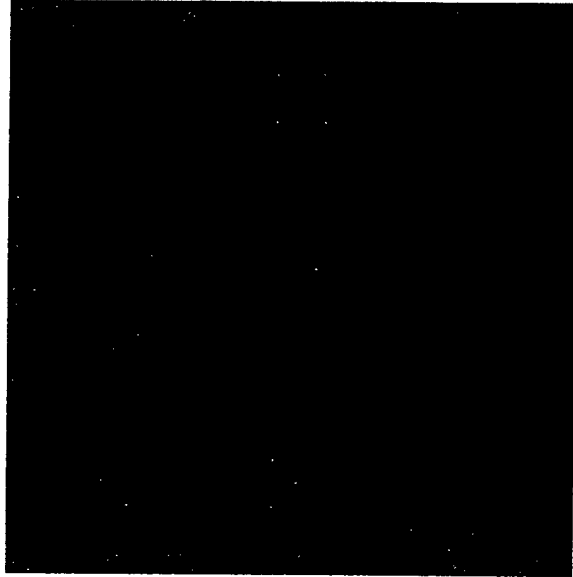


Figure 3. Example image of simulated  $\mu\text{C}$  phantom acquired with the FP system

Xiujiang Rong  
Medical Physics

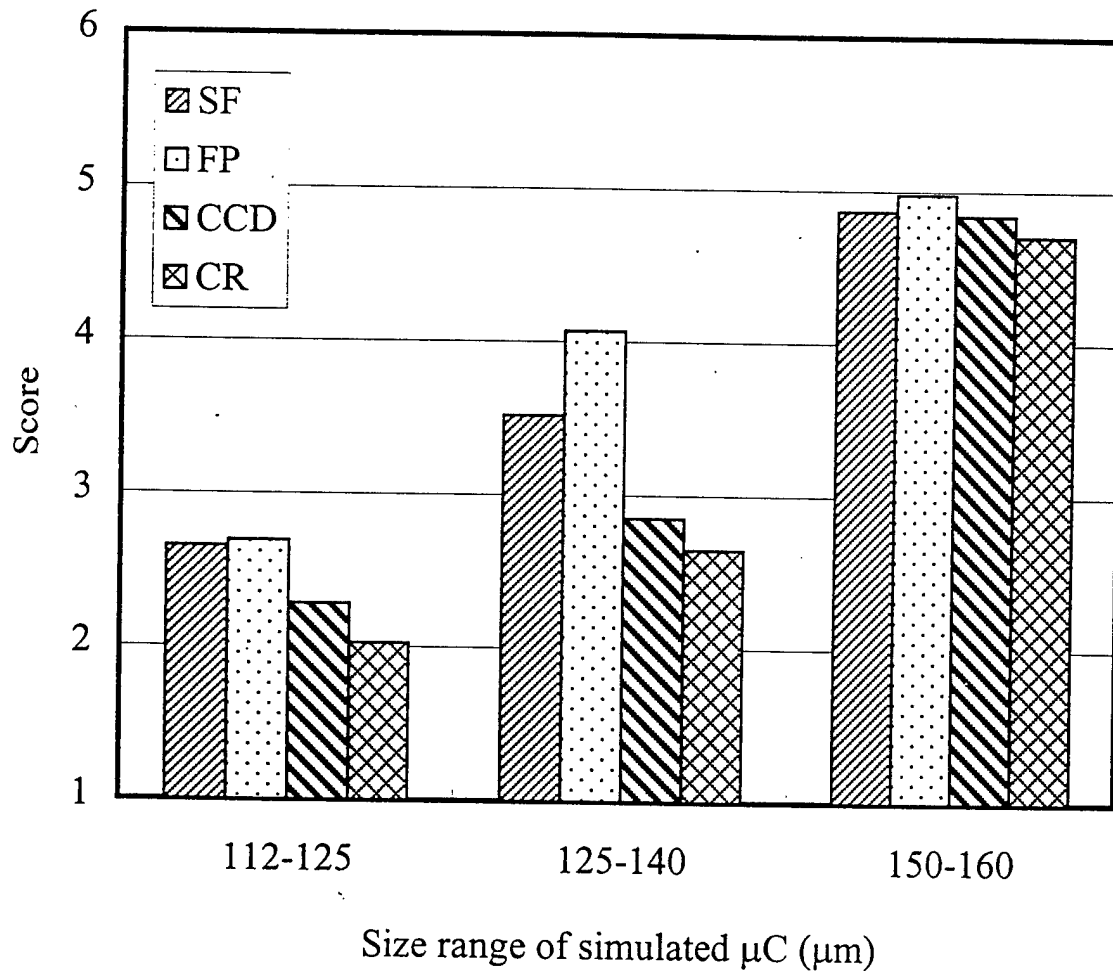


Figure 4  
 Xiujiang Rong  
 Medical Physics

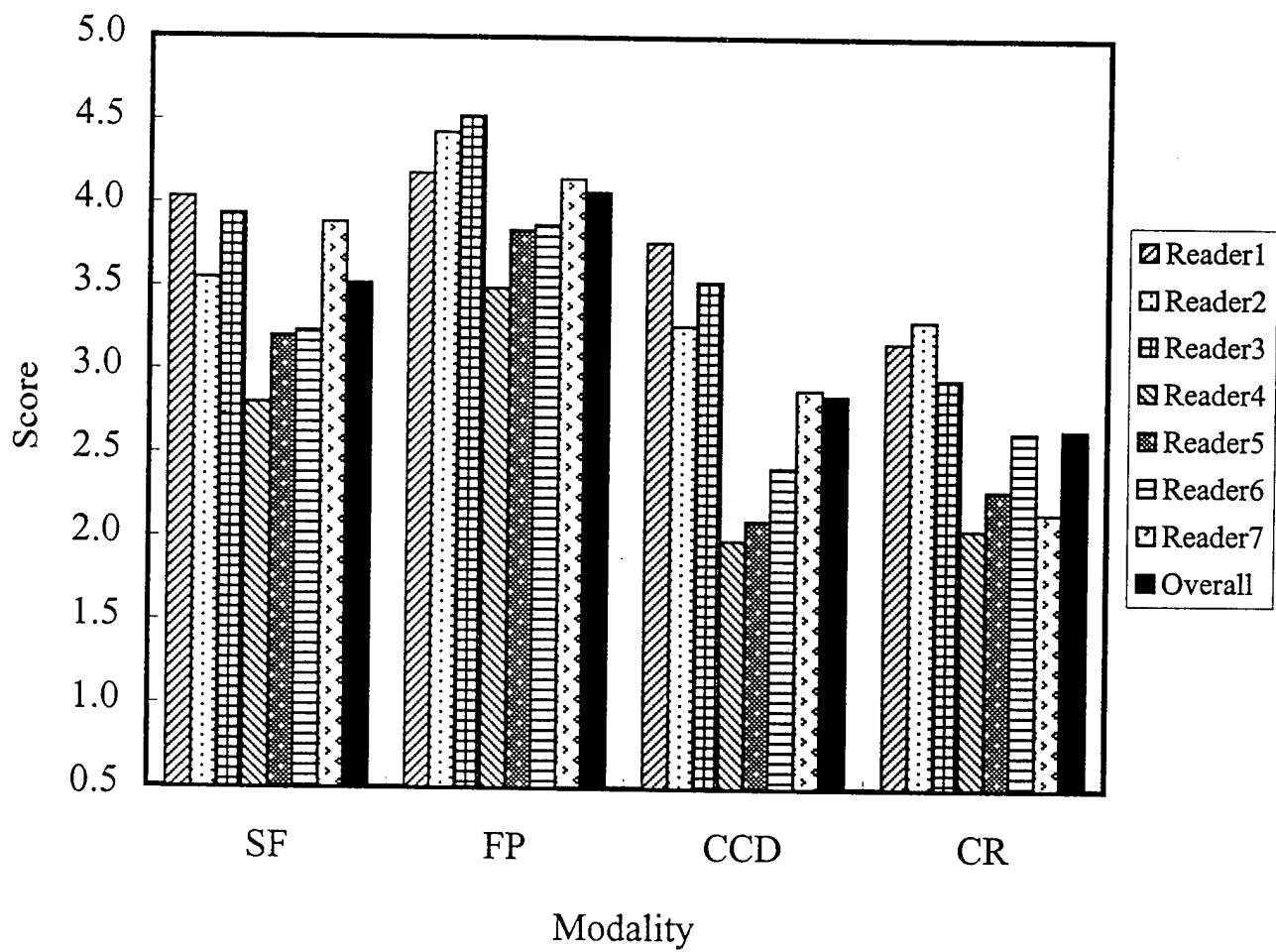


Figure 5  
 Xiujiang Rong  
 Medical Physics

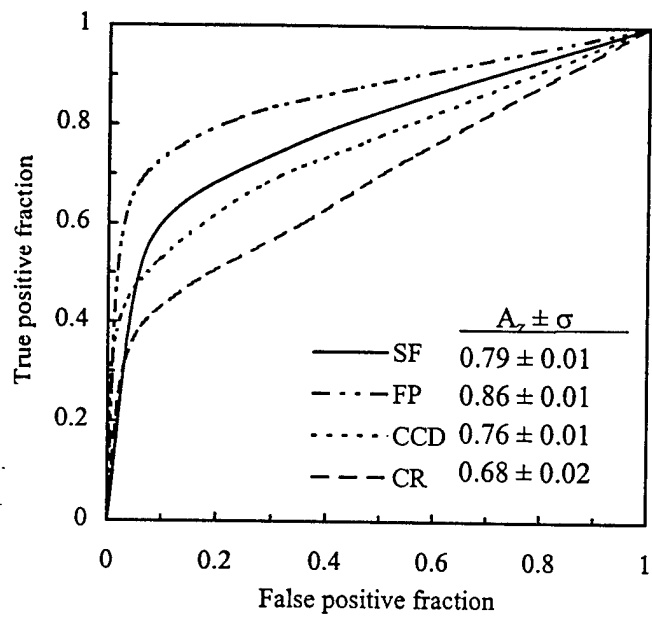


Figure 6  
 Xiujiang Rong  
 Medical Physics

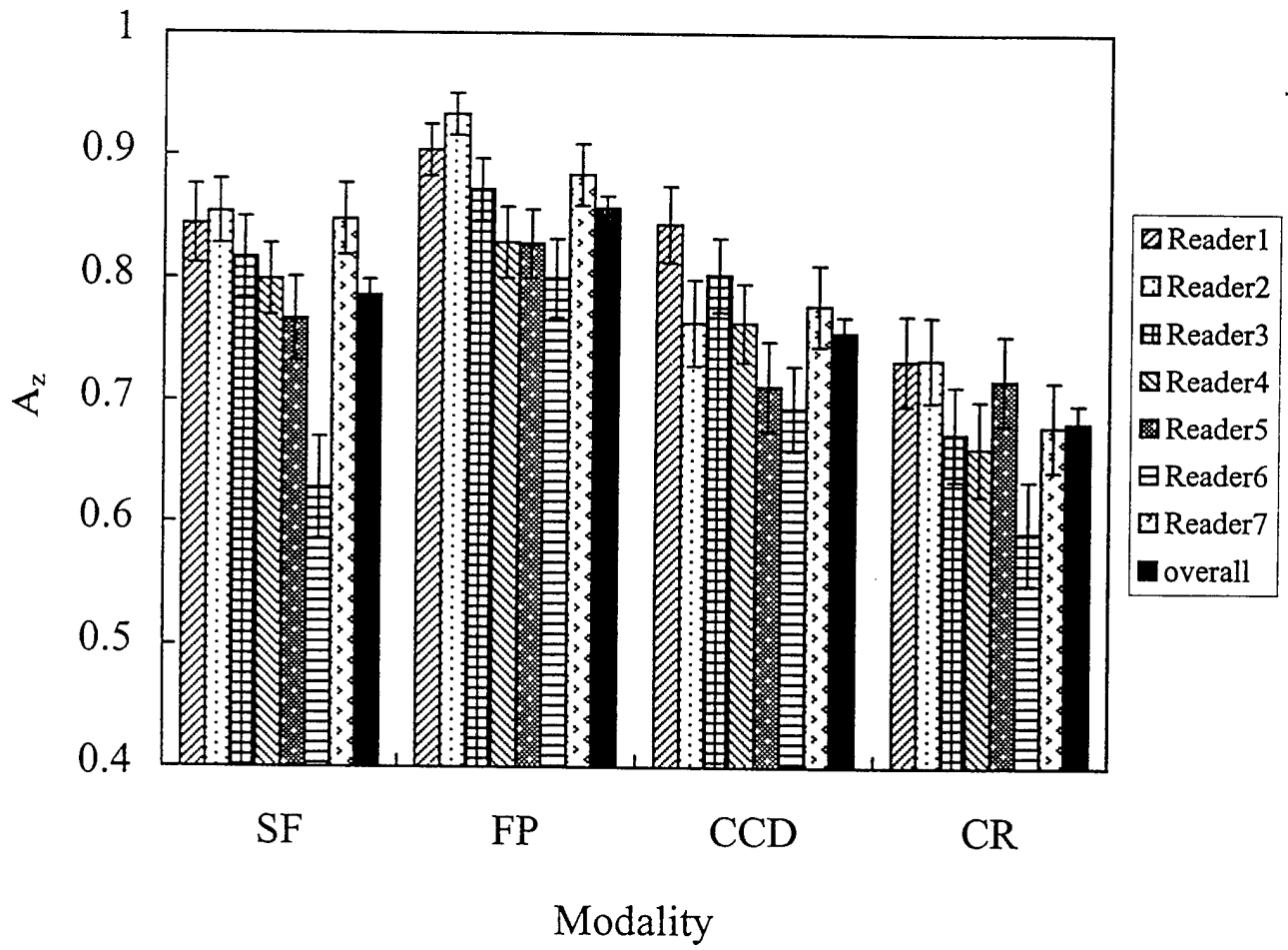


Fig 7a  
 Xiujiang Rong  
 Medical Physics

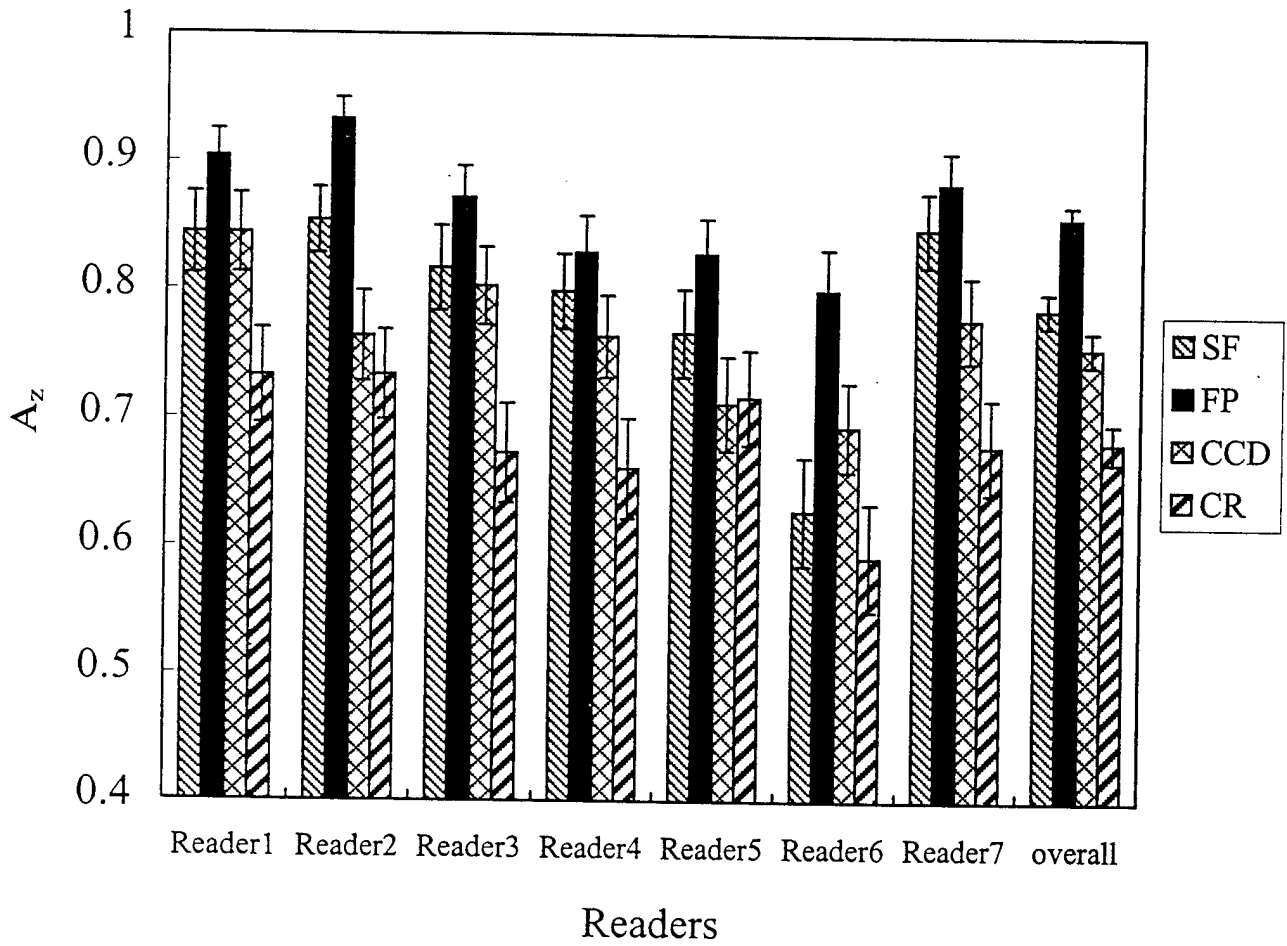


Fig 7b  
 Xiujiang Rong  
 Medical Physics

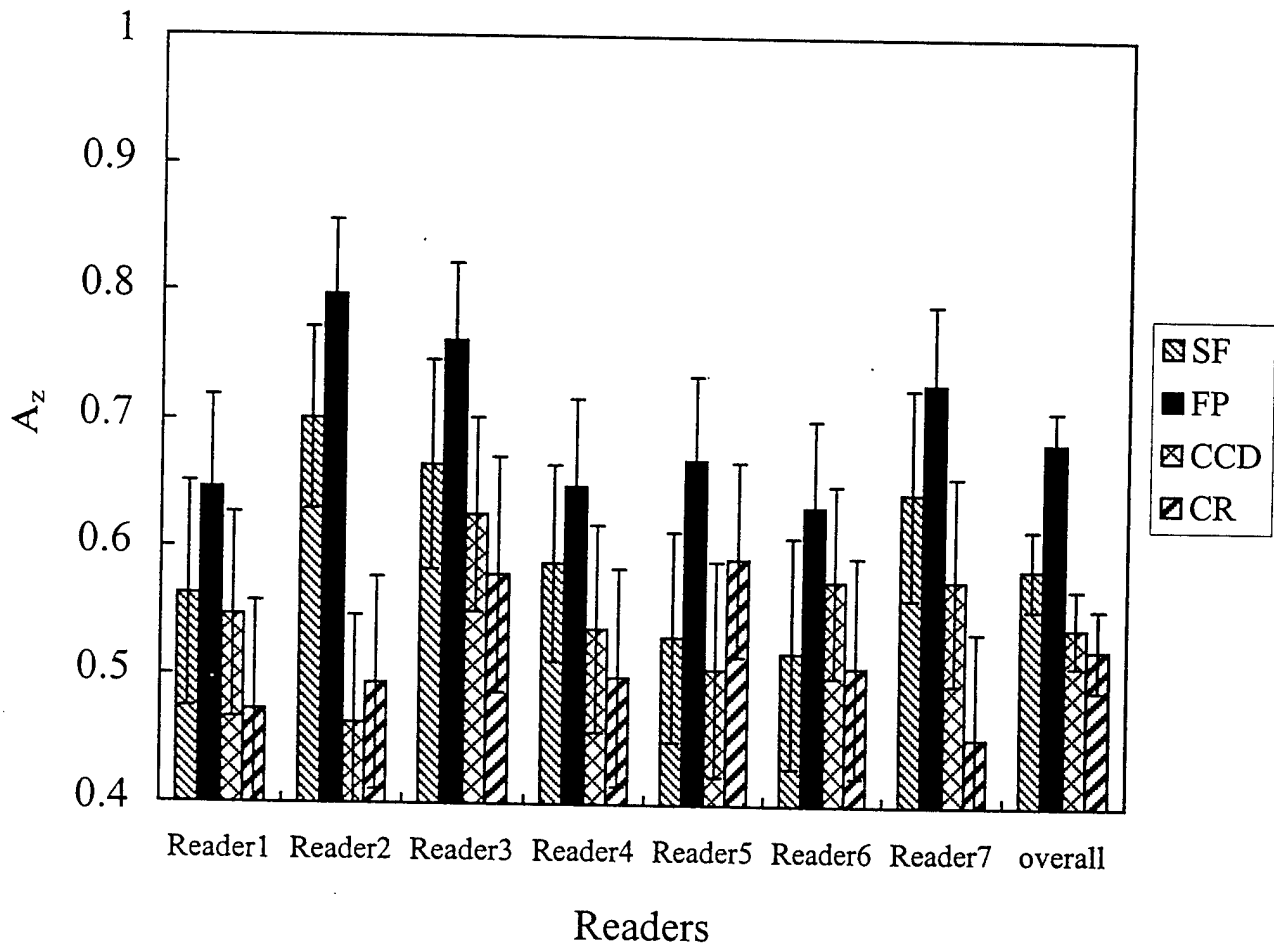


Fig 8a  
 Xiujiang Rong  
 Medical Physics

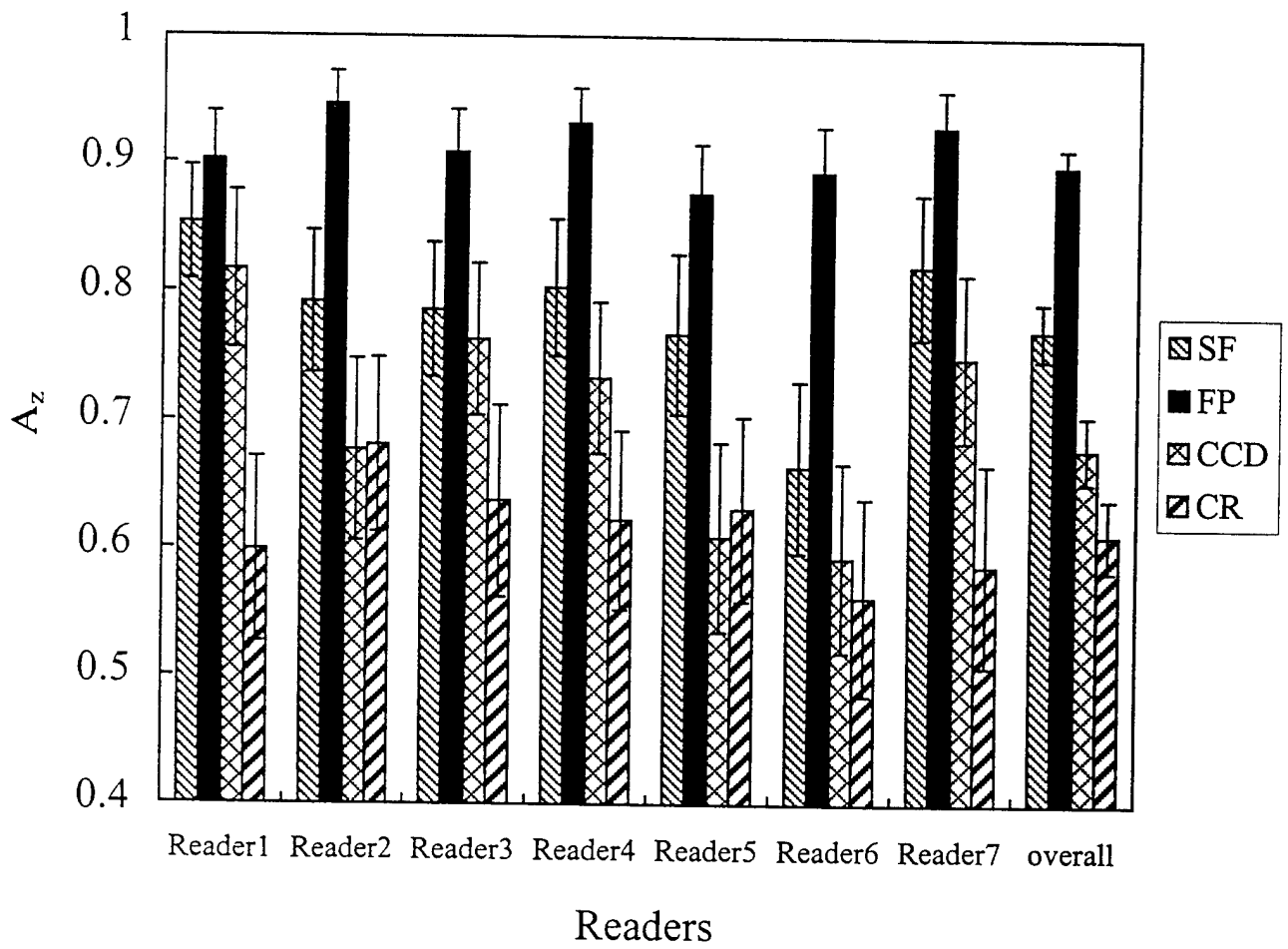


Figure 8b  
 Xiujiang Rong  
 Medical Physics

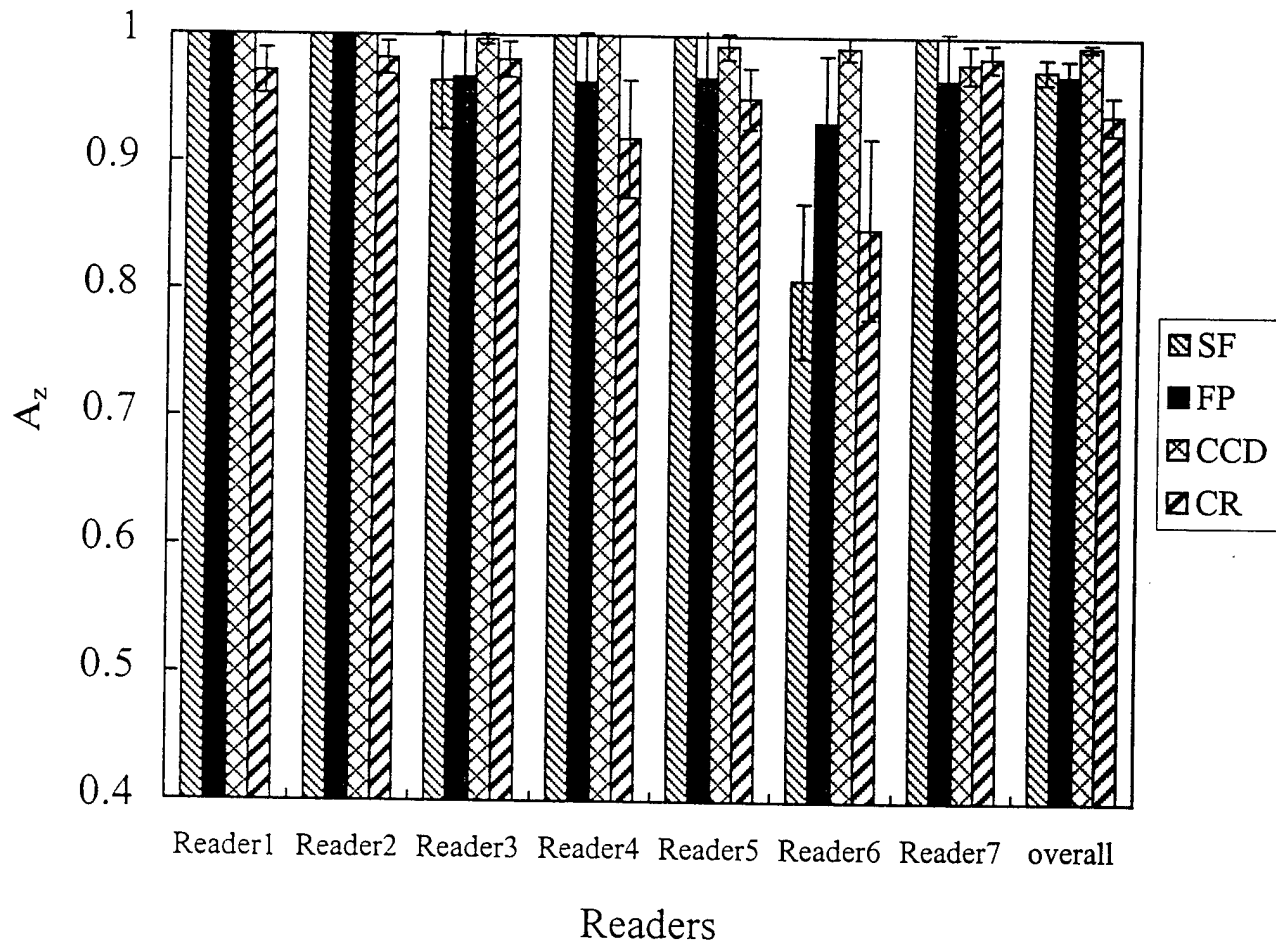


Figure 8c  
 Xiujiang Rong  
 Medical Physics

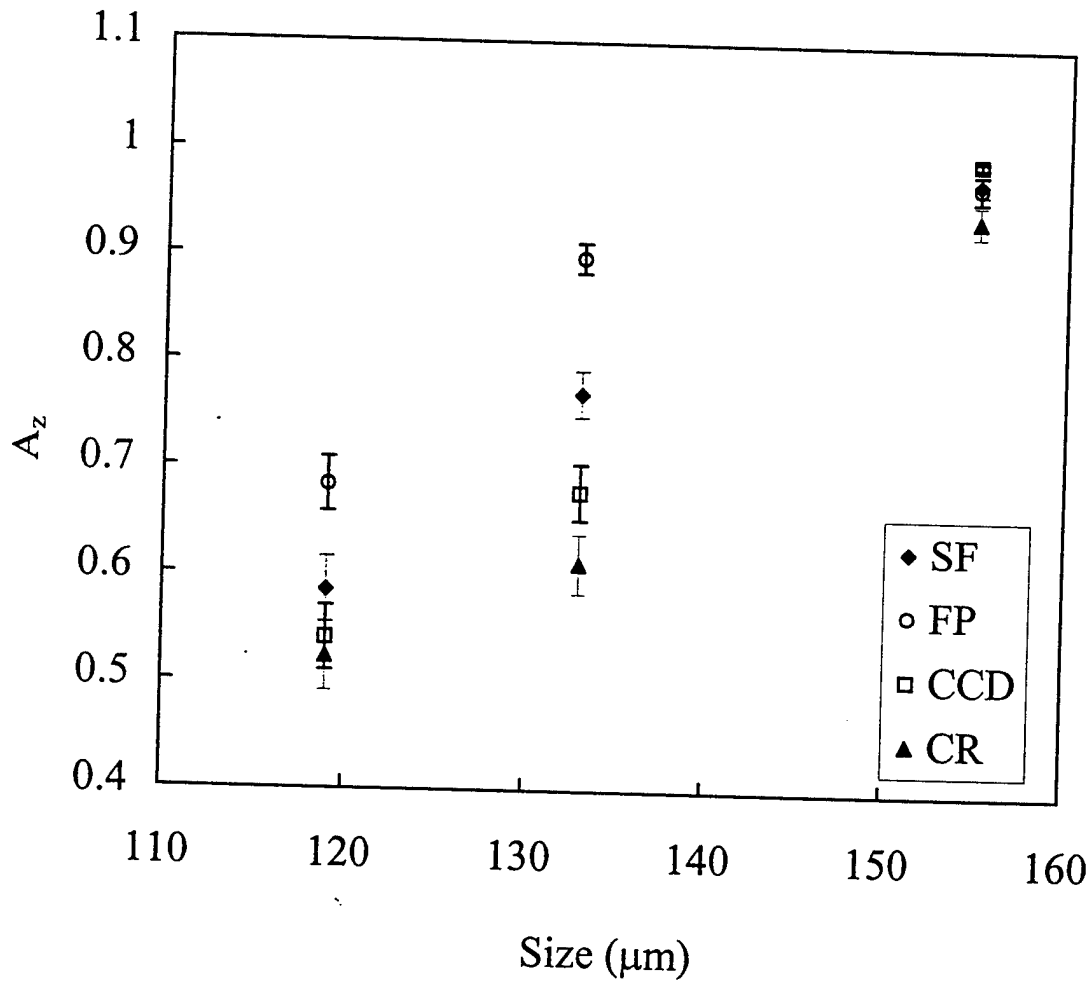


Figure 9  
Xiujiang Rong  
Medical Physics

**A Dual-Energy Subtraction Technique for Enhancing Microcalcifications in Digital  
Mammography – A Signal-to-Noise Analysis**

Michael R. Lemacks, S. Cheenu Kappadath, Chris C. Shaw,  
Xinming Liu, and Gary J. Whitman

Diagnostic Radiology Department  
University of Texas M. D. Anderson Cancer Center  
Houston, TX 77030

This work was supported by a research grant DAMD17-00-1-0316 by the US Department of the Army and by a research grant by the Mike Hogg Foundation

Please address all correspondence to:

Chris C. Shaw, Ph.D.  
Diagnostic Radiology Department  
U. of Texas M. D. Anderson Cancer Center  
Box 57  
1515 Holcombe Boulevard  
Houston, TX 77030  
Tel.: 713-745-2819  
E-mail: [cshaw@di.mdacc.tmc.edu](mailto:cshaw@di.mdacc.tmc.edu)

## Abstract

Microcalcifications ( $\mu$ Cs) are one of the two major symptoms for detection of breast cancer in x-ray mammography. However, detection and visualization of microcalcifications are often obscured by the overlapping tissue structures. Dual-energy subtraction imaging technique offers an alternative approach for imaging and visualizing  $\mu$ Cs. With this technique, separate high- and low-energy images are acquired and their differences are used to “cancel” out the background tissue structure. However, the subtraction process could increase the noise level relative to the calcification contrast or signal. Therefore, a key issue with the dual-energy subtraction imaging technique is to weigh the benefit of removing the cluttered background tissue structure over the drawback of reduced SNR in the subtracted  $\mu$ Cs images.

In this report we estimate the noise levels in the dual-energy subtraction signals for various imaging conditions and optimize the selection of imaging parameters to evaluate the feasibility of using a dual-energy subtraction technique for improved detection and visualization of  $\mu$ Cs. A theoretical framework for calculating the (quantum) noise in the subtraction images is developed and methods for numerical computation are described. The results are presented and used to discuss the effects and selection of imaging parameters such as x-ray spectra,  $\mu$ C size, tissue composition and breast thickness.

**Key words:** medical imaging, dual-energy subtraction imaging, digital mammography, signal-to-noise ratio, numerical simulation

## 1. INTRODUCTION

Screening and diagnosis in x-ray mammography relies on the detection and visualization of microcalcifications ( $\mu$ Cs) and/or soft tissue masses. Early detection of breast cancer is essential for better survival rate. The  $\mu$ Cs are composed of mainly calcium that have greater attenuation properties than soft tissue. This leads to a subject contrast over the soft tissue background. The detection or visualization of  $\mu$ Cs is relatively easy over a uniform tissue background. This is largely governed by the Rose criteria [REFERENCE] which suggests that the contrast signal-to-noise ratio as evaluated over the object area should be above a certain threshold value (say 3–5) in order to be detected or visualized. However, in reality, the visualization of  $\mu$ Cs may be limited by the “clutter” due to overlapping tissue background present in the mammogram. The clutter in tissue background arises from the structures of glandular tissue, ducts, vessels and soft tissue masses in the breast. Depending upon the degree of clutter, contrast of  $\mu$ Cs, and extend of overlap, it may be difficult to detect a  $\mu$ C even though there may be sufficient contrast-to-noise ratio (CNR).<sup>1</sup>

Dual-energy subtraction imaging technique<sup>1-6</sup> offers an alternative approach to the detection and visualization of  $\mu$ Cs. With this technique, separate high- and low-energy images are acquired and “subtracted” from each other in a weighted fashion to cancel out the cluttered tissue structure so as to decrease the obscurity associated with the overlapping tissue structures. However, due to subtraction processing, the calcification CNR in the subtraction images tends to be lower than that in the unsubtracted images.<sup>2</sup> The calcification CNR in the subtraction images depends on the x-ray spectra and other imaging parameters used, in addition to the SNR in the original (unsubtracted) images.

Therefore, the key issue in dual-energy subtraction imaging technique is to weigh the benefit of removing cluttered background against the drawback of reduced calcification CNR in the subtraction images.

In this paper we study the effects of various imaging parameters and optimize their selections by estimating the calcification CNR in the dual-energy subtraction images under various imaging conditions. A theoretical framework for calculating the calcification CNR in the subtraction images is developed. Here, we consider only the propagation of quantum (Poisson) noise from the original (unsubtracted) images to the subtraction images. The methods and data (choice of x-ray spectra,  $\mu\text{C}$  size, tissue composition, and breast thickness) used for computing the calcification CNR are described. Results of the numerical computation are presented and used to demonstrate and discuss the feasibility of using dual-energy subtraction imaging technique to improve the detection and visualization of  $\mu\text{C}$ s in mammograms.

## 2. THEORY

In this section, the formalism for dual-energy subtraction (calcification) imaging is presented. Within this framework, the calcification CNR in the subtraction image are derived for use in the numerical studies. Although the derived framework can be used for situations including both the quantum and system noise, only quantum (Poisson) noise is considered in the present numerical study.

### 2.1 Three-Energy versus Two-Energy Subtraction

In mammography, one can assume that there are three attenuating materials in the breast: adipose tissue, glandular tissue and calcifications (only sparsely present). Ideally, it would be best to use images acquired at three separate energies to estimate the thickness of the three attenuating materials.<sup>3</sup> However, compared to the dual-energy subtraction imaging, three-energy subtraction imaging leads to excessive reduction of image SNR which would potentially require higher patient exposure, increased time to complete the exam (which could lead to motion artifacts), and more complicated subtraction image processing. Mammography differs from other radiographic procedures in that the breast is compressed to a largely uniform thickness (that can be easily measured) beyond which it tapers smoothly towards the edge. With the total breast thickness known, the task of three-material composition measurement can be reduced to that of two-materials.<sup>2</sup> Alternatively, the thickness of adipose and glandular tissue can be determined by using the dual-energy subtraction technique at pixels where no calcifications are present.<sup>4</sup> Although the tissue composition of the breast varies spatially in a complex way, dual-energy imaging can also be used to estimate the total breast

thickness (sum of the adipose and glandular tissue thickness) in the uncompressed part of the breast.

## 2.2 Dual-Energy Microcalcification Imaging Technique

Assume that along the x-ray path, a compressed breast is composed of adipose tissue of thickness  $t_a$ , glandular tissue of thickness  $t_b$ , and a microcalcification of thickness  $t_c$  (Figure 1). The total breast tissue thickness,  $T$  [cm] is be given by:

$$T = t_a + t_b + t_c \quad (1)$$

Assuming that poly-energetic x-rays are used, the measured signal in the low- and high-energy images,  $S_l$  and  $S_h$ , can be expressed as:

$$S_j = \int dE \cdot R_j \cdot d^2 \cdot \Phi_j(E) \cdot e^{-\mu_a(E)t_a - \mu_b(E)t_b - \mu_c(E)t_c} \cdot A(E) \cdot Q(E); j = l, h \quad (2)$$

where,  $R_l$  and  $R_h$  are the unattenuated low- and high-energy x-ray exposures in milliroentgens [mR] at the detector plane,  $d$  is the pixel size in centimeters [cm],  $\Phi_l(E)$  and  $\Phi_h(E)$  are the unattenuated low- and high-energy photon fluence per unit exposure per unit energy [photons/cm<sup>2</sup>/mR/keV] at the detector input,  $A(E)$  is the photon absorption ratio of the detector as a function of photon energy  $E$ [keV], and  $Q(E)$  is the detector response function and represents the signal generated by each detected x-ray photon i.e. gain as a function of photon energy  $E$ [keV]. The energy dependent linear-attenuation coefficients [1/cm] for each of the materials are given by  $\mu_a(E)$ ,  $\mu_b(E)$ , and  $\mu_c(E)$  for adipose tissue, glandular tissue and the calcification, respectively.

Defining  $\Delta\mu_b(E) \equiv \mu_b(E) - \mu_a(E)$  and  $\Delta\mu_c(E) \equiv \mu_c(E) - \mu_a(E)$ , referred to as the difference-attenuation coefficients and solving for  $t_a$  in Eq. 1, the low- and high-energy image signals (Eq. 2) can be rewritten as:

$$S_j = \int dE \cdot R_j \cdot d^2 \cdot \Phi_j(E) \cdot e^{-\mu_a(E)T} \cdot e^{-\Delta\mu_b(E)t_b - \Delta\mu_c(E)t_c} \cdot A(E) \cdot Q(E); j = l, h \quad (3)$$

Analogous to the optical density, define x-ray densities for the low- and high-energy images,  $D_l$  and  $D_h$  as follows:

$$D_j \equiv \ln \left[ \frac{S_j^0}{S_j} \right]; j = l, h \quad (4)$$

where,  $S_j^0$  is the unattenuated reference signal obtained by imaging without the breast present.

Using the signals attenuated by 100% adipose tissue,  $S_j^a = \int dE \cdot R_j \cdot d^2 \cdot \Phi_j(E) \cdot e^{-\mu_a(E)T} \cdot A(E) \cdot Q(E); (j = l, h)$ , as the low- and high-energy reference signals, the modified x-ray densities,  $D'_l$  and  $D'_h$  (now functions of only the glandular tissue thickness,  $t_b$  and calcification thickness,  $t_c$ ) can be defined as:

$$D'_j = F_j(t_b, t_c) \equiv \ln \left[ \frac{S_j^a}{S_j} \right]; j = l, h \quad (5)$$

Substituting Eq. 3 in Eq. 5,  $D'_l$  and  $D'_h$  can be expressed as follows:

$$D'_j = \ln \left[ \frac{\int dE \cdot R_j \cdot d^2 \cdot \Phi_j(E) \cdot e^{-\mu_a(E)T} \cdot A(E) \cdot Q(E)}{\int dE \cdot R_j \cdot d^2 \cdot \Phi_j(E) \cdot e^{-\mu_a(E)T} \cdot e^{-\Delta\mu_b(E)t_b - \Delta\mu_c(E)t_c} \cdot A(E) \cdot Q(E)} \right]; j = l, h \quad (6)$$

The main task of dual-energy subtraction imaging is to determine the mapping functions for glandular tissue thickness,  $t_b = f_b(D'_l, D'_h)$  and calcification thickness,  $t_c = f_c(D'_l, D'_h)$

from the measured functions (images)  $D'_l = F_l(t_b, t_c)$  and  $D'_h = F_h(t_b, t_c)$  i.e. to map the measured x-ray densities,  $D'_l$  and  $D'_h$ , into the glandular tissue and calcification thickness,  $t_b$  and  $t_c$ . Typically, the form of the mapping functions  $f_b$  and  $f_c$  can be determined by interpolation of calibration measurements. The mapping functions vary with  $\Phi_j(E)$ ,  $T$ ,  $A(E)$ , and  $Q(E)$ , hence the calibrations must be performed for different x-ray techniques, breast thickness, absorption ratios and detector response functions.

### 2.3 The Special Case of Mono-energetic X-ray Images

Since the x-ray spectra used in diagnostic imaging are poly-energetic, Eq. 6 cannot be solved analytically for  $t_b$  and  $t_c$ . The use of mono-energetic x-rays allows the inverse functions  $f_b$  and  $f_c$  to be analytically solved. We will therefore demonstrate the reduction of the three-material/energy imaging problem into to a dual-material/energy problem with the use of mono-energetic x-ray sources.

Recall that our model for the breast consists of adipose tissue of thickness  $t_a$ , glandular tissue of thickness  $t_b$ , and a  $\mu C$  of thickness  $t_c$  (Figure 1). If  $p_l^0$  and  $p_l$  are defined as the unattenuated and attenuated signals from the low-energy monoenergetic spectrum, and  $p_h^0$  and  $p_h$  are defined as the unattenuated and attenuated signals from the high-energy spectrum (Figure 1), the x-ray densities  $D_l$  and  $D_h$  defined in Eq. 4 can be expressed as:

$$\begin{aligned} D_l &\equiv \ln(p_l^0 / p_l) \\ &= \mu_{al}(T - t_b - t_c) + \mu_{bl}t_b + \mu_{cl}t_c \\ &= \mu_{al}T + (\mu_{bl} - \mu_{al})t_b + (\mu_{cl} - \mu_{al})t_c \end{aligned} \quad (7)$$

and

$$\begin{aligned}
D_h &\equiv \ln(p_h^0 / p_h) \\
&= \mu_{ah}(T - t_b - t_c) + \mu_{bh}t_b + \mu_{ch}t_c \\
&= \mu_{ah}T + (\mu_{bh} - \mu_{ah})t_b + (\mu_{ch} - \mu_{ah})t_c
\end{aligned} \tag{8}$$

where,  $\mu_{ij}$  ( $i = b, c$ ;  $j = l, h$ ) are the linear attenuation coefficients for glandular tissue ( $i=b$ ) and  $\mu C$  ( $i=c$ ), at low ( $j=l$ ) and high ( $j=h$ ) energies, respectively. Similarly, the modified x-ray densities,  $D'_l$  and  $D'_h$  defined in Eq. 5 can be expressed, using Eqs. 7 and 8, as follows:

$$D'_l \equiv \ln\left(\frac{p_l^a}{p_l}\right) = D_l - \ln\left(\frac{p_l^0}{p_l^a}\right) = \Delta\mu_{bl}t_b + \Delta\mu_{cl}t_c \tag{9}$$

and

$$D'_h \equiv \ln\left(\frac{p_h^a}{p_h}\right) = D_h - \ln\left(\frac{p_h^0}{p_h^a}\right) = \Delta\mu_{bh}t_b + \Delta\mu_{ch}t_c \tag{10}$$

where,  $\Delta\mu_{bj} = \mu_{bj} - \mu_{aj}$ ,  $\Delta\mu_c = \mu_{cj} - \mu_{aj}$ , and  $p_l^a$  and  $p_h^a$  are the low- and high-energy reference signals corresponding to attenuation by 100% adipose tissue. Rearrange Eqs. 9 and 10 into matrix form as follows:

$$\begin{pmatrix} D'_l \\ D'_h \end{pmatrix} = \begin{pmatrix} \Delta\mu_{bl} & \Delta\mu_{cl} \\ \Delta\mu_{bh} & \Delta\mu_{ch} \end{pmatrix} \begin{pmatrix} t_b \\ t_c \end{pmatrix} \tag{11}$$

Solving for  $t_b$  and  $t_c$  yields,

$$\begin{pmatrix} t_b \\ t_c \end{pmatrix} = \begin{pmatrix} \Delta\mu_{bl} & \Delta\mu_{cl} \\ \Delta\mu_{bh} & \Delta\mu_{ch} \end{pmatrix}^{-1} \begin{pmatrix} D'_l \\ D'_h \end{pmatrix} = \begin{pmatrix} k_{bl} & k_{bh} \\ k_{cl} & k_{ch} \end{pmatrix} \begin{pmatrix} D'_l \\ D'_h \end{pmatrix} \tag{12}$$

where,

$$k_{bl} = \frac{\Delta\mu_{ch}}{\Delta\mu_{bl}\Delta\mu_{ch} - \Delta\mu_{cl}\Delta\mu_{bh}} \tag{13}$$

$$k_{bh} = \frac{-\Delta\mu_{cl}}{\Delta\mu_{bl}\Delta\mu_{ch} - \Delta\mu_{cl}\Delta\mu_{bh}} \quad (14)$$

$$k_{cl} = \frac{-\Delta\mu_{bh}}{\Delta\mu_{bl}\Delta\mu_{ch} - \Delta\mu_{cl}\Delta\mu_{bh}} \quad (15)$$

and

$$k_{ch} = \frac{\Delta\mu_{bl}}{\Delta\mu_{bl}\Delta\mu_{ch} - \Delta\mu_{cl}\Delta\mu_{bh}} \quad (16)$$

The glandular tissue thickness ( $t_b$ ) and calcification thickness ( $t_c$ ) mapping functions,  $f_b$  and  $f_c$ , respectively, can now be analytically expressed as functions of the difference attenuation coefficients ( $\Delta\mu_{ij}$ ) and x-ray densities ( $D'_l$  and  $D'_h$ ) as follows:

$$t_b = f_b(D'_l, D'_h) = \frac{\Delta\mu_{ch}D'_l - \Delta\mu_{cl}D'_h}{\Delta\mu_{bl}\Delta\mu_{ch} - \Delta\mu_{cl}\Delta\mu_{bh}} \quad (17)$$

and

$$t_c = f_c(D'_l, D'_h) = \frac{\Delta\mu_{bl}D'_h - \Delta\mu_{bh}D'_l}{\Delta\mu_{bl}\Delta\mu_{ch} - \Delta\mu_{cl}\Delta\mu_{bh}} \quad (18)$$

## 2.4 Noise and SNR in Poly-energetic Images

The noise level in the x-ray densities  $D_l$  and  $D_h$  can be related to the SNR in the low-and high-energy raw images as follows:

$$\sigma_{D_l}^2 = \left( \frac{\partial D_l}{\partial S_l} \right)^2 \sigma_{S_l}^2 = \left( \frac{1}{S_l} \right)^2 \sigma_{S_l}^2 = \frac{1}{SNR_{S_l}^2} \quad (19)$$

and

$$\sigma_{D_h}^2 = \left( \frac{\partial D_h}{\partial S_h} \right)^2 \sigma_{S_h}^2 = \left( \frac{1}{S_h} \right)^2 \sigma_{S_h}^2 = \frac{1}{SNR_{S_h}^2} \quad (20)$$

In Eq. (3), the signal contribution from photons with an energy between  $E$  and  $E+dE$  is proportional to the number of detected photons in that interval [ $n(E)dE = dE \cdot R_j \cdot d^2 \cdot \Phi_j(E) \cdot e^{-\mu_a(E)T} \cdot e^{-\Delta\mu_b(E)t_b - \Delta\mu_c(E)t_c} \cdot A(E)$ ], multiplied by the signal generated by each absorbed x-ray photon (the gain factor =  $Q(E)$ ). Characteristic of the x-ray detection process,  $n(E)dE$ , is a stochastic quantity governed by Poisson statistics. Thus, the variance of the  $n(E)dE$  is equal to  $n(E)dE$  itself. Furthermore, since  $n(E)dE$  is typically large in diagnostic x-ray imaging, it can be assumed to fluctuate with a Gaussian distribution. Strictly speaking, the gain factor  $Q(E)$ , is also a stochastic quantity. However, its contribution to the signal variance can be ignored when the number of scintillating photons generated for each absorbed x-ray photon is reasonably large (e.g. CsI(Tl) scintillator yields ~50 optical photons per keV) i.e. when the gain fluctuations are small. Since the number of absorbed x-rays are subject to an average gain of  $Q(E)$ , the noise variance for the energy interval of  $E$  to  $E+dE$  can be approximated by  $n(E)dE \cdot Q^2(E)$ .<sup>5,6</sup> Summing the variances over all energy intervals, the total noise variances in the low- and high-energy image signals,  $\sigma_{s_j}^2$ ,  $j = l, h$ , can be expressed as:

$$\sigma_{s_j}^2 = \int dE \cdot R_j \cdot d^2 \cdot \Phi_j(E) \cdot e^{-\mu_a(E)T} \cdot e^{-\Delta\mu_b(E)t_b - \Delta\mu_c(E)t_c} \cdot A(E) \cdot Q^2(E) \quad (21)$$

The SNR in the low- and high-energy images can be expressed as follows:

$$SNR_{s_j} = \frac{\int dE \cdot R_j \cdot d^2 \cdot \Phi_j(E) \cdot e^{-\mu_a(E)T} \cdot e^{-\Delta\mu_b(E)t_b - \Delta\mu_c(E)t_c} \cdot A(E) \cdot Q(E)}{\left[ \int dE \cdot R_j \cdot d^2 \cdot \Phi_j(E) \cdot e^{-\mu_a(E)T} \cdot e^{-\Delta\mu_b(E)t_b - \Delta\mu_c(E)t_c} \cdot A(E) \cdot Q^2(E) \right]^{1/2}} \quad (22)$$

## 2.5 Noise and SNR in Subtracted Images

The variations of  $D'_l$  and  $D'_h$  can be expressed as follows:

$$dD'_j = \left( \frac{\partial D'_j}{\partial t_b} \right) dt_b + \left( \frac{\partial D'_j}{\partial t_c} \right) dt_c ; j = l, h \quad (23)$$

The variations  $dD'_l$  and  $dD'_h$  are linear combinations of the variations  $dt_b$  and  $dt_c$ . The parameters  $\partial D'_j / \partial t_i$  ( $i = b, c; j = l, h$ ) can be explicitly derived using Eq. 6 as:

$$\left( \frac{\partial D'_j}{\partial t_i} \right) = \left[ \frac{\int dE \cdot R_j \cdot d^2 \cdot \Phi_j(E) \cdot e^{-\mu_a(E)T} \cdot \Delta\mu_i(E) \cdot e^{-\Delta\mu_b(E)t_b - \Delta\mu_c(E)t_c} \cdot A(E) \cdot Q(E)}{\int dE \cdot R_j \cdot d^2 \cdot \Phi_j(E) \cdot e^{-\mu_a(E)T} \cdot e^{-\Delta\mu_b(E)t_b - \Delta\mu_c(E)t_c} \cdot A(E) \cdot Q(E)} \right] \quad (24)$$

Eq. 24 shows that  $\partial D'_j / \partial t_i$  can be interpreted as the  $\Delta\mu_{ij}(E)$  averaged over the detected energy spectrum, thus,  $\partial D'_j / \partial t_i$  can be represented as  $\overline{\Delta\mu_{ij}}$  ( $i = b, c; j = l, h$ ). The pair of equations described in Eq. 23 can be expressed in matrix form as:

$$\begin{pmatrix} dD'_l \\ dD'_h \end{pmatrix} = \begin{pmatrix} \overline{\Delta\mu_{bl}} & \overline{\Delta\mu_{cl}} \\ \overline{\Delta\mu_{bh}} & \overline{\Delta\mu_{ch}} \end{pmatrix} \begin{pmatrix} dt_b \\ dt_c \end{pmatrix} \quad (25)$$

The variations  $dt_b$  and  $dt_c$  can now be determined as follows:

$$\begin{pmatrix} dt_b \\ dt_c \end{pmatrix} = \begin{pmatrix} \overline{\Delta\mu_{bl}} & \overline{\Delta\mu_{cl}} \\ \overline{\Delta\mu_{bh}} & \overline{\Delta\mu_{ch}} \end{pmatrix}^{-1} \begin{pmatrix} dD'_l \\ dD'_h \end{pmatrix} = \begin{pmatrix} k_{bl} & k_{bh} \\ k_{cl} & k_{ch} \end{pmatrix} \begin{pmatrix} dD'_l \\ dD'_h \end{pmatrix} \quad (26)$$

where,

$$k_{bl} = \frac{\overline{\Delta\mu_{ch}}}{\overline{\Delta\mu_{bl}} \overline{\Delta\mu_{ch}} - \overline{\Delta\mu_{cl}} \overline{\Delta\mu_{bh}}} \quad (27)$$

$$k_{bh} = \frac{-\overline{\Delta\mu_{cl}}}{\overline{\Delta\mu_{bl}} \overline{\Delta\mu_{ch}} - \overline{\Delta\mu_{cl}} \overline{\Delta\mu_{bh}}} \quad (28)$$

$$k_{cl} = \frac{-\overline{\Delta\mu_{bh}}}{\overline{\Delta\mu_{bl}} \overline{\Delta\mu_{ch}} - \overline{\Delta\mu_{cl}} \overline{\Delta\mu_{bh}}} \quad (29)$$

and

$$k_{ch} = \frac{\overline{\Delta\mu_{bl}}}{\overline{\Delta\mu_{bl}\Delta\mu_{ch}} - \overline{\Delta\mu_{cl}\Delta\mu_{bh}}} \quad (30)$$

Recall that  $t_b = f_b(D'_l, D'_h)$ , hence  $dt_b = (\partial t_b / \partial D'_l) \cdot dD'_l + (\partial t_b / \partial D'_h) \cdot dD'_h$ . But from Eq. 26,  $(\partial t_b / \partial D'_l) = k_{bl}$  and  $(\partial t_b / \partial D'_h) = k_{bh}$ , therefore, the variance of  $t_b$ ,  $\sigma_{t_b}^2$  can be expressed as:

$$\sigma_{t_b}^2 = (\partial t_b / \partial D'_l)^2 \cdot \sigma_{D'_l}^2 + (\partial t_b / \partial D'_h)^2 \cdot \sigma_{D'_h}^2 = k_{bl}^2 \cdot \sigma_{D'_l}^2 + k_{bh}^2 \cdot \sigma_{D'_h}^2 \quad (31)$$

Similarly, the variance of  $t_c$ ,  $\sigma_{t_c}^2$  can be expressed as:

$$\sigma_{t_c}^2 = (\partial t_c / \partial D'_l)^2 \cdot \sigma_{D'_l}^2 + (\partial t_c / \partial D'_h)^2 \cdot \sigma_{D'_h}^2 = k_{cl}^2 \cdot \sigma_{D'_l}^2 + k_{ch}^2 \cdot \sigma_{D'_h}^2 \quad (32)$$

The terms  $\sigma_{t_b}$  and  $\sigma_{t_c}$  represent noise levels in the glandular tissue and calcification subtraction images, respectively. Using Eqs. 19 and 20, Eqs. 31 and 32 can be rewritten as follows:

$$\sigma_{t_b}^2 = \frac{k_{bl}^2}{SNR_{S_l}^2} + \frac{k_{bh}^2}{SNR_{S_h}^2} \quad (33)$$

and

$$\sigma_{t_c}^2 = \frac{k_{cl}^2}{SNR_{S_l}^2} + \frac{k_{ch}^2}{SNR_{S_h}^2} \quad (34)$$

The *SNR* of the subtraction signals,  $t_b$  and  $t_c$ , can then be expressed as the follows:

$$SNR_{t_i} = \frac{t_i}{\sqrt{\frac{k_{il}^2}{SNR_{S_l}^2} + \frac{k_{ih}^2}{SNR_{S_h}^2}}}; i=b,c \quad (35)$$

Notice that in the  $\mu\text{C}$  subtraction images ( $t_c$ ) the adipose tissue structures is cancelled out providing a uniform background signal fluctuation around zero. Thus, the signal-to-noise ratio of the  $\mu\text{C}$  in the subtraction image ( $SNR_c$ ) is the same as its CNR.

Since  $SNR_{s_{t,h}}$  is proportional to  $d$  [Eq. 22] and  $SNR_{b,c}$  is proportional to  $SNR_{s_{t,h}}$  [Eq. 35],  $SNR_{b,c}$  is also proportional to  $d$ . This results from the fact that the variance of quantum (Poisson) noise fluctuations in the raw (unsubtracted) images is proportional to the number of photons incident on the image pixel [Eq. 21]. This seems to imply that systems with larger pixel sizes are more advantageous. However, it is important to note that the detectability of an object ( $\mu\text{C}$ ) is directly proportional to the  $SNR^2$  per pixel summed over all pixels in the object ( $\mu\text{C}$ ) area rather than in just one pixel [REFERENCE]. Assuming that the  $SNR^2$  (equal to  $CNR^2$  in  $\mu\text{C}$  subtraction image) is uniform over the object area, the sum of  $SNR^2$  over the object area is equivalent to replacing the pixel area ( $d^2$ ) with the projected object ( $\mu\text{C}$ ) area in Eq. 22. For simplicity, the shape of the  $\mu\text{Cs}$  was assumed to be cubic with a dimension of  $t_c$ . This leads to uniform CNRs but still reflects the fact that smaller calcifications are also lower in contrast due to shorter attenuating thickness. Thus, the pixel area  $d^2$  was replaced by  $t_c^2$  in all numerical computations in this study. This allows the computed CNRs to be directly used to access and compare the detectability of  $\mu\text{Cs}$ .

During the x-ray detection process, only part of the x-ray energy is converted into fluorescent light in the x-ray scintillator. Although the ratio of x-ray photon energy that is converted to optical light varies slightly with energy, to a good approximation we can assume that this ratio is constant in the diagnostic energy range (10–120 keV). Thus, in

our calculations the scintillator gain  $Q(E)$  is modeled as being proportional to  $E$ , i.e.  $Q(E) = \alpha E$ .

## 2.6 Calcification Contrast-to-Noise and Contrast-to-Background Ratio

A problem in detecting  $\mu$ Cs in mammograms are the presence of cluttered tissue structure in the image which constitutes a noise component of a different nature and form than quantum noise. This is referred to as the “tissue structure noise” in the rest of the manuscript. The tissue structure noise is intrinsically different from quantum noise which is random and hence results in Poisson signal distribution. Quantum noise tends to decrease in size relative to the signal as the exposure level increases, thus potentially improving the detectability of the  $\mu$ Cs if no cluttered tissue structure is present in the background. However, the level of tissue structure noise is independent of the exposure level and cannot be improved by increased exposure. (Tissue structure noise represents the limitation for detecting and visualizing microcalcification in single-energy imaging techniques).

While the level of random noise can be quantified by the standard deviation of the fluctuations in a region of uniform exposure; the level of tissue structure noise cannot be easily quantified since the degree of obscurity varies greatly with the pattern of the tissue structure and its relative position with respect to the  $\mu$ C. Despite these differences, it may be instructive to use the range of signal or contrast variations due to tissue structure to represent the level of tissue structure noise, and compute an image quality referred to as the calcification contrast-to-background ratios (*CCBRs*). In analogy to the calcification contrast-to-noise ratio (*CCNRs*), the *CCBRs* are computed as the ratio of calcification contrast to the signal range or contrast of the background tissue structure.

Assuming that for a breast of thickness  $T$ , the background area consists of 50% adipose and 50% glandular tissue. The background signal,  $S_B$  can be computed using Eq. 2 as:

$$S_B = \int dE \cdot R \cdot t_c^2 \cdot \Phi(E) \cdot e^{(-0.5\mu_a(E)-0.5\mu_b(E))T} \cdot A(E) \cdot Q(E) \quad (36)$$

The noise in  $S_B$  can be computed using Eq. 21 as:

$$\sigma = \left[ \int dE \cdot R \cdot t_c^2 \cdot \Phi(E) \cdot e^{(-0.5\mu_a(E)-0.5\mu_b(E))T} \cdot A(E) \cdot Q^2(E) \right]^{\frac{1}{2}} \quad (37)$$

Now assume that within the breast the tissue composition varied between 50% adipose and 50% glandular to 25% adipose and 75% glandular. The signal for a breast of thickness  $T$ , from a representative tissue region consists of 25% adipose and 75% glandular tissue,  $S_T$  can then be expressed as:

$$S_T = \int dE \cdot R \cdot t_c^2 \cdot \Phi(E) \cdot e^{-(0.25\mu_a(E)+0.75\mu_b(E))T} \cdot A(E) \cdot Q(E) \quad (38)$$

Thus, the signal range or contrast of the tissue structure due to tissue composition variation can be computed as  $TC = S_B - S_T$ , which corresponds to the image signal varying between  $S_B$  and  $S_T$ . This can be used to represent the “tissue structure noise” for the above describe tissue structure.

Assuming that a  $\mu C$  replaces a cubic volume of 50% adipose and 50% glandular background tissue with a dimension of  $t_c$ , the image signal over the  $\mu C$  can be computed as:

$$S_C = \int dE \cdot R \cdot t_c^2 \cdot \Phi(E) \cdot e^{-(0.5\mu_a(E)+0.5\mu_b(E))(T-t_c)-\mu_c(E)t_c} \cdot A(E) \cdot Q(E) \quad (39)$$

The difference signal for this  $\mu C$  can then be computed as  $CC = S_B - S_C$ . From our earlier definitions, the calcification contrast-to-noise ratio  $CCNR = CC/\sigma$  and the calcification contrast-to-background ratio  $CCBR = CC/TC$ . The range of tissue

composition between 50% adipose and 50% glandular to 25% adipose and 75% glandular tissue compositions used in this discussion was arbitrarily chosen, since only the general behaviors of CCNR and CCBR were studied.

### 3. MATERIALS AND METHODS

In order to compute the calcification SNR in the subtraction images (Eq. 35), it is necessary to compute the coefficients,  $k_{ij}$  (Eqs. 27–30) and the SNR for low- and high-energy images,  $SNR_{S_j}$  (Eq. 22). However, in order to use these equations, imaging parameters must be selected to simulate clinical imaging conditions; the x-ray spectra, attenuation coefficients and detector absorption ratios must be determined from published data for the energy range studied. The methods for these tasks will be described and discussed in the following sections.

#### 3.1 X-ray Photon Spectra

In this study, both mammographic and general radiographic x-ray spectra were used. Published mammographic x-ray spectra<sup>7</sup> used are for a molybdenum target and a 30  $\mu\text{m}$  molybdenum filter (Mo/Mo) at 25, 30, 35, 40, 45 and 50 kVp; and for a tungsten target and lanthanum filter (W/La) at 50 kVp. The mammographic spectra were used in computations for both single- and dual-energy imaging. Published general radiography x-ray spectra<sup>8</sup> used are for a tungsten target with a 2.0 mm aluminum filter for 50–90 kVp, and a tungsten target with a 0.25 mm copper filter for 100–140 kVp. The radiographic spectra were used in computations for single-energy imaging only. All published spectra data were normalized and converted into the photon fluence spectrum ( $\Phi(E)$ ) with units of [photons per mR per  $\text{mm}^2$ ] at unit energy [keV] intervals.

#### 3.2 Photon Absorption Ratio for Scintillating

Scintillators (e.g. cesium iodide, sodium iodide) are commonly used as x-ray converters in the design of radiographic systems. Although x-ray detectors using photoconductor materials (e.g. selenium) have been developed and commercialized, most

digital mammographic systems still rely on scintillators as x-ray converters. The detection of x-ray signal in a scintillator-based detector consists of two separate processes: (1) conversion of x-ray energy into optical (scintillation) light using a scintillator; and (2) conversion of optical light into charge (via photoelectric effect) that after integration generates the electronic signal (e.g. charge-coupled device (CCD), amorphous silicon (aSi:H) flat panel detector). In this paper, we consider two scintillators commonly used in digital mammography systems; namely, terbium doped gadolinium oxysulfide ( $Gd_2O_2S:Tb$ ) and thallium doped cesium iodide ( $CsI:Tl$ ). Usually, the former is used with CCD based detectors while the latter is used with aSi:H flat panel detectors. The densities of  $Gd_2O_2S:Tb$  and  $CsI:Tl$  are  $7.34 \text{ g/cm}^3$  and  $4.51 \text{ g/cm}^3$ , respectively. Scintillator thickness of  $46 \text{ }\mu\text{m}$  ( $=34 \text{ mg/cm}^2$ ) for  $Gd_2O_2S:Tb$  and  $100 \text{ }\mu\text{m}$  ( $=45 \text{ mg/cm}^2$ ) for  $CsI:Tl$  were used in this numerical study. The  $Gd_2O_2S:Tb$  thickness ( $34 \text{ mg/cm}^2$ ) used are similar to those of Lanex Fine screens whereas the  $CsI:Tl$  thickness ( $45 \text{ mg/cm}^2$ ) approximate commercially available flat-panel mammography systems.

The x-ray absorption ratios,  $A(E)$  were calculated for photon energies between 10 keV and 140 keV at a resolution of 1 keV, using linear-attenuation coefficients interpolated from published data<sup>10</sup> as follows:

$$A(E) = 1 - e^{-\mu_s(E)t_s} \quad (40)$$

where,  $\mu_s(E)$  and  $t_s$  are the energy-dependent linear attenuation coefficient (in  $1/\text{cm}$ ) and thickness (cm) of the scintillator under consideration. Since the doping materials (Tb or Tl) are present only in very small amounts, their presence was neglected in calculations of the attenuation coefficients.

### 3.3 Detectors X-ray Attenuation Coefficients

The elemental compositions of adipose and glandular breast tissue,<sup>9</sup> the  $\mu\text{Cs}$  ( $\text{CaCO}_3$ ), and the scintillators ( $\text{Gd}_2\text{O}_2\text{S:Tb}$  and  $\text{CsI:Tl}$ ) were used to calculate the mass-attenuation coefficients ( $\mu/\rho$ ) for the composite materials using published data from NIST.<sup>10</sup> Since the published attenuation coefficients are provided only for a limited number of discrete photon energies, a log-linear interpolation was used to compute the coefficients for intermediate energies at 1 keV intervals. The interpolation was performed using the following exponential model relating the coefficient to the photon energy:

$$\left(\frac{\mu}{\rho}\right) = \kappa \cdot E^\beta. \quad (41)$$

Taking the logarithms, Eq. 41 can be converted into a linear equation as follows:

$$\ln\left(\frac{\mu}{\rho}\right) = \ln \kappa + \beta \ln E. \quad (41b)$$

Using the published attenuation coefficients,  $(\mu/\rho)_1$  and  $(\mu/\rho)_2$  at two known consecutive energies of  $E_1$  and  $E_2$ , the linear coefficients ( $\ln \kappa$  and  $\beta$ ) valid for energies between  $E_1$  and  $E_2$  were determined as follows:

$$\beta = \frac{\ln\left(\frac{\mu}{\rho}\right)_2 - \ln\left(\frac{\mu}{\rho}\right)_1}{\ln E_2 - \ln E_1} \quad (42)$$

and

$$\ln \kappa = \frac{\ln\left(\frac{\mu}{\rho}\right)_1 \cdot \ln E_2 - \ln\left(\frac{\mu}{\rho}\right)_2 \cdot \ln E_1}{\ln E_2 - \ln E_1}. \quad (43)$$

Substituting the  $\ln\kappa$  and  $\beta$  values from above in Eq. 41,  $(\mu/\rho)$  was computed for intermediate energies between  $E_1$  and  $E_2$  at 1 keV resolution. The interpolated mass-attenuation coefficient values  $(\mu/\rho)$  were then multiplied by the density  $(\rho)$  of the appropriate material to obtain the linear-attenuation coefficients  $(\mu)$ , which were used in the numerical study. The density  $(\rho)$  values used for each material are given in Table 1.

### 3.4 X-ray Exposure Considerations

The entrance exposure for a typical mammogram is about 1000–1200 mR. In dual-energy imaging the total patient exposure is the sum of the individual low- and high-energy exposures. To maintain a fixed exposure risk to the patient while comparing the dual-energy technique with the single-energy technique, the total exposure (unattenuated at the input of the detector) of dual-energy image acquisition was kept at 1000 mR. The optimal distribution of the exposure between the low and high energy was studied by computing the noise levels in the subtraction image signals as a function of the “low-energy exposure ratio”, defined as the ratio of the low-energy exposure to the total exposure.

### 3.5 Noise Level in the Image Signals

A key indicator of image quality is the image noise level. The noise level in the dual-energy subtracted  $\mu\text{C}$  signal,  $\sigma_{t_c}$  was calculated for various low- and high-energy spectral combinations, breast thicknesses, tissue compositions, microcalcification sizes, and low-energy exposure ratios. The breast thickness was varied from 3.5 to 7 cm; the tissue composition varied from 100%adipose-and-0%glandular (100%/0% adipose/glandular) to 0%adipose-and-100%glandular (0%/100% adipose/glandular); the

low-energy exposure ratio varied from 0 to 1 while keeping the total unattenuated exposure at the detector fixed at 1000 mR.

For a given combination of compressed breast thickness, tissue composition, calcification size, and low- and high-energy input spectra, the signals ( $S_l$  and  $S_h$ ) and their associated noise levels for unsubtracted images were calculated using Eqs. 3 and 21, respectively. The average difference-attenuation coefficients,  $\overline{\Delta\mu_{ij}}$  were determined using Eq. 24 and used with Eqs. 27–30 to compute the  $k_{ij}$  values of the inverse matrix in Eq. 26. The resulting  $k_{ij}$  values together with the SNR values from Eq. 22 were then used to calculate the noise levels in the  $\mu\text{C}$  subtraction signals ( $\sigma_{t_c}$ ) using Eq. 34. In order to study the noise fluctuations in the glandular tissue thickness signals, Eq. 33 can be used to compute  $\sigma_{t_b}$ , which may be used to measure tissue compositions. However, such computations were not part of this study.

Step I. Assume a compressed breast thickness of 5 cm, tissue composition of 50%/50% adipose/glandular, and low/high energy input spectra at 25/50 kVp. The noise level in the dual-energy subtracted  $\mu\text{C}$  signal,  $\sigma_{t_c}$  was computed as a function of the low-energy exposure ratio to determine the minimum  $\mu\text{C}$  sizes that would yield an acceptable SNR (3 or higher).

Step II. For a 5 cm thick breast, 50%/50% adipose/glandular tissue composition (as above), and assuming a  $\mu\text{C}$  size of 250  $\mu\text{m}$  (minimum  $\mu\text{C}$  size yielding a  $\text{SNR} \geq 3$  from Step I), the high energy spectrum was varied from 30 to 50 kVp while keeping the low energy spectrum fixed at 25 kVp. The noise  $\sigma_{t_c}$  was computed as a function of the

low-energy exposure ratio for various kVp combinations to determine the optimal energy separation.

Step III. For a 5 cm thick breast, 250  $\mu\text{m}$   $\mu\text{C}$  size, and optimal energy separation of 25/50 kVp (from Step II), the tissue composition was varied from 100%/0% adipose/glandular to 0%/100% adipose/glandular. The noise  $\sigma_{t_c}$  was computed as a function of the low-energy exposure ratio for various tissue compositions.

Step IV. Finally, using the optimal energy separation of 25/50 kVp, 250  $\mu\text{m}$   $\mu\text{C}$  size, and 50%/50% adipose/glandular tissue composition, the compressed breast thickness was varied from 3.5 to 7 cm. The noise  $\sigma_{t_c}$  was computed as a function of the low-energy exposure ratio for various compressed breast thickness.

The optimal exposure ratio was determined as the ratio with which  $\sigma_{t_c}$  was at a minimum. The low-energy exposure ratio ranged from a 0.01 to 0.95. The variations of the optimal low-energy exposure ratio with various imaging factors were studied.

## 4. RESULTS AND DISCUSSION

### 4.1 Photon Absorption Ratios

The x-ray absorption ratios (see Section 3.3) for a 46  $\mu\text{m}$  thick  $\text{Gd}_2\text{O}_2\text{S:Tb}$  scintillator (GdOS) and a 100  $\mu\text{m}$  thick CsI:Tl (CsI) scintillator are shown in Figure 2. The curves are very similar from 10 to  $\sim 33$  keV. The K-edges of CsI are at 33.2 and 36 keV, above which the absorption ratio increases significantly and exceeds that of GdOS. The higher absorption ratio for the CsI scintillator at energies above 33 keV, results in a higher image SNR ( $SNR_{s,i}$ ) and thus a decrease in the  $\sigma_{t_c}$  when compared with images acquired using GdOS. This results in higher overall detection efficiency for CsI than that for GdOS for x-rays generated with a kVp above the CsI K-edge energies.

### 4.2 X-ray Source Spectra

The x-ray source spectra (see Section 3.1), computed for 25 kVp Mo/Mo, 50 kVp Mo/Mo, and 50 kVp W/La target/filter combinations, attenuated by 5 cm thick breast with 50%/50% adipose/glandular tissue composition, are plotted in Figures 3, 4, and 5, respectively. The total counts in the computed spectra are normalized to unity for comparing the spectral shapes. Figures 3–5 illustrate the spectral differences between the low- and high-energy x-ray spectra. The K-edges of the CsI at 33.2 and 36 keV improves its detection efficiency for x-rays generated at kVp values that are higher than the K-edges. This would not be an advantage for x-ray spectra used in regular (single-energy) digital mammography procedures, since these x-rays are typically generated at kVp values lower than the CsI K-edge energies. However, the greater detector efficiency of CsI at higher energies is a significant improvement for dual-energy subtraction imaging

since CsI yields a higher detector efficiency for the high-energy spectrum used in dual-energy imaging.

Figures 3 and 4 clearly show the characteristic x-ray lines of Mo at 17.4 and 19.8 keV. Since the absorption ratio for the two scintillators are similar below  $\sim 33$  keV (Figure 2), the detected signal spectra for 25 kVp Mo/Mo should be similar for both scintillators, as indicated by Figure 3. The bremsstrahlung emission above 20 keV in the 50 kVp Mo/Mo spectrum is seen in Figure 4. The CsI spectrum shows an increase above its K-edge energies. The drop around 39 keV in the 50 kVp W/La spectra (Figure 5) is due to K-edge absorption by the La filter. Combining the increased K-edge absorption by CsI scintillator and the La filter attenuation at the source, a more peaked spectrum is generated, leading to better energy separation for dual energy subtraction imaging.

#### 4.3 CCNR and CBNR in the Unsubtracted Images

As described in Section 3.6, *CCNR* and *CCBR* were calculated using 50%/50% adipose/glandular composition as the signal background and its difference from 25%/75% adipose/glandular composition as the signal level of cluttered tissue structure in a 5 cm thick breast. The calcification contrast signal was computed for a size  $\mu\text{C}$  of 250  $\mu\text{m}$ . The resulting *CCNR* and *CCBR* are plotted in Figure 6 as a function of the x-ray spectrum from 25 to 140 kVp.

The *CCBRs* were found to be significantly lower than the *CCNRs*, indicating that in single energy imaging, the detection of  $\mu\text{Cs}$  can be obscured (difficult to visualize) by the presence of tissue structures even though the *CCNRs* may be sufficiently high for detection over a uniform background. In dual-energy subtraction imaging, the tissue structures are cancelled out, or at least significantly reduced, leading to a much higher

value for the *CCBR*. The benefit of dual-energy imaging is to eliminate or greatly reduce the background tissue structures so that they do not obscure and limit the detection and visualization of  $\mu\text{Cs}$ . However, the drawback of dual-energy subtraction technique is a decrease of *CCNR* due to noise increase from subtraction processes as discussed in Section 2.5. One major task in designing and testing the dual-energy subtraction imaging technique is to ensure that the *CCNR* in the subtracted  $\mu\text{C}$  images are sufficiently high for detecting the  $\mu\text{Cs}$ .

As kVp increased, both the *CCNR* and *CCBR* gradually decreased. The steady decrease of *CCNR* and *CCBR* indicates that even though use of a higher kVp x-rays tends to reduce the background tissue structure, it also causes the calcification contrast to decrease; resulting in only a slight decrease of the *CCBR* with kVp. The sudden drop of *CCNR* at 50 kVp (Figure 6) is due to the change of target/filter combination from Mo/Mo to W/Al at 50 kVp.

#### **4.4 Noise Level in the Microcalcification Images**

##### **Impact of Microcalcification Size**

The noise in the  $\mu\text{C}$  image,  $\sigma_{t_c}$  was calculated for various  $\mu\text{C}$  sizes (100–300  $\mu\text{m}$ ) using 25 and 50 kVp (Mo/Mo), and assuming a 50%/50% adipose/glandular tissue composition and a breast thickness of 5 cm, as a function of the low-energy exposure ratio. The results are plotted for GdOS and CsI scintillators in Figures 7 and 8, respectively. The plots indicate that a  $\mu\text{C}$  size of 250  $\mu\text{m}$  produces an object CNR of approximately 3:1 and 2:1 with the CsI and GdOS scintillators, respectively. The use of CsI scintillator resulted in a lower  $\sigma_{t_c}$  for all  $\mu\text{C}$  sizes. This can be attributed to its higher x-ray absorption ratio (Figure 2).

Thus, a 250  $\mu\text{m}$   $\mu\text{C}$  size was used in all subsequent computations as it may be considered as the minimum detectable  $\mu\text{C}$  size in dual-energy imaging. Furthermore, a 250  $\mu\text{m}$  calcification is on the lower side of the  $\mu\text{C}$  sizes that are routinely detected in mammography.

### **Impact of Spectral Energy Separation**

Using a 250  $\mu\text{m}$   $\mu\text{C}$  size, the  $\mu\text{C}$  image noise,  $\sigma_{t_c}$  was computed for various kVp combinations: low-energy spectrum fixed at 25 kVp (Mo/Mo) and high-energy spectra at 30, 35, 40, 45 and 50 kVp (Mo/Mo). At 50 kVp, the W/La target/filter combination was also used. In Figures 9, the  $\mu\text{C}$  image noise ( $\sigma_{t_c}$ ) is plotted, as a function of the low-energy exposure ratio, for various kVp combinations for the CsI scintillator. The plots show that as the energy separation widened, the  $\mu\text{C}$  image noise decreased. Similar results were observed for the GdOS scintillator, but with slightly higher noise levels due to lower x-ray absorption in the GdOS scintillator.

The combination of 25 kVp (Mo/Mo) and 50 kVp (W/La) x-ray spectra, labeled 25-50 Mo/W in Figure 9, resulted in the lowest  $\sigma_{t_c}$ . Spectra with kVp values greater than 50 were not studied, since the kVp values for most mammography units are limited to 50 kVp or less.

### **Impact of Breast Thickness**

In Figure 11, the  $\mu\text{C}$  image noise,  $\sigma_{t_c}$  is plotted, as a function of the low-energy exposure ratio, for compressed breast thickness ranging from 3.5–7 cm for the CsI scintillator. The  $\sigma_{t_c}$  increased as the thickness of the breast increased, it varied by a factor of  $\sim 2$  over the range of breast thickness considered.

As the breast thickness increases, the x-ray photons have to travel through more attenuating material resulting in more low-energy x-ray photons being attenuated. This attenuation increases the average photon energy used to measure the total x-ray exposure, leading to a decrease in the number of incident photons. With fewer incident photons detected in the unsubtracted image for the same exposure, the  $\mu\text{C}$  image noise increases. Similar results were observed for the GdOS scintillator, but with slightly higher noise levels due to lower x-ray absorption in the GdOS scintillator.

### **Impact of Tissue Composition**

In Figure 10, the  $\mu\text{C}$  image noise,  $\sigma_{t_c}$  is plotted, as a function of the low-energy exposure ratio, for an adipose tissue ratio ranging from 0% to 100%, using CsI as the scintillator. As expected, a higher adipose tissue content results in a lower  $\sigma_{t_c}$  and a higher glandular tissue content results in a higher  $\sigma_{t_c}$ . The  $\mu\text{C}$  image noise,  $\sigma_{t_c}$  varies by as much as ~50% as the composition varies from 100% adipose to 100% glandular.

The density of glandular tissue ( $1.04 \text{ g/cm}^3$ ) is greater than the density for adipose tissue ( $0.93 \text{ g/cm}^3$ ). Hence, for a fixed breast thickness, as the glandular tissue content of the breast increases, the breast density increases and additional low-energy x-ray photons are attenuated. As discussed in the impact of breast thickness, additional attenuation decreases the number of incident photons and hence leads to an increase in the  $\mu\text{C}$  image noise for the same exposure. Similar results were observed for the GdOS scintillator, but with slightly higher noise levels due to lower x-ray absorption in the GdOS scintillator.

#### 4.5 Optimal Low-energy Exposure Ratio

The optimal low-energy exposure ratios are those which minimize the  $\mu\text{C}$  image noise,  $\sigma_c$ . The ratio may be a function of the  $\mu\text{C}$  size, low/high energy spectral combination, tissue composition, and thickness. The optimal low-energy exposure ratio can be determined from the plots in Figures 8–11.

The optimal range of low-energy exposure ratio is defined as the range corresponding to a 10% change of the minimum  $\sigma_c$  value. The optimal range varied with tissue composition from 0.27–0.68 for 0% adipose to 0.19–0.61 for 100% adipose. The optimal range varied with compressed breast thickness from 0.19–0.61 for a 3.5 cm breast to 0.29–0.71 for a 7 cm breast, assuming a 50%/50% adipose/glandular tissue composition for 5cm thick breast. Finally, the optimal range varied with  $\mu\text{C}$  size from 0.21–0.62 for a 100  $\mu\text{m}$   $\mu\text{C}$  to 0.22–0.65 for a 300  $\mu\text{m}$   $\mu\text{C}$ , again assuming a 50%/50% adipose/glandular tissue composition for 5cm thick breast. Based on the overlapping of these ranges, we conclude that for low-energy exposure ratios between 0.29 and 0.61, the estimated  $\mu\text{C}$  image noise levels are within 10% of the optimized values for various tissue composition, breast thickness, and  $\mu\text{C}$  size.

This leads to an important consideration for practical implementation: the exposure can be distributed in a universal manner between the low- and high-energy image over the entire breast, with calcification image noise within 10% of the minimum values. This would also apply for various breast thicknesses. The low/high energy spectral distribution can be varied (from 30%/70% to 40%/60%) without significantly effecting the results. This greatly simplifies the practical implementation of dual-energy

calcification imaging technique. This observation is also self evident from the (flat) shapes of the curves in Figures 8–11.

#### 4.6 Dosimetric Considerations

Another consideration in dual-energy subtraction imaging for mammography is the total mid-glandular tissue dose. If we assume a 5 cm thick, 50%/50% adipose/glandular tissue, the exposure-to-dose conversion factors can be determined from published data for determining the mid-glandular tissue dose.<sup>11</sup> By extrapolating the data, it was determined that using a 50 kVp spectrum would increase the conversion factor by a factor of 1.5 as compared to using a 25 kVp spectrum. This would effectively increase the total mid-glandular tissue dose in dual-energy image acquisition when the total detector exposure (entrance skin exposure) is kept at the level of a regular mammographic image. For example, a 1000 mR exposure (the skin entrance exposure computed from the unattenuated detector exposure via inverse square law) split evenly between the 25 and 50 kVp exposures results in a total mid-glandular tissue dose of ~155 mrad; whereas the same 1000 mR exposure made at 25 kVp results in a dose of only ~123 mrad. Therefore, for the dual-energy case, there is an overall increase in the mid-glandular tissue dose by a factor of 1.25. Thus, in order to compensate for this increase in dose, the total exposure in 25/50 kVp dual-energy imaging would need to be reduced to approximately 80% of the initial exposure, i.e. 800 mR, to keep the mid-glandular dose the same for comparison. The implications are an approximately 10% increase in all noise levels computed including those for the  $\mu\text{C}$  signal,  $\sigma_{t_c}$ . Similar but lower noise increase should be observed for other low/high kVp combinations used in this study since the differences in conversion factors will be smaller. Thus, the noise increase from

normalization to a fixed mid-glandular dose is small and should not significantly affect the results or conclusions of this study based on a fixed total detector exposure of 1000 mR.

## 5. CONCLUSION/SUMMARY

The CsI:Tl scintillator has a higher absorption ratio than Gd<sub>2</sub>O<sub>2</sub>S:Tb at energies greater than ~33 keV (Figure 2) due to its K-edges at 33.2 keV and 36 keV. Since more photons are detected for a given exposure by CsI, the calcification images with CsI scintillator have lower noise (higher SNR) compared with GdOS. A  $\mu$ C size of 250  $\mu$ m yielded an object CNR of approximately 3:1 with the CsI scintillator and approximately 2:1 with the GdOS scintillator (Figures 7 and 8). Hence, CsI is better suited for dual-energy subtraction mammography than the GdOS scintillator.

The *CCNR* and *CCBR* were calculated for energies ranging from 25–140 keV (Figure 6) which showed that there is not an advantage in using higher energies (>50 keV) for dual-energy subtraction mammography because as the energy increases, both the *CCNR* and the *CCBR* decrease. The limitation of the  $\mu$ C visibility due to the *CCBR* can be eliminated by performing dual-energy subtraction.

It was also shown that as the calcification image noise,  $\sigma_t$ , decreased as the spectral energy separation increased (Figure 9). Using 25 kVp Mo/Mo as the low-energy and 50 kVp W/La as the high-energy spectra resulted in the lowest noise. Although Mo/Rh (rhodium) dual-target tubes are available, a Mo/W dual-target tube is not currently available; such a tube could provide an advantage for implementation of dual-energy digital mammography.

Simulations were also done with varying tissue compositions (Figure 10) and total breast thickness (Figure 11). As expected, the noise,  $\sigma_t$ , increased as the attenuation in the breast increased as a result of a higher glandular tissue content or thicker breast. It was also determined that evenly splitting the exposure between the low- and high-energy

images would be sufficient to keep the noise,  $\sigma_t$ , within 10% of the minimum. The low/high kVp exposure can be varied from 30%/70% to 40%/60% without significantly effecting the image quality. This greatly simplifies the practical implementation of dual-energy calcification imaging technique.

## **6. Acknowledgment**

This work was supported by a research grant DAMD17-00-1-0316 by the US Department of the Army and by a research grant by the Mike Hogg Foundation.

## LIST OF TABLES

**Table1.** Table showing the materials and their densities used in the simulation studies. 38

## LIST OF FIGURES

- Figure 1.** A compressed breast of thickness  $T$ , showing the  $\mu\text{C}$  of thickness,  $t_c$  and the adipose and glandular tissue of thickness  $t_a+t_b = a+b$ ..... 39
- Figure 2.** Plot showing the absorption ratios for a 46  $\mu\text{m}$  thick  $\text{Gd}_2\text{O}_2\text{S:Tb}$  scintillator and a 100  $\mu\text{m}$  thick  $\text{CsI:Tl}$  scintillator. The K-edges of  $\text{CsI:Tl}$  scintillator are seen at 33.2 and 36 keV resulting in a higher absorption ratio. The K-edge for  $\text{GdOS}$  lies at 50.2 keV (just out of the plotted energy range)..... 40
- Figure 3.** Plots showing the computed 25 kVp Mo/Mo x-ray spectrum for the  $\text{Gd}_2\text{O}_2\text{S:Tb}$  and  $\text{CsI:Tl}$  scintillators. The characteristic x-ray lines of Mo are seen at 17.4 and 19.8 keV. The total counts in the individual spectra are normalized to unity. The spectra for both scintillators are identical because their absorption ratios are similar upto the CsI K-edge near 33 keV. .... 41
- Figure 4.** Plots showing the computed 50 kVp Mo/Mo x-ray spectrum for the  $\text{Gd}_2\text{O}_2\text{S:Tb}$  and  $\text{CsI:Tl}$  scintillators. The total counts in the individual spectra are normalized to unity. The bremsstrahlung emission is seen above 20 keV, besides the characteristic x-ray lines of Mo below 20 keV. The bump-like structure seen in the CsI spectrum around 35 keV is due to its higher absorption ratio. .... 42
- Figure 5.** Plots showing the computed 50 kVp W/La x-ray spectrum for the  $\text{Gd}_2\text{O}_2\text{S:Tb}$  and  $\text{CsI:Tl}$  scintillators. The total counts in the individual spectra are normalized to unity. The drop around 39 keV is due to K-edge absorption by the La filter. Combining the increased K-edge absorption by CsI scintillator and the La filter attenuation at the source, a more peaked spectrum is generated..... 43
- Figure 6.** The plots of the calcification contrast-to-noise ratio,  $CCNR$  and the calcification background-to-noise ratio,  $CCBR$  for energies ranging from 25 to 140 kVp. Target/filter combinations of Mo/Mo, W/Al, and W/Cu was used between 25–50, 50–90, and 90–140 kVp respectively. The Mo and W represent spectra generated with a molybdenum and tungsten target, respectively. Note that the 50 kVp calculations were performed with both the Mo and the W targets..... 44
- Figure 7.** Plots of the calcification image noise,  $\sigma_{t_c}$  as a function of the low-energy exposure ratio for various  $\mu\text{C}$  sizes using the  $\text{Gd}_2\text{O}_2\text{S:Tb}$  scintillator; assuming a 5 cm thick breast of 50%/50% adipose/glandular tissue and 25/50 (Mo/Mo) low-/high-kVp spectra..... 45
- Figure 8.** Plots of the calcification image noise,  $\sigma_{t_c}$  as a function of the low-energy exposure ratio for various  $\mu\text{C}$  sizes using the  $\text{CsI:Tl}$  scintillator; assuming a 5 cm thick breast of 50%/50% adipose/glandular tissue and 25/50 (Mo/Mo) low-/high-kVp spectra..... 46
- Figure 9.** Plots of calcification image noise,  $\sigma_{t_c}$  as a function of the low-energy exposure ratio for various combinations of energy spectra using the  $\text{CsI:Tl}$  scintillator; assuming a 5 cm thick breast of 50%/50% adipose/glandular tissue and a 250  $\mu\text{m}$   $\mu\text{C}$  size..... 47
- Figure 10.** Plots of calcification image noise,  $\sigma_{t_c}$  as a function of the low-energy exposure ratio for various adipose/glandular tissue compositions using the  $\text{CsI:Tl}$

scintillator; assuming a 5 cm thick breast with a 250  $\mu\text{m}$   $\mu\text{C}$  size and 25/50 (Mo/W) kVp spectra..... 48

**Figure 11.** Plot of calcification image noise,  $\sigma_c$ , as a function of the low-energy exposure ratio for various breast thickness using the CsI:Tl scintillator; assuming a 250  $\mu\text{m}$   $\mu\text{C}$  size, 25/50 (Mo/W) kVp spectra, and 50%/50% adipose/glandular tissue composition. .... 49

**Table1.** Table showing the materials and their densities used in the simulation studies.

<b>Material</b>	<b>Density (g/cm<sup>3</sup>)</b>
CaCO <sub>3</sub>	2.93
Gd <sub>2</sub> O <sub>2</sub> S:Tb	7.34
CsI:Tl	4.51
100% Adipose Tissue	0.93
100% Glandular Tissue	1.04

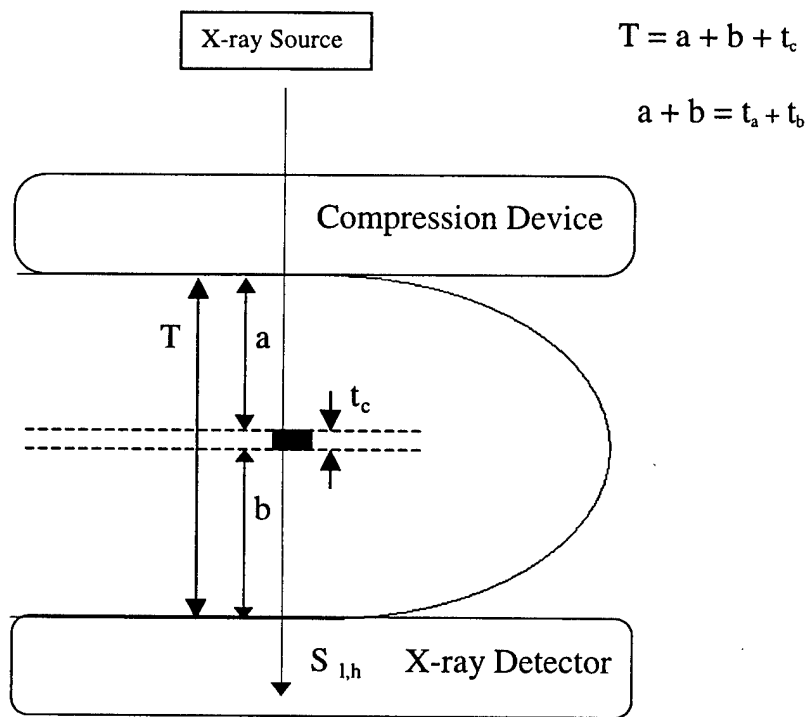


**Figure 1.** A compressed breast of thickness  $T$ , showing the  $\mu C$  of thickness  $t_c$ , and the adipose and glandular tissues of thickness  $t_a$  and  $t_b$ , respectively, where  $t_a + t_b = a + b$ .

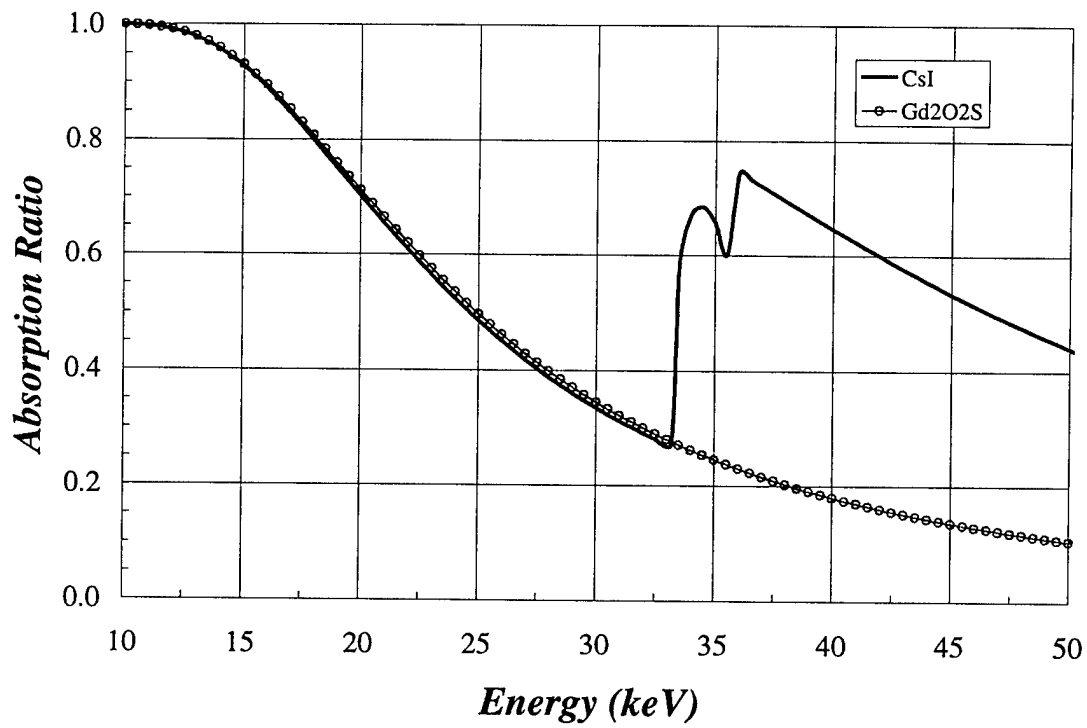


**Figure 2.** Plot showing the absorption ratios for a 46  $\mu\text{m}$  thick  $\text{Gd}_2\text{O}_2\text{S}:\text{Tb}$  scintillator and a 100  $\mu\text{m}$  thick  $\text{CsI}:\text{Tl}$  scintillator. The K-edges of  $\text{CsI}:\text{Tl}$  scintillator are seen at 33.2 and 36 keV resulting in a higher absorption ratio. The K-edge for  $\text{GdOS}$  lies at 50.2 keV (just out of the plotted energy range).

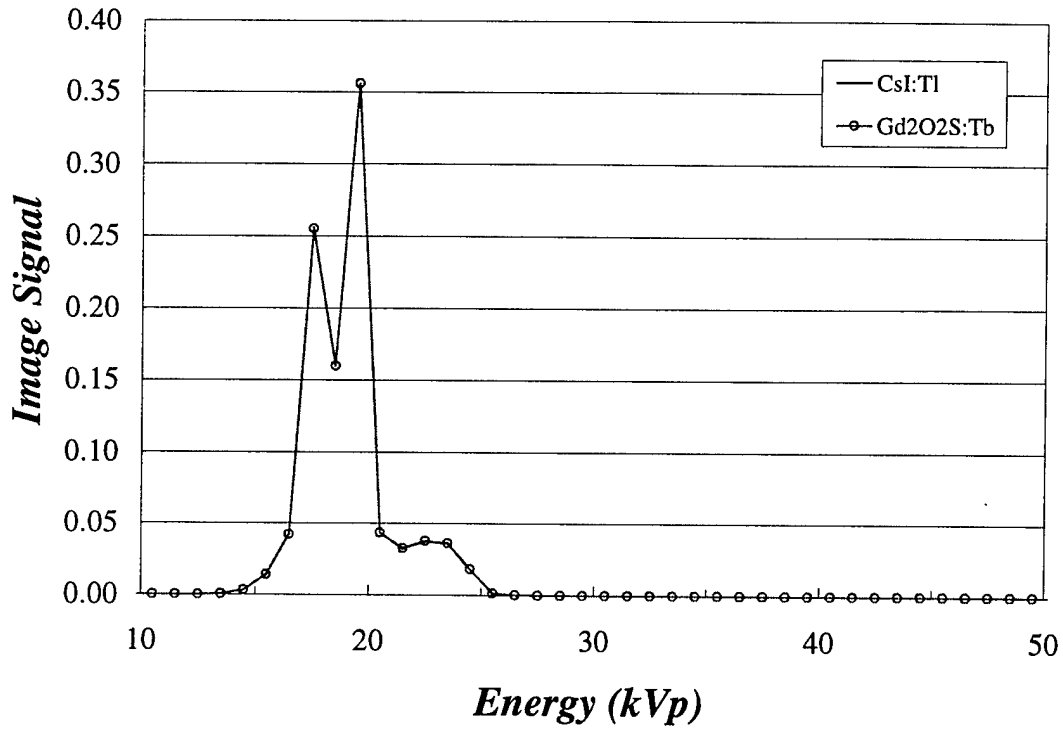


**Figure 3.** Plots showing the computed 25 kVp Mo/Mo x-ray spectrum for the Gd<sub>2</sub>O<sub>2</sub>S:Tb and CsI:Tl scintillators. The characteristic x-ray lines of Mo are seen at 17.4 and 19.8 keV. The total counts in the individual spectra are normalized to unity. The spectra for both scintillators are identical because their absorption ratios are similar upto the CsI K-edge near 33 keV.

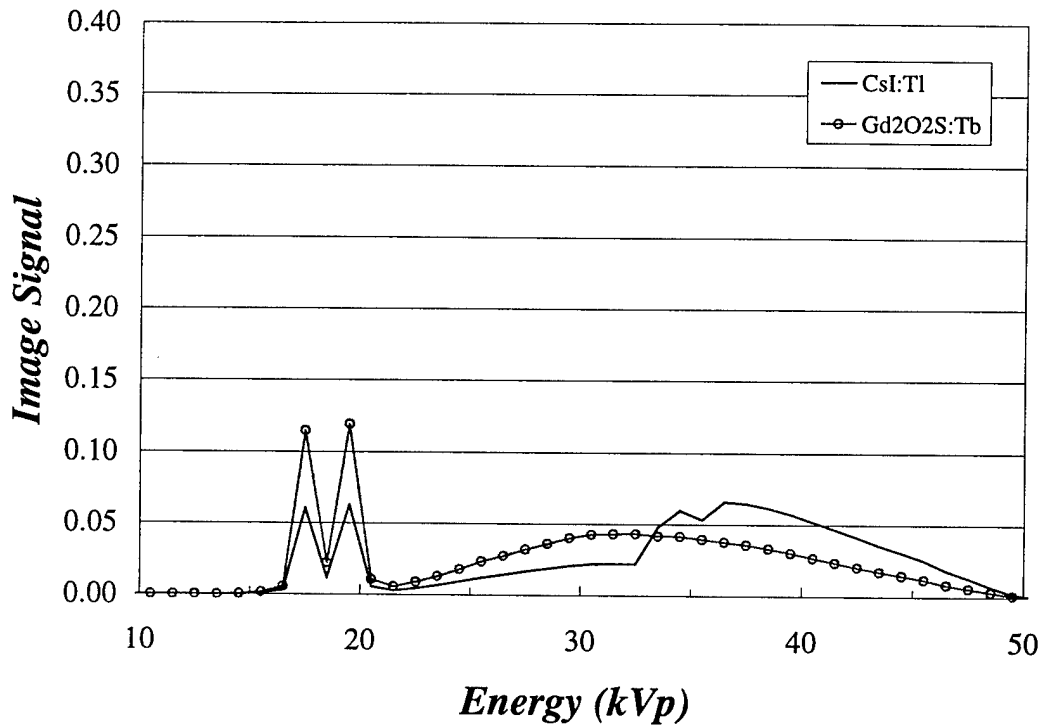


**Figure 4.** Plots showing the computed 50 kVp Mo/Mo x-ray spectrum for the Gd<sub>2</sub>O<sub>2</sub>S:Tb and CsI:Tl scintillators. The total counts in the individual spectra are normalized to unity. The bremsstrahlung emission is seen above 20 keV, besides the characteristic x-ray lines of Mo below 20 keV. The bump-like structure seen in the CsI spectrum around 35 keV is due to its higher absorption ratio.

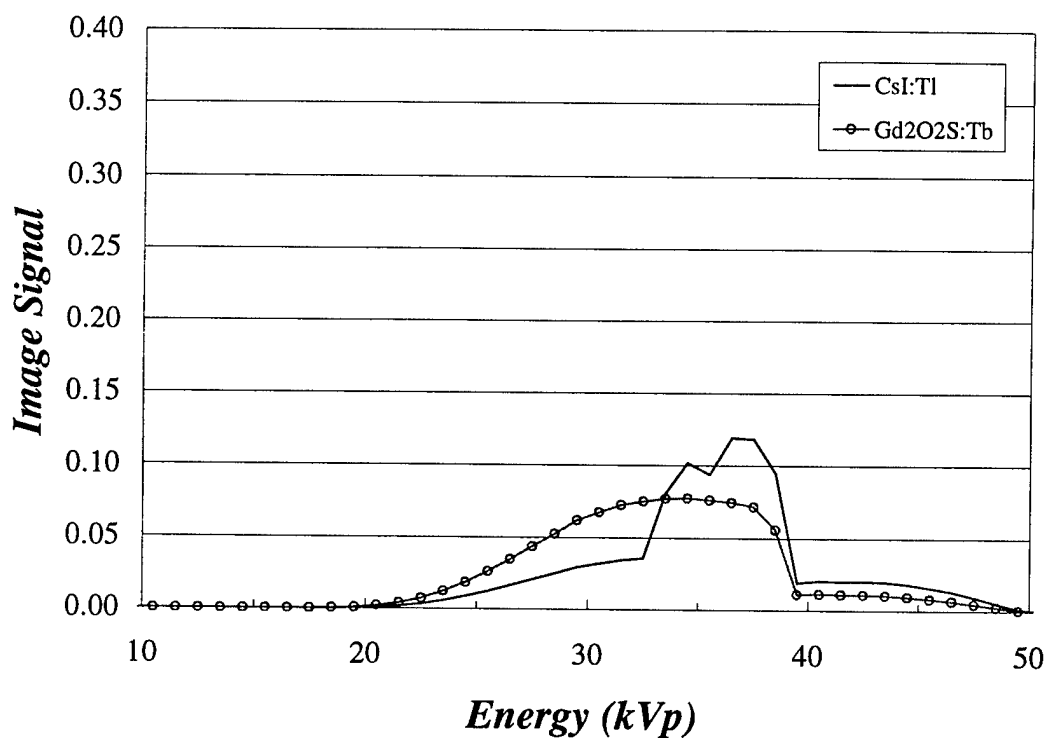


**Figure 5.** Plots showing the computed 50 kVp W/La x-ray spectrum for the Gd<sub>2</sub>O<sub>2</sub>S:Tb and CsI:Tl scintillators. The total counts in the individual spectra are normalized to unity. The drop around 39 keV is due to K-edge absorption by the La filter. Combining the increased K-edge absorption by CsI scintillator and the La filter attenuation at the source, a more peaked spectrum is generated.

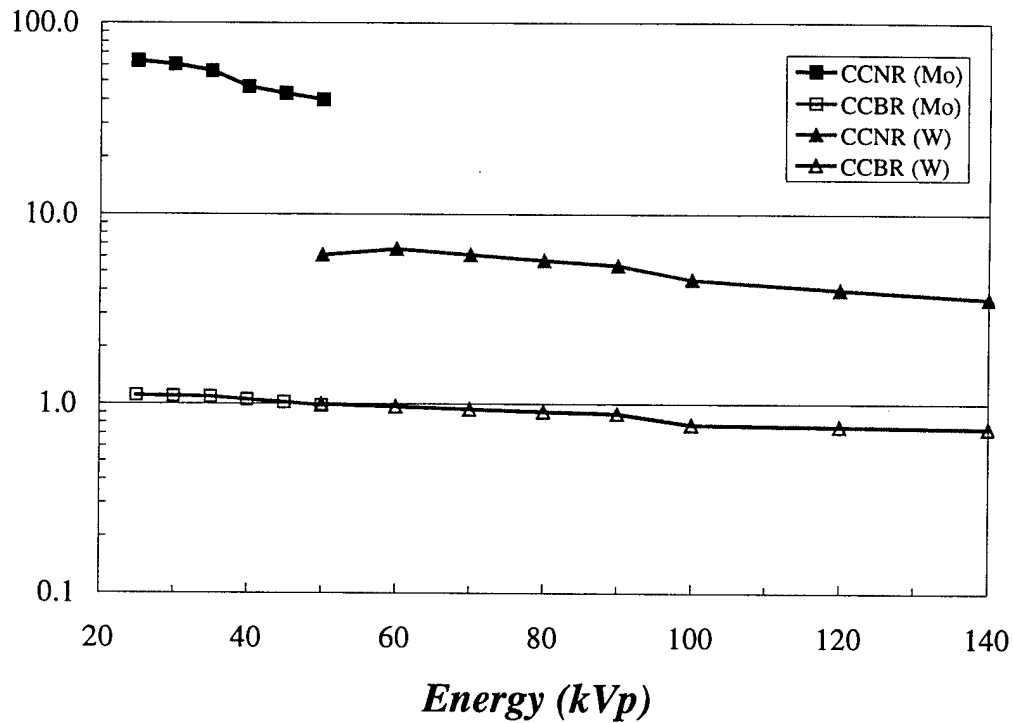


**Figure 6.** The plots of the calcification contrast-to-noise ratio, *CCNR* and the calcification background-to-noise ratio, *CCBR* for energies ranging from 25 to 140 kVp. Target/filter combinations of Mo/Mo, W/Al, and W/Cu was used between 25–50, 50–90, and 90–140 kVp respectively. The Mo and W represent spectra generated with a molybdenum and tungsten target, respectively. Note that the 50 kVp calculations were performed with both the Mo and the W targets.

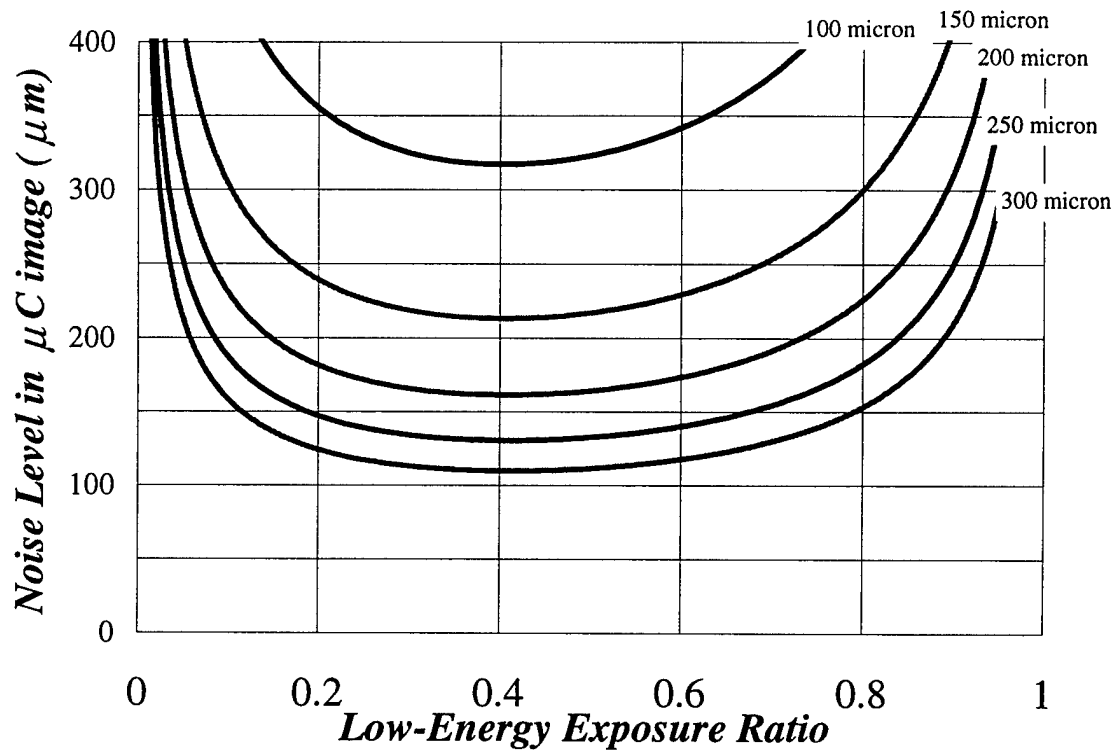


**Figure 7.** Plots of the calcification image noise,  $\sigma_t$ , as a function of the low-energy exposure ratio for various  $\mu\text{C}$  sizes using the  $\text{Gd}_2\text{O}_2\text{S:Tb}$  scintillator; assuming a 5 cm thick breast of 50%/50% adipose/glandular tissue and 25/50 (Mo/Mo) low-/high-kVp spectra.

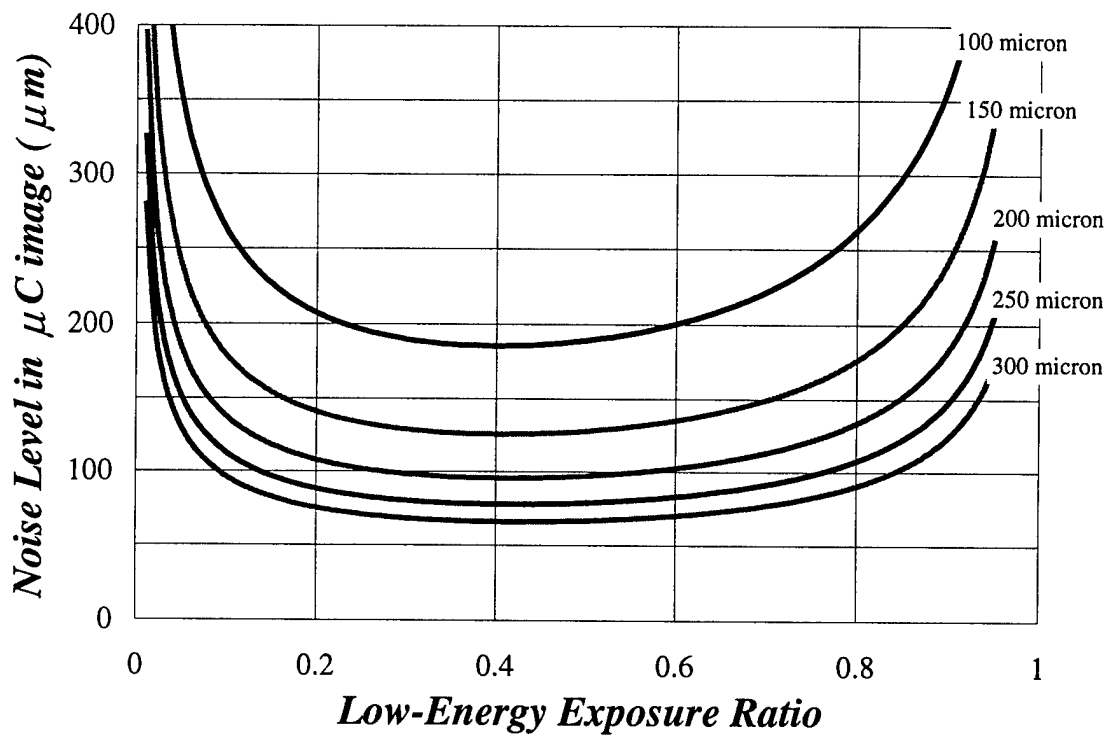


**Figure 8.** Plots of the calcification image noise,  $\sigma_t$ , as a function of the low-energy exposure ratio for various  $\mu\text{C}$  sizes using the CsI:Tl scintillator; assuming a 5 cm thick breast of 50%/50% adipose/glandular tissue and 25/50 (Mo/Mo) low-/high-kVp spectra.

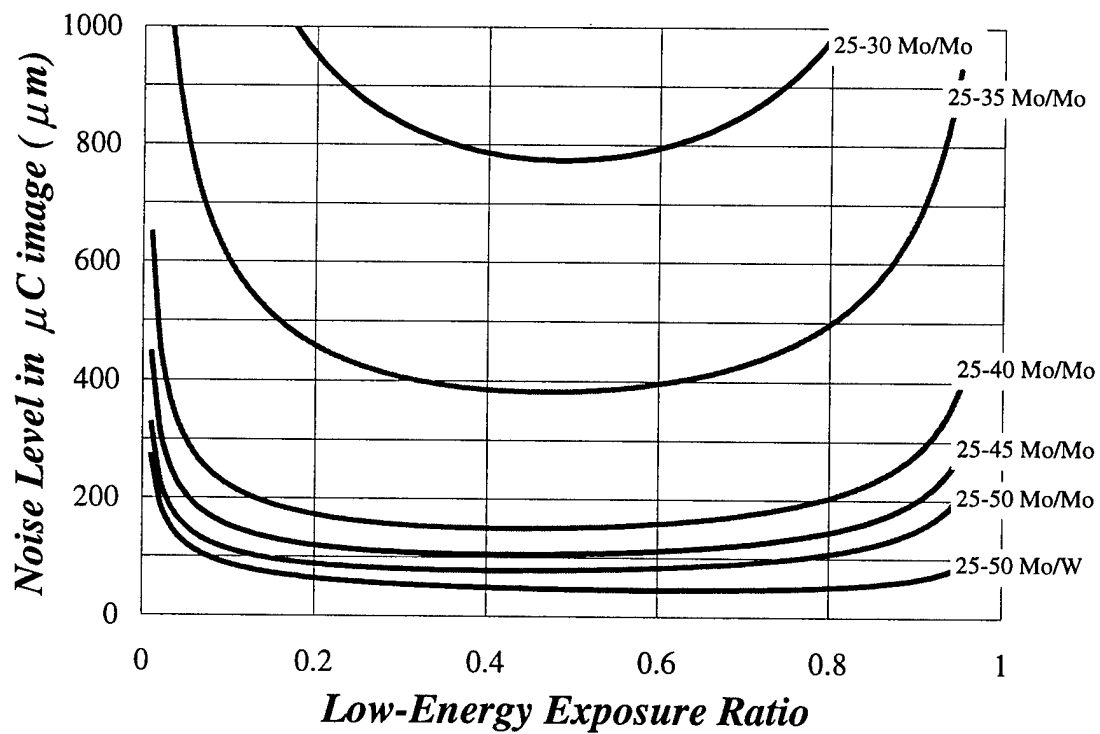


**Figure 9.** Plots of calcification image noise,  $\sigma_{t_c}$ , as a function of the low-energy exposure ratio for various combinations of energy spectra using the CsI:Tl scintillator; assuming a 5 cm thick breast of 50%/50% adipose/glandular tissue and a 250  $\mu\text{m}$   $\mu\text{C}$  size.

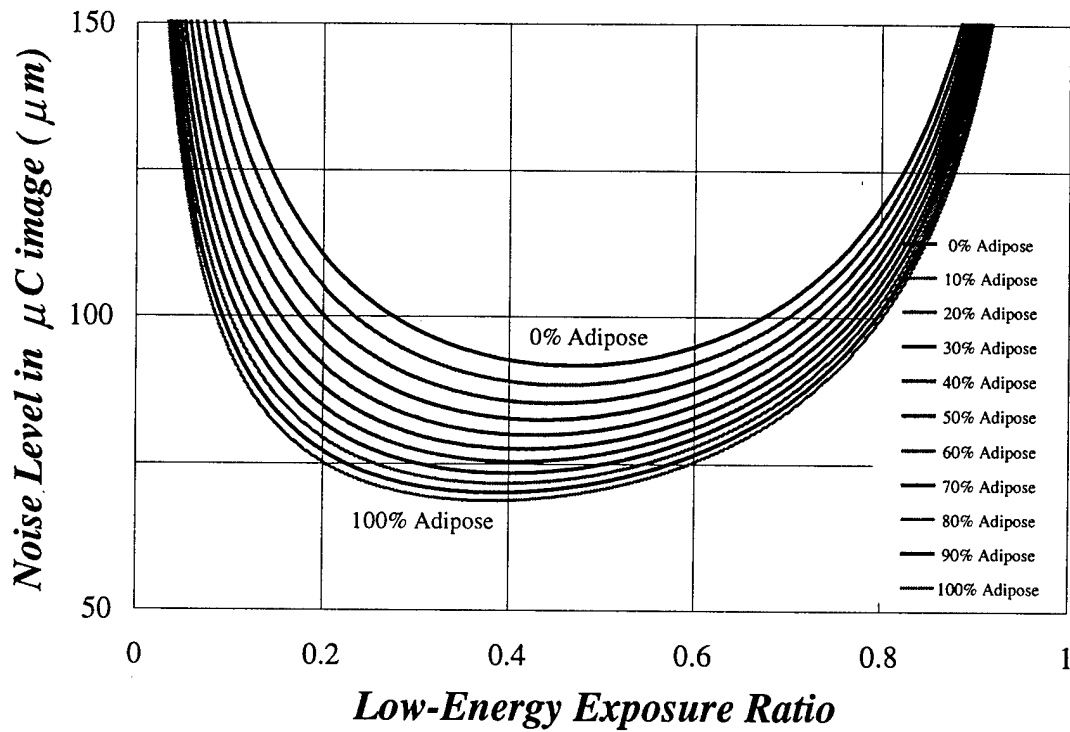


**Figure 10.** Plots of calcification image noise,  $\sigma_{i_c}$  as a function of the low-energy exposure ratio for various adipose/glandular tissue compositions using the CsI:Tl scintillator; assuming a 5 cm thick breast with a 250  $\mu\text{m}$   $\mu\text{C}$  size and 25/50 (Mo/W) kVp spectra.

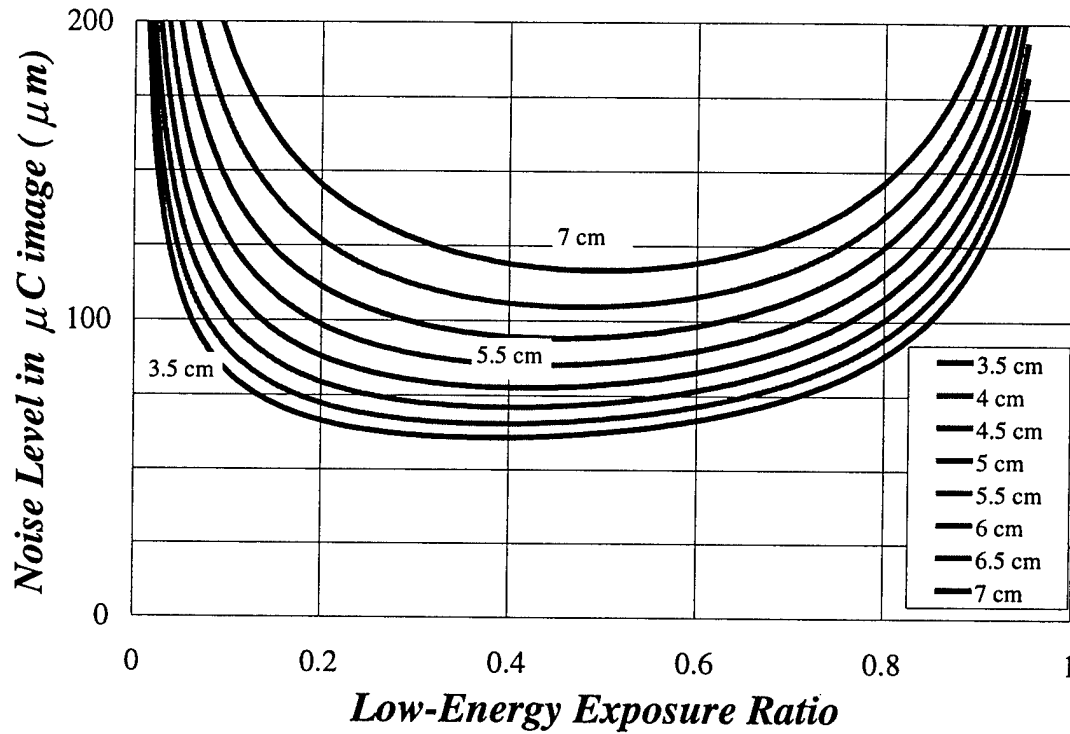


**Figure 11.** Plot of calcification image noise,  $\sigma_{t_c}$ , as a function of the low-energy exposure ratio for various breast thickness using the CsI:Tl scintillator; assuming a 250  $\mu\text{m}$   $\mu\text{C}$  size, 25/50 (Mo/W) kVp spectra, and 50%/50% adipose/glandular tissue composition.

**aSi:H/CsI:Tl flat-panel imaging versus CR for chest imaging:  
image quality measurement\*<sup>+</sup>**

Xinming Liu,<sup>a)</sup> Chris C. Shaw, and Xiujiang Rong

Diagnostic Radiology Department

University of Texas M. D. Anderson Cancer Center

Houston, TX 77030

Please address all correspondence to:

Xinming Liu, Ph.D.

Diagnostic Radiology Department

University of Texas M.D. Anderson Cancer Center

1515 Holcombe Boulevard, Box 57

Houston, TX 77030

E-mail: [xliu@di.mdacc.tmc.edu](mailto:xliu@di.mdacc.tmc.edu)

\*The scientific content of this paper was first presented at the 86<sup>th</sup> Scientific Assembly and Annual Meeting of the Radiological Society of North America held in November 2000, Chicago, Illinois.

<sup>+</sup>This work was supported in part by a research grant CA51248 from the National Cancer Institute and a research grant DAMD17-00-1-0316 from the Department of Army Breast Cancer Research Program.

## 1 **Abstract**

2 Amorphous silicon (aSi:H) flat-panel imaging systems have recently become commercially  
3 available for both chest and mammographic imaging applications. It has been shown that this  
4 new detector technology offers better image quality and various operational advantages over the  
5 widely used computed radiography (CR) and other digital radiography techniques. However,  
6 most image quality measurements reported on flat-panel systems have been performed on  
7 prototype systems in laboratories while those for CR systems were typically independently  
8 performed and reported on as separate studies. To directly compare the new flat panel systems  
9 with CR systems, we have measured the image properties for a commercial cesium iodide  
10 (CsI:Tl) a-Si:H based flat-panel digital chest system and a commercial CR system under clinical  
11 imaging conditions. In this paper, image quality factors, including the modulation transfer  
12 functions (MTFs), noise power spectra (NPSs) and detective quantum efficiencies (DQEs),  
13 measured for the flat-panel system, are presented and compared with those for a CR system.  
14 Methods and issues related to these measurements are discussed. The flat-panel system was  
15 shown to have slightly lower MTF but significantly higher DQEs than the CR system. The DQEs  
16 of the flat-panel system were found to increase with the exposure while those of the CR system  
17 decrease slightly with the exposure.

18  
19 **Key words:** aSi:H/CsI:Tl flat-panel detector, computed radiography, digital radiography,  
20 modulation transfer function, noise power spectra, noise equivalent quanta, detective quantum  
21 efficiency,

22

## 1 I. INTRODUCTION

2

3 Despite advances in new modalities, projection x-ray imaging remains as the primary tool  
4 for initial diagnosis of chest diseases. Conventional projection x-ray imaging has relied on the  
5 use of screen/film (S/F) combinations as the x-ray detector. Although they have been improved  
6 and optimized in quality over decades, there are several drawbacks. Intrinsic to the use of film  
7 density for recording image signal is a non-linear relationship between the optical density and  
8 logarithm of detector exposure, known as the H and D curve. Due to the presence of flattened toe  
9 and shoulder areas, reasonably good image contrast can only be obtained for a narrow range of  
10 exposures. This leads to a limited exposure range and causes a significant number of retakes  
11 from over- or under-exposures. Another drawback in quality aspects is the poor compromise  
12 between spatial resolution and x-ray absorption in the S/F design. To maintain reasonable spatial  
13 resolution, the thickness of the screens used are generally kept relatively thin to contain  
14 scattering of fluorescent light in the phosphors. However, this leads to compromised x-ray  
15 absorption ability, increasing noise fluctuations (quantum mottles) and limiting the ability to  
16 detect low contrast objects in the S/F images. Due to the analog nature of the S/F combinations,  
17 they also have the operational disadvantages in terms of film storage, retrieval, distribution and  
18 display. Films accumulated over years of operation are becoming increasingly difficult and  
19 expensive to store, organize and retrieve. Retrieval and distribution of films are labor intensive  
20 and often leads to loss or misplacement. The use film density to record and represent image  
21 signals results in inflexible and sub-optimal image display. The analog form of the stored images  
22 does not have the provision for post-acquisition processing for image enhancement or analysis.

23 Various digital radiography techniques have been developed and investigated over the

1 last two decades in the hope of improving both the quality and utilization of x-ray image data.<sup>1-17</sup>  
2 However, due to advances of digital and computer technology, the concept of totally digital and  
3 filmless radiology operation become feasible. Thus, the incentives of finding a high quality yet  
4 economic digital image acquisition technique for large-scale implementation of digital  
5 radiography have grown high.

6 The CR technology has been introduced in early 80's and over past decades has been  
7 widely accepted as a viable candidate for large-scale implementation of digital radiography. Due  
8 to its compatibility with existing x-ray equipment, the implementation of CR can be economic  
9 and less demanding in terms of initial cost and personnel training. Its operational advantages  
10 have been well recognized and utilized in areas that demand flexibility and convenience in  
11 operation but so much in image quality, e.g. bedside radiography, imaging in intensive care unit,  
12 emergency room. Furthermore, the CR technology has been easily integrated with the PACS or  
13 filmless radiology, further increasing its installation base. However, despite the ability of CR to  
14 provide processed and enhanced images, the quality of CR images have been measured and  
15 perceived to be lower than that of S/F images. Thus, acceptance in applications demanding high  
16 image quality has been more reserved, including notably primary chest imaging and  
17 mammographic imaging. This lower image quality has been attributed to the poorer x-ray  
18 absorption ability and several other characteristics of the storage phosphors.

19 In the last few years, amorphous silicon flat-panel (FP) detectors have become commercially  
20 available for primary chest and mammographic imaging. The imaging properties of these  
21 systems have been measured and reported on by various groups. However, most of these  
22 measurements have been performed on prototype systems in laboratory settings rather than  
23 clinical systems in clinical imaging settings. Comparison to the widely used CR systems has

1 been difficult because most reports have focused on measurements for a specific imaging system  
2 or one type of technologies. Since these measurements were often conducted under different  
3 conditions or using different methodologies, it is generally difficult to obtain a fair comparison  
4 of the flat-panel systems with CR systems based on studies independently performed and  
5 reported on.

6 In order to obtain a fair and realistic comparison of the flat-panel technique with the CR  
7 technique for chest imaging, we have measured and compared the image properties of a  
8 commercial flat-panel system and a commercial CR system using identical methodology and  
9 under nearly identical conditions. In this paper, the results from these measurements are  
10 presented and compared. The methodology and relevant issues for the measurements are  
11 described and discussed.

12

## 1 II. METHODS AND MATERIALS

### 2 A. Detector systems

#### 3 A.1 a-Si:H/CsI flat-panel system

4 The flat-panel (FP) detector system studied and compared in this investigation was an  
5 amorphous silicon/cesium iodine (a-Si:H/CsI:TI) based system with an active area of 41cm × 41  
6 cm (16" × 16") and a pitch of 200 μm . This system was manufactured as part of a stand-alone  
7 digital chest unit (Revolution XQ/i, General Electric Medical Systems, Milwaukee, WI) and  
8 integrated with a stationary anti-scatter grid. Characteristics and performance of this system has  
9 been previously reported.<sup>1</sup> The detector is divided into a 2048 × 2048 array of image elements,  
10 each of which consists of a photo-diode and a thin-film-transistor (TFT) switch, fabricated with  
11 amorphous silicon coatings deposited on a glass substrate. A thick layer of CsI:TI is directly  
12 grown on top of the a-Si:H circuitry. This scintillator is naturally grown into needle structures  
13 which can effectively act like light channels to keep the fluorescent light generated from  
14 spreading laterally and improve the resulting spatial resolution. The fluorescent light is  
15 channeled to the photo-diodes for conversion into charges which are then read by opening the  
16 TFT switches. The digital values of the flat-panel image cover a range of 14-bits. The system  
17 provides both raw and processed image data for archival, display and printing. For this study, the  
18 raw image data were achieved on a CD-R disk and then transferred to a Sun workstation for  
19 further processing and analysis.

20

#### 21 A.2 Computed radiography system

22 The CR system studied and compared in this investigation was a FCR AC-3 CR image  
23 reader used in conjunction with ST-V<sub>N</sub> plates (Fuji Medical Systems USA, Inc., Stamford, CT).

1 This system has been widely used for general radiography applications and should be a good  
2 representation of current commercial CR systems as designed for general radiography  
3 applications. It reads out images as 12 bit data but process and converts them into 10 bit data for  
4 storage, printing or display. The pixel size for image readout depends on the size of plates used.  
5 For the 14" × 17" plates used in this study, the images were read out with a pixel size of 200 μm.  
6 The ST-V<sub>N</sub> plates has been designed for better x-ray absorption and modest spatial resolution,  
7 aiming for general radiography applications. The CR reader was operated with fixed sensitivity  
8 (S) and latitude (L): S=200 and L=3.0.(Ref) Since the readout image signals were  
9 logarithmically amplified before digitization, the image data were linearized and converted into  
10 12 bit linear data prior to analysis. Specifications of the two detector systems are listed and  
11 compared in Table 1.

12

### 13 **B. Experimental setup**

14 Since the FP detector system was is part of a dedicated digital chest unit, the CR imaging  
15 plates were exposed using a wall Bucky in a separate radiography room. However, the x-ray tube  
16 and generator used for CR imaging are identical in make and model to the ones used in the  
17 dedicated FP chest unit, minimizing the differences in x-ray beam quality. The source-to-detector  
18 distance (SID) was maintained at 183 cm (72") for both FP and CR imaging. Exposures were  
19 made at 70 and 120 kV<sub>p</sub>. The former was often used in previously reported measurements on FP  
20 or CR detectors for chest imaging.<sup>1-7</sup> The latter is a typical kV<sub>p</sub> used in primary chest  
21 radiography procedures. A 0.5-mm thick copper plate was added to simulate average attenuation  
22 and filtration by the patient. The beam qualities for both FP and CR systems were measured and  
23 listed in table 2. The beam quality differences between the two imaging systems were found to

1 be 2.6% and 1.8% for 70 and 120kVp, respectively. Notice the 7mm of Al spectrum of 70kVp is  
2 similar to that used by other investigators.<sup>1-5</sup> For most measurements, the stationary anti-scatter  
3 grid was removed for the FP system. Part of the measurements were repeated with the anti-  
4 scatter left in. For the CR system, the imaging plate was exposed outside the Bucky but placed at  
5 the same SID for measurements without the anti-scatter grid and inside the Bucky for  
6 measurements with the grid.

7

## 8 **C. Image signals**

### 9 **C.1 Signal linearity**

10 Signal transfer function is one of the fundamental measurements in the evaluation of a  
11 medical x-ray imaging system. Conversion of image signals into exposure information, often  
12 referred to as signal linearization, is required for measuring the MTF, NPS, NEQ, and DQE. The  
13 raw image data generated from image acquisition with the FP chest unit are only linearly  
14 amplified and should be directly proportional to the exposure at the detector input. To check the  
15 linear response of the FP detector, uniform exposure images were acquired at various mAs  
16 settings while keeping the kVp fixed at 70 or 120. Mean image signals over a 100×100 region-  
17 of-interest (ROI) at center of the field were then measured as a function of the exposure. The  
18 exposures for these mAs settings were measured by moving the image detectors out of the x-ray  
19 path and placing the ion chamber at the same position of the Bucky-cassette holder (for the CR  
20 imaging plates) or FP detector assembly. The mean signal over the ROI was computed and  
21 averaged over four exposures at each mAs setting and plotted as a function of the measured  
22 exposure.

1           With the CR system used in this study, the readout image signals were logarithmically  
2 amplified prior to digitization. Thus the digital image data need to be converted back to linear  
3 exposure scale prior to measurements of MTF, NPS, NEQ and DQE. The following relationship  
4 was used to linearize CR image data:

$$5 \qquad \qquad \qquad Q = a \cdot \log E + b \qquad \qquad \qquad (1)$$

7  
8 where  $Q$  is the digital value of the CR image,  $E$  is the linearized signal,  $a$  is the gradient, and  $b$  is  
9 the intercept of the curve on the digital value axis. To determine the parameters  $a$  and  $b$ , the  
10 mean signal,  $Q$ , was measured for various exposures,  $E$ . The relationship between the measured  
11 values of  $Q$  and  $\log E$  was then fitted to a straight line with the slope and intercept computed as  $a$   
12 and  $b$ , respectively. The resulting values of  $a$  and  $b$  can then be used to linearize CR image data  
13 using Eq. 1. The validity of using Eq. 1 to represent the relationship between CR image data and  
14 exposure can be checked by evaluating the quality of the fit.

15

#### 16 **D. Modulation transfer function**

17           The modulation transfer function (MTF) is often measured to characterize and quantify the  
18 spatial resolution properties of an image detector system. It is also required for computing the  
19 DQE of an imaging system. The pre-sampling MTFs were measured by using the tilted slit  
20 method in this study. This method has been widely used to measure the pre-sampling MTFs of  
21 digital imaging systems. The measurement technique and procedure have been described in  
22 details by Fujita *et al.*<sup>8</sup> With this method, an x-ray slit is tilted slightly from the vertical or  
23 horizontal directions. Signal profiles across the slit are used to estimate the line spread functions

1 (LSFs) which are then Fourier transformed to compute the MTFs. However, LSFs measured  
2 along successive lines are sampled with slightly shifted phases which reflect the relative position  
3 of the slit center with respect to the sampling points. A series of successive lines can be  
4 identified with the slit center shifting from one sampling point to the next. Signal profiles along  
5 these lines can be combined together into a single profile which covers one or more cycles of  
6 sampling phases and provides an LSF effectively sampled with a much smaller pixel size. This  
7 LSF can be used to compute the so-called pre-sampling MTF as the effective sampling distance  
8 can be substantially reduced. Alternatively, the profiles along these lines can be used to compute  
9 MTFs corresponding to different sampling phases. The results can be averaged to obtain the  
10 phase-averaged MTF which has been suggested for use in computation of DQEs.

11 An x-ray slit camera (model 07-624, Nuclear Associates, Carle Place, NY) was employed to  
12 measure the LSFs. The camera has a built-in slit which is 10  $\mu\text{m}$  wide (with 4° relief angles on  
13 each jaw), 8 mm long and made of 1.5-mm thick tantalum. The slit camera was placed at the  
14 input of the CR cassette, Bucky or detector assembly to minimize image parallax and focal spot  
15 blurring. The slit was tilted at a slight angle (2~3°) to the anode-cathode axis at the center of the  
16 detector. This arrangement was used to acquire finely sampled LSFs for computing the MTFs  
17 along the horizontal direction (perpendicular to the anode-cathode axis). X-rays were generated  
18 with a technique of 400, 200, and 50 mAs at 40, 70, and 120 kV<sub>P</sub> respectively. A 0.5-mm thick  
19 cooper filter was added for measurements at 70 and 120 kV<sub>P</sub>. The small focal spot (0.6-mm) was  
20 used to reduce focal spot blurring during image acquisition. To reduce x-ray and optical scatter,  
21 image areas outside the slit was shielded by closing down the collimator as much as possible and  
22 using additional lead plate for areas right around the slit. This procedure may also help prevent

1 the flat-panel imager from being over-exposed and avoid the unwanted ghost signals which may  
 2 appear in subsequent exposures and persist for a long time

3 Image data were corrected for spatial variation along the slit and across the image lines  
 4 used. The biases of signal profile, a result likely from dark current noise, x-ray and optical  
 5 scatter, were estimated by averaging the signals far away from the slit and subtracted from the  
 6 signal profiles. With the tilting angle used, a complete cycle of sampling phases were found to  
 7 correspond to about 25 successive image lines. These lines were combined into a single finely  
 8 sampled LSF, which was normalized to have a peak value of 1 and then Fourier transformed.  
 9 Finally, the modulus of the transform was divided by a sinc function used to correct for the  
 10 effects of the finite width of the slit used to form the pre-sampling MTF as follows:

$$11 \quad MTF(f) = \frac{|FT(LSF(x))|}{\text{sinc}(x/w)} \quad (2)$$

13

#### 14 **E. Noise power spectrum**

15 To measure the Noise Power Spectra (NPSs), uniform exposure images were acquired with  
 16 70 and 120 kVp x-rays filtered by 0.5-mm thick copper plate. The mAs settings were varied from  
 17 0.5 to 50 for 70kVp and 0.25 to 10 for 120kVp, corresponding to a detector exposure of 0.04 to  
 18 11.3 mR.(? for 70 or 120 kVp) For each setting, four images were acquired and subtracted from  
 19 each other to form 6 subtraction images. In each of these subtraction images, structural patterns  
 20 were cancelled out and only noise fluctuations were left. The subtraction image was then Fourier  
 21 transformed and used to compute the two-dimensional NPS as follows:

22

$$NPS_{normalized}(f_x, f_y) = \frac{\langle |FT\{I(x, y)\} / S|^2 \rangle}{(\sqrt{2} \cdot N)^2} \cdot p_x \cdot p_y \quad (3)$$

1  
2  
3 where the  $NPS_{normalized}$  is the normalized NPS;  $FT$  is the two-dimensional Fourier transform;  
4  $I(x,y)$  is the subtracted image signals;  $N$  is the dimension of the square ROI;  $\sqrt{2}$  was included in  
5 the denominator to compensate for the noise increase due to image subtraction;  $p_x$  and  $p_y$  are the  
6 pixel sizes (in mm) along  $x$  and  $y$  axes (equal in our measurements) and were included to  
7 normalize the NPS computation for a unit area of  $\text{mm}^2$ ; and  $S$  is the mean signal for each ROI;  
8  $\langle \rangle$  represents averaging of all NPSs computed for various subtraction images and ROIs. With  
9 each subtraction image, the NPS was measured over 100  $128 \times 128$  ROIs which together occupy a  
10  $1280 \times 1280$  or  $25.6 \times 25.6 \text{ cm}^2$  area in the central part of the image. With the six subtraction  
11 images formed, a total of 600 ROIs were used for computing the NPSs. The results were  
12 averaged to reduce the fluctuations and obtain a reasonably smooth two-dimensional NPS for  
13 each exposure level. The subtraction (noise) image data were divided by the mean signals over  
14 the ROIs prior to Fourier transform. The resulting NPSs are independent of the size of image  
15 signals and often referred to as the normalized NPSs. A two-dimensional plot of the NPSs would  
16 be the best way to illustrate the noise properties of the detector. The shape of such plots can be  
17 used to identify artifacts in the images as well. In this study, we have limited the measurements  
18 to one-dimensional case and the two-dimensional NPS data were averaged over the nine line  
19 wide thick segment encompassing the horizontal axis.

20

## 1. F. Noise equivalent quanta

2           The noise equivalent quanta (NEQ) is defined as the apparent number of quanta per unit  
3 area contributing to an image if all noise sources in the system are quanta limited. The frequency  
4 dependent (NEQs) can be computed from the MTF and normalized NPS as follows:

$$5 \quad 6 \quad \quad \quad NEQ(f) = \frac{MTF^2(f)}{NPS(f)_{normalized}} \quad (4)$$

7  
8 Although the pre-sampling MTF can be measured from digital image data, the expectation or  
9 phase averaged MTFs, denoted by EMTFs, were used to compute the NEQ(f). Such MTFs were  
10 averaged from MTFs measured from 25 or so successive slit profiles in which the slit center was  
11 located at various positions between two sampling points. The use of EMTFs is consistent with  
12 the fact the NPSs were also based on average of measurements from digital image data which  
13 had been sampled with various phases and subject to effects of aliasing.

14

## 15 G. Detective quantum efficiency

16           By definition, the DQE can be related the NEQ(f) as follows:

17

$$18 \quad \quad \quad DQE(f) = \frac{NEQ(f)}{SNR_{in}^2} = \frac{EMTF^2(f)}{NPS(f)_{normalized} \cdot \phi} \quad (5)$$

19

1 where  $SNR_m$  is the SNR of the signal at the detector input. However, because the input signal is  
 2 the photon fluence incident to the detector, it fluctuates and follows the Poisson statistics. Thus,  
 3  $SNR_m^2$  is equal to the mean x-ray photon fluence,  $\phi$ , and Eq. can be rewritten as follows:

$$4 \quad DQE(f) = \frac{NEQ(f)}{\phi} = \frac{EMTF^2(f)}{NPS(f)_{normalized} \cdot \phi}$$

6  
 7 In addition to the phase-averaged MTF and NPS, the DQE measurement also requires the mean  
 8 signal and input photon flux to be measured or estimated. The mean signal was estimated by  
 9 averaging the mean image signals over the ROIs used for NPS measurement. This is equivalent  
 10 to averaging the image signals over all ROIs together or the  $1280 \times 1280$  area in the middle of  
 11 the image.

12 Thus, information of the input flux is essential to the computation of the DQEs. It was  
 13 estimated by multiplying the measured detector exposure with the published photon flux data for  
 14 the spectrum used (70 or 120 kVp x-rays filtered with 0.5-mm thick copper plate). The detector  
 15 exposure was measured with an ion chamber placed at the input of the Bucky in the case of CR  
 16 system and of detector-grid assembly in the case of FP system. The exposures were measured for  
 17 various mAs settings (for NPS measurement) and kVp settings (for MTF measurement). The  
 18 exposures had to be measured with separate exposures as the chamber would interfere with the  
 19 NPS or MTF measurement if it were placed in the field during acquisition of the uniform  
 20 exposure or slit images. Three successive exposure measurements were repeated to reduce the  
 21 fluctuations at each mAs setting. Results of the measurements were also corrected for the  
 22 difference between the SID and between the center of the chamber and entrance to the storage

1 phosphor or CsI layer. However, the differences were found to be rather insignificant. All  
2 exposures were measured using a calibrated 150 CC ion chamber and a Keithley dosimeter (model  
3 96035B ion chamber with model 35050A dosimeter, Keithly Instruments, Cleveland, OH).

4 The photon fluence was estimated using computer simulation based on published method  
5 and tables.<sup>23, 24</sup> The x-ray fluence per exposure,  $C$ , is expressed by following equation:

6

$$7 \quad C = \frac{\int c(E)q(E)dE}{\int q(E)dE} \quad (6)$$

8

9 where  $c(E)$  is the photon fluence per exposure as a function of energy,  $E$ , and  $q(E)$  is the x-ray  
10 fluence per unit energy as a function of photon energy. The photon fluence for chest imaging  
11 were calculated and listed in table 2.

12

13

### 1 III. RESULTS

2

#### 3 A. Signal linearity

4 Mean signals measured from 70 and 120 kVp uniform exposure images are plotted as a  
5 function of the exposure for FP and CR systems in Figures 1(a) and 1(b), respectively. Because  
6 the measurements were made over a large range of exposures (0.025-12 mR), they are plotted in  
7 log-log scales to better show the entire range of data. The measured signals were indicated by  
8 data labels while the linear fittings were indicated by solid lines. The slopes, intercepts and  
9 correlation coefficients for the linear fittings are also shown on the plots. Linearity between  
10 image signals and detector exposures is required for measuring and computing the MTFs, NPSs  
11 and DQEs. Such linearity is well demonstrated by the plots in Figures 1(a) and 1(b).

12

#### 13 B. Modulation transfer function (MTF)

14 The pre-sampling MTFs measured at 40, 70 and 120 kVp's are plotted for the FP and CR  
15 systems in Figures 2(a) and 2(b), respectively. The plots show that the MTFs of the FP system  
16 were measurably lower but still comparable to those of the CR system. At 1 cycle/mm, the  
17 percentage difference between the MTFs of the CR and FP systems is about 10.6% (using the  
18 MTF values of the FP system as the reference). The difference increases to about 25% at the  
19 Nyquist frequency of both systems (2.5 lps/mm). The plots also show that the x-ray kVp had  
20 little effect on the MTFs of the FP system but had measurable effect on those of the CR system.

21 Imaging blurring in CR imaging occurs mainly in the readout process. As the laser beam  
22 penetrates and stimulate the trapped electrons in the storage phosphor layer of the exposed CR  
23 imaging plate, it spreads laterally and leads to readout of signals from neighboring pixels. Image

1 blurring in the CsI:Tl layer of the FP detector is caused by lateral spreading of the fluorescent  
2 light converted from absorbed x-rays. This appears to be similar to the blurring process in CR  
3 image readout. However, the CsI:Tl layer used in a FP detector can be fabricated with needle  
4 structure (as is the case with the one studied in this paper) which helps channel the fluorescent  
5 light to the photo-diodes with much reduced lateral spreading. Coupled with a better x-ray  
6 absorption capability, CsI:Tl offers a better compromise between spatial resolution and x-ray  
7 absorption as compared to the CR system. However, this can be translated into different benefits  
8 by selecting different scintillator thickness in designing the FP detector. Much improved MTFs  
9 can be achieved by selecting a smaller thickness maintaining the same x-ray absorption  
10 capability as the CR system. Alternatively, much improved x-ray absorption can be achieved by  
11 choosing a thicker scintillator but maintaining the same MTF. The FP detector studied in this  
12 paper apparently takes advantage of the needle structure of CsI:Tl by going for much improved  
13 x-ray absorption while maintaining an MTF similar to those of the CR system.

14 The kVp dependence of the MTFs of the CR system may be attributed to the difference in the  
15 way images are formed with the two detectors. With the CR system, x-ray information is stored  
16 as density of trapped electrons with little blurring. During readout, the trapped electrons are  
17 excited resulting emission of photons which are then collected and converted into electronic  
18 signals by using multiple photo-multiplier tubes (PMTs). Due to the use of laser scanning  
19 readout method, scattering of the light emitted from stimulated trapped electrons does not cause  
20 blurring. The major factors that contribute to image blurring are the laser spot size and lateral  
21 spread of the laser beam inside the storage phosphor. Thus, the later results in an effect highly  
22 dependent upon the depth of the trapped electrons stimulated. The deeper they are, the more the  
23 laser beam spread and the greater the blurring effect is. Thus, the x-ray kVp would have an effect

1 on the overall blurring. At higher kVp's, the distribution of absorbed x-rays tend to be more  
2 uniform over different depths. At lower kVp's, the distribution tend to be weighted more towards  
3 the entrance side, resulting in a larger signal contribution from less spread laser beam.

4 It appears that image blurring in the CsI:Tl scintillator would have similar depth and  
5 therefore kVp dependence. The difference is that x-rays absorbed at deeper level (closer to the  
6 photodiodes in the aSi:H panel) would result in less blurred signals as the fluorescent light  
7 emitted would have to travel a shorter distance to reach the photodiodes and therefore is subject  
8 to less lateral spreading. This would imply an increase of the MTF with higher x-ray kVp.  
9 However, the plots in Figure 2(A) do not show such dependence. This may be attributed to the  
10 use of a reflective coating on the entrance side of the CsI:H layer. Although the coating is used to  
11 provide some protection and help collect light emitted in the backward direction (opposite to  
12 incident x-rays), it also has the side effect of equalizing the depth dependence of the blurring  
13 effect. As an x-ray photon is converted to light in the scintillator, half of the light photons are  
14 emitted in the forward direction while the other half in the backward direction. If we add the  
15 distance traveled by the forwardly emitted photons to that traveled by the backwardly emitted  
16 photons, the sum is equal to double of the scintillator thickness. Thus, the overall blurring effect  
17 would be less dependent on the depth of the scintillation. X-rays absorbed near the exit side  
18 would result in a forward component subject to almost no blurring (propagation distance  $\sim 0$ )  
19 and a backward component subject to maximum blurring (propagation distance  $\sim 2 \times$  scintillator  
20 thickness). On the other hand, x-rays absorbed on the entrance side would result in a forward  
21 component and a backward component with about the same average blurring as both forward and  
22 backward photons need to travel about the same distance ( $\sim$  scintillator thickness) to reach the  
23 photodiodes.

1  
2  
3  
4  
5  
6  
7  
8  
9  
10  
11  
12  
13  
14  
15  
16  
17  
18  
19

### C. Noise Power Spectrum (NPS)

The normalized NPSs of the FP system are plotted as a function of the spatial frequency for various exposure levels in Figures 3(a) (70 kVp) and 3(b) (120 kVp). The normalized NPSs of the CR system are plotted in Figures 4(a) (70 kVp) and 4(b) (120 kVp). Notice that the NPSs plotted have been normalized by the mean signal for a unit area of  $1 \text{ mm}^2$ . Thus the plots show the noise ratio squared for various spatial frequencies and exposures for signals detected in a unit area. For both FP and CR systems, the NPSs decreased with the exposure and spatial frequency. It is obvious that the NPSs for the FP system decreased with the spatial frequency at a significantly faster rate. Since the NPSs were measured for two different sets of exposures at 70 and 120 kVp, it is rather hard to compare the two systems as to how the NPS varied with the exposure or the kVp. For such comparison, the NPSs for 1.25 lps/mm (half of the Nyquist frequency) and 2.0 lps/mm are plotted as a function of the exposure for the two different detector systems and two different kVp's in Figure 5(A) and (B). It becomes apparent with Figure 5(A) and (B) that the normalized NPSs are slightly higher at 120 kVp. Furthermore, the normalized NPSs for the CR system are significantly higher than those for the FP system. The difference increases from a factor of 4.5 for 0.025 mR to a factor of 7 for 12 mR. The difference is expected to be even greater at higher frequencies.

### D. Detective Quantum Efficiency (DQE)

The DQEs of the FP system are plotted as a function of the spatial frequency for various exposure levels at 70 and 120 kVp in Figures 6(a) and 6(b), respectively. Similarly, the DQEs of the CR system are plotted for various exposure levels at 70 and 120 kVp in Figures 7(a) and

1 7(b), respectively. The plots show that DQEs of the FP system were higher by a factor of 2 or  
2 higher than those of the CR system within the clinical exposure range. The DQEs of the FP  
3 system increased with the exposure level while those of the CR system decreased with the  
4 exposure level. This exposure dependence is also shown in Figure 8(A) and (B) in which DQEs  
5 at 1.25 lps/mm and 2.0 lps/mm are plotted as a function of the exposure for both CR and FP  
6 systems.

7

### 8 **E. Measurements with anti-scatter grid on**

9 To demonstrate the effects of anti-scatter grid on NPS and DQE measurements, the NPSs and  
10 DQEs versus exposure at different spatial frequencies are plotted for comparison. Normalized  
11 NPSs at 1.25 lps/mm (half of the Nyquist frequency) and 2.0 lps/mm are plotted as a function of  
12 the exposure for the two different detector systems and two different kVp's in Figure 9(A) and  
13 (B). DQEs at 1.25 lps/mm (half of the Nyquist frequency) and 2.0 lps/mm are plotted as a  
14 function of the exposure for the two different detector systems and two different kVp's in Figure  
15 9(A) and (B) as well.

16

17

## 1   **ACKNOWLEDGMENT**

2           This work was supported in part by a research grant CA51248 from the National Cancer  
3   Institute and a research grant DAMD17-00-1-0316 from the Department of Army Breast Cancer  
4   Research Program.

5

6

## 7   **REFERENCES**

8

- 9   1. P. R. Granfors and R. Aufrichtig, "Performance of a  $41 \times 41$ -cm<sup>2</sup> amorphous silicon flat panel  
10   x-ray detector for radiographic imaging applications," *Med. Phys.* **27**, pp. 1324-1331, 2000.
- 11   2. J. T. Dobbins III, D. L. Ergun, L. Rutz, D. A. Hinshaw, H. Blume, and D. C. Clark, "DQE(f)  
12   of four generations of computed radiography acquisition devices," *Med. Phys.* **22**, pp. 1581-  
13   1593, 1995.
- 14   3. C. D. Bradford, W. W. Pepler, and J. T. Dobbins III, "Performance characteristics of a  
15   Kodak computed radiography system," *Med. Phys.* **26**, pp. 27-37, 1999.
- 16   4. S. M. Kengyelics, A. G. Davies, and A. R. Cowen, "A comparison of the physical imaging  
17   properties of Fuji ST-V, ST-VA, and ST-VN computed radiography image plates," *Med.*  
18   *Phys.* **25**, pp. 2163-2169, 1998.
- 19   5. M. J. Flynn and E. Samei, "Experimental comparison of noise and resolution for 2k and 4k  
20   storage phosphor radiography systems," *Med. Phys.* **26**, pp. 1612-1623, 1999.
- 21   6. R. V. Metter and R. Dickerson, "Objective performance characteristics of a new asymmetric  
22   screen-film system," *Med. Phys.* **21**, pp. 1483-1490, 1994.

- 1 7. D. Lee, L. K. Cheung, B. G. Rodricks, G. F. Powell, "Improved imaging performance of a  
2 14×17-in. Direct Radiography system using a-Se/TFT detector," in Proc. SPIE Medical  
3 Imaging **3336**, pp. 14-23, 1998.
- 4 8. H. Fujita, D.-Y. Tsai, T. Itoh, K. Doi, J. Morishita, K. Ueda, and A. Ohtsuka, "A simple  
5 method for determining the modulation transfer function in digital radiography," IEEE Trans.  
6 Med. Imaging **11**, 34-39, 1992.
- 7 9. M. L. Giger and K. Doi, "Investigation of basic imaging properties in digital radiography. I.  
8 Modulation transfer function," Med. Phys. **11**, 287-295 (1984)
- 9 10. W. Hillen, U. Schiebel, and T. Zaengel, "Imaging performance of a digital storage phosphor  
10 system," Med. Phys. **14**, 774-751 (1987)
- 11 11. H. Fujita, K. Ueda, J. Morishita, T. Fujikawa, A. Ohtsuka, and T. Sai, "Basic imaging  
12 properties of a computed radiographic system with photostimulable phosphors," Med. Phys.  
13 **16**, 52-59 (1989)
- 14 12. J. T. Dobbins III, "Effects of undersampling on the proper interpretation of modulation  
15 transfer function, noise power spectra, and noise equivalent quanta of digital imaging  
16 systems," Med. Phys. **22**, 171-181 (1995)
- 17 13. E. Samei and M. J. Flynn, "Physical measures of image quality in photostimulable phosphor  
18 radiographic systems," in Proc. SPIE Medical Imaging **3032**, pp. 328-338, 1997
- 19 14. H. Fujita, D.-Y. Tsai, T. Itoh, K. Doi, J. Morishita, K. Ueda, and A. Ohtsuka, "A simple  
20 method for determining the modulation transfer function in digital radiography," IEEE Trans.  
21 Med. Imaging **11**, 34-39 (1992)
- 22 15. M. L. Giger and K. Doi, "Investigation of basic imaging properties in digital radiography. I.  
23 Modulation transfer function," Med. Phys. **11**, 287-295 (1984)

- 1 16. W. Hillen, U. Schiebel, and T. Zaengel, "Imaging performance of a digital storage phosphor  
2 system," *Med. Phys.* 14, 774-751 (1987)
- 3 17. J. T. Dobbins III, D. L. Ergun, L. Rutz, D. A. Hinshaw, H. Blume, and D. C. Clark, "DQE(f)  
4 of four generations of computed radiography acquisition devices," *Med. Phys.* 22, 1581-1593  
5 (1995)
- 6 18. H. Fujita, K. Ueda, J. Morishita, T. Fujikawa, A. Ohtsuka, and T. Sai, "Basic imaging  
7 properties of a computed radiographic system with photostimulable phosphors," *Med. Phys.*  
8 16, 52-59 (1989)
- 9 19. J. T. Dobbins III, "Effects of undersampling on the proper interpretation of modulation  
10 transfer function, noise power spectra, and noise equivalent quanta of digital imaging  
11 systems," *Med. Phys.* 22, 171-181 (1995)
- 12 20. E. Samei and M. J. Flynn, "Physical measures of image quality in photostimulable phosphor  
13 radiographic systems," in *Proc. SPIE Medical Imaging 3032*, 328-338 (1997)

1 **LIST OF TABLES**

2 Table 1. Specifications for FP and CR imaging systems.

3 Table 2. Beam qualities for FP and CR image system with a 0.5-mm copper plate added at  
4 70 and 120kVp.

5

## 1 LIST OF FIGURES

- 2 Figure 1 Linearity curves for FP and CR imaging systems measured with a 0.5 mm thick  
3 copper plate added at 70 and 120 kVp plotted in (A) full exposure range (0 - 14  
4 mR) and (B) smaller exposure range (0 - 1.4 mR).
- 5 Figure 2 Pre-sampling MTFs of (A) FP and (B) CR system measured at 40, 70 and  
6 120kVp. A 0.5-mm copper plate was added for 70 and 120kVp measurements.
- 7 Figure 3 Normalized NPSs for FP system versus spatial frequency for various exposure  
8 levels at (A) 70 kVp and (B) 120 kVp, both with a 0.5-mm copper plate added.
- 9 Figure 4 Normalized NPSs for CR system versus spatial frequency for various exposure  
10 levels at (A) 70 kVp and (B) 120 kVp, both with a 0.5-mm copper plate added.
- 11 Figure 5 Normalized NPSs versus exposure at (A) 1.25 lps/mm and (B) 2.0 lps/mm.
- 12 Figure 6 DQEs for FP system versus spatial frequency for various exposure levels at (A)  
13 70 kVp and (B) 120 kVp.
- 14 Figure 7 DQEs for CR system versus spatial frequency for various exposure levels at (A)  
15 70 kVp and (B) 120 kVp.
- 16 Figure 8 DQEs versus exposure at (A) 1.25 lps/mm and (B) 2.0 lps/mm.
- 17 Figure 9 Normalized NPSs versus exposure with grid in at (A) 1.25 lps/mm and (B) 2.0  
18 lps/mm.
- 19 Figure 10 DQEs versus exposure with grid in at (A) 1.25 lps/mm and (B) 2.0 lps/mm.  
20  
21

Detector Type	FP	CR
Active Area (cm)	41×41	35×43
Image Matrix Size	2022×2022	1760×2140
Pixel Size	200μm	200μm
Image Depth	14 bits (linear)	10 bits (log)

Table 1. Specifications of FP and CR systems for chest imaging

X-ray Spectrum	Imaging Type	Al HVL (mm)	Fluence (photons/mm <sup>2</sup> /mR)
70 kVp	FP	7.1 mm	$2.87 \times 10^5$
	CR	6.9 mm	$2.84 \times 10^5$
120 kVp	FP	10.6 mm	$2.85 \times 10^5$
	CR	10.4 mm	$2.85 \times 10^5$

Table 2. Beam qualities for FP and CR imaging system with a 0.5-mm copper plate added at 70 and 120kVp

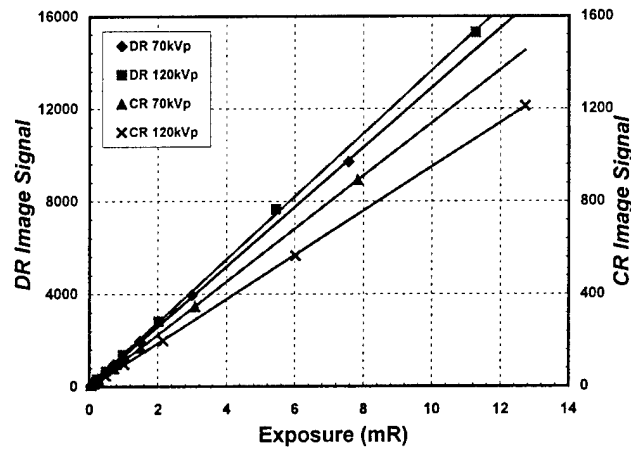


Figure 1. Linearity curves for FP and CR imaging systems measured with a 0.5-mm copper plate added at 70 and 120kVp. (a). full exposure range (0 – 14 mR)

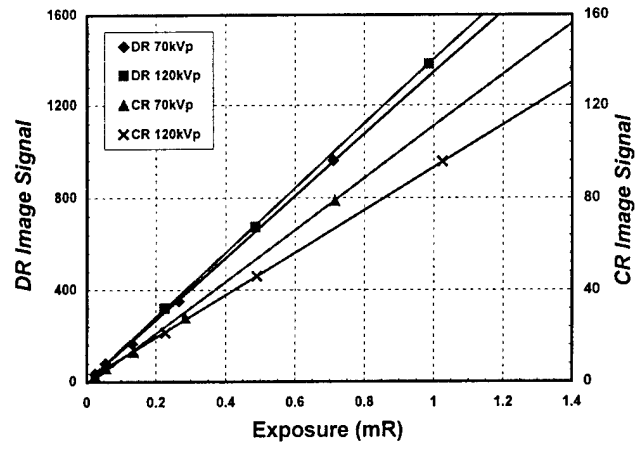


Figure 1. Linearity curves for FP and CR imaging systems measured with a 0.5-mm copper plate added at 70 and 120kVp. (b). small exposure range (0 – 1.4 mR)

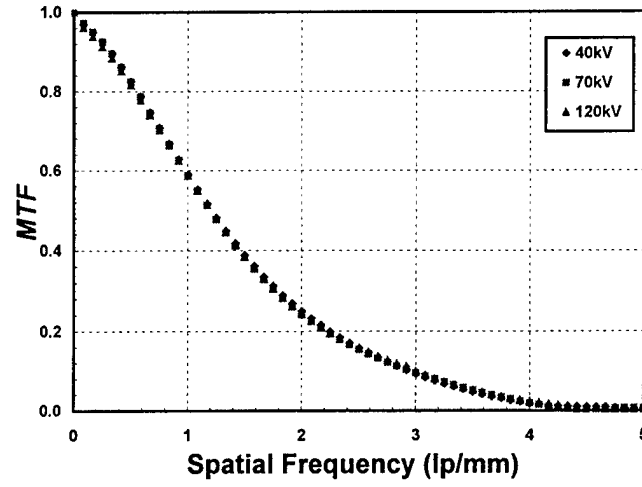


Figure 2(a). Pre-sampling MTF of FP system measured at 40, 70 and 120kVp. A 0.5-mm copper plate was added for 70 and 120kVp measurements.

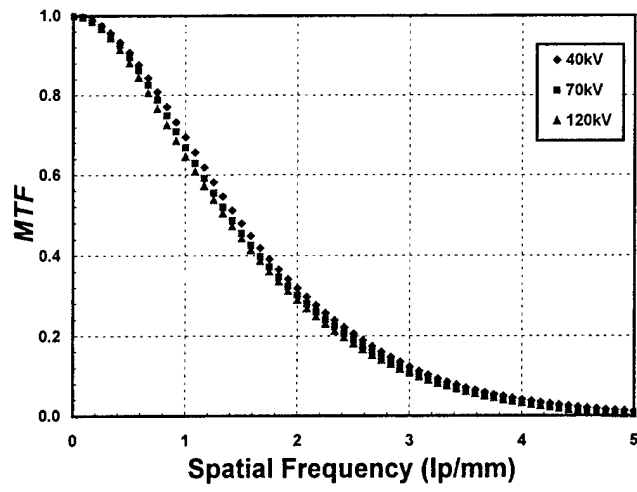


Figure 2(b). Pre-sampling MTF of CR system measured at 40, 70 and 120kVp. A 0.5-mm copper plate was added for 70 and 120kVp measurements.

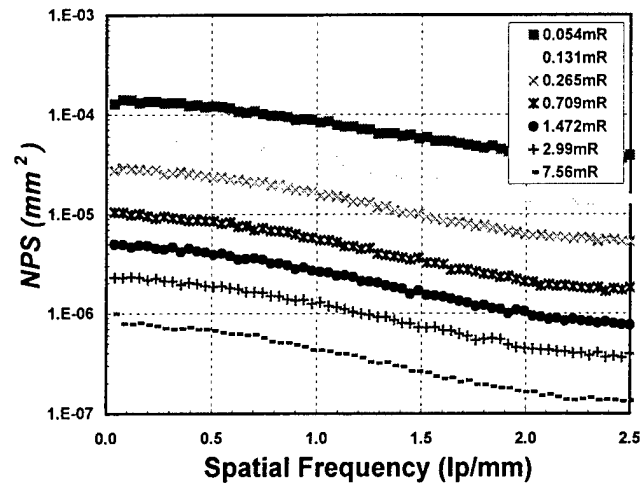


Figure 3 (a). Normalized NPSs for FP image were plotted as a function of the spatial frequency at various exposure levels and 70kVp. A 0.5-mm copper plate was added for the measurements.

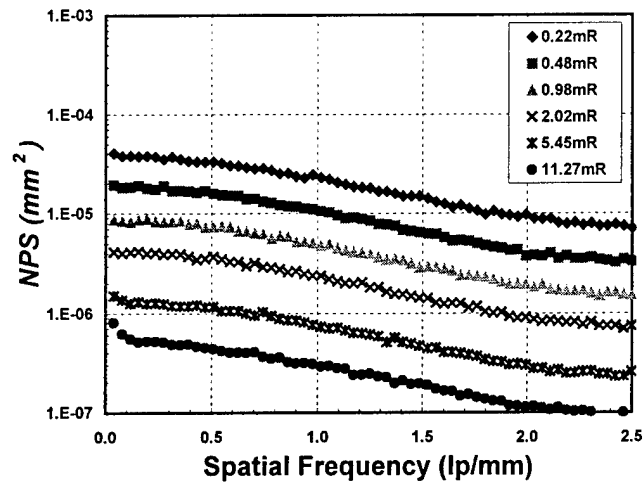


Figure 3 (b). Normalized NPSs for FP image were plotted as a function of the spatial frequency at various exposure levels and 120kVp. A 0.5-mm copper plate was added for the measurements.

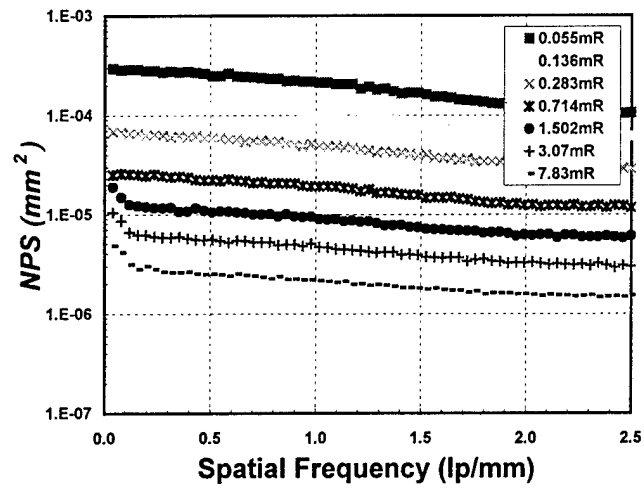


Figure 4 (a). Normalized NPSs for CR image were plotted as a function of the spatial frequency at various exposure levels and 70kVp. A 0.5-mm copper plate was added for the measurements.

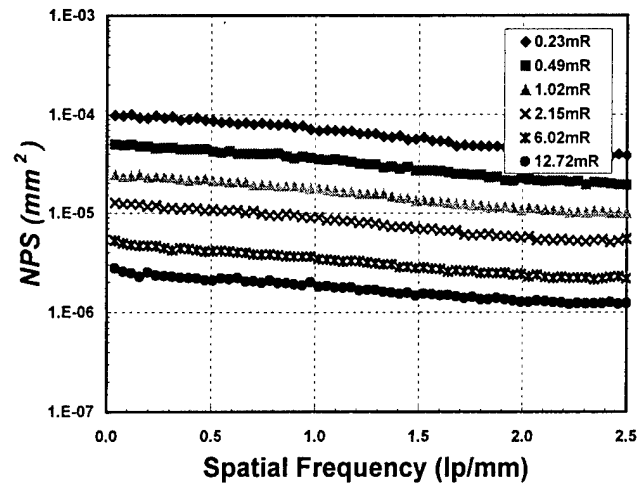


Figure 4 (b). Normalized NPSs for CR image were plotted as a function of the spatial frequency at various exposure levels and 120kVp. A 0.5-mm copper plate was added for the measurements.

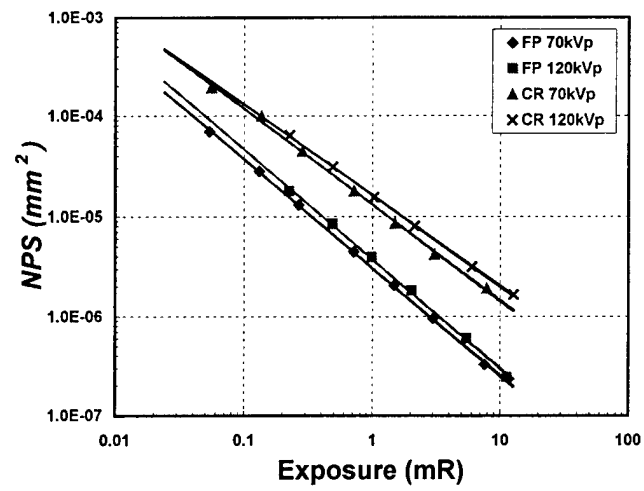


Figure 5 (a). Normalized NPSs were plotted as a function of exposure at 1.25 lp/mm.

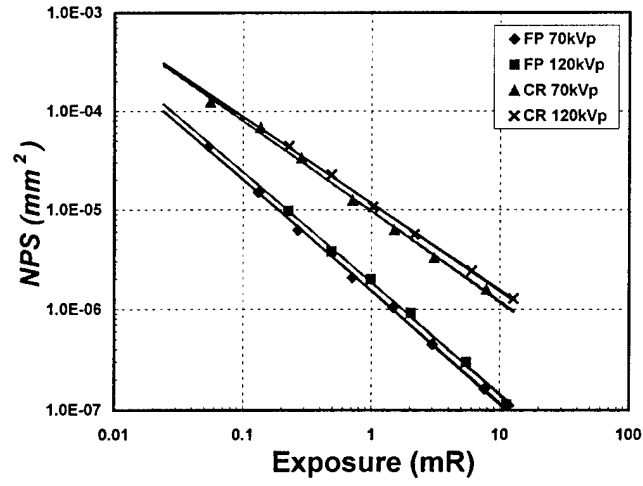


Figure 5 (b). Normalized NPSs were plotted as a function of exposure at 2.0 lp/mm.

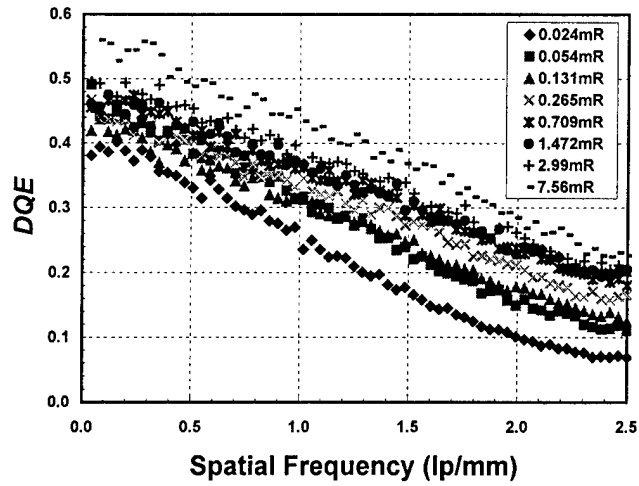


Figure 6 (a). DQEs for FP image were plotted as a function of the spatial frequency at various exposure levels and 70kVp. A 0.5-mm copper plate was added for the measurements.

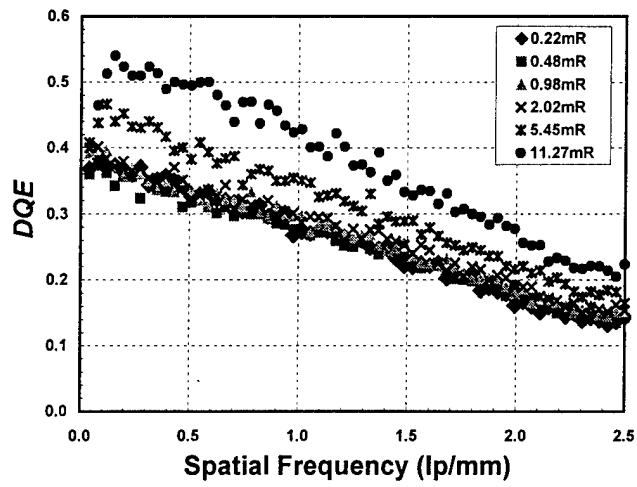


Figure 6 (b). DQEs for FP image were plotted as a function of the spatial frequency at various exposure levels and 120kVp. A 0.5-mm copper plate was added for the measurements.

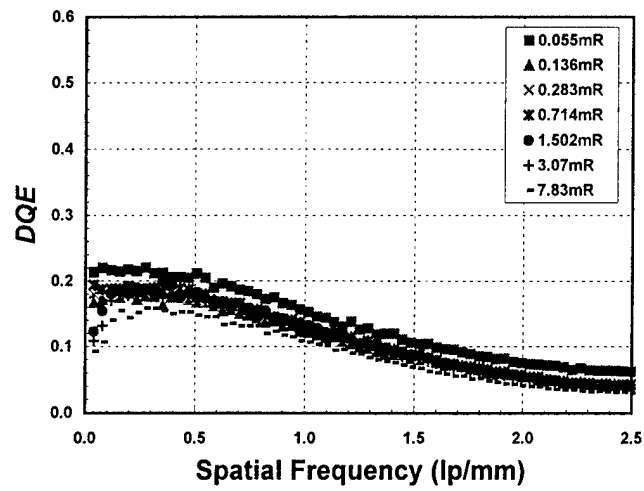


Figure 7 (a). DQEs for CR image were plotted as a function of the spatial frequency at various exposure levels and 70kVp. A 0.5-mm copper plate was added for the measurements.

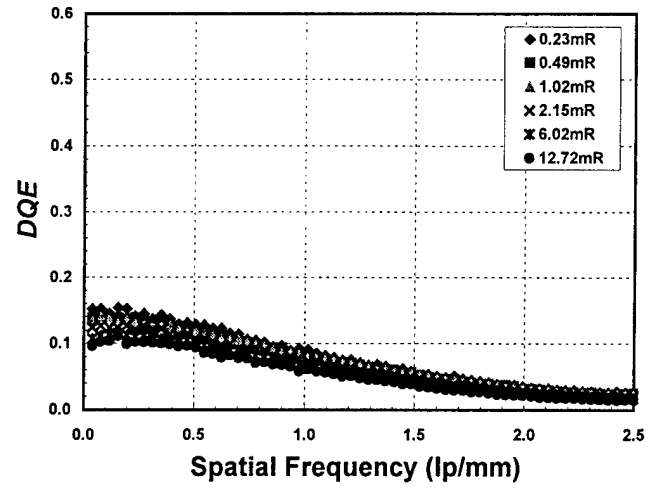


Figure 7 (b). DQEs for CR image were plotted as a function of the spatial frequency at various exposure levels and 120kVp. A 0.5-mm copper plate was added for the measurements.

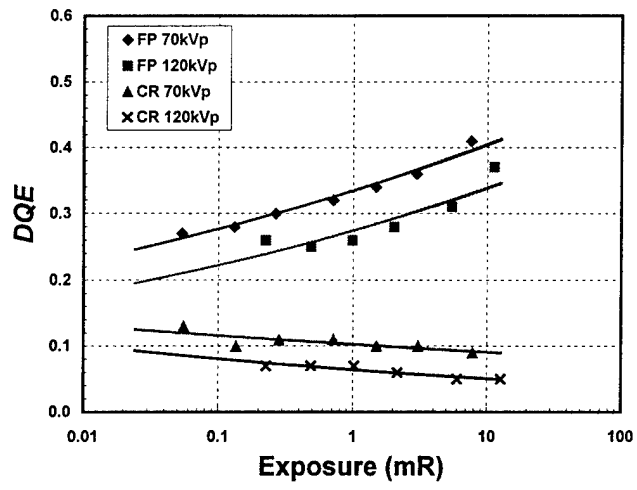


Figure 8 (a). DQEs were plotted as a function of exposure at 1.25 lp/mm.

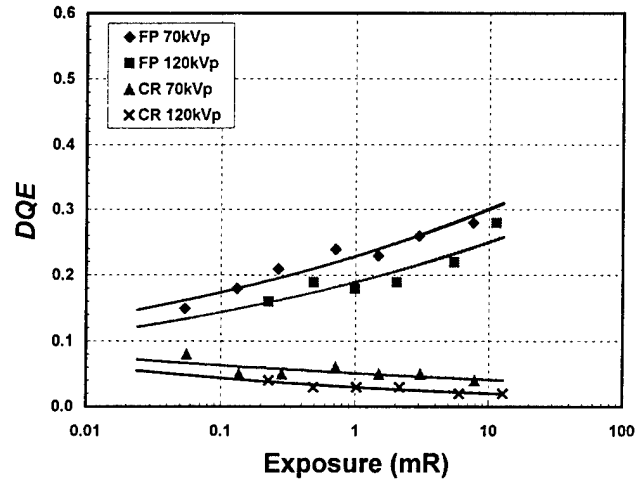


Figure 8 (b). DQEs were plotted as a function of exposure at 2.0 lp/mm.

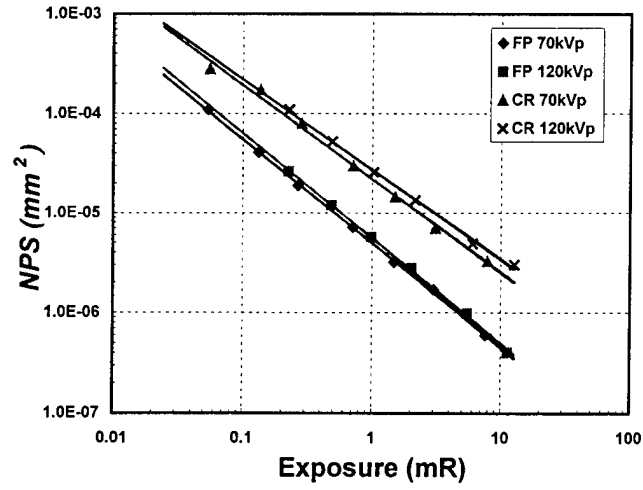


Figure 9 (a). Normalized NPSs were plotted as a function of exposure at 1.25 lp/mm. The stationary grid or the Bucky was not moved out.

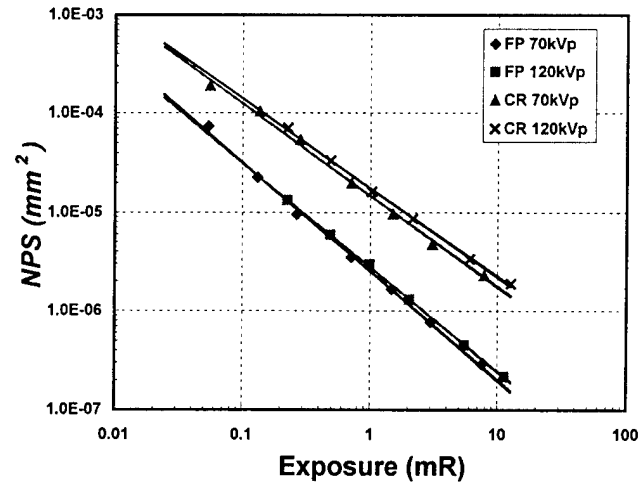


Figure 9 (b). Normalized NPSs were plotted as a function of exposure at 2.0 lp/mm. The stationary grid or the Bucky was not moved out.

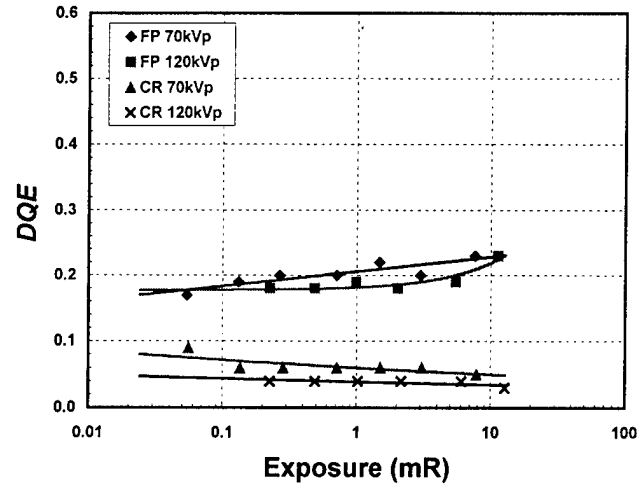


Figure 10 (a). DQEs were plotted as a function of exposure at 1.25 lp/mm. The stationary grid or the Bucky was not moved out.

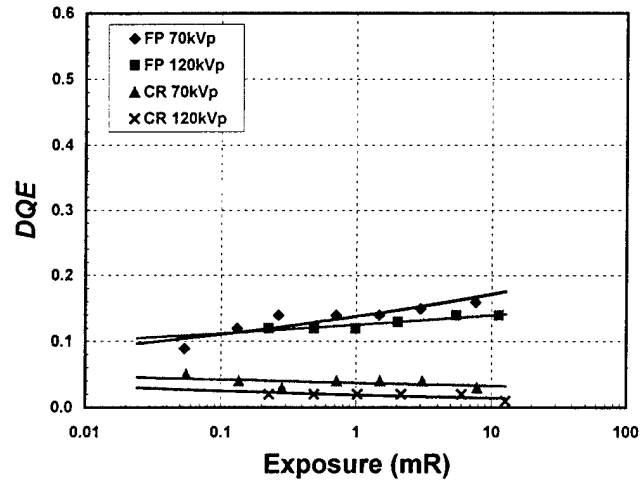


Figure 10 (b). DQEs were plotted as a function of exposure at 2.0 lp/mm. The stationary grid or the Bucky was not moved out.

TWO METHODS FOR IMPROVING THE DETECTABILITY OF  
MICROCALCIFICATIONS IN DIGITAL MAMMOGRAPHY

A  
THESIS

Presented to the Faculty of  
The University of Texas  
Health Science Center at Houston  
Graduate School of Biomedical Sciences  
in Partial Fulfillment

of the Requirements

for the Degree of

Master of Science

By

Michael René Lemacks, B.S.  
Houston, Texas

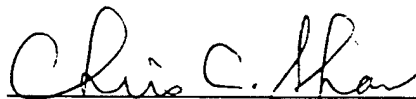
December, 2000

TWO METHODS FOR IMPROVING THE DETECTABILITY OF  
MICROCALCIFICATIONS IN DIGITAL MAMMOGRAPHY

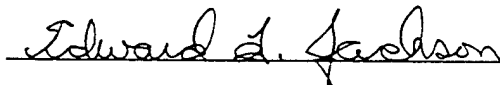
by

Michael René Lemacks, B.S.

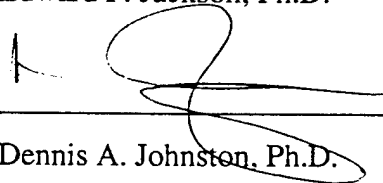
APPROVED:



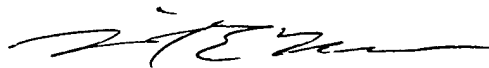
Chris C. Shaw, Ph.D.



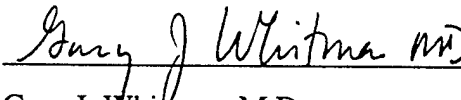
Edward F. Jackson, Ph.D.



Dennis A. Johnston, Ph.D.



Richard E. Wendt III, Ph.D.



Gary J. Whitman, M.D.

APPROVED:

---

Dean, The University of Texas  
Health Science Center at Houston  
Graduate School of Biomedical Sciences

TWO METHODS FOR IMPROVING THE DETECTABILITY OF  
MICROCALCIFICATIONS IN DIGITAL MAMMOGRAPHY

A

THESIS

Presented to the Faculty of  
The University of Texas  
Health Science Center at Houston  
Graduate School of Biomedical Sciences  
in Partial Fulfillment

of the Requirements

for the Degree of

Master of Science

By

Michael René Lemacks, B.S.  
Houston, Texas

December, 2000

## **Dedication**

To my wife, Lisa, for her love, support, encouragement, understanding and sacrifices during the process of achieving this goal. I never would have made it without her in my life.

To my children, Jacob, Hannah Grace and Isabelle, for their love and smiling faces each day.

To Jesus Christ, my Lord and Savior, who gave me the strength, knowledge, wisdom and peace to accomplish this task. "I can do all things through Him who strengthens me" (Philippians 4:13). To God be the Glory!

## Acknowledgements

I would like to thank Dr. Chris C. Shaw, my faculty advisor, for the time, advice and guidance he devoted to me and to this project. He provided knowledge, wisdom and encouragement throughout the course of this research. I would also like to recognize the other members of my Supervisory Committee: Drs. Edward F. Jackson, Dennis A. Johnston, Richard E. (Bud) Wendt III and Gary J. Whitman for their time and efforts in helping me complete this work.

I would also like to thank the members of both the Department of Radiation Physics and the Section of Diagnostic Imaging Physics at The University of Texas M. D. Anderson Cancer Center who provided their support in helping me to achieve my goal and obtain my Masters in Medical Physics. Special thanks to Xinming Liu, John Rong, Richard Willette, Georgeanne Moore, Susan Sprinkle-Vincent and all of the Mammographers at The University of Texas M. D. Anderson Cancer Center. I would also like to extend my appreciation to my fellow graduate students. They offered their advice, time, assisted me with computer programming and provided moral support throughout my research.

I would like to thank my family for their support and encouragement during my research. Special thanks to my wife, Lisa, for believing in me and supporting me throughout this endeavor. Also, I would like to thank the members of Second Baptist Church, Houston, Texas who have always been there to encourage and support me in my research and in life.

This research was supported in part by a research grant DAMD17-00-1-0316 from the US Department of the Army, a research grant CA51248 from the National Cancer Institute and a research grant from the Mike Hogg Foundation. Finally, I would like to acknowledge Dr. Ken Hogstrom and the Robert J. Shalek Premasters Fellowship Fund for supporting my graduate studies during the first year.

## Abstract

Early detection is essential to diagnose and treat breast cancer. Mammography has been the main screening and diagnostic tool for breast cancer. It relies on the detection and visualization of microcalcifications ( $\mu$ Cs) and/or soft tissue masses. The detection or visualization of  $\mu$ Cs is easier with an uncluttered soft tissue background but difficult or problematic in dense breasts. The "cluttered" background present in mammograms also tends to limit the detectability and visibility of  $\mu$ Cs and masses. Also important is an improved ability to depict finer image details in mammograms.

The purpose of this research was to determine: (1) the effects of magnification on the image quality parameters of a digital mammography system, (2) the improvement in the detectability of  $\mu$ Cs by using magnification in digital mammography and (3) the feasibility of using a dual-energy subtraction imaging technique to improve the detectability of  $\mu$ Cs in dense tissue structures.

Measurements were performed to study the effects of magnification on the image quality parameters in digital mammography. A phantom study was performed to compare screen/film and digital images for  $\mu$ C detectability in magnification imaging. Finally, a signal-to-noise ratio analysis was performed to show the feasibility of using a dual-energy subtraction technique to improve the detection of  $\mu$ Cs in digital mammography.

It was found that: (1) magnification can be used to improve the image quality parameters in digital mammography. (2) The digital mammography system performs as well as or better than the screen/film system for the detection of  $\mu$ Cs with magnification imaging. (3) It is feasible to use a dual-energy subtraction imaging technique to improve the detectability of  $\mu$ Cs in digital mammography.

## Table of Contents

Dedication .....	iii
Acknowledgements .....	iv
Abstract .....	v
Table of Contents .....	vi
List of Figures .....	ix
Lists of Tables .....	xii
<b>Chapter 1 – Introduction and Background .....</b>	<b>1</b>
1.1 Introduction.....	1
1.1.1 Statement of the Problem .....	2
1.1.2 Hypotheses .....	2
1.1.3 Goals and Objectives.....	3
1.2 Background.....	4
1.2.1 Digital Mammography .....	4
1.2.2 Magnification Mammography.....	6
1.2.3 Dual-Energy Imaging.....	7
1.3 Summary.....	10
<b>Chapter 2 – Magnification Digital Mammography: Image Quality Parameters 11</b>	
2.1 Introduction.....	11
2.2 Theory.....	14
2.2.1 Modulation Transfer Function (MTF).....	14
A. Spatial Resolution Limitations .....	14
B. MTF and Magnification.....	17
C. MTF Optimization.....	20
2.2.2 Noise Equivalent Quanta (NEQ).....	21
A. Noise Power Spectrum (NPS) .....	21
B. NEQ Computation .....	22

2.3	Materials and Methods.....	24
2.3.1	Imaging System.....	24
2.3.2	MTF Measurements .....	24
2.3.3	NPS Measurements .....	27
2.3.4	NEQ Measurements .....	29
2.4	Results and Discussion .....	30
2.4.1	MTF.....	30
2.4.2	NEQ.....	30
2.5	Summary.....	36
<b>Chapter 3 – Magnification Digital Mammography: Detection of Microcalcifications – A Phantom Study.....</b>		<b>37</b>
3.1	Introduction.....	37
3.2	Materials and Methods.....	38
3.2.1	Imaging System.....	38
3.2.2	Phantom Design .....	39
3.2.3	Image Acquisition .....	43
3.2.4	Image Reading.....	45
3.3	Results and Discussion .....	47
3.3.1	Reader Comments and Observations .....	53
3.4	Summary.....	55
<b>Chapter 4 – Dual-Energy Subtraction Imaging .....</b>		<b>56</b>
4.1	Introduction.....	56
4.2	Theory.....	58
4.2.1	Three-Energy versus Two-Energy Subtraction.....	58
4.2.2	Dual-Energy Microcalcification Imaging .....	58
4.2.3	Special Case: Monoenergetic x-rays .....	61
4.2.4	Noise in the Unsubtracted Image .....	63
4.2.5	Noise in the Subtracted Image .....	64

4.3	Materials and Methods.....	66
4.3.1	X-ray Photon Fluence Spectra.....	67
4.3.2	Attenuation Coefficients .....	67
4.3.3	Photon Absorption Ratio for Detectors.....	68
4.3.4	Exposures .....	70
4.3.5	Noise Levels in the Image Signals .....	71
4.3.6	Image Contrast and CNRs in Unsubtracted Images.....	72
4.4	Results and Discussion .....	73
4.4.1	Photon Absorption Ratio for Detectors.....	73
4.4.2	Signal Spectra.....	73
4.4.3	Contrast, Noise and SNR in Unsubtracted Images .....	78
4.4.4	Mapping X-ray Densities to Tissue Thicknesses .....	80
4.4.5	Noise Levels in the Image Signals .....	82
4.4.6	Optimal Low-energy Exposure Ratio .....	90
4.4.7	Dosimetric Considerations .....	90
4.5	Summary.....	92
<b>Chapter 5 – Conclusion .....</b>		<b>94</b>
5.1	Conclusions.....	94
5.2	Future Studies .....	95
Appendix .....		97
Bibliography.....		98
Vita.....		106

## List of Figures

<b>Figure 2.1.</b> Geometric blurring in magnification mammography is greater on the cathode side (chest wall). The divergence of the x-ray beam allows for better resolution to be seen toward the nipple. ....	12
<b>Figure 2.2.</b> Resolution limit versus magnification factor for detector and focal spot blurring. ....	16
<b>Figure 2.3.</b> (A) A schematic showing how a bar pattern in the object plane is projected to the image plane. (B) A plot of the MTF versus the spatial frequency demonstrating improvement in the MTF by re-scaling the spatial frequency in magnification mammography. ....	19
<b>Figure 2.4.</b> A schematic of the experimental setup for the MTF measurements for magnification digital mammography. ....	25
<b>Figure 2.5.</b> Schematic showing how a composite LSF is generated (C) from the LSFs corresponding to the slit alignment (B) relative to the sampling coordinate (A). ....	26
<b>Figure 2.6.</b> A schematic of the experimental setup for the NPS measurements for magnification digital mammography. ....	28
<b>Figure 2.7.</b> A plot of the MTF (theoretical) versus the spatial frequency showing the effects of magnification on the MTF. The MTF was measured for $M = 1.0$ and then re-scaled for various $M$ s. ....	31
<b>Figure 2.8.</b> A plot of the MTF (measured) versus the spatial frequency showing the effects of magnification on the MTF. ....	32
<b>Figure 2.9.</b> A plot of the measured MTF versus the magnification factor at various spatial frequencies. ....	33
<b>Figure 2.10.</b> A plot of the NPS versus the spatial frequency for various $M$ s. The NPS was measured for $M = 1$ then re-scaled for various $M$ s. ....	34
<b>Figure 2.11.</b> A plot of the NEQ versus the spatial frequency for various $M$ s. The spatial frequency has been re-scaled to the object plane. ....	35
<b>Figure 3.1.</b> A schematic of a phantom piece showing a single arrangement of the $\mu$ Cs on a $2 \times 2 \text{ cm}^2$ Lucite block. ....	40

- Figure 3.2.** Schematic drawing of the tiled Lucite squares showing the placement of the  $\mu\text{C}$  phantom piece. Also shown is the placement of the tiled Lucite squares on the 1 cm 50% adipose/50% glandular tissue phantom. .... 41
- Figure 3.3.** A schematic drawing of the 4 cm phantom showing the placement an additional 3 cm of 50% adipose/50% glandular tissue phantom material..... 42
- Figure 3.4.** A schematic of the experimental setup for the magnification phantom study showing the placement of the  $\mu\text{C}$ s and how  $M$  was determined..... 44
- Figure 3.5.** Plot showing the minimum detectable  $\mu\text{C}$  size of the two imaging systems at various  $M$ s for the 1 cm phantom..... 49
- Figure 3.6.** Plot showing the minimum detectable  $\mu\text{C}$  size of the two imaging systems at various  $M$ s for the 4 cm phantom..... 50
- Figure 3.7.** Comparison of the ROC curves for the detection of  $\mu\text{C}$ s for the two imaging systems using the 1 cm phantom. .... 52
- Figure 3.8.** Comparison of the ROC curves for the detection of  $\mu\text{C}$ s for the two imaging systems using the 4 cm phantom. .... 54
- Figure 4.1.** A compressed breast showing the tissue thickness ( $t_a$ ,  $t_b$  and  $t_c$ ) and the path that the x-ray photons travel when passing through. .... 59
- Figure 4.2.** Plot showing the absorption ratios of the  $\text{Gd}_2\text{O}_2\text{S:Tb}$  and  $\text{CsI:Tl}$  scintillators. The  $\text{CsI:Tl}$  scintillator shows a greater absorption at higher energies due to its k-edges at 33.2 and 36 keV..... 74
- Figure 4.3.** Plot showing the signal spectra for the  $\text{Gd}_2\text{O}_2\text{S:Tb}$  and  $\text{CsI:Tl}$  scintillators using a 25 kVp Mo/Mo incident spectrum. The spectra are identical..... 75
- Figure 4.4.** Plot showing the signal spectra for the  $\text{Gd}_2\text{O}_2\text{S:Tb}$  and  $\text{CsI:Tl}$  scintillators using a 50 kVp Mo/Mo incident spectrum. .... 76
- Figure 4.5.** Plot showing the signal spectra for the  $\text{Gd}_2\text{O}_2\text{S:Tb}$  and  $\text{CsI:Tl}$  scintillators using a 50 kVp W/La incident spectrum. .... 77
- Figure 4.6.** A plot of the  $CCNR$  and  $CCBR$  for energies ranging from 25 to 140 keV. The W represents the spectra that were generated with a tungsten target. .. 79
- Figure 4.7.** A plot of the x-ray densities,  $D'_l$  and  $D'_h$ , as functions of  $t_b$  and  $t_c$  ..... 81

- Figure 4.8.** Plot of  $\sigma_{t_c}$  as a function of the low-energy exposure ratio for various  $\mu C$  sizes using the  $Gd_2O_2S:Tb$  scintillator. .... 83
- Figure 4.9.** Plot of  $\sigma_{t_c}$  as a function of the low-energy exposure ratio for various  $\mu C$  sizes using the  $CsI:Tl$  scintillator..... 84
- Figure 4.10.** Plot of  $\sigma_{t_c}$  as a function of the low-energy exposure ratio for various combinations of energy spectra using the  $Gd_2O_2S:Tb$  scintillator. .... 86
- Figure 4.11.** Plot of  $\sigma_{t_c}$  as a function of the low-energy exposure ratio for various combinations of energy spectra using the  $CsI:Tl$  scintillator. .... 87
- Figure 4.12.** Plot of  $\sigma_{t_c}$  as a function of the low-energy exposure ratio for various tissue compositions using the  $CsI:Tl$  scintillator..... 88
- Figure 4.13.** Plot of  $\sigma_{t_c}$  as a function of the low-energy exposure ratio for various breast thickness using the  $CsI:Tl$  scintillator..... 89

## Lists of Tables

<b>Table 1.1.</b> Table outlining some of the advantages and disadvantages of magnification mammography.....	7
<b>Table 3.1.</b> Table showing the size ranges of the pre-sifted $\mu\text{C}$ 's and the typical sizes used for the analysis. ....	40
<b>Table 3.2.</b> Table showing the mAs values used in acquiring the screen/film and digital images for both the 1 cm and the 4 cm 50% adipose/50% glandular tissue phantoms.....	46
<b>Table 4.1.</b> Table showing the different materials used in the simulation studies and the density values ( $\rho$ ) used to convert ( $\mu/\rho$ ) to ( $\mu$ ).....	69
<b>Table 4.2.</b> Table showing the ranges of low-energy exposure ratios for simulations with various tissue compositions, breast thicknesses and $\mu\text{C}$ thicknesses. ....	91

## Chapter 1 – Introduction and Background

### 1.1 Introduction

“Breast cancer is the most common cancer among women, excluding skin cancer” (<http://www.wcn.org>, 1998). In the United States, 1 out of every 8 women will develop breast cancer, and 1 out of 28 are at risk of dying from it. The increased use of screening mammography has resulted in earlier detection of breast cancer. Earlier detection has led to an increase in the 5-year survival rate from 40% in the 1940’s to 97% today (<http://www.wcn.org>, 1998).

Early mammograms were done using a non-screen, direct film exposure technique. These images were of poor diagnostic quality and required high doses of radiation. In the 1970’s and early 1980’s, xeroradiography became the mammography imaging technique of choice. Its poor contrast sensitivity and high radiation dose led to its being replaced by screen/film mammography in the 1980’s (Bushberg et al., 1994). Currently, screen/film mammography is the clinical standard for breast imaging.

A screen/film system consists of a single emulsion film and a single high-definition screen cassette. The most common type of screen/film system used is a gadolinium oxysulfide terbium doped ( $Gd_2O_2S:Tb$ ) phosphor screen, which emits green light when exposed to radiation, and a green-sensitive single emulsion film (Bushberg et al., 1994). There are many problems inherent in a screen/film imaging system, the most common being the processing of the film. During the imaging processing cycle, image artifacts, light leak or film fogging, incorrect developer temperature, chemical contamination, and/or film jams in the processor may compromise image quality.

The screen also limits the system in the amount of radiation dose needed to correctly expose the film. Using a faster screen means that less dose can be used to acquire the image. The trade-off is that there will be a decrease in the image

resolution. With a slower screen, there is an increase in dose and an increase in image resolution. The film itself can also be a limiting factor of the system. With a faster speed film, the contrast sensitivity of the system will decrease due to an increase in the quantum and grain noise. Although screen/film mammography is the clinical standard, it is far from perfect. In recent years, there have been many technological advances in digital imaging and computed radiography with applications in digital mammography (Karellas et al., 1992; Williams and Fajardo, 1996; Hejazi and Trauernicht, 1997; Vedantham et al., 2000, Vedantham et al., 2000). Many observers believe that screen/film mammography will eventually be replaced by digital mammography.

### **1.1.1 Statement of the Problem**

Digital mammography may become the mammography standard of the future. There has been and continues to be a vast amount of research performed on digital mammography. Currently, the major clinical use of digital mammographic techniques is for stereotactic needle localizations and core biopsies. Digital mammography has been recently initiated at several centers.

Screening and diagnosis in mammography rely on the detection of microcalcifications ( $\mu$ Cs) and/or soft tissue masses. Early detection is important in the diagnosis and treatment of breast disease. The detection and visualization of  $\mu$ Cs is relatively easy with an uncluttered soft tissue background but difficult and problematic in breasts with dense tissue structures. The "cluttered" background present in mammograms also tends to limit the detectability and visibility of  $\mu$ Cs and masses. Also important is an improved ability to depict finer image details in mammograms.

### **1.1.2 Hypotheses**

1. Magnification techniques can be used to improve the physical image quality parameters of a digital mammography system.

2. Magnification techniques can be used to improve the detectability of  $\mu\text{Cs}$  using a digital mammography system.
3. Dual-energy subtraction imaging techniques can be used to improve the detectability of  $\mu\text{Cs}$  in dense tissue structures by removing the background tissue structure from the image.

### **1.1.3 Goals and Objectives**

The goals of this research were to determine (1) the effects of magnification on the image quality parameters of a digital mammography system, (2) improvement of the detectability of  $\mu\text{Cs}$  by using magnification in digital mammography, (3) the feasibility of using a dual-energy subtraction imaging technique to improve the detectability of  $\mu\text{Cs}$  in dense tissue structures.

The objectives for testing the hypotheses for this research were as follows:

1. Measure and study the effects of magnification and focal spot blurring on the modulation transfer function (MTF); measure and compare the effects of magnification on the noise power spectra (NPS) and noise equivalent quanta (NEQ).
2. Perform a phantom study to compare screen/film and digital images for  $\mu\text{C}$  detectability for various magnification factors.
3. Perform numerical studies to determine the optimal dual-energy image acquisition parameters, to study the effects of energy separation,  $\mu\text{C}$  size, breast tissue composition and breast thickness on noise levels in the subtracted images and to show the feasibility of using dual-energy subtraction imaging to improve the detection of  $\mu\text{Cs}$  by performing a signal-to-noise ratio analysis.

## 1.2 Background

### 1.2.1 Digital Mammography

Initial work in digital mammography involved the digitization of screen/film mammograms. The problems resulting from this process were the time needed to digitize the films, the quality of the original image and the quality of the digitizer itself (Parkin, 1995). The next step was computed radiography (CR) using photostimulable phosphors (PSP). Many studies have shown that the resolution of PSPs is less than that of conventional screen/film systems; however, PSPs have a greater range of contrast detail (Funke et al., 1998; Brettle et al., 1994). The resolution of a CR system is limited by the scanning laser used to read out the latent image from the phosphors. The maximum resolution of a PSP system is 5 lp/mm compared to approximately 20 lp/mm for a screen/film system (Funke et al., 1998). Despite this, subjectively better results for CR with PSPs compared to screen/film mammography were found in a clinical study by Brettle et al. (1994). Funke et al. (1998) have also shown that magnification mammography with PSPs is, "... a realistic alternative to conventional screen-film technique in mammography and an intermediate step on the way to direct digital mammography."

Direct digital mammography (DDM) offers many potential advantages over screen/film systems. These include improved processing for the enhancement of specific image features, improved image handling, such as a picture archiving and communication system (PACS), computer-aided diagnosis (CAD), and the possibility of reduced radiation dose (Parkin, 1995; Funke et al., 1998; Schmidt and Nishikawa, 1995). Some of the current DDM technologies include charge-coupled-devices (CCD), amorphous silicon TFT (thin-film transistor) flat-panel detectors, and amorphous selenium digital image detectors (Cowen et al., 1997). Many of these techniques are still under investigation. The expectation is that DDM will produce results similar to, or better than, those from CR.

Boyle and Smith (1970) developed the CCD in 1970. The dynamic range characteristics and compact size of the CCD have led to it replacing vacuum camera

tubes in commercial and home video equipment and it also has many applications in digital imaging (Yaffe and Rowlands, 1997). A CCD is a series of electrodes deposited on a semiconductor substrate. When voltage is applied to the electrodes, the semiconductor material is depleted and charge storage wells are formed. The charge that is injected into the CCD is then stored in these wells and read out to produce an image

The charge in a CCD is transferred over many adjacent elements. Therefore, it is critical that the transfer efficiency be extremely high. A serious loss in spatial resolution will result from a lack of transfer efficiency. The well storage capacity of the CCD is also important. The CCDs used in video applications are designed to have an extremely small (15  $\mu\text{m}$ ) pixel size (Yaffee and Rowlands, 1997). A pixel size of 25-100  $\mu\text{m}$  is desirable for medical applications because the bigger well size, in comparison to that for video applications, is better suited for the demands of spatial resolution (Yaffe and Rowlands, 1997).

In medical imaging, a scintillating or intensifying screen must be imaged onto a CCD in order to produce an image. Due to the higher collection efficiency of fiberoptic couplers, they are generally used to couple the screen to the CCD camera (Karellas et al., 1992; Hejazi and Trauernicht, 1997). This higher collection efficiency means that less exposure is needed to produce an image. A decrease in exposure results in a decrease in the average glandular dose to the tissue. This will also decrease the exposure time and the integration time of the CCD. The spatial resolution of the CCD based detector is less than that of screen/film systems and could be a limiting factor. However, this may be sufficient because of an increase in contrast discrimination in the images (Karellas et al., 1992).

Two areas that may benefit from DDM and CCD technology are spot magnification mammography and dual-energy subtraction imaging. Magnification techniques in screen/film mammography have shown improvement in the detection and analysis of  $\mu\text{Cs}$  (Sickles, 1980; Muntz, 1981; Sickles, 1982; Funke et al., 1998). With digital techniques, the processes of acquiring and viewing a magnified image will be improved over those of screen/film techniques. Dual-energy subtraction

imaging has shown promising results in early studies (Johns et al., 1985; Asaga et al., 1995). Asaga et al. (1995) demonstrated an improvement in diagnostic accuracy in approximately 50% of their patients with breast cancer using dual-energy subtraction. Recent advances in digital imaging may lead to the clinical implementation of dual-energy mammography. With direct digital techniques, image registration should not be a limiting factor. The detector has a fixed area and position. As a result of this, when using dual-exposure techniques, the compressed breast will remain in the same position for both exposures. The patient's comfort will not be a limiting factor either since the length of time needed to make two exposures is negligible.

### 1.2.2 Magnification Mammography

Magnification techniques are often employed in mammography in order to aid in the characterization of  $\mu$ Cs and the margins of masses. Magnification mammography can improve the visibility of fine details and the detectability of breast lesions (Kopans, 1998). Previous studies have been done that showed the advantages of magnification mammography versus normal (contact) mammography (Sickles et al., 1977; Muntz and Logan, 1979; Sickles, 1980; Muntz, 1981; Sickles, 1982). The improvement in image quality with magnification is related to the focal spot size, the x-ray tube output, the detector, the air-gap size and the target dimension in a complicated interplay (Muntz and Logan, 1979). However, due to the technical difficulties involved in producing a magnified image, it is not uncommon to find no improvement in, or even see a degradation in, the image quality when compared to non-magnified images (Peters et al., 1989).

Magnification imaging is not used for the initial screening mammography examination. Magnified images are generally reserved for evaluating suspicious areas in the hope of obtaining an image with more definitive diagnostic information (Peters et al., 1989). Some clinical indications for performing magnification studies include, but are not limited to, determining whether  $\mu$ Cs are present, analyzing the geometry and distribution of  $\mu$ Cs, detecting additional fine calcifications, excluding or

verifying the presence of multiple foci and assessing the extent of carcinomas with  $\mu$ Cs (Heywang-Köbrunner et al., 1997).

Along with the clinical indications for performing magnification imaging, there are also technical and clinical advantages and disadvantages of magnification mammography. Some of the advantages of magnification imaging include increased effective resolution (by the magnification factor), increase in the number of photons per unit object area (reduction of effective image noise due to increased dose), reduction of x-ray scatter reaching the detector and improved low contrast detectability (Bushberg et al., 1994; Egan, 1988; Peters et al., 1989). However, there are also many disadvantages, the most significant being the increase in radiation dose to the patient. Using a magnification factor of 2X could result in an increase in dose of approximately 5.4 times that used for a non-magnified image (Egan, 1988). Table 1.1 outlines some of the advantages and disadvantages of magnification mammography (Bushberg et al., 1994; Egan, 1988; Heywang-Köbrunner et al., 1997; Peters et al., 1989).

**Table 1.1** Table outlining some of the advantages and disadvantages of magnification mammography.

<b>Advantages</b>	<b>Disadvantages</b>
Increased effective resolution	Increased dose to the breast
Reduced scatter	Requires small focal spot
-improved contrast-to-noise ratio	Limited by tube output
-improved low-contrast detectability	Longer exposures
	Increased chance of motion
	Limited field of view

### 1.2.3 Dual-Energy Imaging

The technique of radiographic subtraction was introduced in 1935 by Ziedses des Plantes. The first English paper was published 27 years later by Hanafee and

Stout (1962) (Jeans, 1990). This paper commented on a photographic method of reducing the confusion due to bony structures in angiographic studies. The advantages of image subtraction were summarized as (a) providing image enhancement and (b) improving and bringing out detail in areas hidden by overlying bone or poor contrast (Jeans, 1990).

Jeans (1990) listed three types or techniques for digital subtraction; they are temporal, energy and hybrid subtraction. Temporal subtraction uses a mask image that is subtracted from images that are contrast enhanced. Energy subtraction uses high- and low-energy x-rays. The images are digitized and subtracted and the subtraction images yield either bone or vessel detail (Jeans, 1990). The hybrid method, as the name implies, is a combination of energy subtraction images used to perform a temporal subtraction. The resultant images are able to remove both the overlying bone and any motion artifacts.

Image subtraction is a technique employed in angiography in order to reduce the anatomical image clutter and allow the radiologist to concentrate on the vascular anatomy (Bushberg et al., 1994). This image clutter is referred to as structured noise, and it does limit the quality of the image. The radiographic shadows of the normal anatomy are superimposed on the image over the anatomy of interest. This can obscure the anatomical detail in question and make it more difficult for the radiologist to make an accurate diagnosis. Since angiograms are acquired in sequence, they are ideally suited for image subtraction as a way of removing the background anatomy from the image.

Another method for performing subtraction imaging is dual-energy subtraction. Dual-energy subtraction is a combination of radiographic images obtained using two different x-ray energies to produce either a bone-free or a soft tissue-free image (Ho et al., 1989). An advantage of this method is that the images do not need to be acquired before and after the arrival of a contrast medium. The images for dual-energy subtraction are taken over a very short time interval in which there is no significant patient motion. These images are acquired using different x-ray spectra,

such as those obtained using high- and low-kVp (kilo-voltage peak) energies (Curry et al., 1990).

The differential attenuation between different tissue types is higher at the lower kVp than it is at the higher kVp. Since the photoelectric effect decreases rapidly with increasing energy, the attenuation in dense tissue (i.e., bone) changes more than that in less dense (soft) tissue. When subtracting the two images, high- and low-energy, if the soft tissue contrast is made to be equivalent, the bone contrast will not be. In this case, the resultant image will consist of only the bone and noise that is associated with the image subtraction (Curry et al., 1990).

Dual-energy images can be acquired using either a single- or a dual-exposure technique. For the single-exposure technique, the images are acquired simultaneously using an energy-selective, dual-detector system (Stewart and Huang, 1990). Many such detector systems have been discussed in the literature (Barnes et al., 1985; Stewart and Huang, 1990; Ergun et al., 1990; Fraser et al., 1986; Chakraborty and Barnes, 1989; Boone et al., 1990). These systems, commonly referred to as sandwich detectors, consist of two detectors, either screen/film combinations or CR imaging plates, that are separated by an interdetector filter. The front detector, which is composed of a low atomic number screen or slow screen/film speed combination, preferentially absorbs the low-energy x-ray photons. The high-energy photons pass through the front detector and are absorbed by the back detector, which is composed of a high atomic number screen or a fast screen/film speed combination. The interdetector filter (typically copper) is used to attenuate the photons passing through the primary/front detector and increase the effective x-ray energy of the photons reaching and being absorbed by the back detector (Chakraborty and Barnes, 1989; Stewart and Huang, 1990). Some advantages of the single-exposure technique include the fact that both images are acquired simultaneously, there is less chance for patient motion and misregistration of the images, decreased tube loading complications, and possibly less exposure to the patient when compared to the dual-exposure technique (Chakraborty and Barnes, 1989; Ergun et al., 1990; Fraser et al., 1986). Some of the disadvantages include less energy separation between the high- and low-energy

images, decreased SNR when compared to the dual-exposure technique (Ho et al., 1989), and increased beam hardening (Ergun et al., 1990).

For the dual-exposure technique, two separate images are acquired using pre-determined high- and low-kVps. The images are taken rapidly in succession in order to reduce motion artifacts and misregistration. Some advantages of the dual-exposure technique include a higher SNR in the subtracted image and a higher energy separation when compared to the single-exposure technique (Ho et al., 1989). The main disadvantage of this technique is the amount of radiation exposure required to acquire the images. This results in a higher radiation dose to the patient and also contributes to an increase in x-ray tube loading complications. The dual-exposure dual-energy subtraction technique has been applied to mammography and has shown promising results (Johns and Yaffe, 1985; Johns et al., 1985; Asaga et al., 1995).

### 1.3 Summary

Digital mammography may eventually replace screen/film mammography as the clinical standard for breast imaging. Magnification mammography and dual-energy subtraction imaging are areas that may benefit from the implementation of digital mammography. The purpose of this research was to determine the effects of geometric magnification on the image quality parameters and the improvement in  $\mu\text{C}$  detectability of a digital mammography system and to determine the feasibility of using a dual-energy subtraction imaging technique to improve  $\mu\text{C}$  detectability in dense tissue structures.

## Chapter 2 – Magnification Digital Mammography: Image Quality Parameters

### 2.1 Introduction

Geometric magnification has been widely used in angiography and mammography to improve the image quality and allow more image details to be seen. In contrast to other forms of magnification, geometric magnification is achieved by taking advantage of the fact that the x-rays used in diagnostic imaging originate from a nearly point source- the focal spot. Thus, the divergent x-rays project and magnify the objects onto the input of the detector, referred to as the image plane. This process is illustrated in Figure 2.1 (Bushberg et al., 1994) in which the magnification factor can be calculated as the ratio of the source-to-image distance (SID) to the source-to-object distance (SOD). Because geometric magnification is the only form of magnification addressed in this paper, the word “magnification” will be used to refer to geometric magnification throughout this paper.

Much work has been done previously to study and understand the effects of magnification on image quality in angiography (Burgess, 1977; Kruger, 1982) and to a smaller extent in mammography (Muntz, 1981). Magnification was found to improve the visibility of fine details and the detectability of breast lesions (Kopans, 1998). In addition to magnified image details, the image quality improvement achieved in magnification imaging originates from a reduction of scattered radiation present in the image by increasing the air gap (distance between the breast and the detector) (Muntz, 1979). The increased air gap results in a smaller solid angle with which the detector is exposed to scattered radiation. Due to this scatter rejection effect in magnification imaging, an anti-scatter grid is generally not used for magnification mammography.

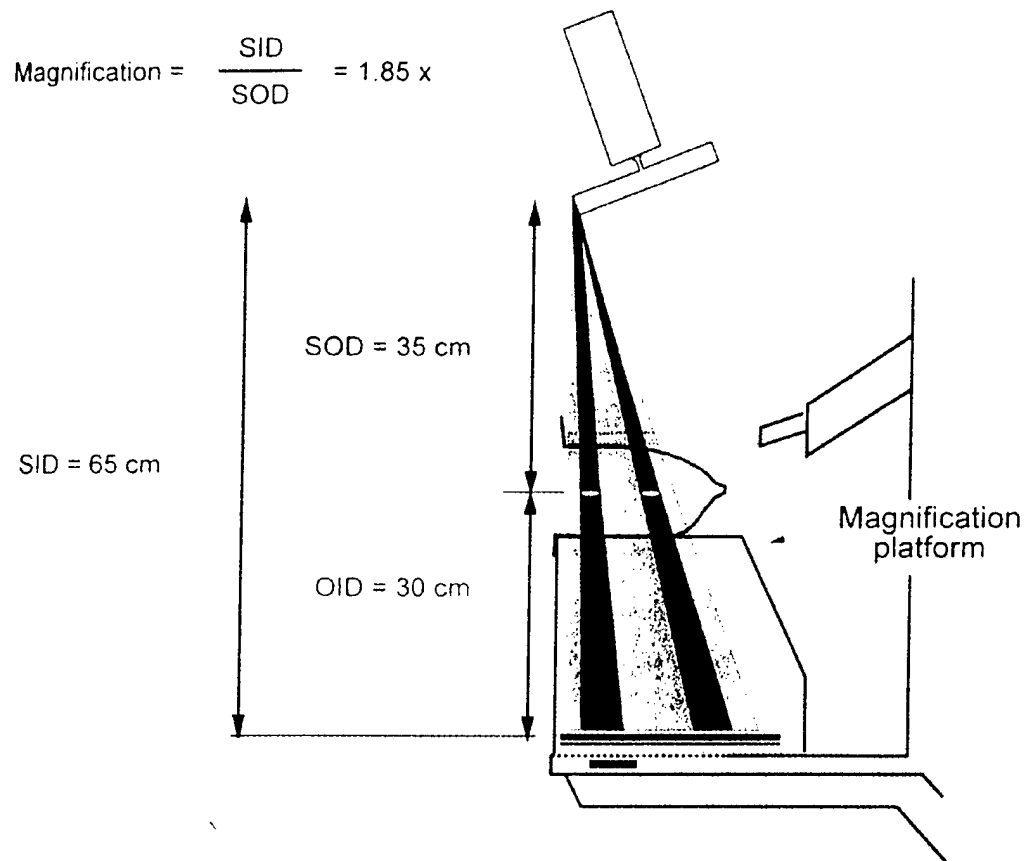


**Figure 2.1.** Geometric blurring in magnification mammography is greater on the cathode side (chest wall). The divergence of the x-ray beam allows for better resolution to be seen toward the nipple.

It is well known that the image quality improvement in magnification imaging is limited by the focal spot blurring effect. The overall image quality depends on the focal spot size, x-ray tube output, detector quality and the air-gap size in a complicated interplay (Muntz and Logan, 1979). It has been reported that magnification could significantly reduce the quantum mottle per unit average dose as well as increase the contrast of the image (Muntz 1979). However, it has also been reported that due to technical difficulties involved in producing magnified images, it is not uncommon to find no improvement or even see a degradation in the resulting image quality when compared to non-magnified images (Peters et al., 1989). Some of these difficulties resulted from the necessity of using a smaller focal spot, which in turn limits the mA setting. This results in prolonged exposures during which patient motion can result in image blurring (Peters et al., 1989).

The improvements and limitations of image quality in magnification imaging have been previously investigated for mammographic imaging (Sickles et al., 1977; Muntz and Logan, 1979; Sickles, 1980; Muntz, 1981; Sickles, 1982). However, such studies have been performed with screen/film techniques. While screen/film mammographic techniques have been substantially improved over the years, the use of film as the image storage and display medium has been recognized as having some limitations in image quality, display, storage and management. Aided by advances in digital technology, digital image acquisition, storage, display and distribution are regarded as the inevitable future direction in mammographic imaging. Out of the need to improve image quality and to generate digital images, various digital mammography techniques have been developed. Due to degradation by the image digitization process, these techniques may be limited in spatial resolution while having better or slightly worse low contrast performance, depending on the detector used. However, most digital techniques offer a linear response over a wide exposure range and the flexibility of reprocessing the image data before image display or printing. These differences in image quality and features may affect the image quality considerations in magnification imaging. Thus, in order to optimize the use of

magnification imaging techniques with digital mammography systems, it is essential to re-examine and study the effects of magnification on digital image quality.

In this section, the effects of magnification on image quality parameters are re-examined in the context of digital mammography. Simple models are described and used to describe and discuss the effects of magnification on the Modulation Transfer Function (MTF), Noise Power Spectrum (NPS) and Noise Equivalent Quanta (NEQ). The effects were measured using a small-field digital mammography system.

## 2.2 Theory

### 2.2.1 Modulation Transfer Function (MTF)

The spatial resolution properties of an imaging system are often characterized by the MTF. The MTF is generally defined as the ratio of the output signal amplitude to the input signal amplitude at a specific frequency when the input signals are sinusoidal:

$$MTF = \frac{\text{output signal amplitude}}{\text{input signal amplitude}} \quad (2.1)$$

By definition, the MTF is equal to 1 at the zero frequency. A simple model for the MTF (Shaw et al., 2000) will be presented and used to discuss the effects of magnification on image quality.

#### A. Spatial Resolution Limitations

The effects of magnification and focal spot blurring on spatial resolution in magnification imaging are well known and have been discussed previously (Kruger, 1982; AAPM Report No. 15, 1985). Most discussions were based on the concept of "resolution limit", which is generally defined as the maximum spatial frequency of the resolvable bar pattern. However, to visualize any low contrast objects, the high frequency bar pattern in this case, the perceived contrast of the object must exceed the noise level in the background. Thus, the spatial resolution limit can be defined

quantitatively as the frequency beyond which the MTF value drops below a certain threshold. Since this threshold is required to exceed the noise level in the background, its value depends on the exposure and other factors affecting the noise levels. For radiographic exposures, this threshold MTF value generally ranges from 5 to 10%.

Using the resolution limits of the detector in the image plane ( $f_0$ ) and the focal spot size ( $a$ ), the resolution limits in the object plane for the detector,  $f_D(M)$ , and focal spot blurring,  $f_F(M)$ , can be expressed as a function of the magnification factor ( $M$ ) as follows:

$$f_D(M) = M \cdot f_0 \quad (2.2)$$

and

$$f_F(M) = \frac{M}{(M-1) \cdot 2a} \quad (2.3)$$

As an example,  $f_D(M)$  and  $f_F(M)$  are plotted for a focal spot size of 0.1 mm and a detector resolution limit of 10 lp/mm in Figure 2.2. It is generally argued that when

$$f_D(M) = f_F(M) \quad (2.4)$$

or

$$M \cdot f_0 = \frac{M}{(M-1) \cdot 2a} \quad (2.5)$$

that  $M$  is optimized for spatial resolution (Shaw et al., 2000). The optimal  $M$ ,  $M_{opt}$ , and the optimized resolution limit,  $f_{opt}$ , are then given by:

$$M_{opt} = 1 + \frac{1}{2a \cdot f_0} \quad (2.6)$$

and

$$f_{opt} = M_{opt} f_0 = f_0 + \frac{1}{2a} \quad (2.7)$$

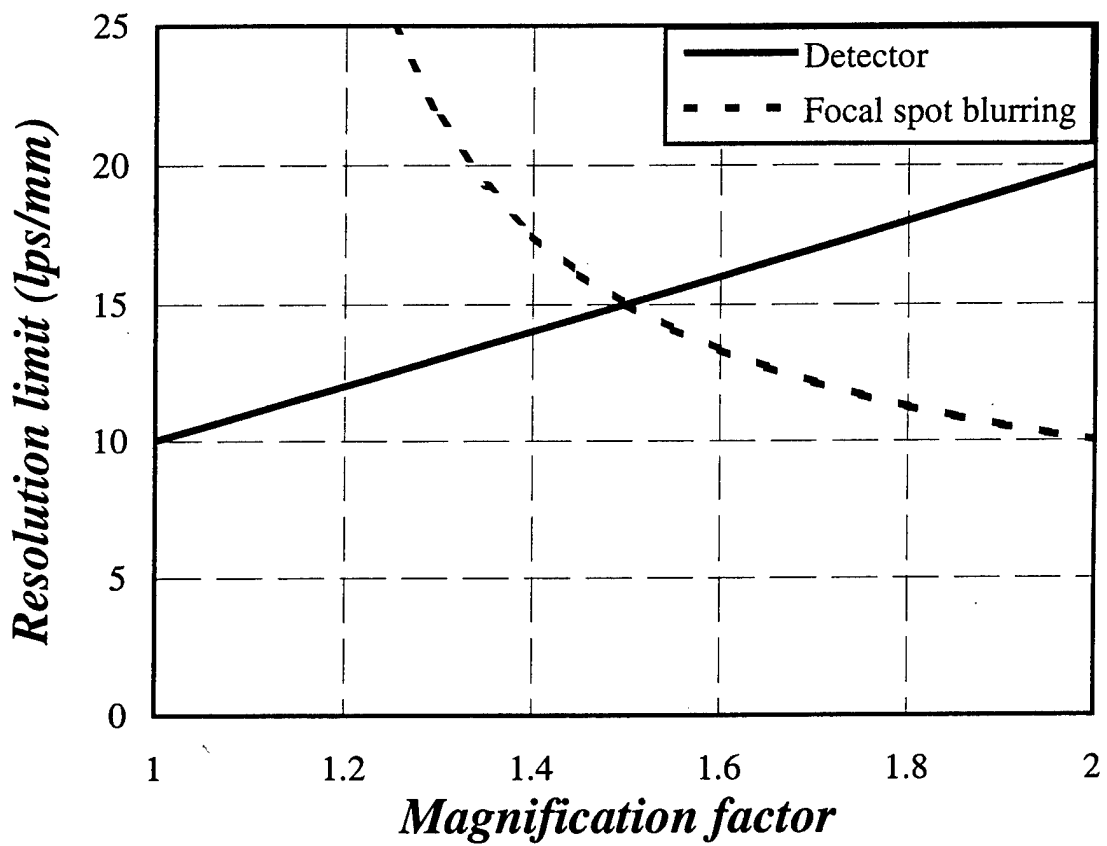


Figure 2.2. Resolution limit versus magnification factor for detector and focal spot blurring.

## B. MTF and Magnification

The above derivation is based on the concept of "spatial resolution limit". However, the spatial resolution of an imaging system is often characterized by measuring the MTF. Thus, it would be more rigorous to study the effects of magnification on the MTF and to optimize the magnification factor for the best MTF. It would also be interesting to see if these two approaches can be related to each other.

The concept of the MTF was originally developed to quantitatively address the image quality of image detectors. These quantities are generally defined and measured as a function of the spatial frequency at the input of the image detector, often referred to as the image plane. In magnification imaging, in addition to blurring in the detector, there is also the focal spot blurring effect, which occurs prior to x-ray detection and is part of the magnification process. The magnification changes the size as well as the sharpness of the objects as seen by the detector. To study and quantify the overall effect of magnification on the overall sharpness in the image, it is necessary to incorporate the image magnification, detector blurring and focal spot blurring into a single MTF. This MTF should be defined and measured as a function of the spatial frequency in the object plane rather than the image plane as this would provide the correct perspective on how well an object can be resolved.

To simplify the discussion, it is assumed that the intensity profile of the focal spot and point spread function for the detector are both Gaussian functions. Limiting the study to a one-dimensional case, the detector MTF at the detector input,  $MTF_D(f;l)$ , can be modeled as a Gaussian function as follows:

$$MTF_D(f;l) = e^{-\frac{cf^2}{f_b^2}}, \quad (2.8)$$

where the constant  $c$  can be adjusted so that the "resolution limit" can be set for various threshold MTF values. With magnification, the MTF can be defined for the object plane. The spatial frequency becomes higher by a factor of  $M$  and the detector MTF in the object plane,  $MTF_D(f;M)$ , is related to that in the image plane,  $MTF_D(f;l)$ , as follows:

$$MTF_D(f; M) = MTF_D\left(\frac{f}{M}; 1\right) = e^{\frac{-cf^2}{(Mf_D)^2}} \geq MTF_D(f; 1). \quad (2.9)$$

Thus, the MTF in the object plane is effectively improved because it corresponds to the MTF in the image plane at a lower frequency (scaled down by a factor of  $M$ ). This is a different way of describing the fact that the object is magnified in the image plane, therefore the same MTF would work better to preserve the sharpness of the object image. Alternatively, the improvement can be attributed to re-scaling of the spatial frequency,  $f$ . This mechanism is illustrated by Figure 2.3.

Also associated with magnification is the focal spot blurring effect. This effect can be modeled and described as a line spread function in the image plane,  $LSF_F(x; 1)$ , as follows:

$$LSF_F(x; 1) = e^{\frac{-x^2}{c[a(M-1)]^2}}, \quad (2.10)$$

where  $a$  is the focal spot size. Depending on the constant  $c$ ,  $a$  can be defined as the Full Width Half Maximum (FWHM),  $1/e^2$  width or other quantities characterizing the focal spot size. The presence of the factor  $M - 1$  reflects the fact that the focal spot is projected onto the image plane through a point in the object plane. To determine the MTF for focal spot blurring in the object plane,  $LSF_F(x; 1)$  can be projected back to the object plane and the LSF in the object plane can be expressed as:

$$LSF_F(x; M) = e^{\frac{-x^2}{c\left[\frac{a(M-1)}{M}\right]^2}}. \quad (2.11)$$

Notice that this is equivalent to back projecting the image of the focal spot and results in a smaller (by a factor of  $M$ ) image in the object plane. Thus, the MTF for focal spot blurring in the object plane,  $MTF_F(f; M)$ , can be expressed as:

$$MTF_F(f; M) = e^{\frac{-cf^2}{\left[\frac{M}{(M-1)a}\right]^2}} = e^{\frac{-cf^2}{f_F(M)^2}}, \quad (2.12)$$

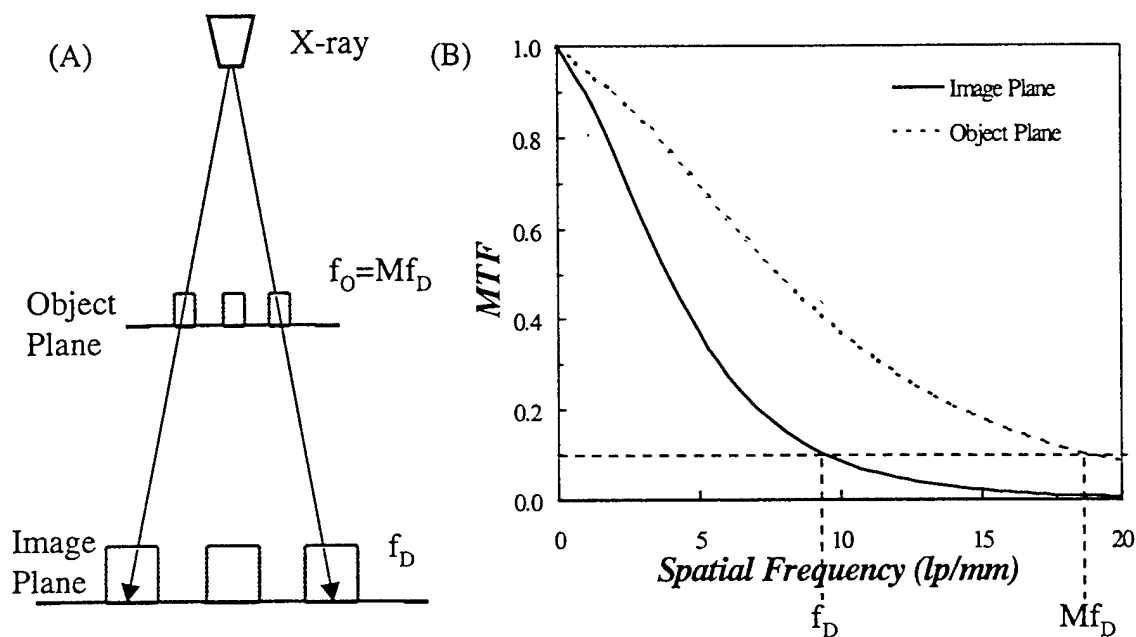


**Figure 2.3.** (A) A schematic showing how a bar pattern in the object plane is projected to the image plane. (B) A plot of the MTF versus the spatial frequency demonstrating improvement in the MTF by re-scaling the spatial frequency in magnification mammography.

where  $f_F(M)$  is the resolution limit for focal spot blurring:

$$f_F(M) = \frac{M}{(M-1)\pi a}. \quad (2.13)$$

The overall MTF in the object plane can then be expressed as:

$$\begin{aligned} MTF_o(f; M) &= MTF_D(f; M) \cdot MTF_F(f; M) \\ &= e^{\frac{-f^2}{(Mf_0)^2}} \cdot e^{\frac{-f^2}{f_F(M)^2}} \\ &= e^{-f^2 \left[ \frac{1}{(Mf_0)^2} + \frac{1}{f_F(M)^2} \right]} \end{aligned} \quad (2.14)$$

The overall resolution limit becomes:

$$f_o(M) = \frac{1}{\sqrt{\frac{1}{(Mf_0)^2} + \frac{1}{f_F(M)^2}}} = \frac{1}{\sqrt{\frac{1}{(Mf_0)^2} + \left[ \frac{(M-1)\pi a}{M} \right]^2}}. \quad (2.15)$$

### C. MTF Optimization

The overall  $MTF_o(f; M)$  is optimized by;

$$\frac{\partial}{\partial M} \left[ \frac{1}{f_o(M)} \right] = \frac{\partial}{\partial M} \left[ \frac{1}{(Mf_0)^2} + \left[ \frac{(M-1)\pi a}{M} \right]^2 \right] = 0. \quad (2.16)$$

This can be easily solved for the optimal magnification factor,  $M_{opt}$ :

$$M_{opt} = 1 + \frac{1}{f_0^2 (\pi a)^2} \quad (2.17)$$

and the optimized resolution limit,  $f_{opt}$ :

$$f_{opt} = M_{opt} f_0 = f_0 + \frac{1}{f_0 (\pi a)^2}. \quad (2.18)$$

Notice that both  $M_{opt}$  and  $f_{opt}$  depend on the term:  $f_0(\pi a)$  which characterizes the resolution limit of the detector in relation to the focal spot size,  $a$ . As  $a \gg \frac{1}{\pi f_0}$ ,

$M_{opt} \approx 1$  and  $f_{opt} \approx f_0$ , indicating that improvement is not feasible. As  $a \ll \frac{1}{\pi f_0}$ ,

$M_{opt} \approx \frac{1}{f_0^2 (\pi a)^2}$  and  $f_{opt} \approx \frac{1}{\pi a}$ , indicating that the improvement is only limited by the focal spot size.

## 2.2.2 Noise Equivalent Quanta (NEQ)

### A. Noise Power Spectrum (NPS)

Noise in digital x-ray imaging may originate from the x-ray detection, light detection or the electronics. The structural pattern of the scintillator can also contribute to the random noise pattern overlapping with anatomical information. The noise originating from x-ray detection is often referred to as the x-ray quantum noise. Noise from other sources is typically referred to as the system noise. A properly designed imaging system should be “quantum-limited,” which means that the x-ray quantum noise is the dominant source of noise. The signal-to-noise ratio (SNR) of a quantum limited imaging system depends mainly on the number of x-ray photons that produce the pixel signal. This equals the product of the number of photons falling on a pixel and the x-ray absorption ratio of the detector. The latter depends on the scintillator used in the imaging system.

The pixel size in digital imaging can have a significant effect on the image noise as computed from the pixel values. Larger pixels receive more x-ray photons than smaller pixels thus producing a better SNR in proportion to the pixel size and  $SNR^2$  in proportion to the pixel size squared. However, the number of pixels used to represent an object or a unit area (e.g.  $mm^2$ ) is inversely proportional to the pixel size squared. Thus, if  $SNR^2$  is measured for the entire object or a unit area, the effect of a smaller pixel size would be offset by the larger number of pixels representing the object or unit area.  $SNR^2$  may depend on the pixel size if the imaging system is not quantum limited or if there is a significant component of system noise.

The NPS is a spectral decomposition of the variance and provides an estimate of the spatial frequency dependence of the pixel-to-pixel fluctuations present in an image (Williams et al., 1999). The NPS can be used to characterize system noise and determine the extent to which the system is quantum-limited. It can also determine

whether the image contains noise due to interference from power sources, clock frequencies, etc. (Yaffe, 1999).

The concept of NPS was originally developed to decompose noise variance into components of various spatial frequencies. The NPS for a unit area (e.g. per  $\text{mm}^2$ ) can be computed from uniform exposure image data as a function of the spatial frequency in the image plane as follows:

$$NPS(f) = \frac{|FT(x, y)|^2}{N_x N_y} \Delta_x \Delta_y. \quad (2.19)$$

where  $|FT(x, y)|^2$  are the squared Fourier magnitudes of the noise image ;  $N_x$  and  $N_y$  are the number of elements in the x and y directions for the rectangular image section used to compute the discrete Fourier transforms (FT);  $\Delta_x$  and  $\Delta_y$  are the pixel sizes in the x and y directions (Dobbins III et al., 1995).

Magnification or focal spot blurring should not alter the uniform exposure image acquired or introduce additional noises. Thus, the NPS in the object plane,  $NPS(f; M)$ , can be linked to the NPS in the image plane,  $NPS(f; 1)$ , by re-scaling the spatial frequency and pixel size as follows (Shaw et al., 2000):

$$NPS(f; M) = \frac{1}{M^2} NPS\left(\frac{f}{M}; 1\right). \quad (2.20)$$

Due to blurring or filtering in the detector system, the NPS generally decreases with the frequency. Thus, re-scaling the frequency from the image plane to object plane would result in higher NPS values at the same frequency. This tends to partially undo what re-scaling does to improve the MTF in magnification imaging when computing the NEQ. Another effect is that since the NPS is generally computed for a unit area (e.g. per  $\text{mm}^2$ ) to characterize the low contrast performance, the NPS needs to be re-normalized for the object plane as the pixel size becomes smaller by a factor of  $M$ .

## B. NEQ Computation

The NEQ is the number of noise equivalent x-ray quanta per unit area that are incident on the detector. (Cunningham, 1999). The NEQ was originally defined for

the image plane and can be computed from the NPS and MTF as follows (Shaw et al., 2000):

$$NEQ(f; M) = \frac{S^2 \cdot MTF(f)^2}{NPS(f)} \quad (2.21)$$

where  $S$  is the mean signal in the region of interest used to measure the NPS. In the object plane, the NEQ can be defined and computed as (Shaw et al., 2000):

$$NEQ(f; M) = \frac{S^2 \cdot MTF(f; M)^2}{NPS\left(\frac{f}{M}; 1\right) \cdot \frac{1}{M^2}} \quad (2.22)$$

Notice that the factor  $1/M^2$  is included in the denominator to reflect the fact that a unit area would be represented by more pixels in the object plane as compared to that in the image plane.

The detective quantum efficiency (DQE) can be defined by normalizing the NEQ by the input x-ray photons as follows:

$$DQE(f) = \frac{NEQ(f)}{\phi_{in}}, \quad (2.23)$$

where  $\Phi_{in}$  is the number of photons per unit area at the input of the detector (Shaw et al., 2000). While  $NEQ(f)$  measures the absolute image quality, the  $DQE(f)$  normalizes the image quality to the input photon fluence. Thus,  $DQE(f)$  quantifies “benefit to cost” or “benefit to risk” where the benefit is the image quality achieved while the cost is the photon fluence used or risk to the patient due to the amount of radiation used. While we can easily extend the concept of NEQ for use in magnification imaging, it appears to be improper to do so for the DQE as it is unclear whether the NEQ should be normalized by photon flux at the detector input or in the object plane. In this thesis, we will use the NEQ to measure and study the absolute image quality of the system for detection of low contrast objects although discussion will be given regarding the “cost” or “risk” factors in magnification imaging.

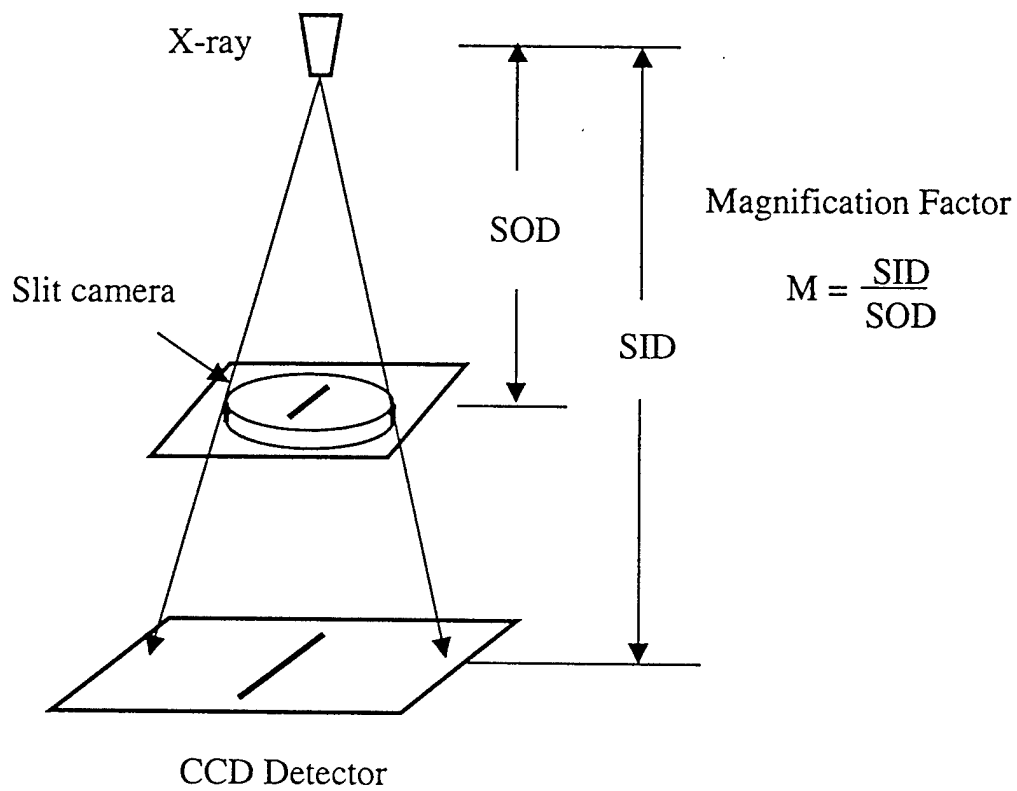
## 2.3 Materials and Methods

### 2.3.1 Imaging System

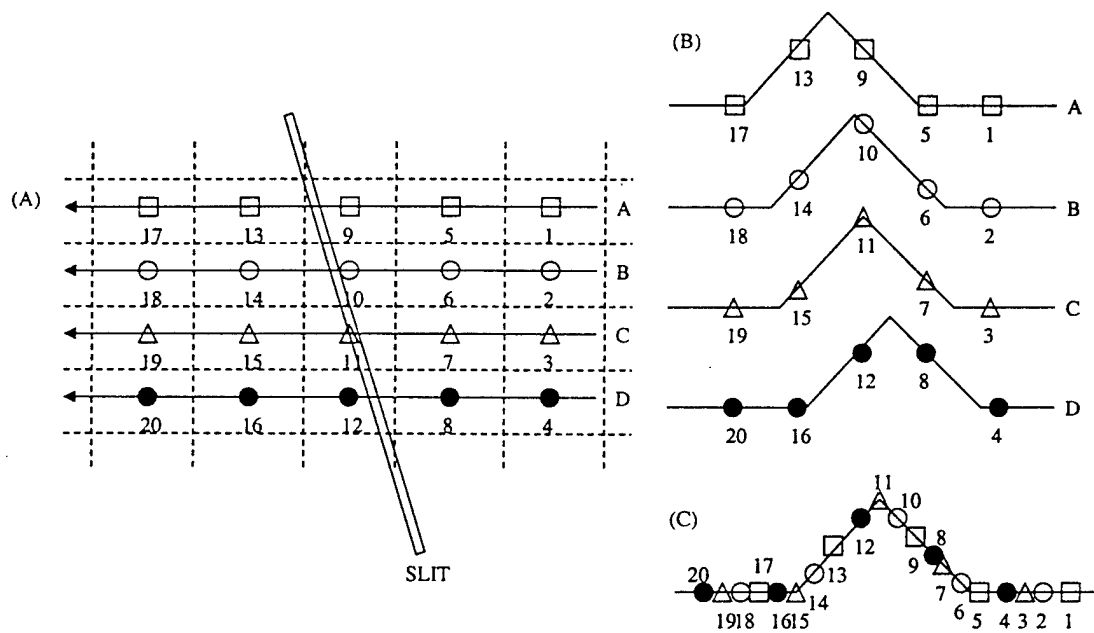
The imaging system studied in this work was a small-field digital mammography unit (SenoVision, General Electric Medical Systems, Milwaukee, WI). The system consists of a mammographic x-ray phosphor screen coupled to a CCD through a 1:1 fiber-optical coupler. The detector assembly has a field of view of  $6 \times 6 \text{ cm}^2$  divided into  $2048 \times 2048$  pixels with a pixel size of  $30 \mu\text{m}$ . It is enclosed in an  $18 \times 24 \text{ cm}^2$  cassette designed to fit into the cassette holder of typical mammography units. This detector assembly, used in conjunction with a mammographic x-ray generator (Senographe DMR+, General Electric Medical Systems, Milwaukee, WI), allows for quick and easy transition from a screen/film system to a digital system.

### 2.3.2 MTF Measurements

An x-ray slit (07-624 Nuclear Associates) was imaged to measure the line spread function (LSF) which was then used to compute the MTF. Exposures were made with a Mo/Mo target/filter combination in the small focal spot (0.1 mm) mode at 80 mAs and 26 kVp, and an SID of 660 mm. The slit,  $10 \mu\text{m}$  wide and 8 mm long, was placed at selected positions between the x-ray tube and the detector to measure the MTF for various magnification factors, ranging from 1.1 to 2.8 (Figure 2.4). A tilted slit method reported by Fujita et al. (1992) was used to measure the pre-sampling MTFs. With this method, the slit is oriented at an angle slightly ( $< 2^\circ$ ) off  $90^\circ$  to the direction of LSF and MTF measurement (Figure 2.5) (Fujita et al., 1992). The slight tilting causes the center of the slit to shift its position relative to the sampling points from one profile line to the next. Thus, a number of consecutive



**Figure 2.4.** A schematic of the experimental setup for the MTF measurements for magnification digital mammography.



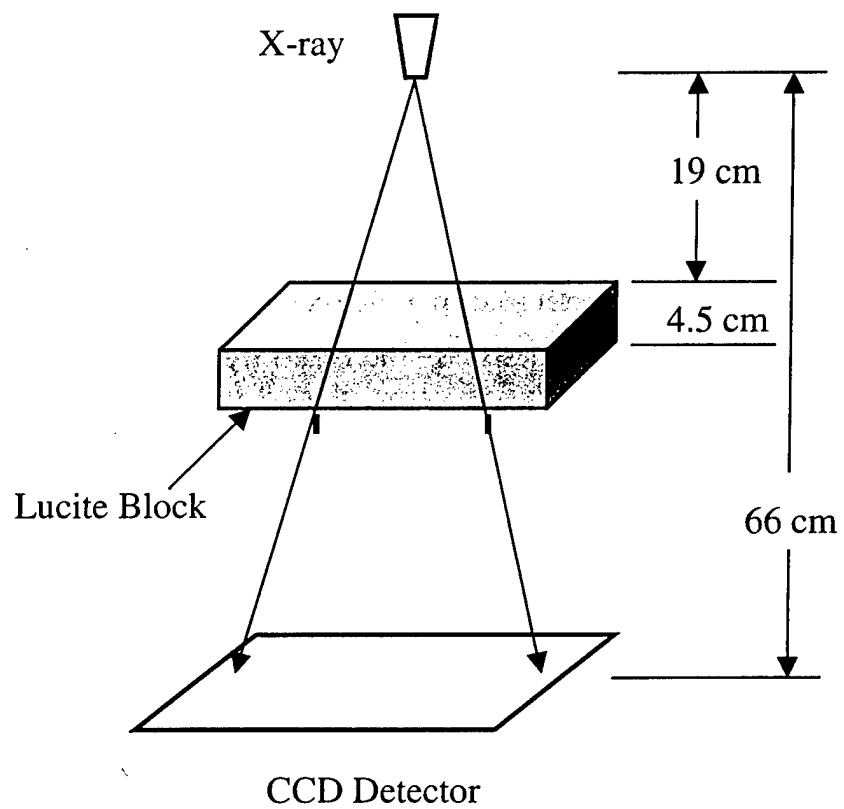
**Figure 2.5.** Schematic showing how a composite LSF is generated (C) from the LSFs corresponding to the slit alignment (B) relative to the sampling coordinate (A).

image lines can be combined together into an LSF with an effective sampling distance reduced by a large factor depending on the angle of tilting. The reduced sampling distance results in a much higher Nyquist frequency, effectively eliminating the aliasing problem. Thus, the FT of the synthesized LSF can be used to compute the estimated pre-sampling MTF (Fujita et al., 1992).

### 2.3.3 NPS Measurements

The difficulties inherent in measuring the NPS of digital imaging systems have been previously discussed (Dobbins III, 1995; Dobbins III et al., 1995; Williams et al., 1999; Vedantham et al., 2000). The NPS can be determined from a "noise only" image by using the indirect method, which computes the FT of the autocorrelation function, or by using the direct method, which computes the square of the modulus of the FT of the image data themselves. The NPS may also be determined by using either a one-dimensional (1-d) or two-dimensional (2-d) approach. With the advent of the fast Fourier transform (FFT) and faster computers, the indirect calculation of the NPS has been largely replaced by the direct method (Williams et al., 1999). For the purpose of this research, the 1-d NPS will be calculated using the direct method.

Uniform exposure images were acquired using approximately a 10 mR incident exposure. A block of Lucite with a thickness of 4.5 cm was placed in the path of the x-ray beam as shown in Figure 2.6. The detector, housed in the magnification (non-grid) cassette holder, was exposed to 25 kVp x-rays generated with a Mo/Mo target/filter combination in the large focal spot (0.3 mm) mode. Two images were acquired with identical techniques and then subtracted and divided by 2 to obtain the noise only image. The factor of 2 accounts for the fact that the variance in the subtracted image gets approximately equal contributions from the uncorrelated noise in each of the original images (Williams et al., 1999). This process was necessary for removing any fixed structural background in the images. One such background is the heel effect, which causes the x-ray intensity to decrease toward the anode side of the x-ray tube. This intensity variation may result in significant Fourier components and artificially inflate the NPS values at low frequencies (Williams et al., 1999). The NPS



**Figure 2.6.** A schematic of the experimental setup for the NPS measurements for magnification digital mammography.

measurement was performed on several noise images that were acquired. The results were averaged to reduce the fluctuation of the resulting NPS measurement.

To compute the NPS, the center 256 x 256 portion of the noise images was selected. This area was further reduced to four 128 x 128 regions of interest (ROIs). The NPS of each line in each of the four ROIs was computed by using the following equation:

$$NPS(f) = \frac{\langle |FT(x, y)|^2 \rangle}{N_x N_y} \Delta_x \Delta_y. \quad (2.24)$$

$\langle |FT(x, y)|^2 \rangle$  represents the ensemble average of the squares of the Fourier amplitudes in each of the four ROIs,  $N_x$  and  $N_y$  are the number of elements in the discrete Fourier transforms (128 and 1 respectively), and  $\Delta_x$  and  $\Delta_y$  are the pixel sizes in x and y (30  $\mu\text{m}$ ) (Dobbins III et al., 1995). The NPS from each of the ROIs were then averaged to obtain the final NPS. The  $NPS(f; M)$  was then calculated for various  $M$  using Eq. 2.20.

### 2.3.4 NEQ Measurements

The NEQ can be computed from the MTF, NPS and mean signal as follows (Dobbins III, 1995):

$$NEQ(f; M) = \frac{S^2 \cdot EMTF^2(f; M)}{NPS(f; M)} \quad (2.25)$$

where  $EMTF(f; M)$  is the digital expectation MTF and  $S$  is the mean signal value over the noise image. The use of  $EMTF(f; M)$  instead of the pre-sampling MTF was necessary because it was impossible to compute the NPS on a pre-sampling basis and the NPS computed may include the aliasing effect and represent the average of various sampling phase differences.  $EMTF(f; M)$  can be computed by computing and averaging the MTFs from 128 consecutive image lines across the slit (Dobbins III et al., 1995).

## 2.4 Results and Discussion

### 2.4.1 MTF

In Figure 2.7, the MTF measured in the image plane is plotted as a function of the re-scaled spatial frequency for selected magnification factors ( $M$ ) ranging from 1 to 2. These curves show the hypothetical improvement in the MTF if there is no focal spot blurring effect. The MTFs actually measured in the object plane are plotted for selected  $M$ s ranging from 1 to 2 in Figure 2.8. Due to the focal spot blurring effect, these MTFs demonstrated more modest improvement by magnification than did the hypothetical MTFs.

In Figure 2.9, the measured MTF is plotted as a function of the magnification factor for various frequencies. The curves show that at low to medium frequencies ( $f = 2-6$  lp/mm), the MTF increases until  $M$  reaches a certain value and then begins to decrease. At high frequencies, however, the MTF continues to increase with  $M$  all the way to the highest magnification ( $M = 3.0$ ). This can be related to the magnitude of the MTF values. At low to medium frequencies, the MTF values are high and the improvement by magnification begins to be limited by focal spot blurring effect as  $M$  increases beyond a certain value ( $M_{opt}$ ). At high frequencies, the MTF values are low. Even after improvement by magnification, they still remain low and are not subject to limitation by the focal spot blurring effect.

### 2.4.2 NEQ

$NPS(f;M)$  was calculated for three different magnification factors:  $M = 1$ , 1.5 and 2.0. The results are shown in Figure 2.10. The plot shows that the NPS improved at lower spatial frequencies (below 8 lp/mm) and that it was relatively unchanged at higher spatial frequencies. The improvement is due to lower noise per unit area in the object plane versus the image plane.

The calculated  $NPS(f;M)$  values were used in conjunction with the measured  $EMTFs$  to compute  $NEQ(f;M)$ . The results are shown in Figure 2.11. The

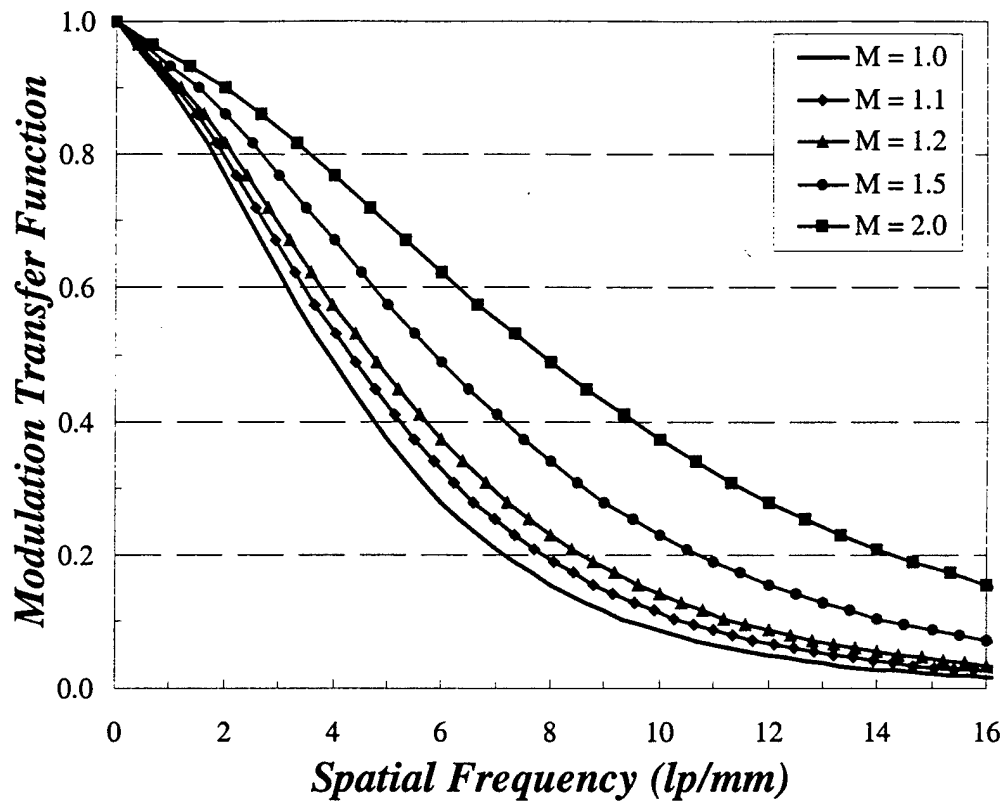


**Figure 2.7.** A plot of the MTF (theoretical) versus the spatial frequency showing the effects of magnification on the MTF. The MTF was measured for  $M = 1.0$  and then re-scaled for various  $M$ s.

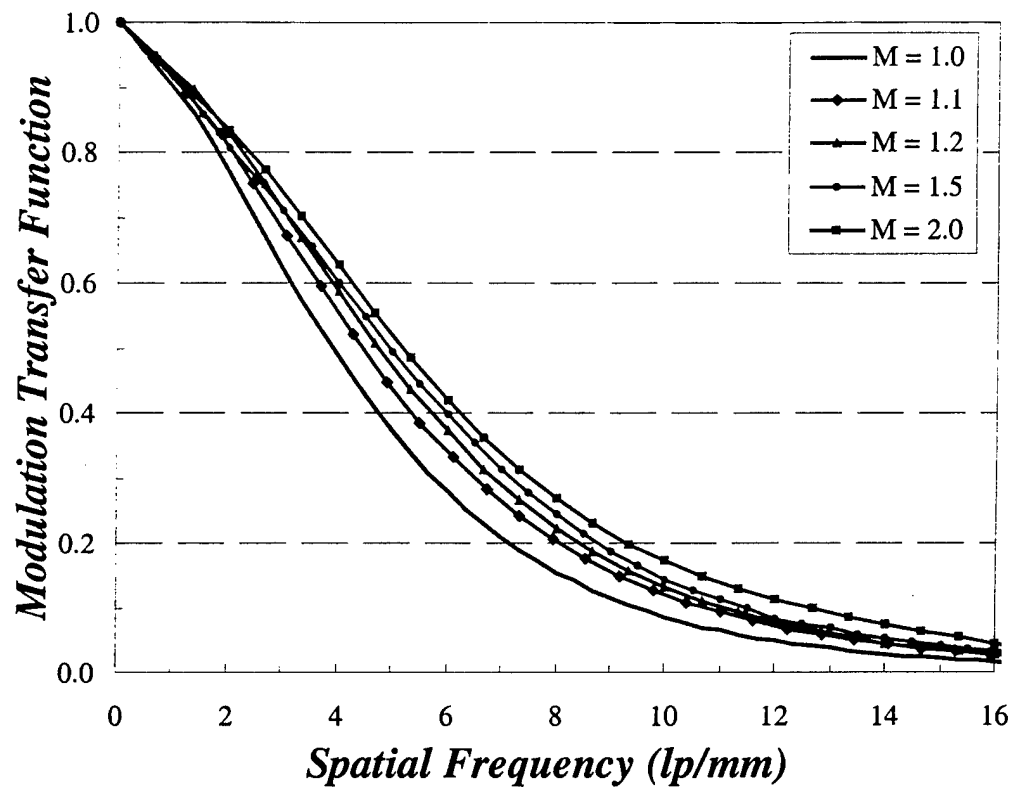


**Figure 2.8.** A plot of the MTF (measured) versus the spatial frequency showing the effects of magnification on the MTF.

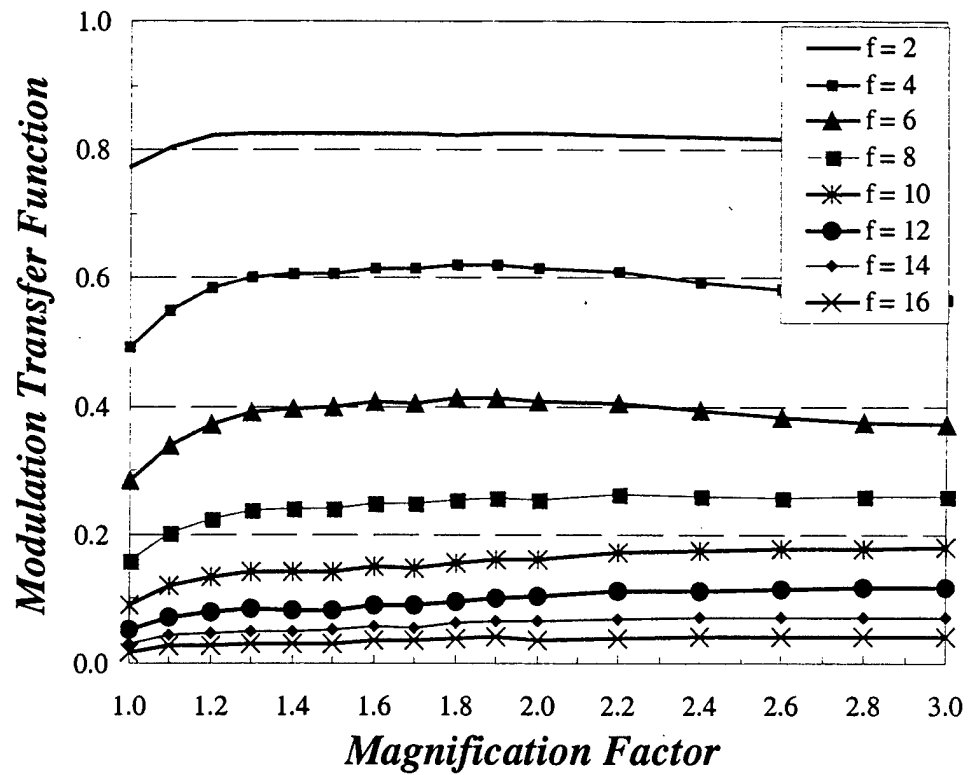


**Figure 2.9.** A plot of the measured MTF versus the magnification factor at various spatial frequencies.

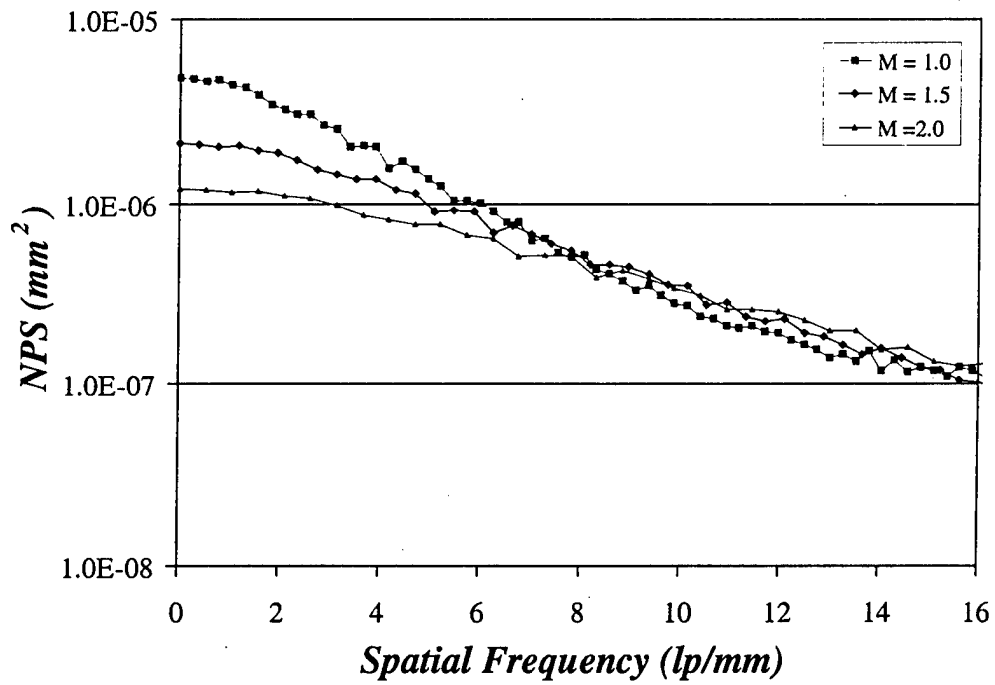


**Figure 2.10.** A plot of the NPS versus the spatial frequency for various  $M$ s. The NPS was measured for  $M = 1$  then re-scaled for various  $M$ s.

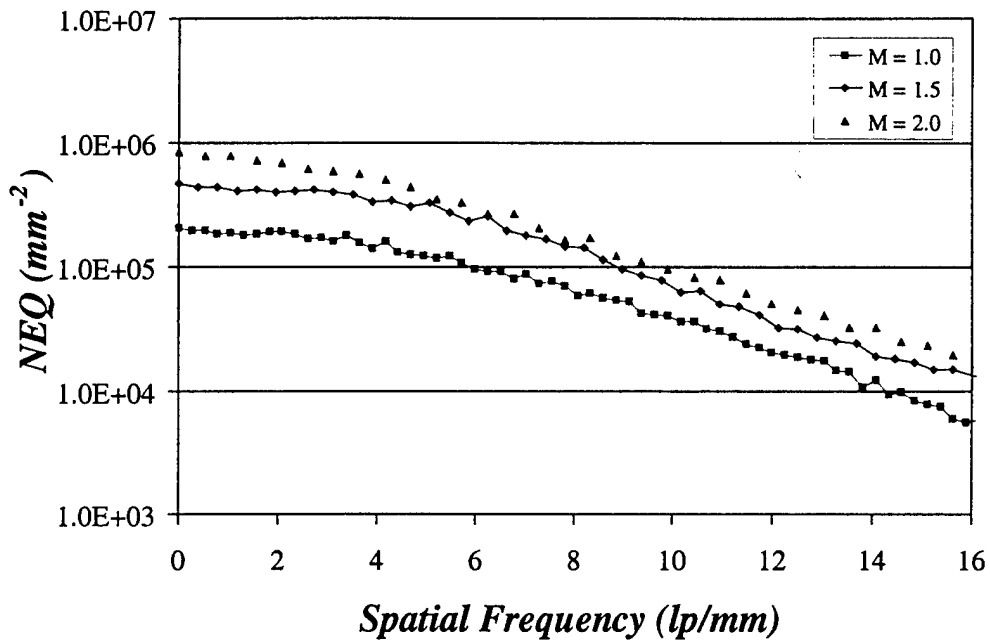


**Figure 2.11.** A plot of the NEQ versus the spatial frequency for various  $M$ s. The spatial frequency has been re-scaled to the object plane.

curves indicate that the NEQ improved with magnification, indicating a better performance for detecting low contrast objects, e.g. microcalcifications ( $\mu$ Cs). However, it is important to examine the cost or risk associated with such improvement. The improvement of  $NEQ(f)$  or the resulting low contrast detectability may be negated by the increased photon fluence in the object plane or increased radiation exposure to the patient. A familiar scenario is that the visualization of  $\mu$ Cs would be improved by bringing the breast closer to the x-ray tube and increasing the magnification. Notice that there would be an improvement even with the same x-ray techniques (mAs). This appears to be an advantage for magnification mammography, especially when a digital mammography system is used. However, this improvement is achieved by gaining a higher photon fluence by bringing the breast closer to the x-ray tube and subjecting the breast to higher exposure. Therefore, a price is paid to achieve image quality improvement in magnification mammography.

## 2.5 Summary

The variation of MTF, NPS and NEQ with magnification were modeled and measured. It was found that the MTF was improved in magnification imaging. However, the improvement was found to be limited by the focal spot blurring effect. The maximum magnification for MTF improvement decreased as the detector resolution limit increased. This maximum magnification was shown to increase with the spatial frequency. The selection of the focal spot size should match the resolution limit of the detector in order to optimize MTF improvement by magnification.

It was shown that in computing the NEQ in magnification imaging, the improvement in the MTF, limited by the focal spot blurring, was largely offset by the increase of the NPS values due to re-scaling of the spatial frequency. Nonetheless, the NEQ was still improved in magnification imaging, mainly due to the increased number of x-rays covered by a unit area moved to the object plane. Alternatively, the improvement can be said to be due to the increased number of x-rays used to image and cover the object.

## Chapter 3 – Magnification Digital Mammography: Detection of Microcalcifications – A Phantom Study

### 3.1 Introduction

Early detection of breast disease is important in the diagnosis and treatment of breast cancer. In screening mammography, images are acquired to survey the breast for signs of malignancy. If there is a suspicious finding, spot and/or magnification views can be performed to further evaluate the suspicious area. Previous studies have been performed that show the advantages of magnification mammography versus normal (contact) mammography (Sickles et al., 1977; Muntz and Logan, 1979; Sickles, 1980; Muntz, 1981; Sickles, 1982).

Magnification mammography can improve the visibility of small structures in the image plane. This can lead to improved visibility of fine details and the detectability of breast lesions (Kopans, 1998). Sickles et al. (1977) showed that direct radiographic magnification is superior to contact imaging in distinguishing malignant from benign breast lesions. Improved visibility also plays an important role in the detection of microcalcifications ( $\mu$ Cs). Sickles (1980) concluded that, "... spot magnification mammography as an adjunct to the conventional mammography examination can greatly improve the diagnostic accuracy on the evaluation of isolated clustered microcalcifications...." Upon further evaluation, Sickles (1982) demonstrated that spot magnification results in superior  $\mu$ C detection over all contact screen/film techniques.

Magnification results in a reduction in the amount of scatter radiation present in the image. The amount of scatter reduction is dependent upon the air-gap or distance between the object and the detector (Muntz, 1979). Magnification also significantly reduces the quantum mottle per unit of average dose and increases the contrast in the image (Muntz, 1979).

Screen/film techniques are currently the clinical standard for both contact and magnification breast imaging. There have recently been many advances in digital mammography. However, the clinical use of digital mammographic techniques is currently limited primarily to stereotactic needle localizations and core biopsies. This study is designed to test the theory that direct digital magnification mammography will improve the detectability of  $\mu$ Cs when compared to direct screen/film mammography. The results from a magnification phantom study comparing the detectability of various sizes of  $\mu$ Cs at different magnification factors using a screen/film system versus a digital imaging system will be presented.

## **3.2 Materials and Methods**

### **3.2.1 Imaging System**

A small-field CCD-based digital detector (SenoVision, General Electric Medical Systems, Inc., Milwaukee WI) was used for this study. The detector consists of a mammographic screen (Kodak MinR 2000™, Eastman Kodak Company, Rochester, NY) which is fiber-optically coupled to a 6 x 6 cm<sup>2</sup> cooled CCD. The CCD is cooled to an operating temperature of 12°C by a liquid circulating system (Vedantham et al., 2000). The CCD array provides a full frame image area of 2048 x 2048 pixels with a pixel size of 30  $\mu$ m. The detector is enclosed in an 18 x 24 cm<sup>2</sup> digital cassette, which is designed to fit into the cassette tray of a mammographic machine. The digital cassette, used in conjunction with a Senographe DMR+ (General Electric Medical Systems, Milwaukee, WI) x-ray generator, allows for a quick and easy transition from a screen/film system to a digital system.

The screen/film images were acquired using the same mammography unit (Senographe DMR+, General Electric Medical Systems, Milwaukee, WI) as that used for the digital images. The screen/film combination used was a Kodak MinR 2000™, (Eastman Kodak Company, Rochester, NY). The films were processed using a standard multiloader daylight processor.

The DMR+ has Automatic Optimization of Parameters (AOP). This feature works by taking a 0.015 second, low-dose pre-exposure to determine which kVp, target/filter combination and mAs are best suited for the density and thickness of the breast being imaged (General Electric Medical Systems, Inc., 1998). When taking screen/film images, the AEC mode can be selected for auto-kVp, auto-time (mAs), or the manual modes can be used. With the SenoVision, the exposure options are dense AEC, contrast AEC or manual settings.

### 3.2.2 Phantom Design

Pre-sifted  $\mu\text{C}$ 's (Computerized Imaging Reference Systems, Inc., Norfolk, VA) were used to construct the phantom pieces. The size ranges of the  $\mu\text{C}$ 's are shown in Table 3.2. The phantom pieces consisted of four  $\mu\text{C}$ 's arranged on a  $2 \times 2 \text{ cm}^2$  Lucite block. The thickness of the Lucite block was approximately 3 mm. A sample pattern of the  $\mu\text{C}$  arrangement is shown in Figure 3.1. A random number generator was used in order to randomize the  $\mu\text{C}$  pattern that was used for each image.

Since the size of the CCD detector is  $6 \times 6 \text{ cm}^2$ , nine  $2 \times 2 \text{ cm}^2$  Lucite squares were tiled to form the  $\mu\text{C}$  phantom piece. The square with the  $\mu\text{C}$ s was placed in the lower middle section of the tiled array (see Figure 3.2). The  $\mu\text{C}$ s were placed in this position so that they were visible at all magnification levels. The  $6 \times 6 \text{ cm}^2$  tile of Lucite squares was imaged overlying a 1 cm thick 50% glandular tissue 50% adipose tissue (50/50) equivalent phantom (Computerized Imaging Reference Systems, Inc., Norfolk, VA) (Figure 3.2). The square that contains the  $\mu\text{C}$ s was easily interchangeable to allow for quick changes in the  $\mu\text{C}$  size and arrangement when acquiring images. Since the average compressed breast thickness is approximately 4.5 cm, the study was repeated with an additional 3 cm of 50/50 material overlying the phantom piece (Figure 3.3). The total thickness of the phantom was approximately 4.3 cm.

**Table 3.1** Table showing the size ranges of the pre-sifted  $\mu\text{C}$ 's and the typical sizes used for the analysis.

Size Range ( $\mu\text{m}$ )	Typical $\mu\text{C}$ Size ( $\mu\text{m}$ )
150-160	155
125-140	133
112-125	119
90-106	98
75-90	83
63-75	69
53-63	58
43-53	48

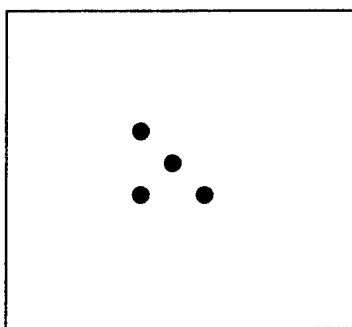


**Figure 3.1.** A schematic of a phantom piece showing a single arrangement of the  $\mu\text{C}$ s on a  $2 \times 2 \text{ cm}^2$  Lucite block.

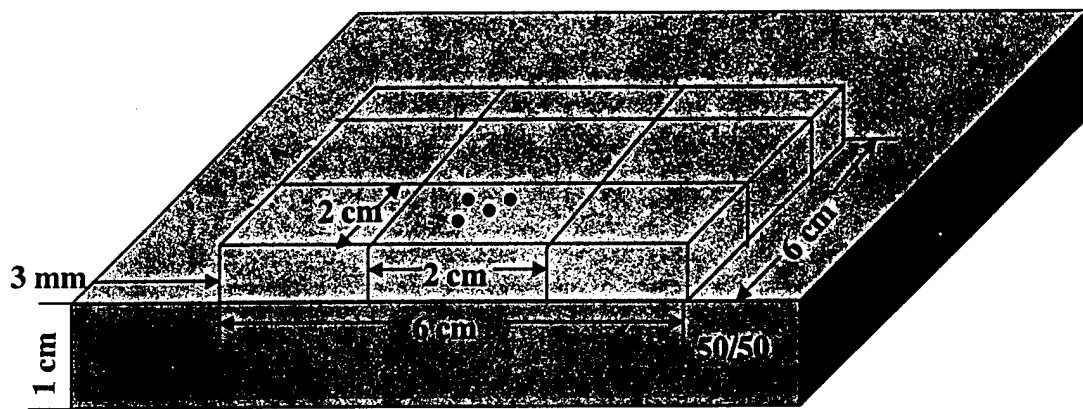


**Figure 3.2.** Schematic drawing of the tiled Lucite squares showing the placement of the  $\mu$ C phantom piece. Also shown is the placement of the tiled Lucite squares on the 1 cm 50% adipose/50% glandular tissue phantom.

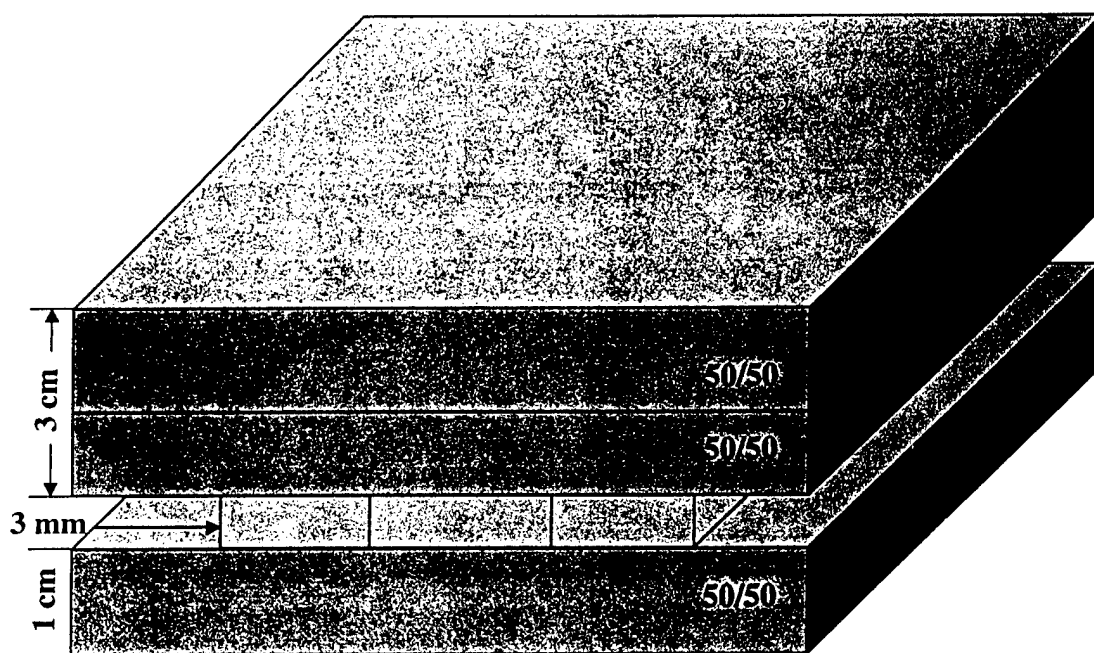


**Figure 3.3.** A schematic drawing of the 4 cm phantom showing the placement an additional 3 cm of 50% adipose/50% glandular tissue phantom material.

### 3.2.3 Image Acquisition

Images were acquired using magnification factors ( $M$ ) ranging from 1.01 – 3.0. The magnification was changed by placing the phantom on the compression paddle and moving the  $\mu$ Cs closer to the target. The distance from the target to the level of the  $\mu$ Cs was measured (Figure 3.4) and  $M$  was calculated as the ratio of the source-to-image distance (SID) to the source-to-object distance (SOD). A magnification cassette holder, which does not have a grid, was used. Since the small focal spot is generally used in magnification mammography in order to minimize focal spot blurring, it was used throughout the study.

Due to the differences in the AEC modes available for screen/film and digital acquisition, the kVp was pre-set to 26 and a Mo/Mo target/filter combination and the phototimer were used. The screen/film images were acquired first in the phototimer mode and the mAs for each exposure was recorded. The recorded mAs values were then used to acquire the corresponding digital images.

The images could be normalized in one of three ways: (1) to the detector exposure, (2) to the breast exposure or (3) to the object ( $\mu$ C) exposure. When performing magnification mammography using a system with a fixed SID, the most logical choice for normalization was the detector exposure. In order to maintain the same breast or object (not necessarily the same) exposure when performing magnification imaging, the SID would have to be changed so that the SOD could remain constant. Another difficulty in normalizing to the breast or object exposure is that as  $M$  increases, the incident exposure would have to decrease. By varying the incident exposure, the density of the resulting image would not be sufficient, particularly for the screen/film system. By normalizing to the detector exposure, the x-ray fluence incident on the detector should be the same for both imaging systems. With the same photon fluence, there should not be a bias in the  $\mu$ C detectability for the digital images.

With the 1 cm 50/50 phantom, the mAs was 6.3 at  $M = 1.01$  and 7 for all other  $M$  values. With the thicker 4 cm 50/50 phantom, the mAs values were less consistent.

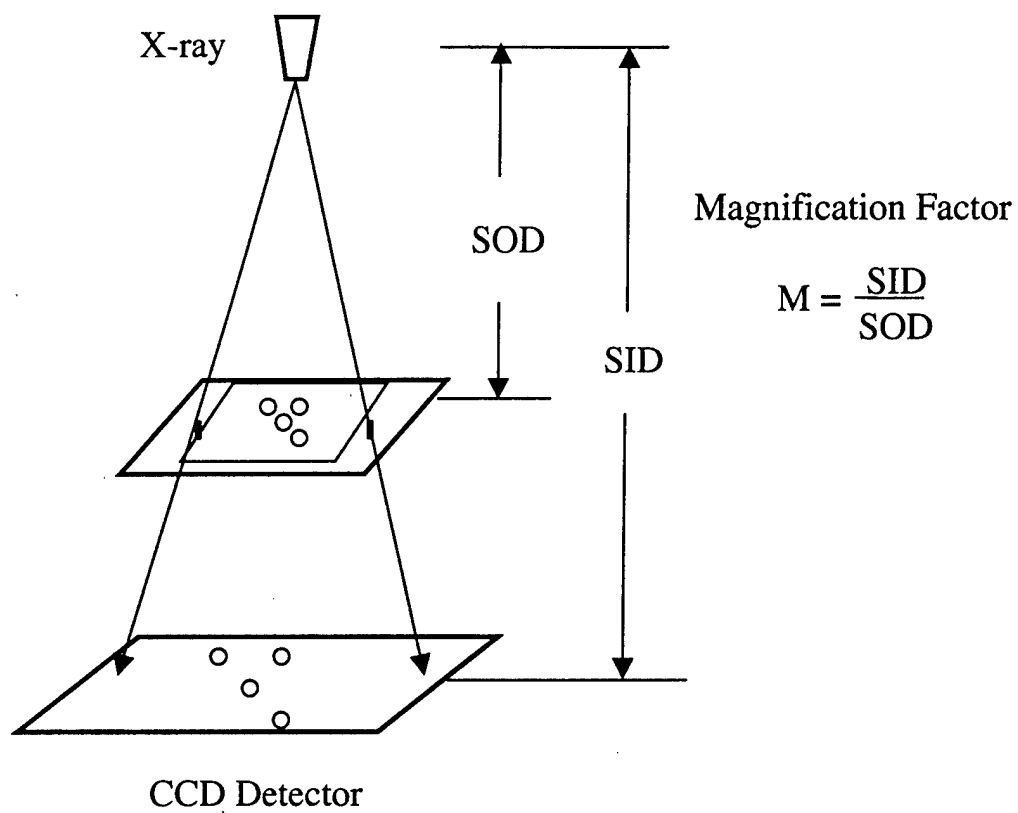


**Figure 3.4.** A schematic of the experimental setup for the magnification phantom study showing the placement of the  $\mu$ Cs and how  $M$  was determined.

For the screen/film images, the mAs varied from 58 to 82. Three exposures were obtained at each  $M$ ; the mAs values, at each  $M$ , for the screen/film images were averaged to determine the mAs to be used for the corresponding digital images. Due to the limited mAs values available when using the SenoVision in the manual mode, the mAs values that were nearest those used for the screen/film images were selected. Table 3.3 shows the mAs values that were used for the screen/film and digital images for both the 1 cm and 4 cm phantoms. Due to the size of the 4 cm phantom and its proximity to the exit window of the x-ray tube housing, images with  $M > 2.6$  could not be performed.

### 3.2.4 Image Reading

The screen/film images were numbered and separated into two groups. One group contained the images obtained using the 1 cm 50/50 phantom and the other group those obtained using the 4 cm 50/50 phantom. The images were randomized in each group and the readers viewed one group in each reading session. The digital images were divided into four groups and sent to a remote viewing station for reading. Each group contained a combination of images that were acquired using both the 1 cm and 4 cm 50/50 phantoms. The digital images were read two groups at a time in two viewing sessions. The readers were given a brief training session prior to viewing the images. The training session consisted of sample images and, for the digital images, instruction on how to utilize the soft copy display processing tools. Each viewing session, for both the screen/film and digital images, lasted approximately one hour.

The digital images were read using a soft copy display and the readers had the capability to window/level and magnify the images. The screen/film images were read using a standard mammographic light box with all of the ambient light blocked and the room lights turned off. The readers were allowed to use a magnifying glass as deemed appropriate. Three medical physicists and one medical physics graduate student participated as readers. The readers were asked to record the image number

**Table 3.2** Table showing the mAs values used in acquiring the screen/film and digital images for both the 1 cm and the 4 cm 50% adipose/50% glandular tissue phantoms.

M	1 cm Phantom		4 cm Phantom	
	Screen/Film	SenoVision	Screen/Film	SenoVision
1.01	6.3	6.3	59	63
1.2	7	7	70	71
1.4	7	7	75	80
1.5	7	7	76	80
1.7	7	7	77	80
1.84	7	7	79	80
2.0	7	7	80	80
2.2	7	7	81	80
2.6	7	7	80	80
3.0	7	7	-	-

and to place an x on the score sheet where a  $\mu\text{C}$  was seen. A sample score sheet is shown in the appendix.

The number of true positives (correctly identified  $\mu\text{Cs}$ ) in each image was recorded for each reader. The results from the four readers were then added together. In each image there were four  $\mu\text{C}$  detection tasks. The total for all four readers combined was sixteen. If a score of 75% (twelve out of sixteen) was obtained for a given  $M$  and  $\mu\text{C}$  size, the detection was considered to be positive. The smallest  $\mu\text{C}$  size to obtain a score of 75% at a given  $M$  was the smallest detectable size. Plots were generated showing the smallest detectable  $\mu\text{C}$  size versus the  $M$  using the 1 cm 50/50 phantom and the 4 cm 50/50 phantom. A comparison of the  $\mu\text{C}$  detectability for the digital system and the screen/film system was performed.

An ROC analysis (Metz, 1986) was performed (Johnston, 2000) to compare the  $\mu\text{C}$  detectability between the digital and screen/film systems for various  $M$ s. Three different  $\mu\text{C}$  sizes were evaluated at each  $M$  for both imaging systems. Each reader's results were added together to obtain an overall score for a particular  $M$ . The ROC program was modified to permit the entry of 2x2 matrices for the analysis (Johnston, 2000). The results from all four readers, at each  $M$ , were then used to generate the ROC curves. Data on the true positive fraction (TPF) and the false positive fraction (FPF) were obtained from the Chi Square ( $\chi^2$ ) analyses and used to fit a binormal ROC curve for each imaging system and each phantom (Dorfman and Alf, 1969). The index  $A_z$ , which represents the area under the binormal ROC curve when plotted on the unit square, was then calculated for each of the fitted curves as well as the standard deviations of the respective areas. The ROC curves were then analyzed using a "two-tailed" Student's t-test for paired data to the imaging system-specific  $A_z$  index values.

### 3.3 Results and Discussion

A lower mAs at  $M = 1.01$  was expected because a significant amount of scatter reached the detector. With the 1 cm phantom, as soon as  $M$  increased, a

significant reduction in the amount of scatter that reached the film occurred. The mAs changed abruptly with an increase in  $M$ . With a thin phantom, scatter is significant for contact imaging but becomes less significant as  $M$  increases. At higher  $M$ s, the mAs values remained constant, which means that there was no further reduction in scatter. With the 4 cm phantom, a more gradual change in the mAs was seen. Here, scatter is significant when performing contact imaging and over a larger range of  $M$ s. As  $M$  increased, a reduction in scatter and thus an increase in the exposure was seen up to  $M = 2.0$ . For  $M > 2.0$  there was not a further reduction in scatter.

The results from the reader detectability study are shown in Figures 3.5 and 3.6 for the 1 cm and 4 cm 50/50 phantoms, respectively. The 1 cm 50/50 phantom was used to simulate breast specimen imaging. As seen in Figure 3.5, the  $\mu$ C detectability is the same for both the screen/film system and the SenoVision with small  $M$  (1.01 and 1.4). For  $M = 1.5$ , the screen/film images did not exhibit a minimum detectability while the SenoVision remained constant at 119  $\mu$ m. At  $M = 1.7$ , both systems showed an increase in the minimum detectability, a decrease in  $\mu$ C size, to a  $\mu$ C size of 98  $\mu$ m. At  $M = 1.84$ , a separation in the detectability is seen. The SenoVision shows a  $\mu$ C detectability of 83  $\mu$ m and the screen/film system a detectability of 119  $\mu$ m. The poorer minimum detectability performance for the screen/film system may be attributed to the random fluctuations in the input spectra or to the noise fluctuations in the image. The SenoVision outperforms the screen/film system using the  $M$ s that are available clinically on the DMR+: 1.5, 1.7 and 1.84. Over this range, the SenoVision demonstrated an increasing detectability from 119  $\mu$ m at  $M = 1.5$  to 83  $\mu$ m at  $M = 1.84$ . The screen/film system shows an improvement from 119  $\mu$ m at  $M = 1.84$  to 83  $\mu$ m at  $M = 2.0$ . However, at  $M = 2.2$ , the detectability decreases from 83  $\mu$ m at  $M = 2.0$  to 98  $\mu$ m. The detectability increased back to 83  $\mu$ m for  $M = 2.6$  and 3.0. The SenoVision displayed a constant detectability of 83  $\mu$ m for  $M \geq 1.84$ .

The 4 cm 50/50 phantom was used to simulate spot magnification mammography. Figure 3.6 shows that with  $M = 1.01$  (contact image), the SenoVision outperformed the screen/film system. For the  $M$ s that are available clinically, the two

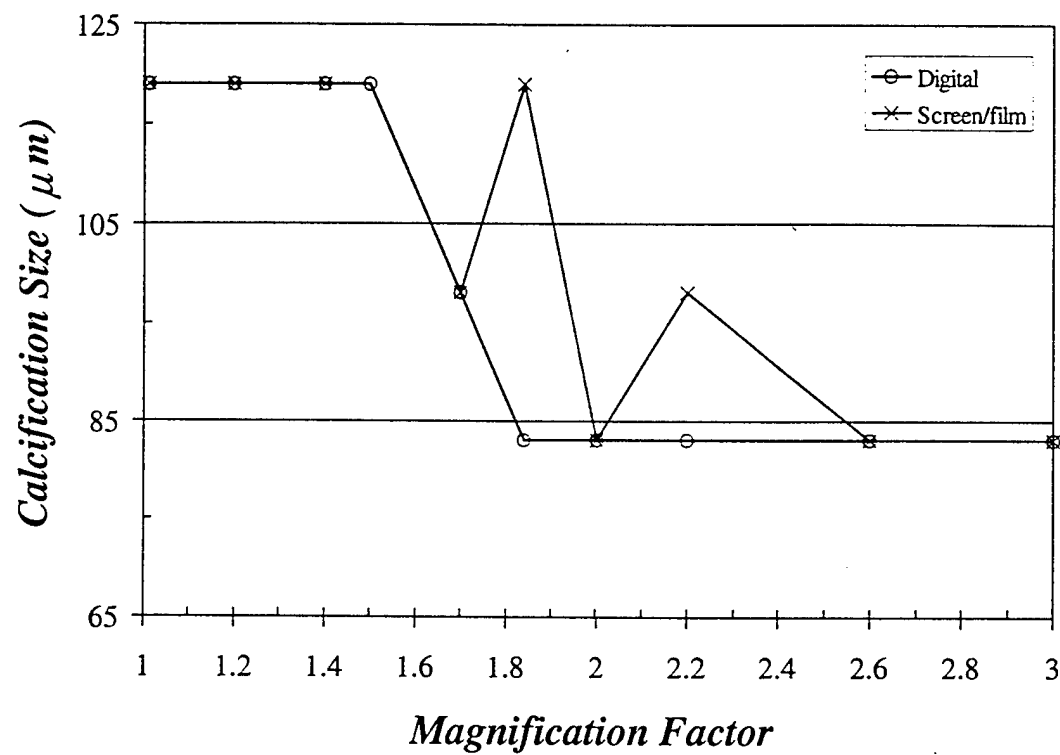


**Figure 3.5.** Plot showing the minimum detectable  $\mu C$  size of the two imaging systems at various  $M$ s for the 1 cm phantom.

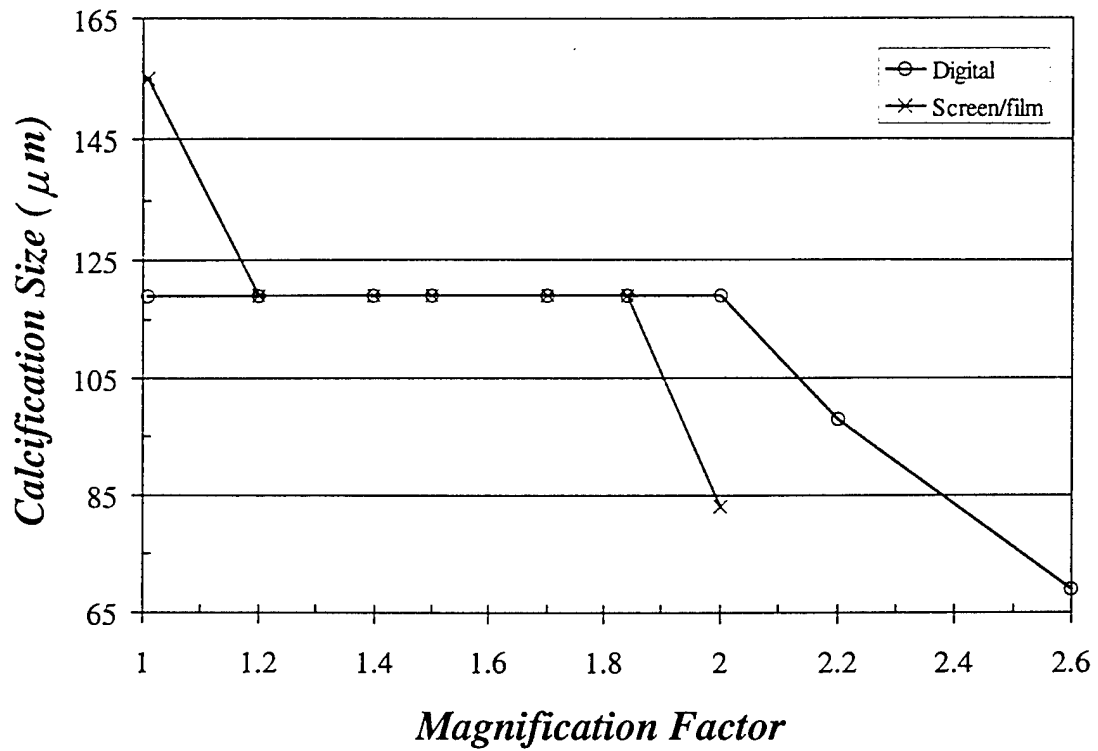


Figure 3.6. Plot showing the minimum detectable  $\mu C$  size of the two imaging systems at various  $M$ s for the 4 cm phantom.

systems exhibited identical performances. There were not any discrepancies seen in the comparison of the two systems for  $M = 1.2$  to  $1.84$ . At  $M = 1.84$ , the screen/film system outperformed the SenoVision with a minimum detectability of  $83 \mu\text{m}$  versus  $119 \mu\text{m}$ . The SenoVision showed a minimum detectability of  $98 \mu\text{m}$  at  $M = 2.2$  and  $68 \mu\text{m}$  at  $M = 2.6$ . The screen/film system did not exhibit a minimum detectability for the sizes of  $\mu\text{Cs}$  imaged at  $M > 2.0$ . This finding could be due to the random fluctuations in the input spectra or to the noise fluctuations in the image. The curve for the SenoVision also shows that there was not much improvement in the minimum detectability,  $119 \mu\text{m}$  for  $M = 1.01$  to  $2.0$ ,  $98 \mu\text{m}$  for  $M = 2.2$  and  $68 \mu\text{m}$  for  $M = 2.6$ . The screen/film system did exhibit an improvement in  $\mu\text{C}$  detectability from  $155 \mu\text{m}$  at  $M = 1.01$  to  $119 \mu\text{m}$  for  $M = 1.2 - 1.84$  and to  $83 \mu\text{m}$  at  $M = 2.0$ .

As shown previously in chapter 2, as  $M$  increases, the MTF increases. An increase in the MTF leads to an improvement in resolution. As expected, with increasing magnification, the  $\mu\text{C}$  detectability of both systems improves. The factor that has limited the implementation of digital mammography clinically is the resolution. Screen/film systems, in general, exhibit a better resolution than digital systems. Therefore, one would expect that the screen/film system would outperform the SenoVision.

Both systems studied employ the same scintillator and the images were acquired using the same exposure factors. The ability to adjust the window/level of the digital images is the factor that probably allows the SenoVision to outperform the screen/film system. With the SenoVision, the window/level can be adjusted to suit the reader and the image can also be inverted or magnified. These tools are extremely useful in reading the images and determining the detectability of  $\mu\text{Cs}$ .

The ROC curves for the 1 cm phantom are shown in Figure 3.7. The detectability of  $\mu\text{Cs}$  is better with the SenoVision. The area under the ROC curve ( $A_c$ ) indicates the  $\mu\text{C}$  detection accuracy. The  $A_c$  index was  $0.847 \pm 0.017$  for the SenoVision and  $0.756 \pm 0.022$  for the screen/film system. The results from the two-

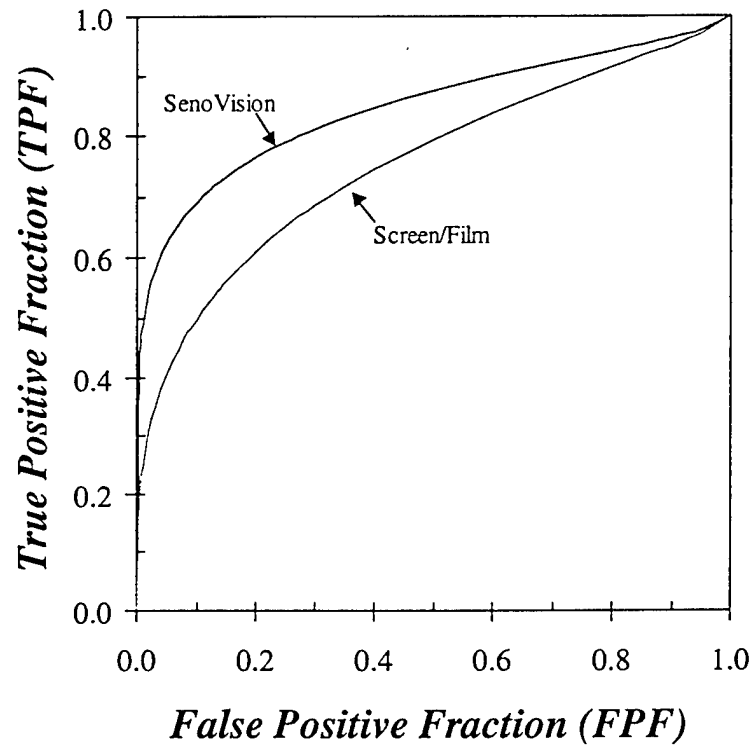


**Figure 3.7.** Comparison of the ROC curves for the detection of  $\mu$ Cs for the two imaging systems using the 1 cm phantom.

tailed paired Student's t-test showed that the SenoVision has a significantly greater detectability for  $\mu$ Cs ( $p = 0.005$ ). The improvement in the detectability with the SenoVision can most likely be attributed to the ability of the reader to window/level and zoom the images. These features allow the reader to view the images in various ways and the ability to modify the image display may allow the readers to make a more accurate diagnosis.

The ROC curves for the 4 cm phantom are shown in Figure 3.8. Once again, the detectability of  $\mu$ Cs is better with the SenoVision. The  $A_z$  index was  $0.744 \pm 0.033$  for the SenoVision and  $0.513 \pm 0.045$  for the screen/film system. The results from the two-tailed paired Student's t-test showed that the SenoVision has a significantly greater detectability for  $\mu$ Cs at the  $p = 0.001$  level.

### 3.3.1 Reader Comments and Observations

There were approximately 150 (80 digital and 70 screen/film) images read by each reader for this study. Two of the readers preferred reading the digital images and two preferred the screen/film images. Those who preferred the digital images felt that not having to manually change films was beneficial. However, three out of the four readers thought that the screen/film images were easier to read. This was due to the fact that "what you see is what you get". There were no manipulations with the screen film studies, so the task of reading the images was easier. Three readers also found that it took 10 – 20% longer to read the digital images. This may be because there were approximately 10% more digital images than there were screen/film images, or perhaps, that more time was spent trying to identify a finding in the digital images.

All readers used the window/level and zoom features that are available when reading soft-copy digital images. The readers felt that this gave them an advantage in that they could manipulate the images. Three readers also used the magnifying glass when reading the digital images. The digital zoom feature was preferred over the magnifying glass because there was not any advantage gained when using the magnifying glass.

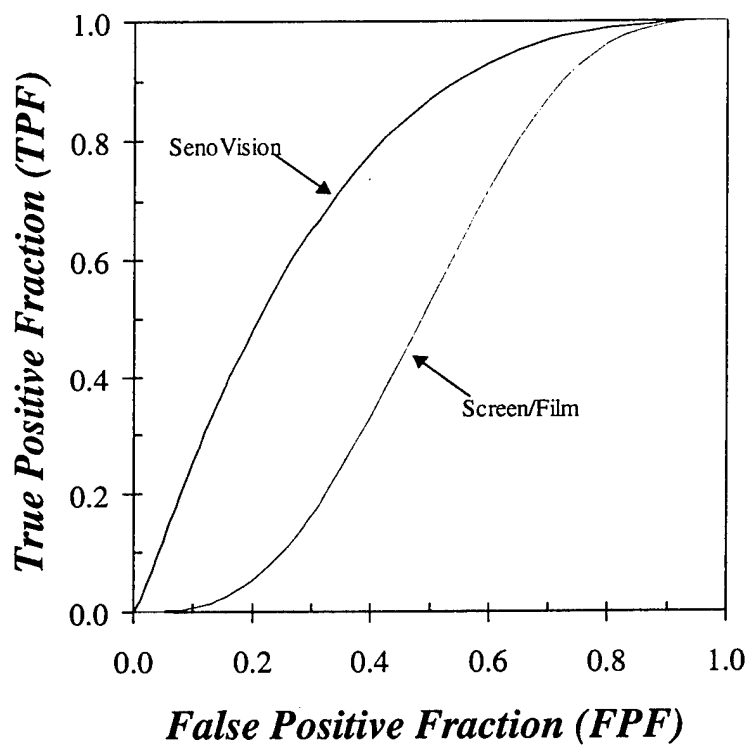


**Figure 3.8.** Comparison of the ROC curves for the detection of  $\mu$ Cs for the two imaging systems using the 4 cm phantom.

### 3.4 Summary

A phantom study was conducted to compare direct digital magnification mammography with direct screen/film magnification mammography for the detectability of  $\mu$ Cs. The results from a minimum detectability analysis showed that the SenoVision performs as well as or better than the screen/film system for minimum  $\mu$ C detectability with increasing magnification. It was also shown, with the 1 cm phantom, that increasing magnification does increase the detectability of  $\mu$ Cs. There was also an increase in the  $\mu$ C detectability with the 4 cm phantom. However, the findings in  $\mu$ C detectability were not as prominent as that seen with the 1 cm phantom.

A ROC analysis comparing the  $\mu$ C detectability of both imaging systems was performed. The overall  $\mu$ C detectability using both phantom sizes at various magnification levels was compared. The  $A_z$  indexes were used to perform a two-tailed paired Student's t-test and showed that the SenoVision had a significantly better  $\mu$ C detectability than the screen/film system.

## Chapter 4 – Dual-Energy Subtraction Imaging

### 4.1 Introduction

Screening and diagnosis in mammography relies on the detection of microcalcifications ( $\mu$ Cs) and/or soft tissue masses. Early detection is important in the diagnosis and treatment of breast cancer.  $\mu$ Cs are composed mainly of calcium and have greater attenuation properties than soft tissue masses and the soft tissue background structures of the breast. This leads to a comparatively higher subject contrast relative to the soft tissue masses and background. The detection or visibility of  $\mu$ Cs is relatively easy with a uniform soft tissue background. However, the detectability of  $\mu$ Cs may be limited by the “cluttered” background present in mammograms. The “cluttered” background is due to glandular tissue, ducts, vessels and/or soft tissue masses that are present in the breast. Therefore, it may be difficult to detect a  $\mu$ C even though there may be an adequate signal-to-noise ratio (SNR) (Brettle and Cowen, 1994).

The density of the breast tissue can further inhibit the detection of  $\mu$ Cs. There is overall greater attenuation in dense breasts, which leads to more beam hardening. This beam hardening can degrade the contrast of  $\mu$ Cs relative to that of the background tissue structure. Beam hardening also tends to decrease the contrast of  $\mu$ Cs relative to the image noise. Both factors contribute to a greater difficulty in  $\mu$ Cs being detected.

The  $\mu$ Cs or masses can be isolated from background tissue structure by tomosynthesis, which can isolate image details (including  $\mu$ Cs and masses if any) inside a thin layer, from the background tissue structure that is outside of the layer. Thus, by reconstructing information in layers at various depths,  $\mu$ Cs and/or masses can potentially be detected in a less cluttered background. This technique is being developed and evaluated in a number of laboratories. The issues to be resolved

include the accuracy of tomosynthesis algorithms, potential increases in dose, complexity and cost of a gantry system required for moving the x-ray tube and detector and a detector system allowing a rapid framing rate in image acquisition.

An alternative approach is to use a dual-energy subtraction imaging technique. With this technique, high- and low-energy images are acquired. The difference of these two images largely cancels out the background tissue structure (structured noise) and generates either a tissue-composition or calcification-specific image. This technique could be useful mainly in helping detect  $\mu$ Cs by removing the cluttered background tissue structures. However, during the subtraction processing, quantum noise would be propagated from the original image data into the subtraction image (Shaw and Gur, 1992). The noise levels in the subtraction images depend on the noise present in the original images, the x-ray spectra used, and the subtraction algorithm used. Due to subtraction processing, the noise levels tend to be higher than those in unsubtracted images. Therefore, the detection/visualization of  $\mu$ Cs in subtraction images would be limited by a higher x-ray noise component. However, the advantage of removing the cluttered background tissue structure may outweigh the drawbacks of increased noise.

There have been efforts to investigate and implement dual-energy digital mammography (Johns et al., 1985; Chakraborty and Barnes, 1989; Boone et al., 1990; Brettle and Cowen, 1994; Asaga et al., 1995). Several detectors have been studied for the implementation of dual-energy digital mammography (Boone et al., 1990; Chakraborty and Barnes, 1989). Promising results have been reported (Johns et al., 1985; Brettle and Cowen, 1994; Asaga et al., 1995).

The objectives of this study were to estimate the noise levels in the subtraction signals for various imaging conditions, to optimize the selection of imaging parameters and to evaluate the feasibility of using a dual-energy subtraction technique for improved detection and visualization of  $\mu$ Cs. This was accomplished by performing numerical computations in order to study the effects of x-ray spectra,  $\mu$ C size, tissue composition and breast thickness on the noise levels in subtracted images.

A theoretical background for the numerical study and the results from the numerical studies will be presented and discussed in this section.

## 4.2 Theory

Although dual-energy subtraction imaging can potentially be used to eliminate the structural background from tissue contrast, additional noise is generated during the subtraction processing. In this section, the framework of the dual-energy subtraction technique and the resulting noise levels in the subtraction images are derived for use in the numerical simulation studies.

### 4.2.1 Three-Energy versus Two-Energy Subtraction

In mammography, one can assume that there are three attenuating materials: adipose tissue, glandular tissue and calcification (sparse presence). With a compressed breast, the total breast thickness is uniform except near the borders. Ideally, it would be best to use three energies to image the three attenuating materials (Kelcz et al., 1977). Three-energy subtraction has many disadvantages including: increased patient exposure, increased time to complete the exam (which could lead to motion artifacts), and complicated post image processing. The total breast thickness, as well as the thicknesses of the attenuating materials, can be determined by using a dual-energy subtraction technique. Assuming that the total, compressed breast thickness is known, the three-material problem can be reduced to a two-material one. The theory used for the simulation studies is based on the methodology of Shaw and Gur (1992).

### 4.2.2 Dual-Energy Microcalcification Imaging

Suppose that we have a compressed breast consisting of adipose tissue with a thickness of  $t_a$ , glandular tissue with a thickness of  $t_b$ , and a  $\mu\text{C}$  with a thickness of  $t_c$  (Figure 4.1). The total tissue thickness can be given by,

$$T = t_a + t_b + t_c. \quad (4.1)$$

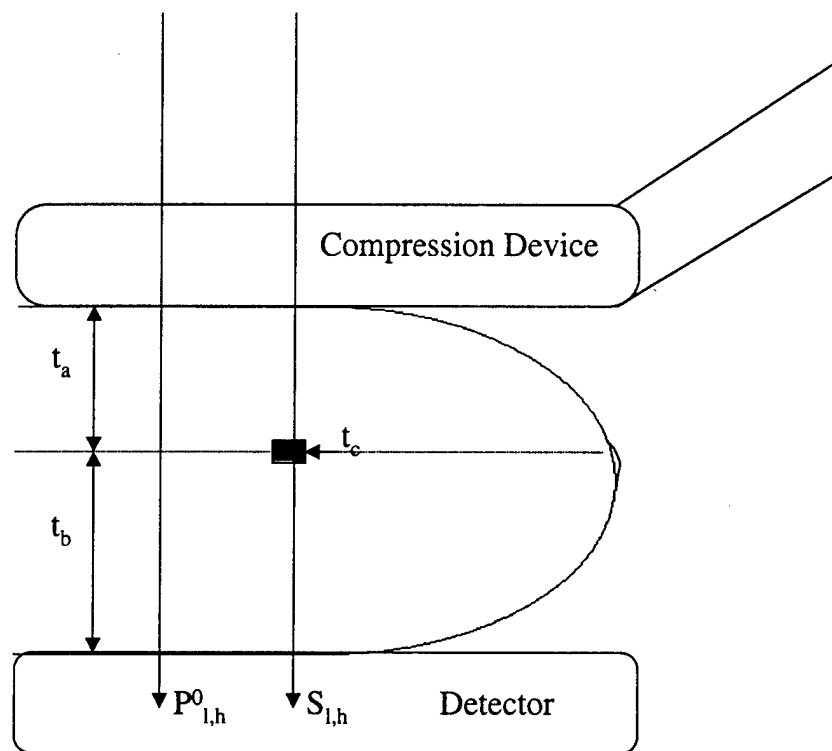


**Figure 4.1.** A compressed breast showing the tissue thickness ( $t_a$ ,  $t_b$  and  $t_c$ ) and the path that the x-ray photons travel when passing through.

Assuming that polyenergetic x-rays are used, the signal in the low- and high-energy images,  $S_l$  and  $S_h$ , can be expressed as follows:

$$S_j = \int dE \cdot R_j \cdot d^2 \cdot \Phi_j(E) \cdot e^{(-\mu_a(E)x_a - \mu_b(E)x_b - \mu_c(E)x_c)} \cdot A(E) \cdot Q(E), j = l, h, \quad (4.2)$$

where  $R_l$  and  $R_h$  are the unattenuated low- and high-energy x-ray exposures in milliroentgens at the detector plane;  $d$  is the pixel size in cm;  $\Phi_l$  and  $\Phi_h$  are the unattenuated photon flux per unit exposure per unit energy (photons/cm<sup>2</sup>/mR/keV) at the detector input;  $A(E)$  is the photon absorption ratio of the detector; and  $Q(E)$  is the detector response function and represents the signal generated by each photon with an energy near  $E$ (keV). The energy dependent linear attenuation coefficients (1/cm) for each tissue are given by  $\mu_a(E)$ ,  $\mu_b(E)$ , and  $\mu_c(E)$  for adipose tissue, glandular tissue and the calcification respectively.

Solving Eq. 4.1 for  $t_a$ , letting  $\Delta\mu_b(E) = \mu_b(E) - \mu_a(E)$  and  $\Delta\mu_c(E) = \mu_c(E) - \mu_a(E)$  and assuming that  $Q(E)$  is proportional to  $E$ , Eq. 4.2 can be rewritten as follows:

$$S_j = \int dE \cdot R_j \cdot d^2 \cdot \Phi_j(E) \cdot e^{-\mu_a(E)x} \cdot e^{(-\Delta\mu_b(E)x_b - \Delta\mu_c(E)x_c)} \cdot A(E) \cdot \alpha E, j = l, h, \quad (4.3)$$

where  $\alpha$  is a proportional constant. In analogy to the optical densities, the x-ray densities for the low- and high-energy images,  $D_l$  and  $D_h$ , can be defined as follows:

$$D_j \equiv \ln \left[ \frac{S_j^0}{S_j} \right], j = l, h \quad (4.4)$$

where  $S_j^0$  is the unattenuated signal in the image.  $D_l$  and  $D_h$  can be defined as follows:

$$D_j^a \equiv \ln \left[ \frac{S_j^a}{S_j} \right], j = l, h \quad (4.5)$$

where  $S_j^a = \int dE \cdot R_j \cdot d^2 \cdot \Phi_j(E) \cdot e^{-\mu_a(E)x} \cdot A(E) \cdot (\alpha E)$ ,  $j = l, h$ , are the low- and high-energy signals attenuated by 100% adipose tissue and are used as reference signals.

$D_l$  and  $D_h$ , are functions of the glandular tissue and calcification thickness'  $t_b$  and  $t_c$ . Using Eq. 4.3, they can be expressed as follows:

$$D_j = F_j(t_b, t_c) = \ln \left[ \frac{S_j^a}{S_j} \right] \\ = \ln \left[ \frac{\int dE \cdot R_j \cdot d^2 \cdot \Phi_j(E) \cdot e^{-\mu_a(E)T} \cdot A(E) \cdot (\alpha E)}{\int dE \cdot R_j \cdot d^2 \cdot \Phi_j(E) \cdot e^{-\mu_a(E)T} \cdot e^{(-\Delta\mu_b(E)t_b - \Delta\mu_c(E)t_c)} \cdot A(E) \cdot (\alpha E)} \right], j = l, h \quad (4.6)$$

The main task of dual-energy subtraction imaging is to determine  $f_b(D_l, D_h)$  and  $f_c(D_l, D_h)$  as measures of the inverse functions of  $F_l(t_b, t_c)$  and  $F_h(t_b, t_c)$  and use them to map the measured x-ray densities,  $D_l$  and  $D_h$ , into the glandular tissue and calcification thickness'  $t_b$  and  $t_c$ . Typically,  $F_l$ ,  $F_h$  and  $f_b$ ,  $f_c$  can be determined by interpolation of calibration measurements. These functions must be determined for each different breast thickness.

### 4.2.3 Special Case: Monoenergetic x-rays

Eq. 4.6 cannot be solved analytically for  $t_b$  and  $t_c$ . Although x-rays used in diagnostic imaging are mostly polyenergetic, it is more feasible to use a monoenergetic approach to demonstrate how the three-material/energy imaging problem is reduced to a dual-material/energy one. The advantage of using monoenergetic x-rays for this demonstration is the ability to analytically solve the energy subtraction problem.

Suppose that we have a compressed breast consisting of adipose tissue with a thickness of  $t_a$ , glandular tissue with a thickness of  $t_b$ , and a  $\mu\text{C}$  with a thickness of  $t_c$  (Figure 4.1). If  $p_l^0$  and  $p_l$  are defined as the unattenuated and attenuated signals from the low-energy spectrum, and  $p_h^0$  and  $p_h$  are defined as the unattenuated and attenuated signals from the high-energy spectrum (Figure 4.1), the x-ray densities, in analogy with optical densities,  $D_l$  and  $D_h$ , can be defined and expressed as follows:

$$\begin{aligned}
D_l &\equiv \ln(p_l^0 / p_l) = \mu_{al}(T - t_b - t_c) + \mu_{bl}t_b + \mu_{cl}t_c \\
&= \mu_{al}T + (\mu_{bl} - \mu_{al})t_b + (\mu_{cl} - \mu_{al})t_c
\end{aligned} \tag{4.7}$$

and

$$\begin{aligned}
D_h &\equiv \ln(p_h^0 / p_h) = \mu_{ah}(T - t_b - t_c) + \mu_{bh}t_b + \mu_{ch}t_c \\
&= \mu_{ah}T + (\mu_{bh} - \mu_{ah})t_b + (\mu_{ch} - \mu_{ah})t_c
\end{aligned} \tag{4.8}$$

where  $\mu_{ij}$ ,  $i = b, c$  and  $j = l, h$ , are the tissue linear attenuation coefficients for glandular tissue and for the  $\mu_C$ , respectively. Eqs. 4.7 and 4.8 may be rewritten as follows:

$$D_l^i \equiv \ln\left(\frac{p_l^a}{p_l}\right) = D_l - \ln\left(\frac{p_l^0}{p_l^a}\right) = \Delta\mu_{bl}t_b + \Delta\mu_{cl}t_c \tag{4.9}$$

and

$$D_h^i \equiv \ln\left(\frac{p_h^a}{p_h}\right) = D_h - \ln\left(\frac{p_h^0}{p_h^a}\right) = \Delta\mu_{bh}t_b + \Delta\mu_{ch}t_c \tag{4.10}$$

where  $\Delta\mu_{bj} = \mu_{bj} - \mu_{aj}$ ,  $\Delta\mu_c = \mu_{cj} - \mu_{aj}$  and are referred to as the difference attenuation coefficients;  $p_{l,h}^a$  are the signals attenuated by 100% adipose tissue and are used as new reference signals;  $D_l^i$  and  $D_h^i$  are new x-ray densities obtained by using  $p_{l,h}^a$  as the new reference signals. Eqs. 4.9 and 4.10 can be reorganized into matrix form as follows:

$$\begin{pmatrix} D_l^i \\ D_h^i \end{pmatrix} = \begin{pmatrix} \Delta\mu_{bl} & \Delta\mu_{cl} \\ \Delta\mu_{bh} & \Delta\mu_{ch} \end{pmatrix} \begin{pmatrix} t_b \\ t_c \end{pmatrix} \tag{4.11}$$

Solving for  $t_b$  and  $t_c$  yields

$$\begin{pmatrix} t_b \\ t_c \end{pmatrix} = \begin{pmatrix} \Delta\mu_{bl} & \Delta\mu_{cl} \\ \Delta\mu_{bh} & \Delta\mu_{ch} \end{pmatrix}^{-1} \begin{pmatrix} D_l^i \\ D_h^i \end{pmatrix} = \begin{pmatrix} k_{bl} & k_{bh} \\ k_{cl} & k_{ch} \end{pmatrix} \begin{pmatrix} D_l^i \\ D_h^i \end{pmatrix} \tag{4.12}$$

where

$$k_{bl} = \frac{\Delta\mu_{ch}}{\Delta\mu_{bl}\Delta\mu_{ch} - \Delta\mu_{cl}\Delta\mu_{bh}} \tag{4.13}$$

$$k_{bh} = \frac{-\Delta\mu_{cl}}{\Delta\mu_{bl}\Delta\mu_{ch} - \Delta\mu_{cl}\Delta\mu_{bh}}, \quad (4.14)$$

$$k_{cl} = \frac{-\Delta\mu_{bh}}{\Delta\mu_{bl}\Delta\mu_{ch} - \Delta\mu_{cl}\Delta\mu_{bh}} \quad (4.15)$$

and

$$k_{ch} = \frac{\Delta\mu_{bl}}{\Delta\mu_{bl}\Delta\mu_{ch} - \Delta\mu_{cl}\Delta\mu_{bh}}. \quad (4.16)$$

As will be shown later, the  $k_{ij}$ 's are useful for the computation of the noise signals in the subtraction tissues,  $t_b$  and  $t_c$ . The glandular tissue and the calcification thickness',  $t_b$  and  $t_c$ , can now be expressed as a function of the difference attenuation coefficients,  $\Delta\mu_{ij}$ 's, and the x-ray densities  $D_l$  and  $D_h$  as follows:

$$t_b = \frac{\Delta\mu_{ch}D_l - \Delta\mu_{cl}D_h}{\Delta\mu_{bl}\Delta\mu_{ch} - \Delta\mu_{cl}\Delta\mu_{bh}} \quad (4.17)$$

and

$$t_c = \frac{\Delta\mu_{bl}D_h - \Delta\mu_{bh}D_l}{\Delta\mu_{bl}\Delta\mu_{ch} - \Delta\mu_{cl}\Delta\mu_{bh}}. \quad (4.18)$$

#### 4.2.4 Noise in the Unsubtracted Image

Returning to the polyenergetic model, the noise levels in the x-ray densities  $D_l$  and  $D_h$  can be expressed as,

$$\sigma_{D_l}^2 = \left( \frac{\partial D_l}{\partial S_l} \right)^2 \sigma_{S_l}^2 = \left( \frac{1}{S_l} \right)^2 \sigma_{S_l}^2 = \frac{1}{SNR_l^2} \quad (4.19)$$

and

$$\sigma_{D_h}^2 = \left( \frac{\partial D_h}{\partial S_h} \right)^2 \sigma_{S_h}^2 = \left( \frac{1}{S_h} \right)^2 \sigma_{S_h}^2 = \frac{1}{SNR_h^2}. \quad (4.20)$$

In Eq. (4.3), the signal contribution from photons with an energy between  $E$  and  $E+dE$  is proportional to the number of detected photons in that interval,  $n(E)dE = dE \cdot R_j \cdot d^2 \cdot \Phi_j(E) \cdot e^{-\mu_a(E)T} \cdot e^{(-\Delta\mu_b(E)\gamma_b - \Delta\mu_c(E)\gamma_c)} \cdot A(E)$ , multiplied by the gain

factor  $Q(E)$  or  $\alpha E$ . Characteristic of the x-ray detection process,  $n(E)dE$ , is a stochastic quantity governed by Poisson statistics. Thus, the variance of the  $n(E)dE$  is equal to  $n(E)dE$  itself. Furthermore, as  $n(E)dE$  is typically large in diagnostic x-ray imaging, it can be assumed to fluctuate with a Gaussian distribution with its variance equal to  $n(E)dE$ . The gain factor,  $Q(E)$ , strictly speaking, is also a stochastic quantity. However, its fluctuation can be ignored when the image is quantum limited and the number of light photons scintillated from each x-ray photon is reasonably large: 5-10 or greater. Thus, the signal variance for the signal component from the energy interval of  $E$  to  $E+dQ$  can be approximated by  $n(E)dEQ(E)$  or  $n(E)dE\alpha E$  (Barnes, 1984). Summing the variances over all energy intervals, the total noise variances in the low- and high-energy image signals,  $\sigma_j^2$ ,  $j = l, h$ , can be expressed as;

$$\sigma_{s_j}^2 = \int dE \cdot R_j \cdot d^2 \cdot \Phi_j(E) \cdot e^{-\mu_a(E)T} \cdot e^{(-\Delta\mu_b(E)\gamma_b - \Delta\mu_c(E)\gamma_c)} \cdot A(E) \cdot (\alpha E)^2. \quad (4.21)$$

The  $SNR$ 's in the low- and high-energy images can be expressed as follows:

$$SNR_{s_j} = \frac{\int dE \cdot R_j \cdot d^2 \cdot \Phi_j(E) \cdot e^{-\mu_a(E)T} \cdot e^{(-\Delta\mu_b(E)\gamma_b - \Delta\mu_c(E)\gamma_c)} \cdot A(E) \cdot (\alpha E)}{\left[ \int dE \cdot R_j \cdot d^2 \cdot \Phi_j(E) \cdot e^{-\mu_a(E)T} \cdot e^{(-\Delta\mu_b(E)\gamma_b - \Delta\mu_c(E)\gamma_c)} \cdot A(E) \cdot (\alpha E)^2 \right]^{1/2}}. \quad (4.22)$$

#### 4.2.5 Noise in the Subtracted Image

From Eq. 4.6, the variations of  $D_l$  and  $D_h$ ,  $dD_l$  and  $dD_h$ , can be expressed as a linear combination of variations in  $t_b$  and  $t_c$ ,  $dt_b$  and  $dt_c$ , as follows:

$$dD_j = \left( \frac{\partial F_j}{\partial t_b} \right) dt_b + \left( \frac{\partial F_j}{\partial t_c} \right) dt_c, \quad j = l, h. \quad (4.23)$$

The parameters,  $\partial F_j / \partial t_i$  ( $i = b, c$ ;  $j = l, h$ ), can be explicitly derived using Eq. 4.6 and expressed as:

$$\left( \frac{\partial F_j}{\partial t_i} \right) = \left[ \frac{\int dE \cdot R_j \cdot d^2 \cdot \Phi_j(E) \cdot e^{-\mu_a(E)T} \cdot \Delta\mu_i(E) \cdot e^{(-\Delta\mu_b(E)\gamma_b - \Delta\mu_c(E)\gamma_c)} \cdot A(E) \cdot (\alpha E)}{\int dE \cdot R_j \cdot d^2 \cdot \Phi_j(E) \cdot e^{-\mu_a(E)T} \cdot e^{(-\Delta\mu_b(E)\gamma_b - \Delta\mu_c(E)\gamma_c)} \cdot A(E) \cdot (\alpha E)} \right]. \quad (4.24)$$

Eq. 4.24 shows that the  $\partial F_j / \partial t_i$ 's are actually the  $\Delta \mu_{ij}$ 's averaged over the detected low- or high-energy spectra, thus, the  $\partial F_j / \partial t_i$ 's can be represented as  $\bar{\mu}_{ij}$  where,  $i = b, c$ ;  $j = l, h$ , and expressed in matrix form as follows:

$$\begin{pmatrix} dD_l \\ dD_h \end{pmatrix} = \begin{pmatrix} \bar{\Delta \mu}_{bl} & \bar{\Delta \mu}_{bh} \\ \bar{\Delta \mu}_{cl} & \bar{\Delta \mu}_{ch} \end{pmatrix} \begin{pmatrix} dt_b \\ dt_c \end{pmatrix}. \quad (4.25)$$

Then,  $dt_b$  and  $dt_c$  can be determined as follows:

$$\begin{pmatrix} dt_b \\ dt_c \end{pmatrix} = \begin{pmatrix} \bar{\Delta \mu}_{bl} & \bar{\Delta \mu}_{cl} \\ \bar{\Delta \mu}_{bh} & \bar{\Delta \mu}_{ch} \end{pmatrix}^{-1} \begin{pmatrix} dD_l \\ dD_h \end{pmatrix} = \begin{pmatrix} k_{bl} & k_{bh} \\ k_{cl} & k_{ch} \end{pmatrix} \begin{pmatrix} D_l \\ D_h \end{pmatrix} \quad (4.26)$$

where

$$k_{bl} = \frac{\bar{\Delta \mu}_{ch}}{\bar{\Delta \mu}_{bl} \bar{\Delta \mu}_{ch} - \bar{\Delta \mu}_{cl} \bar{\Delta \mu}_{bh}}, \quad (4.27)$$

$$k_{bh} = \frac{-\bar{\Delta \mu}_{cl}}{\bar{\Delta \mu}_{bl} \bar{\Delta \mu}_{ch} - \bar{\Delta \mu}_{cl} \bar{\Delta \mu}_{bh}}, \quad (4.28)$$

$$k_{cl} = \frac{-\bar{\Delta \mu}_{bh}}{\bar{\Delta \mu}_{bl} \bar{\Delta \mu}_{ch} - \bar{\Delta \mu}_{cl} \bar{\Delta \mu}_{bh}} \quad (4.29)$$

and

$$k_{ch} = \frac{\bar{\Delta \mu}_{bl}}{\bar{\Delta \mu}_{bl} \bar{\Delta \mu}_{ch} - \bar{\Delta \mu}_{cl} \bar{\Delta \mu}_{bh}}. \quad (4.30)$$

Assuming that  $dD_l$  and  $dD_h$  fluctuate randomly with normal distributions, the noise variances can be expressed as follows:

$$\sigma_{t_b}^2 = k_{bl}^2 \cdot \sigma_{D_l}^2 + k_{bh}^2 \cdot \sigma_{D_h}^2 \quad (4.31)$$

and

$$\sigma_{t_c}^2 = k_{cl}^2 \cdot \sigma_{D_l}^2 + k_{ch}^2 \cdot \sigma_{D_h}^2. \quad (4.32)$$

Using Eqs. 4.19 and 4.20, Eqs. 4.31 and 4.32 can be rewritten as follows:

$$\sigma_{t_b}^2 = \frac{k_{bl}^2}{SNR_{S_l}^2} + \frac{k_{bh}^2}{SNR_{S_h}^2} \quad (4.33)$$

and

$$\sigma_{t_c}^2 = \frac{k_{cl}^2}{SNR_{S_l}^2} + \frac{k_{ch}^2}{SNR_{S_h}^2}. \quad (4.34)$$

The  $SNR$  of the subtraction signals,  $t_b$  and  $t_c$ , can then be expressed as the follows:

$$SNR_{t_i} = \frac{t_j}{\sqrt{\frac{k_{ij}^2}{SNR_{S_j}^2} + \frac{k_{ij}^2}{SNR_{S_j}^2}}}. \quad (4.35)$$

Notice that in subtraction images, the tissue structures should be cancelled out and the signals should be zero. Thus,  $SNR_{t_i}$  is the same as the CNR, which can be compared to the  $CCNR$  (calcification contrast-to-noise ratio) in the unsubtracted image. Also notice that  $SNR_{S_j}$  increases in proportion to  $d$ . As a result,  $SNR_{t_i}$  also increases in proportion to  $d$ . This seems to imply that systems with larger pixel sizes have an advantage. However, it is important to note that the low contrast performance or detectability is directly related to the number of photons incident on the object that are in the detector plane rather than just one pixel. Thus, although all equations derived so far apply to the image signals that are formed for each pixel, they should not be directly used to characterize the detectability of  $\mu Cs$ . Instead,  $d^2$  should be replaced by the object area. For the purpose of this work, the shape of the  $\mu Cs$  was assumed to be cubic with a dimension of  $t_c$ . This reflects the fact that smaller calcifications are also lower in contrast due to shorter attenuating thickness. Thus,  $d$  was replaced by  $t_c$  in all numerical computations for this study in order to allow the results to be directly applied to the estimation and comparison of the detectability of  $\mu Cs$ .

### 4.3 Materials and Methods

In order to use Eq. 4.35 to compute the calcification CNR in the unsubtracted or subtraction images, it is necessary to compute the coefficients,  $k_{ij}$ 's, and the SNRs for low and high-energy images,  $SNR_{S_j}$ , using Eqs. 4.22, 4.27 – 4.30. However, in

order to use these equations, imaging parameters must be selected to simulate clinical imaging conditions; the x-ray spectra, attenuation coefficients and detector absorption ratios must be determined from published data for the energy range studied. The methods for these tasks will be described and discussed in the following sections.

#### 4.3.1 X-ray Photon Fluence Spectra

In this study, both mammographic and general radiography x-ray spectra were used. The mammographic x-rays were assumed to be generated by a Mo target and a 30  $\mu\text{m}$  Mo filter (Mo/Mo) at 25, 30, 35, 40, 45 and 50 kVp (Fewell and Shuping, 1978). A 50 kVp spectrum generated by a tungsten target and a lanthanum filter (W/La) was also used. These spectra were used in computations for both single- and dual-energy imaging. The general radiography x-rays were assumed to be generated by a tungsten target at 50-140 kVp with various filtrations (Birch et al., 1979). For x-rays at 100-140 kVp, a 0.25 mm copper (Cu) filter was assumed to be used. For x-rays at 50-90 kVp, a 2.0 mm Al filter was assumed to be used. All published spectra data were normalized and converted into the photon fluence spectrum per unit exposure  $\Phi(E)$  or number of photons per mR per  $\text{mm}^2$  for each 1 keV energy interval.

#### 4.3.2 Attenuation Coefficients

The energy dependent photon mass attenuation coefficients ( $\mu/\rho$ ) were interpolated from published data (Hubbell and Seltzer, 1996). The elemental compositions of 100% adipose and 100% glandular breast tissue (Hammerstein et al., 1979), the  $\text{Gd}_2\text{O}_2\text{S:Tb}$  and  $\text{CsI:Tl}$  scintillators, and  $\text{CaCO}_3$  were used to calculate the weighting factors which are then used to superimpose the ( $\mu/\rho$ ) of the content elements into those of the composite attenuating materials.

The published attenuation coefficients are given, but only at a limited number of selected energies, and had to be interpolated for intermediate energies at which the

spectra data are given (every keV). The interpolation was performed using the following exponential model relating the coefficient to the photon energy:

$$\left(\frac{\mu}{\rho}\right) = \alpha \cdot E^{\beta}. \quad (4.36)$$

Taking logarithms on both sides, Eq. 4.36 can be converted into a linear equation as follows:

$$\ln\left(\frac{\mu}{\rho}\right) = \ln \alpha + \beta \ln E. \quad (4.36b)$$

Using published attenuation coefficients at two ends of an energy interval,  $E_1$  and  $E_2$ ,  $\ln \alpha$  and  $\beta$  were determined using the following equations:

$$\beta = \frac{\ln\left(\frac{\mu}{\rho}\right)_2 - \ln\left(\frac{\mu}{\rho}\right)_1}{\ln(E)_2 - \ln(E)_1} \quad (4.37)$$

and

$$\ln(\alpha) = \frac{\ln\left(\frac{\mu}{\rho}\right)_1 \cdot \ln(E)_2 - \ln\left(\frac{\mu}{\rho}\right)_2 \cdot \ln(E)_1}{\ln(E)_2 - \ln(E)_1}. \quad (4.38)$$

Using Eq. 4.36 in conjunction with the  $\alpha$  and  $\beta$  values determined,  $(\mu/\rho)$  was computed for intermediate energies. The  $(\mu/\rho)$  values were then multiplied by the density ( $\rho$ ) of the appropriate material to obtain the linear attenuation coefficients ( $\mu$ ), which were used in the numerical study. The density ( $\rho$ ) values used for each material are given in Table 4.1.

### 4.3.3 Photon Absorption Ratio for Detectors

The generation of x-ray image signals consists of two separate processes: (1) conversion of x-rays into light or charge and (2) conversion of light or charge into electronic signal. The process of converting x-rays into light is often referred to as scintillation. This has been the primary form of x-ray detection. However, in recent years, conversion of x-rays into charges with a photo-conductor material like

**Table 4.1.** Table showing the different materials used in the simulation studies and the density values ( $\rho$ ) used to convert ( $\mu/\rho$ ) to ( $\mu$ ).

Material	Density ( $\rho$ ) ( $\text{g}/\text{cm}^3$ )
$\text{CaCO}_3$	2.93
$\text{Gd}_2\text{O}_2\text{S:Tb}$	7.34
CsI:Tl	4.51
100% Adipose Tissue	0.93
100% Glandular Tissue	1.04

selenium has been used in the design of digital radiography systems. In this paper, we considered only two types of scintillators: gadolinium oxysulfide doped with terbium ( $\text{Gd}_2\text{O}_2\text{S:Tb}$ ) and thallium-doped Cesium Iodide ( $\text{CsI:Tl}$ ). These two materials were selected because they are being employed in many digital mammography systems as the scintillator materials. Because the doping materials (Tb or Tl) are present only in very small amounts, their presence was neglected in calculations of the absorption ratios. The density and thickness of the  $\text{Gd}_2\text{O}_2\text{S:Tb}$  phosphor was assumed to be  $7.34 \text{ g/cm}^3$  and  $46 \text{ }\mu\text{m}$ , respectively, in calculations of the absorption ratio for the  $\text{Gd}_2\text{O}_2\text{S:Tb}$  scintillator. The thickness was an estimate for the screen only and does not include any of the scintillator backing or binding materials. The density and thickness for the  $\text{CsI:Tl}$  scintillator were assumed to be  $4.51 \text{ g/cm}^3$  and  $100 \text{ }\mu\text{m}$  respectively in the calculation of the absorption ratio for the  $\text{CsI:Tl}$  scintillator.

The x-ray absorption ratios were calculated for photon energies of 10 – 140 keV using the attenuation coefficients that were interpolated from published data (Hubbell and Seltzer, 1996) as follows:

$$A(E) = 1 - e^{-\mu_s(E)t_s}, \quad (4.39)$$

where  $\mu_s(E)$  and  $t_s$  are the linear attenuation coefficient (in  $1/\text{cm}$ ) and thickness (cm) of the scintillator.

#### 4.3.4 Exposures

The entrance exposure for a typical mammogram is about 1000-1200 mR. Thus, the total exposure of dual-energy image acquisition was kept at 1000 mR, unattenuated at the input of the detector. This exposure must be divided between low- and high-energy image acquisitions. The optimal distribution of the exposure was studied and determined by computing the noise of subtraction image signals as a function of the low-energy exposure ratio, defined as the ratio of the low-energy exposure to the total exposure.

### 4.3.5 Noise Levels in the Image Signals

The noise level in the subtraction signal,  $\sigma_{t_c}$ , was calculated for various combinations of low- and high-energy mammographic spectra and various breast thicknesses, tissue compositions and calcification thicknesses. The breast thickness was varied from 3.5 to 7 cm. The tissue composition was varied from 100% adipose/0% glandular to 0% adipose/100% glandular. The total unattenuated exposure at the detector input was kept fixed at 1000 mR with various weighting of low- and high-energy image acquisitions.

The image signals for the non-subtracted images using 25 and 50 kVp as the low- and high-energy input spectra,  $S_l$  and  $S_h$ , were calculated using Eq. 4.3. The total breast thickness used was 5 cm and the tissue composition was 50% adipose/50% glandular (50/50). The noise levels associated with the non-subtracted image signals were computed by taking the square root of Eq. 4.21. The SNR values calculated using Eq. 4.22 were used in computing the inverse matrix in Eq. 4.26. The resulting  $k_{ij}$  values were then used to calculate the noise levels in the tissue signals,  $\sigma_{t_b}$  and  $\sigma_{t_c}$ , for the subtraction images by taking the square root of Eqs. 4.33 and 4.34, respectively. A plot of  $\sigma_{t_c}$  as a function of the low-energy exposure ratio was generated for various  $\mu\text{C}$  sizes.

A  $\mu\text{C}$  size that would yield a SNR of approximately 3:1 was chosen to complete the remaining simulations. Using the same breast thickness and tissue composition as above, the energy separation between the low- and high-energy input spectra was varied from 25/30 kVp to 25/50 kVp. A plot of  $\sigma_{t_c}$  as a function of the low-energy exposure ratio was generated for the various energy separations. Once the optimal energy separation was determined, the tissue composition was varied and a plot of  $\sigma_{t_c}$  as a function of the low-energy exposure ratio was generated for the various tissue compositions. Finally, a simulation with a constant  $\mu\text{C}$  size and 50/50 tissue composition with varying breast thickness was performed. A plot of  $\sigma_{t_c}$  as a

function of the low-energy exposure ratio was generated for the various breast tissue thicknesses.

The optimal exposure ratio was determined by varying the ratio of the incident exposure for the low-energy image. The ratio ranged from a 0.01 to 0.95. The optimal exposure ratio was determined when  $\sigma_r$  was at a minimum. The optimal low-energy exposure ratios for the various simulations were compared.

#### 4.3.6 Image Contrast and CNRs in Unsubtracted Images

Image contrast in unsubtracted images can be quantified by the image signal difference between the background and that in the contrast object regions. A problem in detecting  $\mu$ Cs in mammography is the presence of tissue contrast in the background, which can be considered as a type of noise. However, this type of noise is different from random noise, such as the quantum, electronic, and even the phosphor grain noises. They are actually structural patterns, which can obscure the visibility of  $\mu$ Cs. Although the psychophysical principles and details of this obscuring effect are not well known, it would be beneficial to quantify and compare the calcification contrast-to-noise ratios (*CCNRs*) and calcification contrast-to-background ratios (*CCBRs*), which are defined as the ratio of calcification contrast to the tissue contrast in relation to a common background.

The image signal for a common background area consisting of 50% adipose and 50% glandular tissue with a total thickness of  $T$  can be computed as:

$$S_0 = \int dE \cdot R \cdot d^2 \cdot \Phi(E) \cdot e^{(-0.5\mu_a(E) - 0.5\mu_b(E))T} \cdot A(E) \cdot Q(E). \quad (4.40)$$

The noise in  $S_0$  can be computed as:

$$\sigma = \left[ \int dE \cdot R \cdot d^2 \cdot \Phi(E) \cdot e^{(-0.5\mu_a(E) - 0.5\mu_b(E))T} \cdot A(E) \cdot Q(E)^2 \right]^{1/2}. \quad (4.41)$$

Assuming that the image signal generated by 25% adipose and 75% glandular tissue can be expressed as:

$$S_T = \int dE \cdot R \cdot d^2 \cdot \Phi(E) \cdot e^{-(0.25\mu_a(E) + 0.75\mu_b(E))T} \cdot A(E) \cdot Q(E), \quad (4.42)$$

and the difference signal corresponding to tissue contrast can be computed as  $TC = S_0 - S_T$ . Similarly, assuming that a calcification replaces a cubic volume of background tissue (50% adipose and 50% glandular) with a dimension of  $t_c$ , the image signal can be computed as:

$$S_C = \int dE \cdot R \cdot d^2 \cdot \Phi(E) \cdot e^{-(0.5\mu_a(E) + 0.5\mu_b(E))(T-t_c) - \mu_c(E)t_c} \cdot A(E) \cdot Q(E) \quad (4.43)$$

and the difference signal corresponding to the calcification contrast can then be computed as  $CC = S_0 - S_C$ . Thus,  $CCNR$  and  $CCBR$  can be calculated as  $CC/\sigma$  and  $CC/TC$ .

## 4.4 Results and Discussion

### 4.4.1 Photon Absorption Ratio for Detectors

The absorption ratios for the  $Gd_2O_2S:Tb$  (Gd) and  $CsI:Tl$  (CsI) scintillators are shown in Figure 4.2. The curves are very similar up to approximately 33 keV. The CsI scintillator has k-edges at 33.2 keV and 36 keV. After the first k-edge, the absorption ratio in the CsI scintillator is improved compared to that in the Gd scintillator. A higher absorption in the scintillator at higher energies should result in a higher SNR, thus a decrease in  $\sigma_{t_c}$  when the CsI scintillator is used. This is an important fact due to the increase in  $\sigma_{t_c}$  that is associated with dual-energy subtraction imaging.

### 4.4.2 Signal Spectra

The signal spectra for a 25 kVp Mo/Mo, 50 kVp Mo/Mo and 50 kVp W/La x-rays attenuated by a 5 cm thick, 50/50 breast are shown in Figures 4.3, 4.4 and 4.5 respectively. The total signals of the spectra are normalized to one and are shown for both scintillators. Figure 4.3 shows that the spectra were the same for both scintillators at 25 kVp. This was expected since the attenuation coefficients

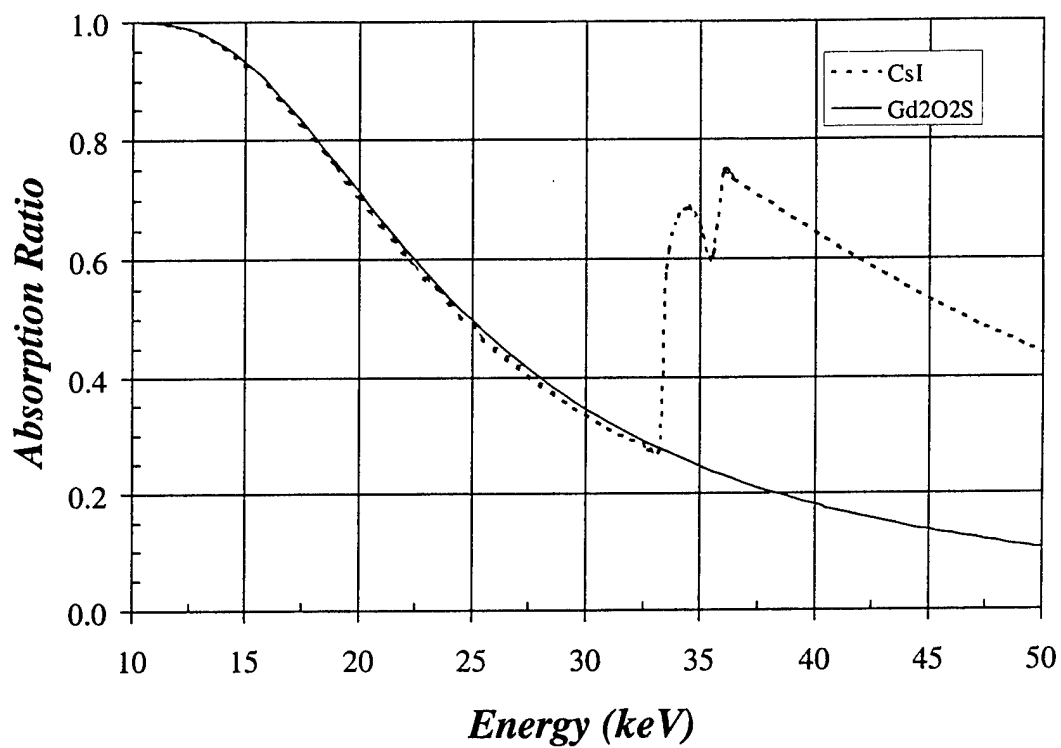


**Figure 4.2.** Plot showing the absorption ratios of the Gd<sub>2</sub>O<sub>2</sub>S:Tb and CsI:Tl scintillators. The CsI:Tl scintillator shows a greater absorption at higher energies due to its k-edges at 33.2 and 36 keV.

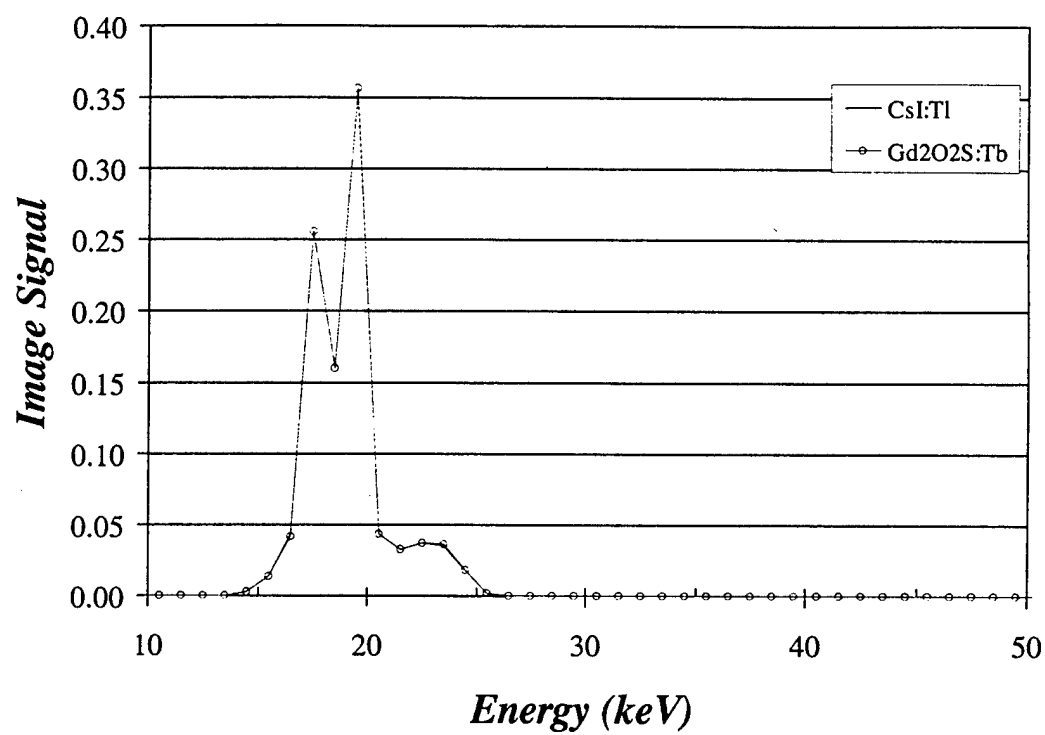


**Figure 4.3.** Plot showing the signal spectra for the  $Gd_2O_2S:Tb$  and  $CsI:Tl$  scintillators using a 25 kVp Mo/Mo incident spectrum. The spectra are identical.

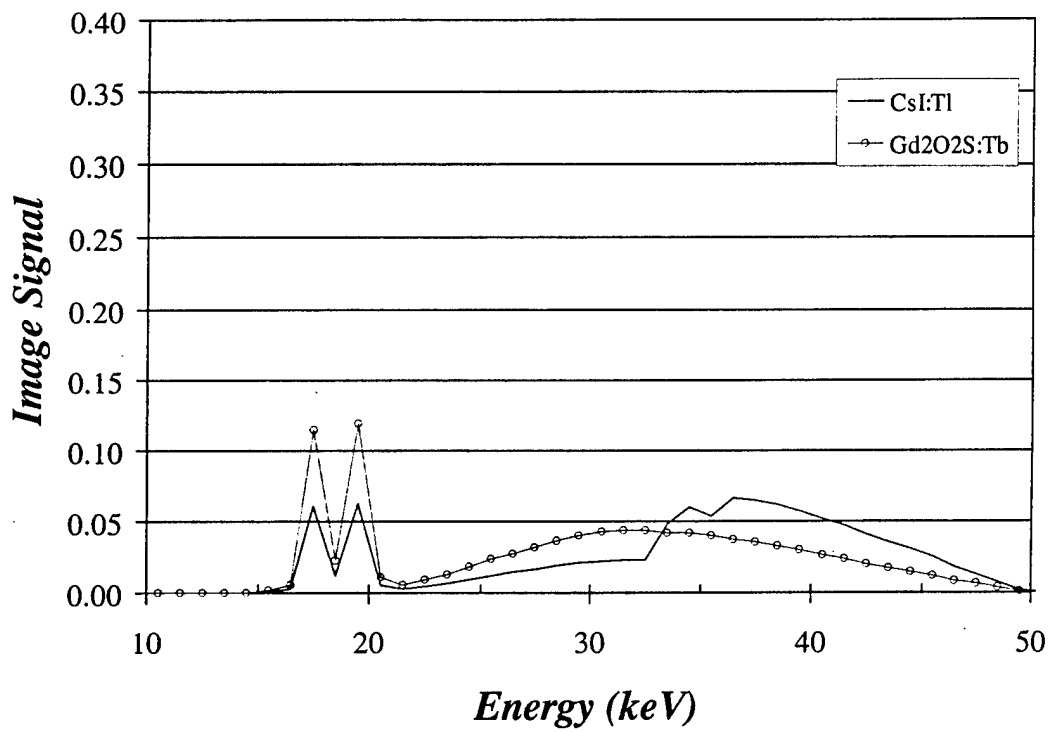


**Figure 4.4.** Plot showing the signal spectra for the Gd<sub>2</sub>O<sub>2</sub>S:Tb and CsI:Tl scintillators using a 50 kVp Mo/Mo incident spectrum.

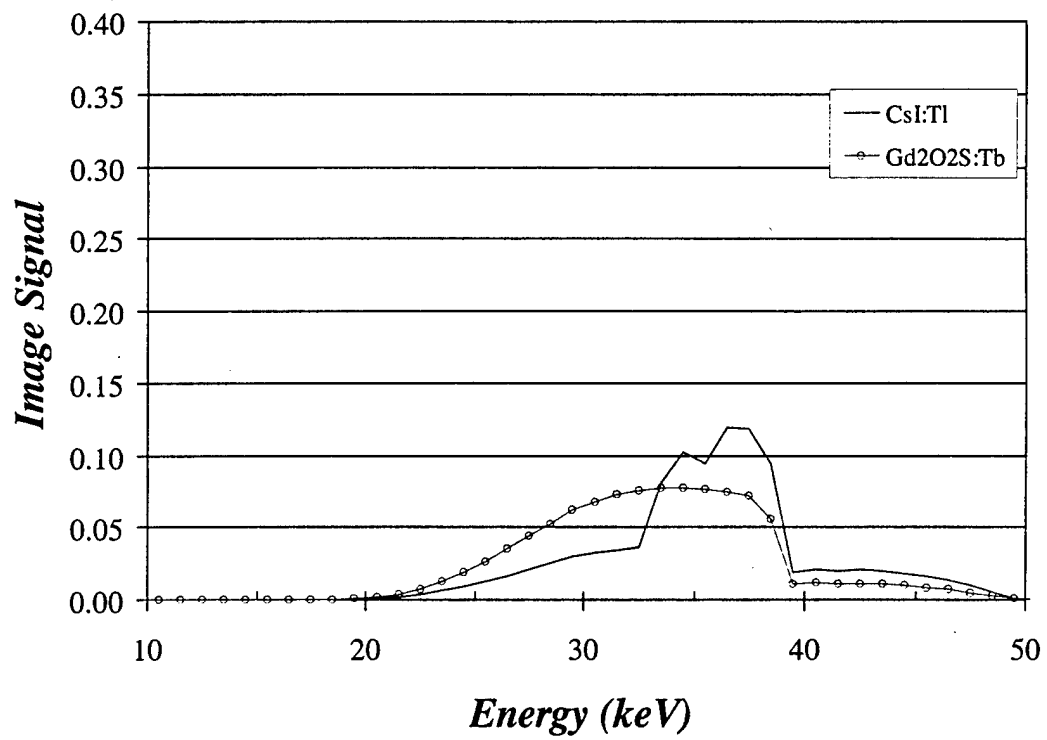


**Figure 4.5.** Plot showing the signal spectra for the Gd<sub>2</sub>O<sub>2</sub>S:Tb and CsI:Tl scintillators using a 50 kVp W/La incident spectrum.

(absorption ratio) for the two scintillators are similar at energies below the CsI k-edges (33 and 36 keV).

In Figure 4.4, the Gd spectrum has a higher signals at energies below the CsI k-edges (16 keV to 33 keV). At energies above, the CsI spectrum has significantly higher signals which are produced by the greater absorption by CsI (Figure 4.2). The signals at the Mo k-edge energies (17.5 and 19.5 keV) were significantly lower when compared with the 25 kVp spectra for both scintillators. The k-edge absorption by the CsI scintillator results in higher average energy and better energy separation for dual-energy subtraction imaging.

In Figure 4.5, the Gd spectrum increases steadily until it reaches the La k-edge (39 keV), where the signal dropped sharply and then decreased slowly as the energy is increased. The CsI spectrum was lower at energies below the CsI k-edges (33 and 36 keV) and higher at energies above. The CsI spectrum also dropped sharply at the La k-edge and then slowly decreased with increasing energy. Again, the k-edge absorption by the CsI scintillator results in a higher average energy and therefore better energy separation for dual-energy subtraction imaging.

#### 4.4.3 Contrast, Noise and SNR in Unsubtracted Images

The *CCNR* and *CCBR* were calculated using signals for 5 cm thick, 50/50 tissue background, 25/75 tissue composition for tissue contrast and a 250  $\mu\text{m}$   $\mu\text{C}$  for the calcification contrast. The results are plotted as a function of x-ray kVp ranging from 25 to 140 in Figure 4.6. As the kVp was increased, both *CCNR* and *CCBR* gradually decreased. The steady decrease of the *CCBR* indicates that even though use of high kVp x-rays tends to reduce the tissue contrast, it reduces the calcification contrast even more, causing the *CCBR* to decrease with the x-ray kVp. There was a sudden drop of *CCNR* at 50 kVp. This may be explained as the result of the change of target material from molybdenum to tungsten.

The *CCBRs* were found to be significantly lower than the *CCNRs*, indicating that in single energy imaging, the detection of  $\mu\text{Cs}$  can be obscured by the presence

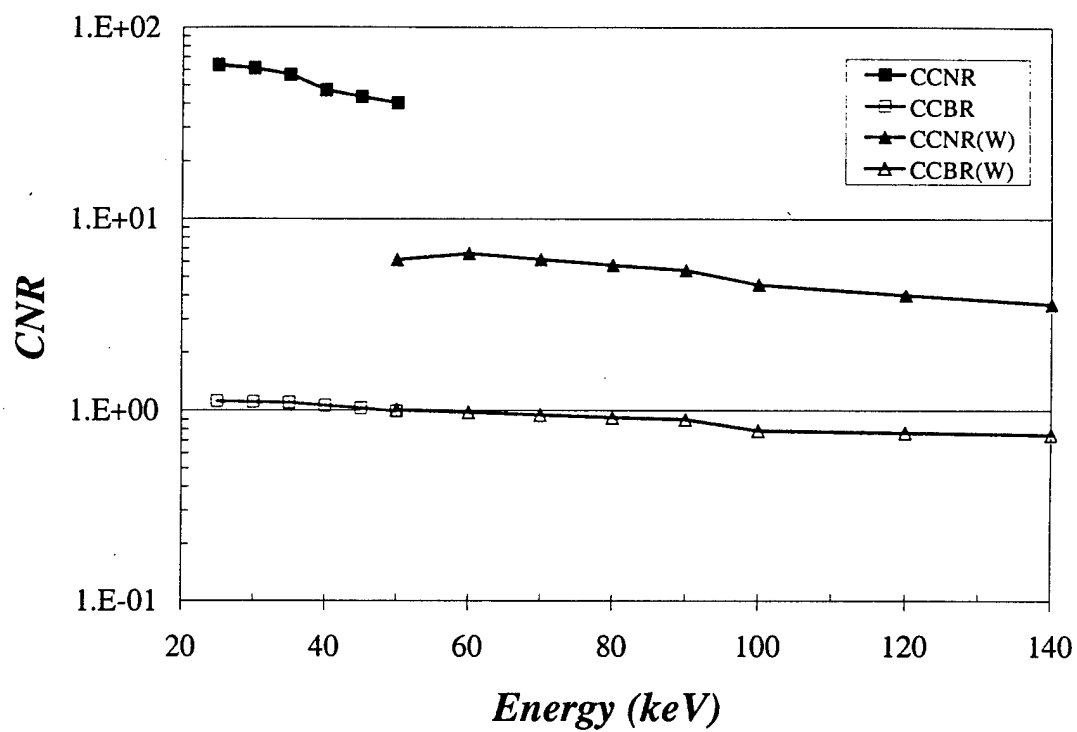


**Figure 4.6.** A plot of the *CCNR* and *CCBR* for energies ranging from 25 to 140 keV. The W represents the spectra that were generated with a tungsten target.

of tissue structures even though the *CCNRs* may be sufficiently high for detection over a uniform background. This demonstrates the benefit of dual-energy subtraction imaging. As the tissue structures are cancelled out, the *CCBRs* rise to very high values and the tissue structures do not obscure the detection and visualization of  $\mu\text{Cs}$  any more. However, the side effect of dual-energy subtraction processing is a decrease of the *CCNR*. One major task in designing and testing the dual-energy subtraction imaging technique is to ensure that there is still sufficient *CCNR* (generally 3 or higher) for detecting the  $\mu\text{Cs}$ .

#### 4.4.4 Mapping X-ray Densities to Tissue Thicknesses

To demonstrate the mapping between  $D'_l$ ,  $D'_h$  and  $t_b$ ,  $t_c$ , the adipose referenced x-ray densities,  $D'_l$  and  $D'_h$ , were computed as functions of  $t_b$  and  $t_c$  using Eq. 4.6. The results are shown in Figure 4.7. The plot, looking like an elongated grid, shows contours corresponding to fixed values of  $t_b$  or  $t_c$ . In the figure, the contour connecting A, B and C corresponds to  $t_b = 0$  and  $t_c$  values ranging from 0  $\mu\text{m}$  to 500  $\mu\text{m}$  and then to 1 mm. The contour connecting D, E and F corresponds to  $t_b = 2.5$  cm and  $t_c$  values ranging from 0  $\mu\text{m}$  to 500  $\mu\text{m}$  and then to 1 mm. Finally, the contour connecting H, I and J corresponds to  $t_b = 5$  cm and  $t_c$  values ranging from 0  $\mu\text{m}$  to 500  $\mu\text{m}$  and then to 1 mm. The contours ABC, DEF and HIJ correspond to regions with glandular tissue ratios of 0% ( $t_b = 0$  cm), 50% ( $t_b = 2.5$  cm) and 100% ( $t_b = 5$  cm) respectively. As the  $\mu\text{C}$  thickness or  $t_c$  increases from 0  $\mu\text{m}$  to 1 mm, the  $(D'_l, D'_h)$  changes from A to C, D to F or H to J depending on the tissue composition.

The contour connecting ADH corresponds to  $t_c = 0$  (no  $\mu\text{Cs}$ ) and  $t_b$  varies from 0 cm (0% glandular) to 2.5 cm (50% glandular) and then to 5 cm (100% glandular). The contour connecting BEI corresponds to  $t_c = 500$   $\mu\text{m}$  and  $t_b$  varies from 0 cm to 2.5 cm and then to 5 cm. Finally, the contour connecting CFJ corresponds to  $t_c = 1$  mm and  $t_b$  varies from 0 cm to 2.5 cm and then to 5 cm. The

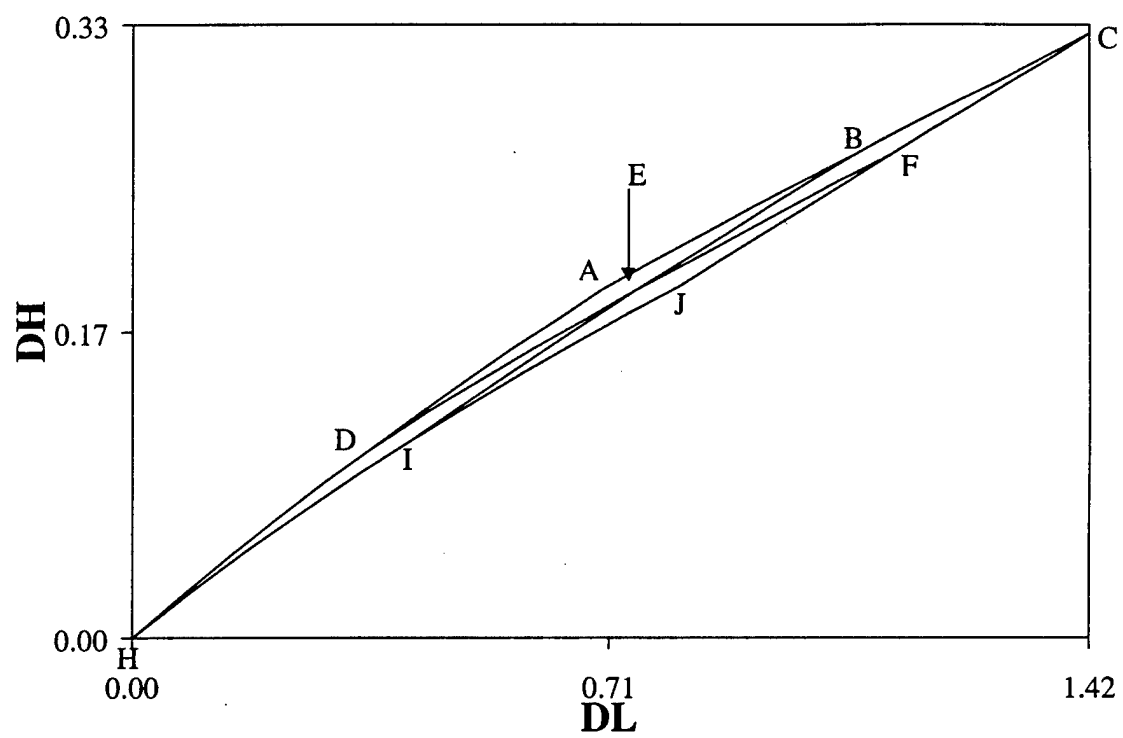


Figure 4.7. A plot of the x-ray densities,  $D_i$  and  $D_h$ , as functions of  $t_b$  and  $t_c$ .

contours ADH, BEI and CFJ correspond to  $\mu\text{C}$  thicknesses of 0  $\mu\text{m}$ , 500  $\mu\text{m}$  and 1 mm regions of respectively. As the glandular tissue component of the breast or  $t_b$  changes from 0 cm (0% glandular) to 2.5 cm (50% glandular) and then to 5 cm (100% glandular), the  $(D'_i, D'_h)$  changes from A to H, B to I or C to J depending on  $t_c$  ( $\mu\text{C}$  size).

#### 4.4.5 Noise Levels in the Image Signals

##### CNR vs. $\mu\text{C}$ Size

Noise in the  $\mu\text{C}$  signals,  $\sigma_{t_c}$ , was calculated as a function of low-energy exposure ratio for various  $\mu\text{C}$  sizes (100 – 300  $\mu\text{m}$ ) using 25 and 50 kVp as the low- and high-energy incident spectra, and assuming a 50/50 tissue composition and a 5 cm breast thickness. The results are shown using both Gd and CsI as scintillators in Figures 4.8 and 4.9, respectively. The use of CsI as a scintillator resulted in a significantly lower  $\sigma_{t_c}$  for all  $\mu\text{C}$  sizes. This may be explained as the result of higher x-ray absorption at higher photon energies as shown in Figure 4.2. The plots in Figures 4.8 and 4.9 indicate that a  $\mu\text{C}$  size of 250  $\mu\text{m}$  could produce an object CNR of approximately 3:1 with the CsI scintillator. However, the object CNR is only approximately 2:1 with the Gd scintillator. Thus, a 250  $\mu\text{m}$   $\mu\text{C}$  size was used in most of the simulation computations in this study. This is a good size to choose as it is on the lower side of  $\mu\text{C}$  sizes that are routinely seen in clinical mammography.

##### Energy Separation

Using 250  $\mu\text{m}$  as the  $\mu\text{C}$  size,  $\sigma_{t_c}$  was computed for a series of different kVp combinations with a Mo/Mo target/filter combination. A fixed low-energy spectrum (25 kVp) and various high-energy spectra (30, 35, 40, 45 and 50 kVp) were used. A 50 kVp W/La target/filter combination was also used as the high-energy spectra in the calculation.  $\sigma_{t_c}$  was plotted as a function of the low-energy exposure ratio for various

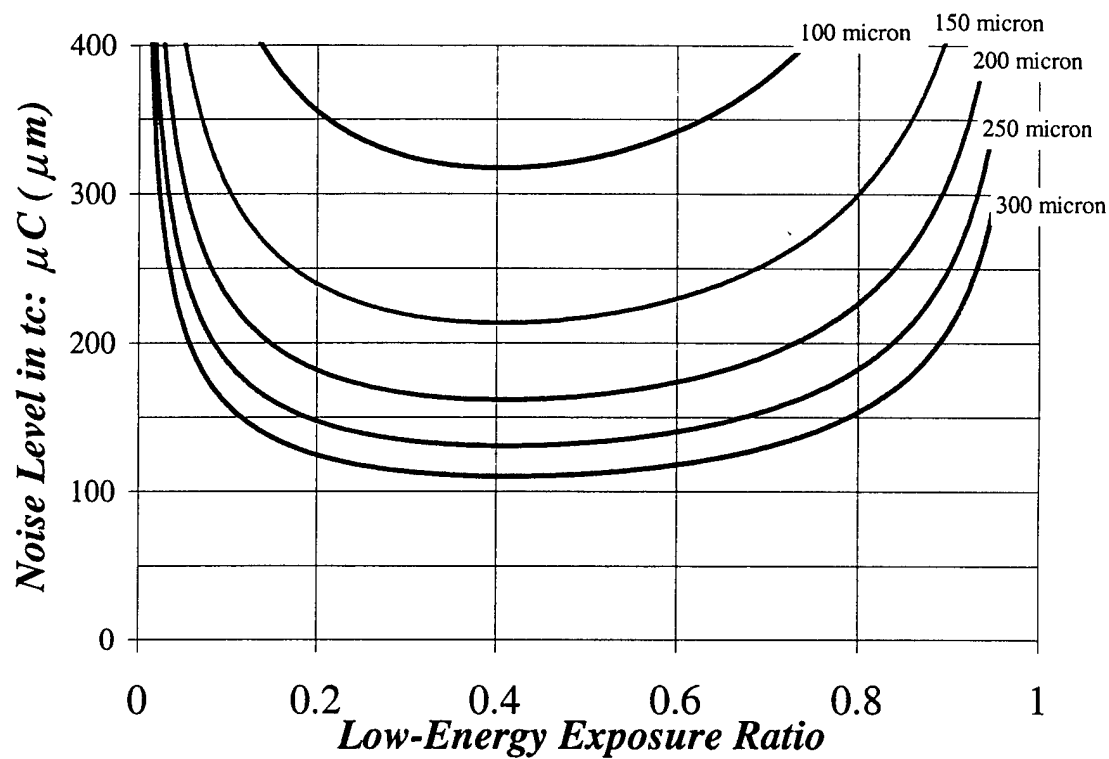


**Figure 4.8.** Plot of  $\sigma_{tc}$  as a function of the low-energy exposure ratio for various  $\mu C$  sizes using the  $Gd_2O_2S:Tb$  scintillator.

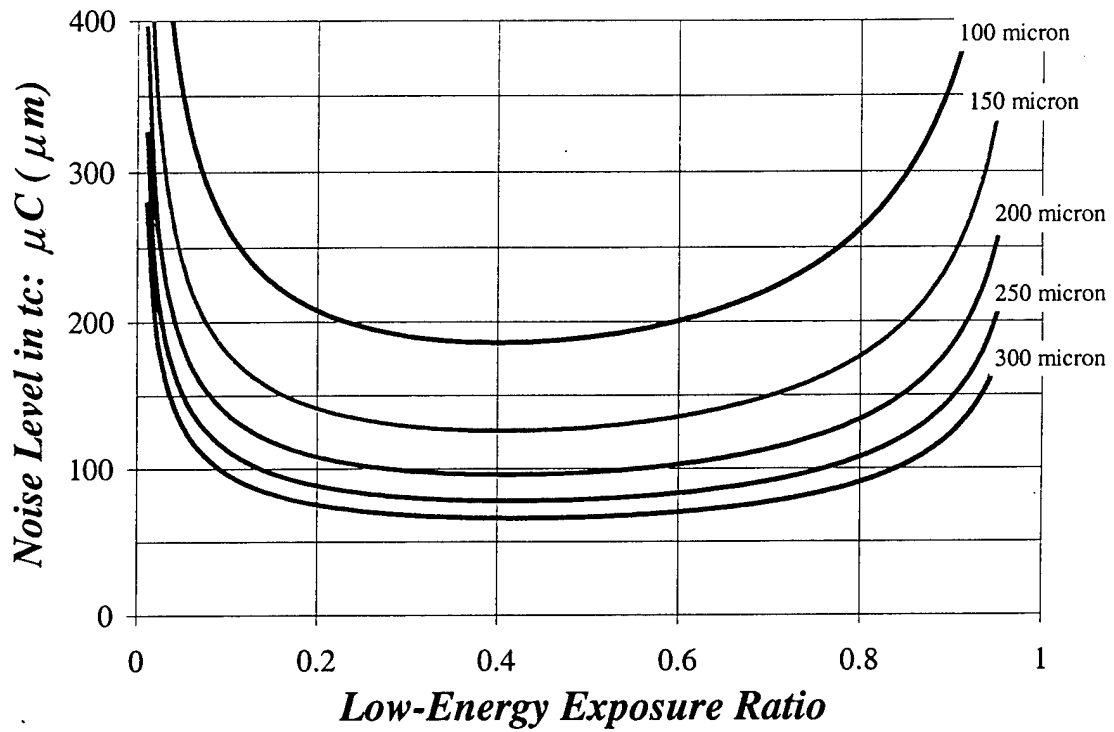


**Figure 4.9.** Plot of  $\sigma_{tc}$  as a function of the low-energy exposure ratio for various  $\mu C$  sizes using the CsI:Tl scintillator.

combinations of energy spectra for both the Gd and CsI scintillators in Figures 4.10 and 4.11, respectively. It was obvious that as the energy separation increased,  $\sigma_{t_c}$  decreased. For smaller energy separations, 25 and 30 and 25 or 35 kVp,  $\sigma_{t_c}$  was approximately the same for both scintillators. With higher energy separations,  $\sigma_{t_c}$  was lower for the CsI scintillator. This may be explained as the result of greater x-ray absorption in the CsI scintillator at higher energies (refer to Figure 4.2). Energy separation by using 25 and 50 kVp x-rays resulted in lowest  $\sigma_{t_c}$ . The plots also show that the energy separation provided by 25 kVp Mo/Mo and 50 kVp W/La resulted in an even lower  $\sigma_{t_c}$ . Although Mo/Rh (rhodium) dual-target tubes are available, a Mo/W dual-target tube is not known to be commercially available. However, such a tube could provide an advantage for implementation of dual-energy digital mammography. Higher energy spectra, greater than 50 kVp, were not studied because the kVp is limited to 50 or less for most known mammographic x-ray tubes.

#### **Effects of Tissue Composition**

In Figure 4.12,  $\sigma_{t_c}$  is plotted as a function of the low-energy exposure ratio for various tissue compositions using CsI as the scintillator. As would be expected, a higher adipose tissue content results in a lower  $\sigma_{t_c}$  and a higher glandular tissue content results in a higher  $\sigma_{t_c}$ . As the tissue becomes denser, with higher glandular content, more low-energy x-ray photons would be attenuated. This beam hardening leads to an increase in the noise in the unsubtracted image and, therefore, an increase in  $\sigma_{t_c}$ .

#### **Effects of Breast Thickness**

In Figure 4.13,  $\sigma_{t_c}$  is plotted as a function of the low-energy exposure ratio for various breast thicknesses using CsI as the scintillator material. As the breast thickness increases, the x-ray photons have to travel through more attenuating material, resulting in prevalent beam hardening. As seen with denser

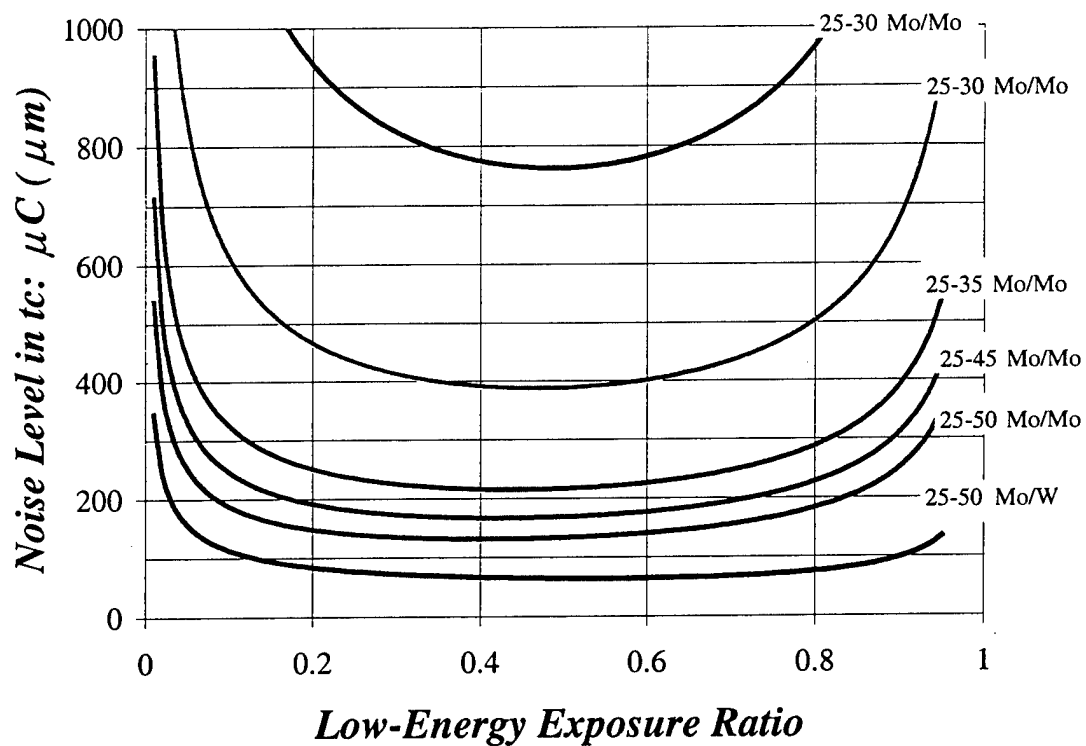
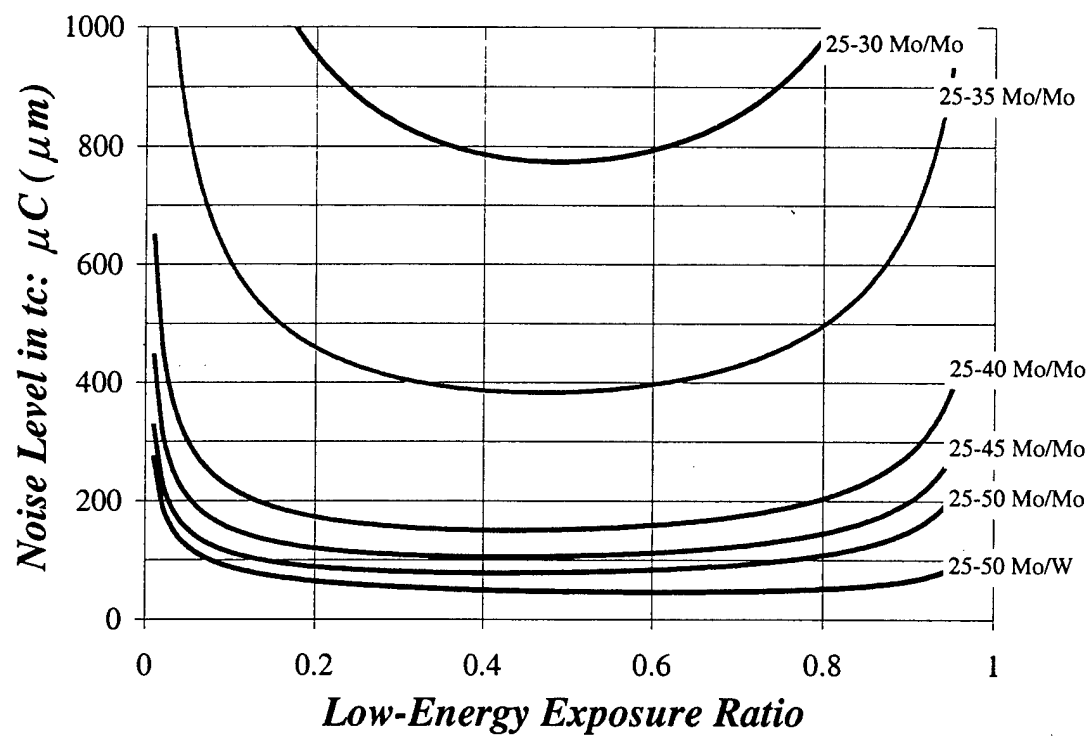


Figure 4.10. Plot of  $\sigma_{tc}$  as a function of the low-energy exposure ratio for various combinations of energy spectra using the  $Gd_2O_2S:Tb$  scintillator.



**Figure 4.11.** Plot of  $\sigma_{tc}$  as a function of the low-energy exposure ratio for various combinations of energy spectra using the CsI:Tl scintillator.

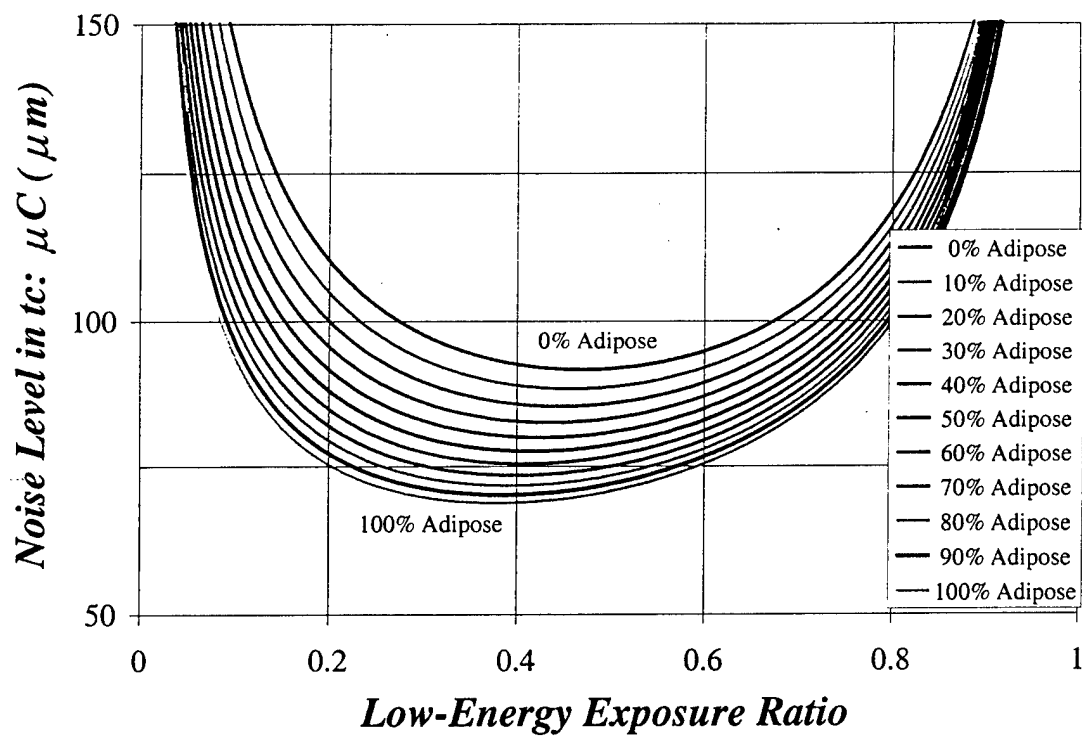


Figure 4.12. Plot of  $\sigma_{tc}$  as a function of the low-energy exposure ratio for various tissue compositions using the CsI:Tl scintillator.

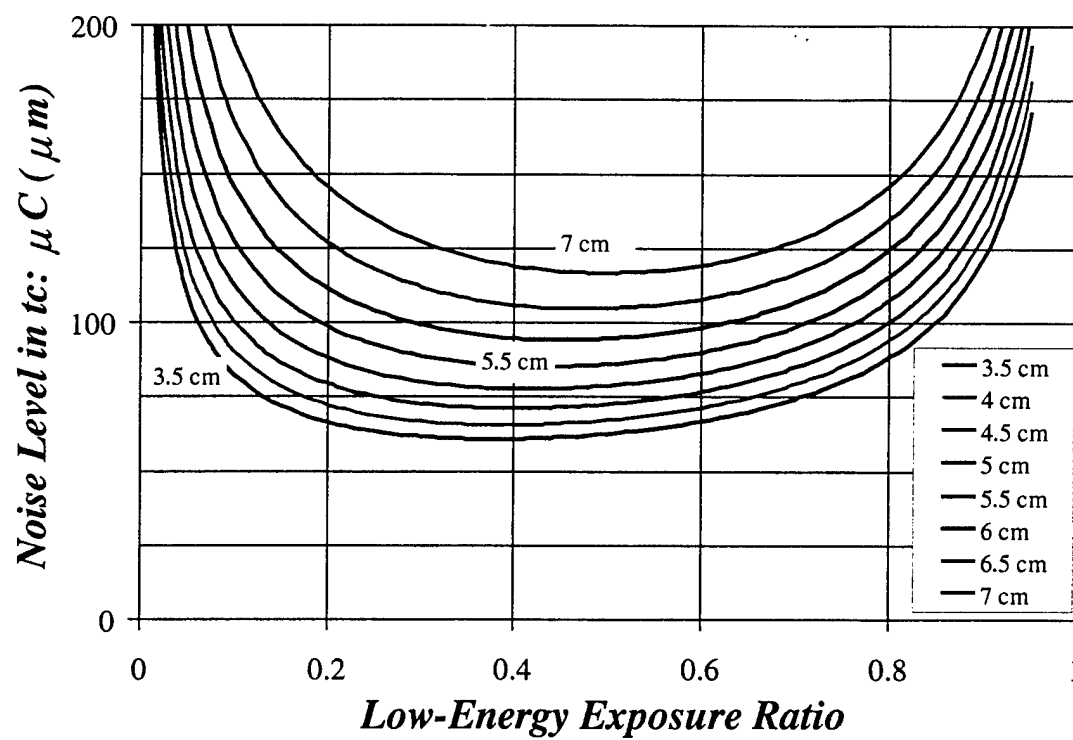


Figure 4.13. Plot of  $\sigma_{tc}$  as a function of the low-energy exposure ratio for various breast thickness using the CsI:Tl scintillator.

breast tissue, increased beam hardening tends to increase the noise in the image, thus increasing  $\sigma_{t_c}$ .

#### 4.4.6 Optimal Low-energy Exposure Ratio

The optimal low-energy exposure ratio can be determined from the plots in Figures 4.9, 4.11, 4.12 and 4.13 as the ratio at which  $\sigma_{t_c}$  is at a minimum. As seen in the plots,  $\sigma_{t_c}$  varies around the optimal ratio. Thus, it is more practical to determine a range of ratios over which  $\sigma_{t_c}$  is within a certain percentage of the minimum value. The ranges of the low-energy exposure ratios for the different simulation studies are shown in Table 4.2. The plots in Figures 4.12 and 4.13 demonstrate a shift in the optimal low-energy exposure ratio towards the lower end (30% – 40%) as the attenuation decreases (i.e., a higher adipose tissue content or a thinner breast thickness). The  $\sigma_{t_c}$ 's in Figures 4.9 and 4.11 are fairly flat over the middle range of the low-energy exposure ratios (between 30% – 60%). The data in Table 4.2 show that a 50/50 split in the exposure between low- and high-energy images should be sufficient to keep  $\sigma_{t_c}$  within 10% of the minimum  $\sigma_{t_c}$ . This was observed for various tissue compositions, breast thicknesses and  $\mu\text{C}$  sizes. This also indicates that a 50/50 split of the low- and high-energy exposures can be used over the entire breast area even though tissue composition varies from region to region.

#### 4.4.7 Dosimetric Considerations

Another consideration in dual-energy subtraction imaging for mammography is the total mid-glandular tissue dose. If we assume a 5 cm thick 50% glandular/50% adipose tissue breast, the mid-glandular tissue dose can be determined from published tables for exposure to dose conversion factors (Wu et al., 1991). By extrapolating the data, it was determined that using a 50 kVp spectrum would increase this conversion factor by a factor of 1.5 over that for a 25 kVp spectrum. This would effectively increase the total mid-glandular tissue dose in dual-energy image acquisition if the

**Table 4.2.** Table showing the ranges of low-energy exposure ratios for simulations with various tissue compositions, breast thicknesses and  $\mu\text{C}$  thicknesses.

Tissue Composition Adipose/Glandular	Optimal Low-Energy Exposure Ratio Range	Breast Thickness	Optimal Low-Energy Exposure Ratio Range	$\mu\text{C}$ Thickness	Optimal Low-Energy Exposure Ratio Range
0%/100%	27 - 68	3.5 cm	19 - 61	100 $\mu\text{m}$	21 - 62
10%/90%	26 - 67	4.0 cm	20 - 61	150 $\mu\text{m}$	22 - 63
20%/80%	25 - 66	4.5 cm	21 - 62	200 $\mu\text{m}$	22 - 63
30%/70%	24 - 66	5.0 cm	22 - 65	250 $\mu\text{m}$	22 - 65
40%/60%	23 - 65	5.5 cm	24 - 65	300 $\mu\text{m}$	22 - 65
50%/50%	22 - 65	6.0 cm	26 - 66		
60%/40%	22 - 63	6.5 cm	26 - 69		
70%/30%	22 - 61	7.0 cm	29 - 71		
80%/20%	20 - 62				
90%/10%	20 - 61				
100%/0%	19 - 61				

total detector exposure (hence the entrance skin exposure) is kept at the level of a regular mammographic image. For example, if a 1 R exposure was split 50/50 between the low- and high-energy exposures, the total mid-glandular tissue dose would be approximately 155 mrad versus 123 mrad for a 25 kVp exposure only with the skin entrance exposure computed from the unattenuated detector exposure via the inverse square law. This would result in an overall increase in the mid-glandular tissue dose by a factor of 1.25. In order to compensate for this increase in dose, the total exposure would need to be reduced to approximately 80% of the initial exposure (i.e. 800 mR). There would also be an approximately 10% increase in all noise levels computed including those for the  $\mu\text{C}$  signal. Since the increase in noise applies to all noise computed and is rather small in magnitude, it should not significantly affect the conclusions or indications from our studies based on a fixed total detector exposure of 1 R.

#### 4.5 Summary

The absorption ratios of the CsI and Gd scintillator were calculated and compared. The results (Figure 4.2) showed that the CsI scintillator has a better absorption ratio at energies higher than 33 keV due to its k-edges at 33.2 and 36 keV. As a result of the difference in the absorption ratio, the results from the simulation studies showed that the CsI scintillator is better suited for dual-energy subtraction mammography than is the Gd scintillator (Figures 4.8, 4.8, 4.10 and 4.11).

The *CCNR* and *CCBR* were calculated for energies ranging from 25 – 140 keV (Figure 4.8). This demonstrated that there is not an advantage in using higher energies (>50 keV) for dual-energy subtraction mammography because as the energy increases, both the *CCNR* and the *CCBR* decrease. The limitation of the  $\mu\text{C}$  visibility due to the *CCBR* can be eliminated by performing dual-energy subtraction.

It was determined that using a  $\mu\text{C}$  size of 250  $\mu\text{m}$  would result in an object CNR of approximately 3:1 with the CsI scintillator and approximately 2:1 with the Gd scintillator (Figures 4.8 and 4.9). A 250  $\mu\text{m}$   $\mu\text{C}$  size was then used for the remaining simulation computations.

It was also shown that as the energy separation increased,  $\sigma_{t_c}$  decreased (Figures 4.10 and 4.11).  $\sigma_{t_c}$  was lower for the CsI scintillator and energies of 25 and 50 kVp resulted in the lowest  $\sigma_{t_c}$  values. Using 50 kVp W/La as the high-energy spectra resulted in an even lower  $\sigma_{t_c}$ . Although Mo/W dual-target tubes are not available, such a tube could provide an advantage for implementation of dual-energy digital mammography.

Simulations were also done with varying tissue compositions and total breast thicknesses (Figures 4.12 and 4.13 respectively). As the attenuation in the breast increased (i.e. a higher glandular tissue content or thicker breast),  $\sigma_{t_c}$  decreased. Beam hardening leads to an increase in the noise in the unsubtracted image and therefore in  $\sigma_{t_c}$ . It was also determined that a 50/50 split in the exposure between the low- and high-energy images should be sufficient to keep  $\sigma_{t_c}$  within 10% of the minimum  $\sigma_{t_c}$  (Table 4.2).

## Chapter 5 – Conclusion

### 5.1 Conclusions

The purpose of this research was to study two methods for improving the detectability of  $\mu$ Cs using digital mammography: geometric magnification and dual-energy subtraction imaging. The conclusions from this research in relation to the hypotheses are summarized below.

1. The effects of magnification on the MTF, NPS, and NEQ for a digital imaging system were studied. Magnification can bring out more details by improving the MTF. However, the size of the focal spot and the spatial frequency of the object limit the improvement in MTF. There was an increase in the NPS, but a slight improvement in the NEQ due to the coverage of the object with more x-ray photons. However, this improvement is obtained at the expense of a higher exposure to the breast.
2. A phantom study was conducted to compare magnification digital mammography with magnification screen/film mammography for the detection of  $\mu$ Cs. The results from a minimum detectability analysis showed that an increase in the  $\mu$ C detectability is seen with an increase in the magnification. The results also show that the digital system performs as well as or better than the screen/film system for detection of  $\mu$ Cs in magnification imaging. A ROC analysis comparing the  $\mu$ C detectability of the two imaging systems showed that the digital system was significantly better than the screen/film for overall  $\mu$ C detection at various  $M$ s ranging from 1 to 3.

3. The numerical simulations demonstrated that it is feasible to use a dual-energy subtraction imaging technique to improve the detectability of  $\mu\text{Cs}$ . The results demonstrated that the SNR after subtraction allows for the visualization of  $\mu\text{Cs}$  with a diameter of 250  $\mu\text{m}$  or greater. It was also determined that a 50/50 split in the exposure between the low- and high-energy images should be sufficient to keep the noise in the subtraction signals within 10% of the minimum noise level and that a CsI:Tl scintillator is better suited for dual-energy subtraction mammography than the  $\text{Gd}_2\text{O}_2\text{S:Tb}$  scintillator due to the k-edge absorption at 33.2 and 36 keV.

## 5.2 Future Studies

### Magnification

Future studies should include improving and expanding the phantom study that was performed for this research. Some possible improvements could include: (1) a better phantom design that would have the  $\mu\text{Cs}$  embedded in breast equivalent tissue, (2) using the same set of  $\mu\text{C}$  sizes at each  $M$  for both imaging systems, (3) increasing the number of exposures and  $\mu\text{Cs}$  to improve the statistical power, (4) increasing the number of readers, (5) changing the qualifications of the readers to include board-certified radiologists and or radiology residents and (6) having the readers use a 5-point confidence rating scale (1 = definitely no  $\mu\text{Cs}$ ; 2 = probably no  $\mu\text{Cs}$ ; 3 =  $\mu\text{Cs}$  possibly present; 4 =  $\mu\text{Cs}$  probably present; 5 =  $\mu\text{Cs}$  definitely present).

Since full-field digital mammography systems are now commercially available, the effects of magnification on the image quality parameters of these systems should also be studied. In addition, the magnification phantom study should also be performed to compare the  $\mu\text{C}$  detectability between the full-field digital and screen/film systems. The significance of such a study would be greater because in this research the use of a small-field digital system limited the field of view and therefore the practical value of the magnification technique.

### **Dual-Energy Subtraction Imaging**

Future studies for dual-energy subtraction imaging would include developing a technique to map the x-ray densities to the tissue thicknesses. Once the mapping technique is developed, phantom studies could be performed to implement and evaluate the dual-energy algorithm. Other considerations for dual-energy subtraction imaging would include performing dose estimation studies to determine the proper techniques to be used and to explore its applications in screening mammography and diagnostic work-ups.



## Bibliography

- AAPM Report No. 15 (1985) *Performance Evaluation and Quality Assurance in Digital Subtraction Angiography*. New York, American Institute of Physics.
- Asaga T, Masuzawa C, Yoshida A, and Matsuura H (1995) Dual-Energy Subtraction Mammography. *Journal of Digital Imaging* **8**(1), Suppl. 1, 70-73.
- Barnes GT (1985) Noise analysis of radiographic imaging. In: Doi K, Lanzl L, and Lin PJP, Editors *Recent Advances in Digital Imaging, Proceedings of the 1984 AAPM Summer School*. New York, American Institute of Physics, pp. 16-38.
- Barnes GT, Sones RA, Tesic MM, Morgan DR, and Sanders JN (1985) Detector for dual-energy digital radiography. *Radiology* **156**(2), 537-540.
- Birch R, Marshall M and Ardan GM (1979) *Catalogue of Spectral Data For Diagnostic X-rays*. London, The Hospital Physicists' Association.
- Boone JM (1994) X-ray imaging concepts: Mathematics and modeling. In: Seibert JA, Barnes GT, and Gould RG, Editors *Specification, Acceptance Testing and Quality Control of Diagnostic X-ray Imaging Equipment, Medical Physics Monograph No. 20*. New York, American Institute of Physics, pp.75-108.
- Boone JM, Shaber GS and Tecotzky M (1990) Dual-energy mammography: A detector analysis. *Medical Physics* **17**(4), 665-675.

- Boyle WS and Smith GE (1970) Charged coupled semiconductor devices. *Bell System Technical Journal* **49**, 587-593.
- Brettle DS and Cowen AR (1994) Dual-energy digital mammography utilizing stimulated phosphor computed radiography. *Physics in Medicine and Biology* **39**, 1989-2004.
- Brettle DS, Ward SC, Parkin GJS, Cowen AR, and Sumsion HJ (1994) A clinical comparison between conventional and digital mammography utilizing computed radiography. *The British Journal of Radiology* **67**, 464-468.
- Burgess, AE and Humphrey, K (1977) Visual perception limits in angiography. *Proceedings of the SPIE* **127**, 51-59.
- Bushberg JT, Seibert JA, Leidholt EM Jr., and Boone JM (1994) *The Essential Physics of Medical Imaging*. Baltimore, Williams and Wilkins. Chapters 5, 8 and 9.
- Chakraborty DP and Barnes GT (1989) An energy sensitive cassette for dual-energy mammography. *Medical Physics* **16**(1), 7-13.
- Cowen AR, Parkin GJS, and Hawkrigde P (1997) Direct digital mammography image acquisition. *European Radiology* **7**, 918-930.
- Cunningham IA. (1999) Image Quality and Dose. In: Seibert JA, Filipow LJ and Andriole KP, Editors *Practical Digital Imaging and PACS, Medical Physics Monograph No. 25*. Madison, Medical Physics Publishing, pp. 225-258.
- Curry TS III, Dowdey JE. and Murray, RC Jr. (1990) *Christensen's Physics of Diagnostic Radiology*. Philadelphia, Lea & Febiger. Chapter 22.

- Dobbins JT III (1995) Effects of undersampling on the proper interpretation of modulation transfer function, noise power spectra, and noise equivalent quanta of digital imaging systems. *Medical Physics* **22**(2), 171-181.
- Dobbins JT III, Ergun DL, Rutz L, Hinshaw DA, Blume H and Clark DC (1995) DQE(f) of four generations of computed radiography acquisition devices. *Medical Physics* **22**(10), 1581-1593.
- Dorfman, DD and Alf, E (1969) Maximum likelihood estimation of parameters of signal detection theory and determination of confidence intervals – rating data method. *Journal of Mathematical Psychology* **6**, 487-496.
- Dowsett DJ, Kenny PA and Johnston RE (1998) *The Physics of Diagnostic Imaging*. New York, Chapman & Hall Medical. Chapter 8.
- Egan RL (1988) *Breast Imaging: Diagnosis and Morphology of Breast Diseases*. Philadelphia, W. B. Saunders Company. Chapter 6.
- Ergun DL, Mistretta CA, Brown DE, Bystriany RT, Sze WK, Kelcz F and Naidich DP (1990) Single-exposure dual-energy computed radiography: Improved detection and processing. *Radiology* **174**(1), 243-249.
- Fewell TR, and Shuping RE (1978) *Handbook of Mammographic X-ray Spectra*. Rockville, BRH (FDA).
- Fraser RG, Hickey NM, Niklason LT, Sabbagh EA, Luna RF, Alexander CB, Robinson CA, Katzenstein AA and Barnes GT (1986) Calcification in pulmonary nodules: Detection with dual-energy digital radiography. *Radiology* **160**(3), 595-601.

- Fujita H, Tsai D, Itoh T, Doi K, Morishita J, Ueda K and Ohtsuka A (1992) A simple method for determining the modulation transfer function in digital radiography. *IEEE Transactions on Medical Imaging* **11**(1), 34-39.
- Funke M, Breiter N, Hermann KP, Oestmann JW, and Grabbe E (1998) Storage phosphor direct magnification mammography in comparison with conventional screen-film mammography- a phantom study. *The British Journal of Radiology* **71**, 528-534.
- Hammerstein R, Miller D, White D et al. (1979) Absorbed Dose in Mammography. *Radiology* **130**, 485-491.
- Hanafee, W and Stout, P (1962) Subtraction technique. *Radiology* **79**, 658-661.
- Hejazi S and Trauernicht DP (1997) System considerations in CCD-based x-ray imaging for digital chest radiography and digital mammography. *Medical Physics* **24**(2), 287-297.
- Heywang-Köbrunner SH, Schreer I, and Dershaw DD (1997) *Diagnostic Breast Imaging*. New York, Thieme Stuttgart. Chapters 3 and 20.
- Ho J, Kruger RA and Sorenson JA (1989) Comparison of dual and single exposure techniques in dual-energy chest radiography. *Medical Physics* **16**(2), 202-208.
- Hubbell JH and Seltzer SM (1996) *Tables of X-ray Mass Attenuation Coefficients and Mass Energy-Absorption Coefficients*.  
<http://physics.nist.gov/PhysRefData/XrayMassCoef/cover.html>.

- Jeans WD (1990) The development and use of digital subtraction angiography. *The British Journal of Radiology* **63**(747), 161-168.
- Johns PC, Drost DJ, Yaffe MJ, and Fenster A (1985) Dual-energy mammography: Initial experimental results. *Medical Physics* **12**(3), 297-304.
- Johns PC and Yaffe MJ (1985) Theoretical optimization of dual-energy imaging with application to mammography. *Medical Physics* **12**(3), 289-296.
- Johnston, DA (2000) Private Communication, The University of Texas M.D. Anderson Cancer Center, Houston, TX.
- Karellas A, Harris LJ, Liu H, Davis MA, and D'Orsi CJ (1992) Charge-coupled device detector: Performance considerations and potential for small-field mammographic imaging applications. *Medical Physics* **19**(4), 1015-1023.
- Kelcz F, Mistretta CA and Riederer SJ (1977) Spectral considerations for absorption-edge fluoroscopy. *Medical Physics* **4**(1), 26-35.
- Kopans DB (1998) *Breast Imaging*. Philadelphia, Lippincott - Raven. Chapter 5.
- Kruger. RA (1982) Basics of computerized fluoroscopy difference imaging. In: Mistretta, CA, Crummy, AB, Strother, CM and Sackett, JF, Editors *Digital Subtraction Arteriography: An Application of Computerized Fluoroscopy*. Chicago, Year Book Medical Publishers, Inc., pp. 16-22.
- Metz CE (1986) ROC methodology in radiologic imaging. *Investigative Radiology* **21**(9), 720-733.

- Muntz EP (1979) Analysis of the significance of scattered radiation in reduced dose mammography, including magnification effects, scatter suppression, and focal spot and detector blurring. *Medical Physics* **6**(2), 110-117.
- Muntz EP (1981) On the comparison of actual and calculated improvements in the imaging of calcifications using magnification mammography. *Medical Physics* **8**(4), 496-501.
- Muntz EP and Logan WW (1979) Focal spot size and scatter suppression in magnification mammography. *American Journal of Radiology* **133**, 453-459.
- Parkin GJS (1995) Clinical Aspects of Direct Digital Mammography. *Journal of Digital Imaging* **8**(1) Suppl. 1, 61-66.
- Peters ME, Voegeli DR, and Scanlan KA (1989) *Handbook of Breast Imaging*. New York, Churchill Livingstone. Chapter 4.
- Schmidt RA and Nishikawa RM (1995) Clinical use of digital mammography: The present and the prospects. *Journal of Digital Imaging* **8**(1), Suppl. 1, 74-79.
- Seongraphe DMR Mammography System, GE Medical Systems Technical Publication (1998). GE Medical Systems, Milwaukee, WI.
- Shaw CC and Gur D (1992) Comparison of three different techniques for dual-energy subtraction imaging in digital radiography: A signal-to-noise analysis. *Journal of Digital Imaging* **5**(4), 262-270.

- Shaw CC, Liu X, Lemacks MR, Rong JX and Whitman GJ (2000) Optimization of MTF and DQE in magnification radiography – a theoretical analysis. In: Dobbins JT III and Boone JM, Editors *Medical Imaging 2000: Physics of Medical Imaging, Proceedings of SPIE 3977*, 466-475.
- Sickles EA (1980) Further experience with microfocal spot magnification mammography in the assessment of clustered breast microcalcifications. *Radiology* **137**, 9-14.
- Sickles EA (1982) Mammographic detectability of breast microcalcifications. *American Journal of Radiology* **139**, 913-918.
- Sickles EA, Doi K and Genant HK (1977) Magnification film mammography: Image quality and clinical studies. *Radiology* **125**, 69-76.
- Sprawls P (1997) Digital imaging concepts and applications. In: Frey GD and Sprawls P, Editors *The Expanding Role of Medical Physics in Diagnostic Imaging, Proceedings of the 1997 AAPM Summer School*. Madison, Advanced Medical Publishing, pp. 17-36.
- Stewart BK and Huang HK (1990) Single-exposure dual-energy computed radiography. *Medical Physics* **17**(5), 866-875.
- Vedantham S, Karellas A, Suryanarayanan S, Albagli D, Han S, Tkaczyk JE, Landberg CE, Opsahl-Ong B, Granfors PR, Levis I, D'Orsi CJ and Hendrick RE (2000) Full breast digital mammographic imaging with an amorphous silicon-based flat panel detector: Physical characteristics of a clinical prototype. *Medical Physics* **27**(3), 558-567.

- Vedantham S, Karellas A, Suryanarayanan S, Levis I, Sayag M, Kleehammer R, Heidsieck R and D'Orsi CJ (2000) Mammographic imaging with a small format CCD-based digital cassette: Physical characteristics of a clinical system. *Medical Physics* **27**(8), 1832-1840.
- Williams MB and Fajardo LL (1996) Digital mammography: Performance considerations and current detector designs. *Academic Radiology* **3**, 429-437.
- Williams MB, Mangiafico PA and Simoni PU (1999) Noise power spectra of images from digital mammography detectors. *Medical Physics* **26**(7), 1279-1293.
- Women's Cancer Network, Gynecologic Cancer Information Web Page, [http://www.wcn.org/cancer\\_info/breast1.html](http://www.wcn.org/cancer_info/breast1.html).
- Wu X, Barmes GT and Tucker DM (1991) Spectral dependence of glandular tissue dose in screen-film mammography. *Radiology* **179**, 143-148.
- Yaffe MJ and Rowlands JA (1997) X-ray detectors for digital radiography. *Physics in Medicine and Biology* **42**, 1-39.
- Yaffee, M. J. (1999) Digital mammography. In: Seibert JA, Filipow LJ and Andriole KP, Editors *Practical Digital Imaging and PACS, Medical Physics Monograph No. 25*. Madison, Medical Physics Publishing, pp. 177-223.

## Vita

Michael René Lemacks was born in Columbia, South Carolina on November 5, 1968, the son of Roger and Carolyn Lemacks. After graduating from Spring Valley High School in 1986, he entered the United States Army where he served for two years. In 1989 he entered Midlands Technical College in Columbia, SC and received an Associate Degree in Radiological Sciences in 1991. For the next six years, he worked at Richland Memorial Hospital as an X-ray Technologist. In 1994 he entered The University of South Carolina in Columbia, SC and received a Bachelor of Science degree in Physics with a minor in Math in 1997. In August of 1997 he entered The University of Texas Health Science Center at Houston Graduate School of Biomedical Sciences.

Permanent address:  
10 Constable Lane  
Columbia, SC 29223

SUPPLEMENT TO *Radiology*

November 1999 • Volume 213 (P)

# 1999 Scientific Program

*Radiological Society of North America*

*85th Scientific Assembly and Annual Meeting*

*November 28–December 3, 1999*

*McCormick Place, Chicago*

A CENTURY  
OF RESEARCH & EDUCATION

RSNA 1999

**RSNA**

Radiological Society  
of North America  
Founded in 1915



American Association  
of Physicists in Medicine

**METHOD AND MATERIALS:** Images were made at several different radiographic techniques using equal doses on a Kodak Min-R 2000 system and on a prototype full-field digital unit that used a CsI phosphor and amorphous silicon detector. For each target/film/kVp combination (Mo/Mo/26, Mo/Rh/28, Rh/Rh/30), exposures at 10 different mAs settings were made. This resulted in images that had film optical densities ranging from 0.21 to 4.2. Three observers read each image and determined the number of disks visible for each contrast level. SNRs were measured directly from the images by calculating the difference between the mean pixel value inside and outside the disk; and, by calculating the standard deviation in the mean pixel value in ten different regions of equal size and shape to the disk, sampled outside the disk. In addition, the SNRs were calculated using the standard formula based on modulation transfer function, noise power spectrum, characteristic curve, and exposure data for each system.

**RESULTS:** Visually, the digital images were superior to the screen-film images in over 90% of the comparisons (i.e. more disks were visible in the digital images). This was particularly true for images taken at low and high mAs. The measured and calculated SNRs showed good agreement within experimental error. There was general agreement between the observer results and the calculated SNRs after incorporating the human visual system response into the calculation.

**CONCLUSIONS:** Full-field digital mammograms have higher image quality (i.e., higher SNR) than screen-film mammograms over a wide variety of exposure conditions. (RMLN is a shareholder in R2 Technology, Inc. (Los Altos, CA).)

#### 1165 • 2:39 PM

##### Comparison of Conventional Screen-Film Mammography and a Direct Digital Magnification System: Detection of Simulated Small Masses and Calcifications with Usual and Reduced Dose

K. Hermann, PhD, Goettingen, Germany • M. Funke, MD • E.H. Grabbe, MD

**PURPOSE:** Comparison of a direct digital magnification mammography system using a large-area amorphous silicon image receptor and a conventional screen-film mammography system with regard to the detection of simulated small masses and calcifications. Evaluation of the impact of a dose reduction with the digital flat-panel detector was of special interest.


**METHOD AND MATERIALS:** A scintillator coupled self-scanning flat-panel detector, based on amorphous silicon technology with 127 x 127  $\mu\text{m}$  pixel size, 2,232 x 3,200 matrix and 16 bit digital output was used. This digital detector was part of a new magnification mammography system, which performs full-sized overview mammograms in 2.1fold magnification. The direct digital system was compared with a state-of-the-art conventional mammography system. Images were taken at the same dose as screen film mammograms and at significantly reduced doses. A contrast-detail mammography phantom (CDMAM) consisting of an aluminum base with gold disks of orderly decreasing thickness and diameter located in small squares in a 16 x 16 matrix simulating both small masses and calcifications was used to estimate the contrast-detail resolution. The correct observation ratio (COR) as a figure of the detail resolution was calculated as the percentage of correctly identified disks of the total number of disks. Receiver operating characteristic (ROC) analysis was performed for observations made by three independent observers. Student's *t* test (95% confidence-level) was used for statistical analysis.

**RESULTS:** ROC analysis showed that images taken with the direct digital mammography system at the same dose as screen-film mammograms were significantly superior to this conventional images with respect to the detectability of small masses and calcifications. The digital system with almost bisected dose achieved the COR values of conventional screen-film mammography.

**CONCLUSIONS:** The results of this phantom study indicate that a amorphous silicon detector technology in combination with direct magnification technique holds promise in terms of dose reduction in mammography without loss of diagnostic accuracy compared with conventional screen-film mammography.

#### 1166 • 2:48 PM

##### A Dual-Energy Subtraction Imaging Technique for Enhanced Microcalcification Imaging and Tissue Composition Measurement in Digital Mammography

 C.C. Shaw, PhD, Houston, TX • X. Liu, PhD • G.J. Whitman, MD

**PURPOSE:** To describe and demonstrate a dual-energy subtraction imaging technique to enhance microcalcification imaging and to obtain tissue composition measurements.

**METHOD AND MATERIALS:** A dual-energy subtraction technique was used to generate two images representing the adipose and glandular tissue thickness on a pixel-by-pixel basis, respectively. The total breast thickness information was added to separate and image a third attenuating material: calcification. The two thickness images were also used to generate a

pixel-by-pixel measurement of tissue composition. Theoretical and numerical studies were conducted to investigate the properties of the calcification signals and effects of various parameters including the x-ray kVp/filtration, breast thickness and composition, exposure distribution and scatter-to-primary ratio. Phantom images were obtained with digital mammography units to demonstrate the feasibility of this technique.

**RESULTS:** It has been shown that the calcification signals are proportional to the thickness of the calcifications. The calcification signal-to-noise ratios are degraded. However, the structured background of tissue contrast was largely removed, resulting in improved visualization of microcalcifications. Although radiation scatter resulted in un-cancelled background, the residual background signals were small and smooth. Tissue composition measurements from the subtraction images were significantly affected by the presence of scatter. Its accuracy remains to be improved by scatter rejection or correction methods.

**CONCLUSIONS:** It is feasible to use dual-energy subtraction imaging technique to enhance the visualization of microcalcifications and to obtain tissue composition measurements. (This work was supported by a grant CA51248 from the National Cancer Institute and a grant from the Mike Hogg Foundation.)

#### 1167 • 2:57 PM

##### Stereomammography: Evaluation of Depth Perception Using a Virtual 3D Cursor

M.M. Goodsitt, PhD, Ann Arbor, MI • H. Chan, PhD • L.M. Hadjiiski, PhD

**PURPOSE:** We are evaluating the usefulness of stereomammography in improving breast cancer diagnosis. One area we are investigating is whether the improved depth perception associated with stereomammography might be significantly enhanced with the use of a virtual 3-D cursor. A study was performed to evaluate the accuracy of absolute depth measurements made in stereomammograms with such a cursor.

**METHOD AND MATERIALS:** A biopsy unit was used to produce digital stereo images of a phantom containing 50 low contrast fibrils (0.5 mm diameter monofilaments) at depths ranging from 0 to 10 mm, with a minimum spacing of 2 mm. Half the fibrils were oriented perpendicular (vertical) and half parallel (horizontal) to the stereo shift direction. The depth and orientation of each fibril were randomized, and the horizontal and vertical fibrils crossed simulating overlapping structures in a breast image. Left and right eye images were generated at angles of +/- 2.5 degrees. Three observers viewed these images on a computer display with stereo glasses and adjusted the position of a cross-shaped virtual cursor to best match the perceived location of each fibril. The x, y and z positions of the cursor were indicated on the display. The z (depth) coordinate was separately calibrated using known positions of fibrils in the phantom. The observers analyzed images of two configurations of the phantom. Thus, each observer made 50 vertical filament depth measurements and 50 horizontal filament depth measurements. These measurements were compared with the true depths.

**RESULTS:** The correlation coefficients between the measured and true depths of the vertically oriented fibrils for the 3 observers were 0.99, 0.97, and 0.89 with standard errors of the estimates of 0.39 mm, 0.86 mm, and 1.39 mm. Corresponding values for the horizontally oriented fibrils were 0.91, 0.28, and 0.08, and 1.91 mm, 4.37 mm, and 3.33 mm.

**CONCLUSIONS:** All observers could estimate the absolute depths of vertically oriented objects fairly accurately in digital stereomammograms; however, only one observer was able to accurately estimate the depths of horizontally oriented objects. This may relate to different aptitudes for stereoscopic visualization. The orientations of most objects in actual mammograms are combinations of horizontal and vertical. Further studies will be performed to evaluate absolute depth measurements of fibrils oriented at various intermediate angles and of objects of different shapes. The effects of the shape and contrast of the virtual cursor on the accuracy of the depth measurements will also be investigated.

#### 1168 • 3:06 PM

##### Comparison of Contrast-Detail Characteristics of Tomosynthetic Reconstruction Techniques for Digital Mammography

S. Suryanarayanan, MS, Worcester, MA • A. Karellas, PhD • S. Vedantham, MS • S.J. Glick, PhD • C.J. D'Orsi, MD • R.L. Webber, DDS, PhD

**PURPOSE:** To compare different tomosynthetic reconstruction techniques on the basis of their contrast-detail characteristics in a cluttered background.

**METHOD AND MATERIALS:** A contrast-detail phantom was fabricated with cluttered structures surrounding objects of interest, which were holes ranging from 0.18 mm to 4.82 mm in diameter and 0.06 mm to 0.73 mm in depth (Med-Optics, Tucson, AZ). A clinical prototype full-field flat panel mammographic imager (GE Medical Systems) was used throughout the study. The data were acquired at 7 discrete angles (in 60 steps) by moving the x-ray source through a 360 arc. The planar images were acquired at 26 kVp, 80 mAs and 26 kVp, 225 mAs respectively. The exposure parameters used for tomosynthesis were 26 kVp, 10 mAs/view and 26 kVp, 32

# CHICAGO

2000

World Congress on Medical Physics and Biomedical Engineering

JULY 23-28, 2000 NAVY PIER, CHICAGO, IL

## WELCOME LETTERS

### ORGANIZATIONAL INFORMATION

- Organizing Societies ◀
- Incorporated Meetings ◀
- Collaborating Organizations ◀
- Sponsoring Organizations ◀

### ORGANIZING COMMITTEE

### INTERNATIONAL ADVISORY COMMITTEE

### SCIENTIFIC PROGRAM COMMITTEE

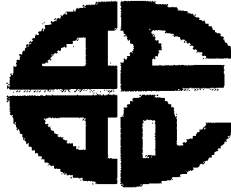
#### SCIENTIFIC PROGRAM

- How the Meeting is Organized ◀
- Keynote / Plenary Sessions ◀
- Program at a Glance/Exhibit Hours ◀
- Index of Scientific Tracks and Sessions ◀
- Student Paper Competition Presentations ◀
- Program of Meeting/Calendar of Events ◀
- Author Index ◀

### SOCIAL and COMPANIONS' PROGRAM



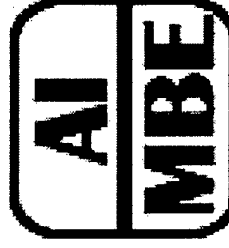
International Union for  
Physical and Engineering  
Sciences in Medicine



American Association of  
Physicists in Medicine



COMPOCPM  
Canadian Organization of Medical Physicists



The American Institute For Medical  
and Biological Engineering

International Federation  
for Medical and  
Biological Engineering



International Organization  
for Medical Physics



The Engineering in Medicine  
and Biology Society of the IEEE

## Tuesday, July 25, 2000 (continued)

- 3:10 pm TU-E206-05 Prelecture Quizzes Using WebCT in a Bioinstrumentation Course - J. Webster \*
- 3:20 pm TU-E206-06 Cardiovascular Anatomy, Physiology and Engineering - A Distance Learning Course - M. Lenart, P. Tarjan \*
- 3:30 pm TU-E206-07 Strategic Internet Tools for Education in the Context of the Medical Curriculum and Biomedical Engineering - M. Nyssen \*, R. Tielemans

-Room: 301

## TU-E301 Track 09: Auditory Prostheses

Chair: Mario Svirsky, Indiana University School of Medicine, Indianapolis, IN

- 2:00 pm TU-E301-01 Application of Stochastic Resonance in Electrical Stimulation - J. Rubinstein \*
- 2:20 pm TU-E301-02 Measurement of Auditory Nerve Activity in Response to Electrical Stimulation Using Neural Response Telemetry - P. Abbas \*, C. Brown, M. Hughes, C. Miller
- 2:40 pm TU-E301-03 Simulations of Cochlear Implant Signal Processing - P. Loizou \*, M. Dorman
- 3:00 pm TU-E301-04 A Computational Model of the Identification of Speech Sounds by Cochlear Implant Users - M. Svirsky \*
- 3:20 pm TU-E301-05 On the Optimization of Information Transmission Via a Cochlear Implant - L. Collins \*, S. Throckmorton, W. Ferguson

-Room: 303

## TU-E303 Track 01: Optical Imaging

Chair: Robert Kruger, Indiana University Medical Center, Indianapolis, IN

- 2:00 pm TU-E303-01 Optical Imaging of Biological Tissues in Turbid Media with Temporal Profile of Diffuse Photon - C. Wang \*, C. Sun, C. Chou, Y. Kiang, C. Yang, C. Lin
- 2:10 pm TU-E303-02 Analysis of Spectral Reflectance of Mucous Membrane for Endoscopic Diagnosis - M. Sambongi \*, M. Igarashi, T. Obi, M. Yamaguchi, N. Ohshima, M. Kobayashi, Y. Sano, S. Yoshida, K. Gono
- 2:20 pm TU-E303-03 Classification of Corneal Layers in Confocal Microscopy - A. Ruggeri \*, S. Pajaro, A. Vita
- 2:30 pm TU-E303-04 Cell Contour Detection in Corneal Endothelium In-Vivo Microscopy - M. Foracchia, A. Ruggeri \*
- 2:40 pm TU-E303-05 Automatic Detection and Quantification of Exudates in Retinal Images Using Shape Connectivity Measure - S. Krishnan \*, H. Li, O. Chutatape, D. Wong
- 2:50 pm TU-E303-06 Efficient Readout and Control Interface for Multi-Element Light Sensors in Low-Light-Level Applications. - Biological Tissue Fluorometry - J. Domingues \*, C. Correia
- 3:00 pm TU-E303-07 A New Transillumination System for the Correct Assessment of Subsurface Caries Lesions and Root Canals in Teeth - A. Wist \*, R. Sterne, P. Moon
- 3:10 pm TU-E303-08 In Situ Optical Biopsy with a Confocal Microendoscope - A. Gmitro \*, A. Rouse, Y. Sabharwal
- 3:20 pm TU-E303-09 An Efficient Approach for 3D Diffraction Tomography Using Spherical Wave Sources - X. Pan \*, M. Anastasio
- 3:30 pm TU-E303-10 Consistency Conditions and Data Redundancy in Nonlinear Diffraction Tomography - M. Anastasio \*, X. Pan

## Tuesday, July 25, 2000 (continued)

-Room: 305

## TU-E305 Track 01: CT/CT Reconstruction

Chair: Charles Wilson, Medical College of Wisconsin, Milwaukee, WI

- 2:00 pm TU-E305-01 Multislice CT Scanners: Image Quality Evaluation and Dose - D. Goodenough \*, S. Dyer
- 2:10 pm TU-E305-02 Patient Dose Optimisation Using a Four-Slice Spiral CT - F. Verdun \*, R. Meuli, P. Schnyder, J. Valley
- 2:20 pm TU-E305-03 CT Measurement of Lung Nodule Volumes - P. Judy \*, F. Jacobson, K. Zou, J. Levy
- 2:30 pm TU-E305-04 On Cone-Beam Reprojection of a 3-D Reconstruction and Its Applications - R. Galigekere \*, K. Wiesent, D. Holdsworth
- 2:40 pm TU-E305-05 Volume Reconstruction by a Fuzzy Logic Method in Tomographic Imaging - S. Vial, E. Coste \*, D. Gibon, J. Caudrelier, C. Vasseur, J. Rousseau
- 2:50 pm TU-E305-06 Multi-Slice CT Reconstruction Algorithm With Nonlinear Interpolation - J. Hsieh \*
- 3:00 pm TU-E305-07 A New Halfscan Algorithm for Multi-Slice CT Fluoroscopy - J. Hsieh \*
- 3:10 pm Student Paper Competition Finalist:  
TU-E305-08 Favorable Noise Properties of Fourier-Based Approaches to Interpolation in Helical CT with Implications for 3D Visualization - P. La Riviere \*, X. Pan
- 3:20 pm TU-E305-09 Analysis and Reduction of Image Noise in Short-Scan Fan-Beam Computed Tomography - X. Pan, P. La Riviere \*
- 3:30 pm TU-E305-10 Using Low Cost Graphics Hardware for CT Reconstruction - R. Molthen \*, R. Johnson, C. Dawson, S. Haworth

-Room: 307

## TU-E307 Track 01: Digital Mammography

Chair: Andrew Maidment, Thomas Jefferson University Hospital, Philadelphia, PA

- 2:00 pm TU-E307-01 Computer Aided Characterization of Mammographic Breast Parenchyma - R. Vargas-Voracek \*, C. Floyd
- 2:10 pm TU-E307-02 Monte Carlo and Experimental Evaluation of Scatter Characteristics in Mammography - V. Cooper \*, J. Boone, J. Seibert
- 2:20 pm TU-E307-03 Improved Contrast-To-Noise Ratios in Digital Mammography by Bayesian Image Processing - A. Baydush \*, C. Floyd
- 2:30 pm TU-E307-04 Automated 3-D Limited-View Binary Reconstruction of Breast Calcifications - A. Maidment \*, M. Albert
- 2:40 pm TU-E307-05 An Investigation of the Performance of Direct and Indirect Detection, Active Matrix, Flat-Panel Imagers (AMFPIs) Designed for Mammography - K. Jee \*, L. Antonuk, Y. El-Mohri, C. Cionca, M. Maolinbay, S. Nassif, Q. Zhao
- \* 2:50 pm TU-E307-06 Dual-Energy Digital Mammography With A Full Field Amorphous Silicon/Cesium Iodide Flat-Panel Detector - M. Lemacks \*, X. Liu, C. Shaw, G. Whitman, X. Rong
- 3:00 pm TU-E307-07 Generation and Evaluation of Physically Inspired Synthetic Mammograms - P. Bakic \*, M. Albert, D. Brzakovic, A. Maidment

## **Dual-Energy Digital Mammography With A Full Field Amorphous Silicon/Cesium Iodide Flat-Panel Detector**

M Lemacks\*, X Liu, C Shaw, G Whitman, X Rong, University of Texas M. D. Anderson Cancer Center

**Scientific Session:** *TU-E307-06* Digital Mammography

**Track:** 01 Diagnostic Physics, Medical Imaging, and Image Processing

Microcalcifications are often obscured by dense tissue structures present in mammography. This effect prevents breast cancer from being effectively detected in its early stage. A dual-energy digital mammography technique has been developed and investigated to improve detection and visualization of microcalcifications by eliminating the background tissue structures in the mammogram. The technique has been implemented and tested using a small field charge-coupled device (CCD) based detector and a full field amorphous silicon/cesium iodide flat-panel detector (both manufactured by General Electric Medical Systems, Inc., Milwaukee, WI) for digital mammography. Mammographic phantom images were obtained using 25-49 kVp x-rays generated with a Rhodium/Rhodium target/filter combination. The dual-energy subtraction algorithm employs externally measured total breast thickness information and fat images as a reference. Simulated microcalcifications of various sizes were overlapped with background tissue structures to demonstrate and quantify the improvement resulting from dual-energy subtraction imaging. The low- and high-energy images were subtracted with the weighting factors determined for optimal cancellation of background tissue structures. The resulting images demonstrated an increase in the noise level, which was expected, and an improvement in the detection and visualization of microcalcifications due to the removal of the background tissue structures. In this paper, dual-energy acquisition and subtraction processing schemes will be described and demonstrated with phantom images. Measured reduction of signal-to-noise ratios will be presented and discussed along with the accuracy of background cancellation.



*SPIE International Symposium on*

*Medical*

*Imaging*

*2001*

**17-22 February 2001**

**Town and Country Hotel  
San Diego, California USA**

### 4320-83, Poster Session

#### Dual Energy X-Rays Absorptiometry Using a 2D Digital Radiography Detector. Application to Bone Densitometry

Jean-Marc Dinten, Christine Robert-Coutant, Michel Darboux, (LETI CEA-Technologies Avancées, Département Systemes, CEA-Grenoble, 38054 Grenoble Cedex 9 France)

Dual Energy X-Rays Absorptiometry (DXA) is commonly used to separate soft tissues and bone contributions in radiographs. This decomposition leads to bone mineral density (BMD) measurement. Most clinical systems use pencil or fan collimated X-Rays beam with mono detectors or linear arrays. On these systems BMD is computed from 2D images obtained by scanning. Our objective is to take advantage of the now available flat panels detectors to propose a DXA approach without scanning, based on the use of cone beam X-Rays associated with a 2D detector. This approach leads to bone densitometry systems with an equal X and Y resolution, fast acquisition and reduced risk of patient motion.

Scatter becomes in this case an important issue. While on collimated systems scattering is insignificant, on cone beam systems its level and geometrical structure may severely alter BMD measurement. In our presentation an original DXA method taking into account scattering is proposed. This new approach leads to accurate BMD values.

In order to evaluate the accuracy of our new approach, a phantom representative of the spine regions tissue composition (bone, fat, muscle) has been designed. The comparison between the expected theoretical and the reconstructed BMD values validates the accuracy of our method. Results on anthropomorphic spine and hip regions are also presented.

### 4320-84, Poster Session

#### Dual-energy evaluation with a digital X-Ray detector

Régis Guillemaud, Christine Robert-Coutant, Michel Darboux, Jean-Jacques Gagelin, Jean-Marc Dinten ( LETI (CEA - Technologies Avancées), Département systèmes, CEA/Grenoble, 17. rue des Martyrs, F 38054 GRENOBLE cedex 9 FRANCE)

Dual-energy imaging has been proposed as a method for producing material-specific images, thus permitting separate examination of bone and soft-tissue structures. Interesting clinical results, particularly for chest, have usually been presented for screen-film or phosphor plate detectors and with single exposure. The purpose of the paper is to investigate double exposure dual-energy with a digital X-Ray detector.

The study is performed with a CCD-based large field digital X-Ray detector (Paladio detector, Apelem) installed on a remote table. Dual exposure is feasible on this detector with little registration problem because we have a very short delays ( $< 0.5s$ ) between two acquisitions

For each examination, two radiographies are acquired at two different high and low energies and with adapted X-ray tube filtrations. X ray generator energy voltages and filtrations are optimised in order to obtain thin energy peak spectra with good spectral separation (50 keV), much better than with single exposure system.

Tissue decomposition images are estimated from both acquisitions. The decomposition process is helped by the nice spectral separation. Scatter correction, applied to the raw dual-exposure acquisitions, provides an improvement of tissue decomposition. Results are presented for a chest phantom.

### 4320-86, Poster Session

#### Practical X-ray Scatter Measurements for Volume CT Detector Design

Timothy R. Fox, David T. Nisius, Hiroshi Aradate, Yasuo Saito (TF, DN Bio-Imaging Research, Lincolnshire, IL 60069. HA, YS Toshiba Medical Systems R & D Center, Otawara, Tochigi 324-8550 Japan)

To help design a volume CT scanner, we measured x-ray scatter through large irradiated volumes, with and without detector collimator. An x-ray tube (125 to 150 kV) with diaphragm irradiates volumes 25 to 200 mm thick. The scattering objects are water cylinders (diameters 200, 300,

and 500 mm). Complementary apertures (between the object and the detector collimator, along a line from the source) select "scatter" or "direct" detector signals. A direct-defining hole in a lead plate mounts over a pilot hole in a thin plastic sheet. With the lead plate removed, a scatter-defining plug fits into the pilot hole to block the same solid angle. We tested three styles of collimator: (1) Blades are two thick steel bars; the length changes and the spacing equals the detector aperture diameter. (2) In aluminum-interspaced lead grids, the spacing is smaller than the detector aperture. (3) Stacks are equally-spaced thin metal sheets, with gaps comparable to the detector aperture, and achieve low scatter at large aspect ratio. As a useful design approximation, for a given voltage and collimator, the scatter-to-direct ratio depends only on the irradiated volume.

### 4320-87, Poster Session

#### Direct Conversion Flat Panel Detector for Region-of-Interest Angiography

Arundhuti Ganguly, Stephen Rudin, Daniel R. Bednarek, Kenneth R. Hoffmann, Chang-Ying Yang, Zhou Wang (Departments of Physics, Neurosurgery, Radiology, Physiology and Biophysics, Toshiba Stroke Research Center, SUNY Buffalo, Buffalo, NY-14214)

Minimally invasive image-guided interventions require very high image resolution and quality, specifically over regions-of-interest (ROI) crucial to the procedure. An ROI high quality image allows limited patient radiation exposure while permitting rapid frame transfer rates. Considering current developments in direct conversion Flat Panel Detectors (FPDs), advantages of such an imager for ROI angiography were investigated. The performance of an amorphous-selenium based FPD was simulated to evaluate improvements in MTF and DQE under various angiographic imaging conditions. The detector envisioned incorporates the smallest pixel size of 70  $\mu m$ , reported to date, and a photoconductor thickness of 1000  $\mu m$  to permit angiography.

The MTF of the FPD is calculated to be 65% at the Nyquist frequency of 7.1 lp/mm compared to 6% for a previously reported CsI(Tl) based ROI CCD camera. The DQE(0) of the FPD at 1.5mR and 70 kVp is 75% while for the CCD camera is 35%. At 7.1 lp/mm, the FPD's DQE is 31% while for the CCD camera it is 6%. Images of an undeployed stent with 70  $\mu m$  pixel mammography FPD prototype, compare favorably with images acquired with the CCD camera.

Thus a practical direct flat-panel ROI detector with both improved performance and physical size is proposed.

### 4320-88, Poster Session

#### Comparison of a-Si:H CsI Flat-Panel Digital Imaging Systems with a CCD based System, CR Systems, and Conventional Screen-Film systems – A Contrast-Detail Phantom Study

John X. Rong, Chris C. Shaw, Xinming Liu, Michael Lemacks, and Stephen K. Thompson (Univ. of Texas M. D. Anderson Cancer Center, Houston, TX 77030)

The contrast detail curves for a flat-panel digital chest system were measured and compared to those measured for a CR system and a conventional screen/film system. Exposures were varied to study the potential for the reduction of patient exposure. kVp and image processing protocols were varied to study their effects on contrast detail curves. The results demonstrated that in chest imaging, the flat-panel system performed significantly better than the CR and screen/film systems while the latter two systems performed about the same. Alternatively, an exposure reduction by at least 70% is possible if the same performance is maintained. It was found that the kVp has little effect on contrast detail curves. Image processing protocol, on the other hand, is essential to achieving optimal contrast detail curves for digital imaging techniques. For mammographic imaging, minimum detectable calcification size was determined and compared for a flat-panel system, a CCD-based system, a high resolution CR system and the conventional screen/film system. Images of simulated calcifications of pre-sorted sizes were acquired and

read to determine the minimum detectable calcification size for various imaging conditions. The results will be presented to compare the low contrast performance of the four different mammographic imaging systems.

**4320-89, Poster Session**

\* **Comparison of a-Si:H/CsI Flat-Panel Digital Imaging Systems with CR and CCD Based Systems- Image Quality Measurements**

Xinming Liu, Chris C. Shaw, Xiujiang J. Rong, Michael Lemacks (University of Texas M.D. Anderson Cancer Center, Houston, TX 77030 4009)

For chest imaging, an a-Si:H/CsI flat-panel system (Revolution XQ/i, GEMS) and a CR system (AC3 with ST-VN plate, Fuji Medical Systems) were compared for their MTFs and DQEs at selected exposure levels. For mammographic imaging, a flat-panel system (SenoGraphe2000, GEMS), a CCD-based system (SenoVision, GEMS) and a CR system (AC3 with HR-V plate) were compared. The tilted slit method was used to measure the MTFs. The 2-D Fourier transform method was used to measure the NPSs and DQEs. Measurements over multiple Region-of-Interest's from a series of identical exposures were averaged to reduce fluctuations.

For chest imaging, the flat-panel system was shown to have slightly lower MTF but significantly higher DQEs than the CR system. For mammographic imaging, the CCD-based system was found to have the highest MTF, followed in order by the flat-panel and CR systems. The flat panel system was found to have the highest DQEs, followed in order by the CCD-based and CR systems. The DQEs of the flat-panel systems were found to increase with exposure while those of the CR systems decrease slightly with the exposure in both chest and mammographic imaging. The DQEs of the CCD-based system were also found to increase with the exposure but only slightly.

**4320-90, Poster Session**

**DQE Measurement Results for Direct and Indirect Digital Radiography Detectors**

Ehsan Samei, Michael J. Flynn, Harrell G. Chotas, James T. Dobbins, III (Department of Radiology, Duke University Medical Center, Durham, NC 27710-3302) (MJF: Department of Radiology, Henry Ford Health System, Detroit, MI 48202)

Current flat-panel detectors either use direct conversion of x-ray energy to electronic charges or use indirect conversion with an intermediary optical conversion process. The purpose of this work was to compare the direct and indirect detectors in terms of the modulation transfer function (MTF), the noise power spectrum (NPS), and the detective quantum efficiency (DQE) of these systems. Measurements were made on four flat-panel detectors, Philips Digital Diagnost, GE Revolution XQ/i, Direct-Ray/Hologic DR1000, and Varian Pixscan2520. The presampled MTF of the systems was measured using an edge method (Samei et al. *Med Phys* 25:102, 1998). The NPS of the systems at 70 and 120 kVps and a range of exposure levels was determined by 2D Fourier analysis of uniformly-exposed radiographs (Flynn et al. *Med Phys* 26:1612, 1999). The DQE was assessed from the measured MTF, NPS, and exposures, and estimated values for the ideal signal-to-noise ratio. To date, measurements have been made on a Pixscan-2520 system. MTF was relatively independent of kVp and direction, resulting in a MTF of 0.1 at 3.9 cycles/mm. The DQE(0) was 0.86 and 0.57 at 70 kVp and 120 kVp, respectively. At the meeting, results will be reported on the other detector devices.

**4320-91, Poster Session**

**Comparison of the Imaging Physics Performance of a Prototype Flat Panel Detector with a 400 Speed Screen-Film System**

Walter Huda, Kent Ogden, Marsha L Roskopf, Charles Rush (SUNY Upstate Medical University, Syracuse, NY 13210) (CR InfiMed Inc., Liverpool, NY 13088)

The study compared the performance of a digital radiography system that included a prototype flat panel detector (StingRay) with a 400 speed screen-film system. The flat panel detector consisted of a 500 micron CsI scintillator and an image matrix of 3k. The limiting spatial resolution of screen-film (~4 line pairs/mm) was superior to that of the flat panel detector (~2.5 line pairs/mm). The digital detector had an excellent linearity response ( $r^2 = 0.997$ ), a dynamic range of ~20,000:1, and saturated at ~60 mR. At exposures > 50 µR, the flat panel noise performance was dominated by quantum mottle. At the radiation exposure level required to produce a film density of 1.8, the low contrast performance of the flat panel detector was similar to that of the screen-film system. Changes in radiation exposure, however, significantly affected the performance of the flat panel detector, whereas the performance of screen-film was constant for film densities between 1.5 and 2.5. The flat panel imaging system produced images for review in ~13 seconds, which is much faster than the 90 second processing time of film. Raw image data sets acquired using the digital detector demonstrated the four individual sub-panels, which can ultimately be eliminated by processing, and were not deemed to interfere with clinical diagnosis. The flat panel detector investigated in this work offers a wide dynamic range, excellent linearity performance and the rapid availability of digital images. The digital detector will permit a reduction in radiation exposure where the detection task is relatively easy, or when the radiation to the patient is of specific concern.

**4320-92, Poster Session**

**Low Light Level Charge-Coupled Device; Evaluation and Performance for Application in Medical Imaging**

Emma Harris, Gary Royle, Robert Speller (Department of Medical Physics, University College London, Shropshire House, 11-20 Capper Street, London WC1E 6JA U.K.)

Work is being undertaken to evaluate the performance of a new low light level CCD that exhibits low noise characteristics and a greatly improved sensitivity, for the application to digital fluoroscopy. The low light level CCD has been developed by Marconi Applied Technologies. The image sensor in the camera is a frame transfer charge-coupled device with an image size of 576 x 288 pixels and a pixel size is 20 x 30 µm<sup>2</sup>. The readout is standard 625-line video producing 25 frames per second at a pixel read out rate of 11.109MHz.

An optical evaluation of CCD performance characteristics has been undertaken using a diffuse LED light source. Measurements of system gain, device linearity, dynamic range and the maximum SNR achievable has been obtained. In order to evaluate the x-ray imaging capabilities measurements of DQE have been made using x-ray phosphor screens optically coupled to the CCD. The implications of these results to image quality will be discussed. An evaluation of the image quality achievable at low light level (low x-ray exposure) will be given including the minimum exposure necessary to obtain the image quality required for digital fluoroscopy.

**4320-93, Poster Session**

**Electronic noise analysis of a 127 micron pixel TFT/photodiode array**

Richard L. Weisfield, Robert Bennett (dpiX, Palo Alto, CA, 94304)

In this paper we examine origins of electronic noise in a 127 micron pixel TFT/ photodiode image sensor array. The imaging array is a 1536 data line by 1920 gate line sensor array connected to low noise charge

# Medical Physics

AVAILABLE ONLINE—See <http://www.medphys.org>

August 2001

Volume 28, Number 8

<b>RADIATION PROTECTION PHYSICS</b> .....	1543–1551
<b>Point/Counterpoint</b> .....	1543–1545
<b>RADIATION IMAGING PHYSICS</b> .....	1552–1619
<b>MAGNETIC RESONANCE IMAGING</b> .....	1620–1651
<b>ULTRASONOGRAPHY</b> .....	1652–1659
<b>NUCLEAR MEDICINE PHYSICS</b> .....	1660–1678
<b>RADIATION THERAPY PHYSICS</b> .....	1679–1792
<b>THERMOTHERAPY PHYSICS</b> .....	1793–1805
<b>FLUORESCENCE MEASUREMENTS</b> .....	1806–1810
<b>Ph.D. THESES ABSTRACTS</b> .....	1811–1812
<b>WORKS IN PROGRESS: 2001 AAPM ANNUAL MEETING</b> .....	1815–1834

Reproduced From  
Best Available Copy

Published by the American Association of Physicists in Medicine (AAPM) with the association of the Canadian Organization of Medical Physicists (COMP) and the Canadian College of Physicists in Medicine (CCPM) through the American Institute of Physics. *Medical Physics* is the official science journal of the AAPM and is an official science journal of COMP/CCPM.

**SU-HH-EXH C-14****Microcalcification Detectability for Four Mammographic Detectors: Flat-Panel, CCD, CR and Screen/Film**

J Rong\*, C Shaw, D Johnston, M Lemacks, X Liu, G Whitman, T Stephens, M Dryden, S Thompson, K Krugh, M.D. Anderson Cancer Center, Houston, TX

Amorphous silicon/cesium iodide (a-Si:H/CsI:TI) flat-panel based full-field digital mammography (FFDM) systems have recently become commercially available for clinical use. Some investigations on physical properties and imaging characteristics of these types of detectors have been conducted and reported on. In this perception study, a phantom containing simulated microcalcifications of various sizes was imaged with four detector systems: a flat-panel based, a charge coupled device (CCD) based, a high resolution computed radiography (CR) and a conventional screen/film system. The images were reviewed by mammographers as well as non-radiologist participants. Scores reflecting confidence levels were given and recorded for each detection task. The results were used to determine the minimum detectable calcification size. Receiver Operating Characteristics (ROC) analysis was also performed to evaluate and compare the overall detection accuracy for these four detector systems. Differences in microcalcification detectability were found to be insignificant for the larger group (150 - 160  $\mu\text{m}$  in size) or smaller group (112 - 125  $\mu\text{m}$  in size). For calcifications of 125 - 140  $\mu\text{m}$  in size, the flat-panel system was found to have the best performance: the smallest minimum detectable calcification size and the highest detection accuracy in the ROC analysis. The screen/film system was ranked the second with a performance significantly better than those of the CR or the CCD systems. In the ROC analysis, the CCD system showed better detection accuracy than the CR system. However, no significant difference was observed in the minimum detectable calcification size between the CCD and the CR systems.

**SU-HH-EXH C-15****Comparison of Flat-panel, CR and CCD Based Detectors for Digital Mammography: MTF and DQE Measurements**

X Liu\*, C Shaw, X Rong, UT M.D. Anderson Cancer Center, Houston, TX

The amorphous silicon/cesium iodide (a-Si:H/CsI:TI) flat panel imaging systems have recently become commercially available for mammographic imaging applications. We have measured the Modulation Transfer Functions (MTFs) and Detective Quantum Efficiencies (DQEs) for a commercial flat-panel based full-field digital mammography (FFDM) system (SenoGraphe 2000, GE Medical Systems, Milwaukee, WI) and compare them with those for a CR (AC3 reader with HR-V plate, Fuji Medical Systems, Stamford, CT) and a CCD based (SenoVision, GE Medical Systems, Milwaukee, WI) system. The tilted slit method was used to measure the pre-sampling and phase-averaged MTFs. Noise Power Spectra (NPSs) were computed from uniform exposure data using the 2-D Fourier transform method. Subtraction of image pairs from a series of identical exposures was used to remove structured variations. Measurements over multiple region-of-interest's (ROIs) and from different image pairs were averaged to reduce fluctuations. MTF, NPS and DQE measurements were performed for various detector exposures to study their effects on image quality.

It was found that the CCD-based system has the best MTF, followed by the flat-panel and then by the CR system. The flat-panel system has higher DQEs than the CCD-based system at higher exposure levels. The DQEs of the two systems are comparable to each other at lower exposures but followed distantly by those of the CR system. The DQEs of flat-panel system increase with exposure while those of CR system decrease with exposure.

**SU-HH-EXH C-16****A New Temperature Imaging Scheme for MR-Guided Focused Ultrasound Breast Tumor Ablation**

T. Wu, J. Felmlee\*, R. Grimm, J. Rydberg, Mayo Clinic, Rochester, MN

Water proton resonant frequency (WPRF) shift imaging has been used by most researchers for temperature monitoring during MR-guided focused ultrasound (FUS) ablation therapy. Currently, FUS ablation treatment for breast cancer is undergoing clinical trial at our site. Due to high percentage of fat content in the breast, WPRF shift imaging cannot provide adequate temperature monitoring for the treatment. In this study, we are developing a new temperature-imaging scheme to solve this problem. A prototype MR-compatible FUS ablation system and a 1.5T MR imaging system were used in the study. Experiments were conducted in a cadaver breast and tissue-mimicking bovine gelatin phantoms. A spin-echo sequence was modified and optimized to acquire three temperature images in 4 seconds with 16-cm FOV, 256x64 acquisition matrix, TR=100 ms, TE=20 ms and a 5-inch coil. Temperature images were acquired using this modified spin-echo sequence, and also a fast spin-echo and a fast gradient-echo sequences. All the images were compared based on acquisition time, spatial resolution, SNR, volume coverage and the capability for simultaneous WPRF shift imaging and T1 relaxation temperature mapping. The spin-echo sequence showed its overall superiority. Currently, we are implementing a spin-echo based MR imaging sequence, in which a gradient-echo readout was added after the regular spin-echo readout gradient, to simultaneously monitor both magnitude and phase change caused by temperature variation. It is anticipated that the new spin-echo based imaging sequence will provide sufficient contrast for temperature change in both fat and muscle tissues with required temporal resolution.

**SU-HH-EXH C-17****Methods for Determining Myocardial Blood Volume & Flow using Contrast-Enhanced MRI**

N Pongnapang<sup>1</sup>, G Clarke\*<sup>1</sup>, B Rubal<sup>2</sup>, C Belden<sup>2</sup>, M Lane<sup>2</sup>, (1) UT Health Sciences Center, San Antonio, TX, US, (2) Brooke Army Medical Center, Fort Sam Houston, TX

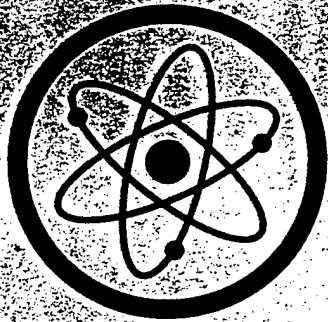
Clinical cardiac MRI packages have recently become available for evaluating myocardial perfusion using rapid cardiac imaging methods and power-injected contrast agents. This presentation will review the basic methodology and present examples using data obtained from two different makes of MRI scanners obtained in both humans and a porcine model. We shall also explain how this approach can be used to obtain significant physiological measurements with proper calibration. Both myocardial blood volume and myocardial blood flow can be determined if the arterial input function and the change in the longitudinal relaxation time ( $T_1$ ) during the time that the contrast agent is traversing the myocardium can be determined. We shall look at two approaches for ascertaining  $T_1$ , one that relies on external calibration of samples of the contrast agent at known dilutions and a second method that attempts to evaluate the myocardial  $T_1$  directly. Blood volume and blood flow are then analyzed by using a tracer-kinetic model that yields a first-order differential equation and solving that equation for the partition coefficient and the blood volume using a Levenberg-Marquardt algorithm. The presentation shall end with a discussion of potential applications of this method, including a brief discussion of parallels and contrasts with thallium SPECT myocardial perfusion imaging.

**SU-HH-EXH C-18****Correlation of Myelination Determination by Magnetization Transfer Imaging and Proton Spectroscopy in the Developing Brain**

B Rajagopalan\*, D Wilson, Oklahoma University Health Sciences Center, Oklahoma, OK

The development of cognitive and motor skills in children is an area of intense interdisciplinary research where the knowledge of the structure and function of the brain is integrated. Magnetic resonance imaging (MRI) and magnetic resonance spectroscopy (MRS) provide anatomical and functional information and thus has the potential to study brain maturation *in vivo*. One such aspect of brain maturation that has been studied by MRI and MRS is the myelination process. The creation of myelin in the

# Scientific Programs



from  
**Science**  
to  
**Patient Care**  
RSNA 2001

## 87th Scientific Assembly and Annual Meeting

Including sessions in joint sponsorship with  
American Association of Physicists in Medicine

November 25 - 30, 2001

McCormick Place — Chicago, Illinois

# RSNA

Radiological Society  
of North America  
Founded in 1916

820 Jorie Boulevard  
Oak Brook, IL 60523  
630/571-2670  
FAX: 630/571-7837  
E-MAIL: [programs@rsna.org](mailto:programs@rsna.org)

Paper No.: 969

Title: Comparison of an a-Si:H/CsI:Tl Flat-Panel-based Digital Mammography System with CR and CCD-based Systems

Scheduled For: Wednesday, November 28, 2001 at 11:06AM

Location: S402AB

Presentation Time: 6 minutes with a 3 minute discussion period

Presenter:

Xinming Liu, PhD

Dept of Diagnostic Radiology (Box 57)

MD Anderson Cancer Center

1515 Holcombe Blvd

Houston, TX 77030

We are pleased to inform you that your above captioned abstract has been accepted for presentation as a scientific paper at our 87th Scientific Assembly and Annual Meeting at the time and place indicated. The enclosed information will give you complete details concerning procedures and requirements. Please read it thoroughly as each item has been carefully prepared to optimize your presentation.

Your abstract will be published in the program book which is also a part of the permanent literature, citable for authors and retrievable for readers. The program will be mailed in mid-October to all members of the Society and to all subscribers of *Radiology*. The circulation is in excess of 34,000. The program is also available at the meeting and is posted on the RSNA Web site.

It is very important that you return the enclosed forms A,B,C and D by **July 27, 2001** signifying that you accept this offer of presentation. If you wish to make a change in the presenter of your paper, indicate this on form A. If you have any questions please contact the Society office at 630-571-7874 or by e-mail at [programs@rsna.org](mailto:programs@rsna.org).

We strongly encourage early submission of a complete manuscript (three copies) for publication in *Radiology*, or *Medical Physics*.

Also, please be sure to register early for the meeting. Meeting presenters who register before the registration deadline of October 26 receive complimentary registration. After this date the registration fee is \$100.

Please accept our congratulations on your success and our thanks for your support of the RSNA.

Sincerely,

George S. Bisset III, MD

Chairman

RSNA Program Committee

David R. Pickens, PhD

Chairman

AAPM Program Committee

## **Comparison of an a-Si:H/CsI:Tl Flat-Panel Based Digital Mammography System with CR and CCD Based Systems**

Xinming Liu, Chris C. Shaw, Xiujiang J. Rong

**PURPOSE:** To investigate and compare the physical properties of a cesium iodide/amorphous silicon based flat-panel digital mammography system with computed radiography (CR) and CCD based systems.

**METHOD/MATERIALS:** The performance of a cesium iodide/amorphous silicon flat-panel based full-field digital mammography unit (SenoGrappe 2000D by General Electric Medical System) has been evaluated and compared to those of a high resolution CR system (AC-3 reader with HR-V plates, Fuji Medical Systems) and a CCD based small field mammography system (SenoVision by General Electric Medical System). Signal linearity, modulation transfer function (MTF), noise power spectrum (NPS), noise equivalent quanta (NEQ), and detective quantum efficiency (DQE) were measured at selected mammographic techniques. The results were used to characterize and compare the properties of the three imaging systems.

**RESULTS:** The pre-sampling MTF of the flat-panel system was slightly lower than that of CCD based system but higher than that of CR system. The NPSs of the flat-panel system were generally lower than those of CCD based and CR systems. The flat-panel system was found to have the highest DQEs, followed in order by the CCD-based and CR systems. The DQEs of the flat-panel system were found to increase significantly with the exposure while those of the CR system decrease slightly with the exposure. The DQEs of the CCD-based system were found to vary little for exposures ranging from 0.9 to 30.3mR.

**CONCLUSIONS:** It has been found from our measurements that the CCD based system demonstrated highest spatial resolution while the flat-panel system demonstrated highest DQEs for detector exposures ranging from 3.85 to 31.3mR.

This work was supported in part by a research grant CA51248 from the National Cancer Institute and a research grant DAMD17-00-1-0316 from the US Army Breast Cancer Research program.